

**FRACTURE MECHANISMS AND STRUCTURAL FRAGILITY OF
HUMAN FEMORAL CORTICAL BONE**

by

Tengteng Tang

A DISSERTATION SUBMITTED IN PARTIAL FULFILLMENT OF
THE REQUIREMENTS FOR THE DEGREE OF

DOCTOR OF PHILOSOPHY

in

The Faculty of Graduate and Postdoctoral Studies
(Materials Engineering)

THE UNIVERSITY OF BRITISH COLUMBIA

(Vancouver)

April 2018

© Tengteng Tang, 2018

Abstract

Hip fracture has serious repercussions at both the societal and personal levels. For better fracture prevention, it is essential to understand the material changes of femoral cortical bone that contribute to hip fragility, and the deformation and fracture process during hip fractures. Therefore, the aim of this dissertation was to study the mechanisms of hip fracture from both structural and mechanical perspectives.

Using quantitative backscattered electron (qBSE) imaging and polarized Raman microspectroscopy, periosteal hypermineralization in aged human proximal femur was found with significantly higher mineral content/mineral-to-matrix ratio than lamellar bone. Accompanying the increased mineralization was the “brittle” cracking behavior upon microindentation in the hypermineralized tissue. Small- and wide-angle X-ray scattering (SAXS/WAXS) measurement showed substantially thinner, shorter and more irregularly distributed mineral platelets in the hypermineralized region, indicating the material changes at the ultrastructural level.

Combined second harmonic generation (SHG) and two photon excitation fluorescence (TPEF) techniques were used to study shear microcracking and its association with the organization of collagen fibrils in the femoral cortical bone. Unique arc-shaped shear microcracks, differing from either tensile or compressive microcracks, were identified at the peripheral zone of the osteons. These microcracks were further located within the “bright” lamellae where collagen fibrils are primarily oriented at the circumferential direction to the osteons’ long axes.

Microcracking analysis on clinically retrieved femoral neck components identified shear, compressive and tensile microcracks associated with major fractures. The results pointed to the central role of the superior cortex in resisting a hip fracture, whereby higher density of microcracks

and buckling failure were found in the superior cortical bone. BSE imaging at the fracture sites found the direct involvement of hypermineralization, which lacked crack deviation and had fewer microcracks than the tough lamellar bone.

This dissertation answered fundamental questions regarding the role of femoral cortical bone in clinical hip fractures, and elucidated the underlying failure mechanisms due to microstructural changes and the complex stress states under external loading. The findings thus provided new insights into better identifying at-risk population of hip fracture.

Lay Summary

Hip fractures befall more than 1.66 million people globally per year, resulting in a hip fracture event every twenty seconds. About 20 % of the hip fracture patients die within the first year following the incident, and up to one third of those who survive the hip fracture never regain their previous level of function. This injury typically occurs in the older adults due to low-energy falls, which rarely happen in younger people. Thus, the questions intended to be addressed here are why some seniors are more susceptible to such injuries, and what makes his or her hip bone fragile. A novel approach was adopted to answer this question by starting from patients who have sustained a hip fracture. By combining laboratory material and micromechanical analyses on the elderly femoral bone tissue and fracture analysis of the clinically retrieved femoral bone components, this thesis shed light on the material and structural nature of hip fragility.

Preface

A version of Chapter 4 has been re-submitted for publication after revision. T. Tang, W. Wagermaier, R. Schuetz, P. Fratzl, and R. Wang (2017). Hypermineralized tissue in human proximal femur has smaller and disorganized bone minerals. T. Tang conducted all the experiments with the exception of a few Raman microscopy measurements (RS). T. Tang wrote the manuscript. Note that part of the Introduction in the manuscript has been moved to the literature review (Chapter 1).

A version of Chapter 5 has been published as an original full length paper. T. Tang, V. Ebacher, P. Cripton, P. Guy, H. McKay, and R. Wang (2015). Shear deformation and fracture of human cortical bone. *Bone*. 71:25-35. T. Tang conducted all the experiments and wrote the manuscript. Note that part of the Introduction in the original publication has been moved to the Introduction (Chapter 1) of this dissertation.

A version of Chapter 6 has been published as an original full length paper. T. Tang, P. Cripton, P. Guy, H. McKay, and R. Wang (2018). Clinical hip fracture is accompanied by compression induced failure in the superior cortex of the femoral neck. *Bone*. 108:121-131. T. Tang conducted all the experiments. T. Tang wrote the manuscript. Note that part of the Introduction in the original publication has been moved to the Introduction (Chapter 1) of this dissertation.

The study was approved by the Clinical Research Ethics Review Board at the UBC (Ethics Certificate #H09-02073).

Table of Contents

Abstract	ii
Lay Summary	iv
Preface.....	v
Table of Contents	vi
List of Tables	xi
List of Figures	xii
List of Symbols	xxiv
List of Abbreviations	xxv
Acknowledgements.....	xxvi
Dedication	xxviii
Chapter 1 Introduction	1
1.1 Hip anatomy and types of fracture.....	3
1.1.1 The hip joint.....	3
1.1.2 Intra- and extra-capsular hip fractures	4
1.2 Age-related hip fractures: an overview on etiology.....	5
1.2.1 Sideways falls in the elderly	5
1.2.2 Clinical assessment	6
1.3 The material bone: the hierarchical structure.....	7
1.3.1 Cortical and trabecular bone	7
1.3.2 Unique features of human femoral neck.....	9
1.3.3 The microstructure	11
1.3.4 Bone minerals and organic matrix	15
1.4 Bone biomechanics	19
1.4.1 Human proximal femur under a sideways fall.....	19
1.4.2 Deformation and fracture mechanisms of bone	21
1.5 Summary of current problems	27
Chapter 2 Goal and Objectives	29
Chapter 3 Hypermineralized Tissue in Human Proximal Femur: Distribution, Mineralization and Micromechanical Properties	32

3.1 Experimental.....	33
3.1.1 Specimen preparation.....	33
3.1.2 Optical microscopy	35
3.1.3 Quantitative backscattered electron (qBSE) imaging.....	35
3.1.4 Microindentation.....	37
3.1.5 Statistical analysis.....	39
3.2 Results.....	39
3.2.1 Morphological features	39
3.2.2 Area fraction and thickness ratio of hypermineralized tissue in total cortical bone.....	42
3.2.3 Bone mineralization density distributions (BMDDs)	43
3.2.4 Micromechanical properties of hypermineralized tissue	47
3.3 Discussion.....	49
3.3.1 Occurrence of hypermineralization.....	49
3.3.2 Mineral content and the higher degree of mineralization in hypermineralized tissue	50
3.3.3 The easier cracking behavior of hypermineralized tissue.....	51
3.3.4 Limitations	53
3.4 Conclusions.....	54
Chapter 4 The Size and Organization of Mineral Platelets in the Hypermineralized Tissue*	55
4.1 Experimental.....	56
4.1.1 Specimen preparation.....	56
4.1.2 Optical microscopy and backscattered electron imaging.....	57
4.1.3 Polarized Raman microspectroscopy	58
4.1.4 Scanning small angle X-ray scattering (SAXS).....	59
4.1.5 Scanning small- and wide-angle X-ray scattering (SAXS/WAXS) using synchrotron radiation	61
4.1.6 Statistical analysis.....	62
4.2 Results.....	63
4.2.1 Relative mineral/organic contents and polarization effects	63
4.2.2 Mineral platelet thickness and degree of orientation	66

4.2.3 Mineral platelet thickness and length using synchrotron SAXS/WAXS.....	69
4.2.4 Spatial organization of mineral platelets using $G(x)$ curves	72
4.3 Discussion.....	73
4.3.1 Mineral-to-matrix ratio and matrix organization	73
4.3.2 Thinner, shorter and less organized mineral platelets in the hypermineralized tissue	74
4.3.3 Implication to fracture risk.....	76
4.3.4 Limitations	76
4.4 Conclusions.....	77
Chapter 5 Shear Deformation and Fracture of Human Femoral Cortical Bone*	78
5.1 Materials and methods	79
5.1.1 Specimen preparation.....	79
5.1.2 Shear testing.....	81
5.1.3 Digital image correlation and strain analysis.....	82
5.1.4 Microcracking analysis	83
5.2 Results.....	85
5.2.1 Effects of loading orientation on mechanical properties and strain development.....	85
5.2.2 Macro-scale fracture patterns.....	89
5.2.3 Microcracking and unique arc-shaped microcracks	91
5.2.4 Relation between microcracks and bone lamellae	93
5.3 Discussion.....	96
5.3.1 The anisotropic shear behavior and the structural effects on fracture	97
5.3.2 Shear-induced microcracks: the unique microcracking pattern.....	98
5.3.3 Role of osteonal lamellae, collagen fibrils, cement line and lamellar interface	99
5.3.4 Limitations	102
5.4 Conclusions.....	103
Chapter 6 Fracture Mechanisms of Clinical Hip Fractures and the Possible Role of Hypermineralization*	104
6.1 Experimental.....	105

6.1.1 Subjects and samples collection.....	105
6.1.2 Specimen preparation.....	105
6.1.3 Microcrack analysis	108
6.1.4 Microstructural analysis.....	110
6.2 Results.....	111
6.2.1 Macroscopic fracture	111
6.2.2 The amount of microcracks	113
6.2.3 Microcrack patterns in normal cortical bone and the dominant stress states	116
6.2.4 Occurrence of hypermineralization.....	120
6.2.5 Macro- and micro-cracking in hypermineralized tissue	123
6.3 Discussion.....	125
6.3.1 Macroscopic features of clinical hip fractures	126
6.3.2 Different strain and stress conditions in the superior versus the inferior cortex	127
6.3.4 The possible role of hypermineralization in clinical hip fracture	130
6.3.5 Limitations	131
6.4 Conclusions.....	133
Chapter 7 Conclusions and Recommendations.....	134
General conclusions	134
Recommendations for future work	138
References.....	140
Appendix	180
Appendix A chapter 3—supplemental materials	180
Donor information, total proximal femur areal bone mineral density (aBMD) and <i>T</i> -scores.....	180
Morphological features associated with femoral neck hypermineralization	181
Hypermineralization with optical microscopy and backscattered electron imaging	182
Validation of backscattered electron imaging linearity	183
Microhardness in calcified fibrocartilage	184

Appendix B chapter 4—supplemental materials	185
Donor information, total proximal femur areal bone mineral density (aBMD) and <i>T</i> -scores	185
Carbonate-to-phosphate ratio	186
Mineral thickness, length and degree of orientation measured by synchrotron radiation	187
<i>G</i> (<i>x</i>) curves and the fitted parameters obtained from laboratory SXA measurements	189
Appendix C chapter 5—supplemental materials	190
Pre-existing microcracks.....	190
Different failure modes of 30°-oriented specimens	191
Different types of microcracks found in the human cortical bone under shear ..	193
Appendix D chapter 6—supplemental materials	195
Information on all the retrieved femoral neck fractured samples	195
Macroscopic fractures for all the retrieved femoral neck samples	197
Microcrack density scores at various locations and the highest microcrack density score	198
Microcrack pattern at the fracture surface of inferior cortical bone	199

List of Tables

Table 3. 1 Ca_{peak} values obtained from the BMDDs as measured by qBSE in the Haversian bone (Hav), interstitial bone (Int) and hypermineralized tissue (Hymin) of six human proximal femora from different anatomical locations.....	46
Table 4. 1 Mineral platelets thickness (T) and degree of orientation (ρ) as measured by laboratory SAXS. The tests were performed in cortical bone (Cort), trabecular bone (Trab) and hypermineralized tissue (Hymin), and at mid-femoral neck (Neck) and intertrochanter (Tro)....	69
Table 5. 1 Bone mineral density, shear mechanical properties and fracture features of human cortical bone under shear at different orientations.....	87
Table S3. 1 Donor sex, age, side from which the femur was obtained and DXA-measured BMD and T -scores for the femora used in this study	180
Table S4. 1 Donor sex, age, side from which the femur was obtained and DXA-measured BMD and T -scores for the femora used in this study	185
Table S6. 1 Sex, Age, and the fracture side (L= left, R= right) from which specimens were obtained	195

List of Figures

- Fig. 1. 1** Illustration of human proximal femur from the posterior view (left) and anterior view (right). Main structure features include femoral head, neck, greater and lesser trochanter. Graphic reprinted and adapted from [22] (Fig. 6.8) with permission from Elsevier. 4
- Fig. 1. 2** Camera and X-ray images and illustration of the general features found in the human proximal femur: (a) A coronal plane showing the porous trabecular bone core and the surrounding cortical bone shell. Reprinted and adapted from [77] (Fig. 7) with permission from Elsevier; (b) Characteristic structural features of the cortical bone: Haversian systems/osteons, interstitial bone, circumferential periosteal and endosteal lamellae, and periosteum. Reprinted and adapted from [56] (Fig. 2.2, p41 and Fig. 2.3 p43) with permission from Springer. 10
- Fig. 1. 3** Lamellar bone microstructure: (a) White reflective light image of a transverse section (with respect to the long axis of the femoral shaft) showing Haversian system (e.g. white dashed frame); (b) SHG signal demonstrates a better contrast and finer details of the collagen orientation in the osteon. The bright red signal corresponds to collagen fibres oriented at large angle to the osteon's long axis, and the darker layer corresponds to collagen fibres aligned at smaller angle to the osteon's long axis; (c) SEM image of a fracture surface of the lamellar bone; (d) Schematic illustration of the rotated plywood structure where each pair of lamellae consists of five sublayers. (c) and (d) reprinted and adapted from [87] with permission from Elsevier. 13
- Fig. 1. 4** Bone structure at the nanometer scale: (a) Schematic illustration of periodic staggered collagen molecules and the associated gaps filled with minerals. Note that bone minerals also grow outside the gaps which are not shown here; (b) Backscattered electron (BSE) image superimposed by the white bars that represent mineral orientation. The orientation and the degree of alignment of the bone minerals are indicated by the direction and the length of the bars, respectively. (a) and (b) reprinted and adapted from [53] and [52] with permission from Elsevier. 16
- Fig. 1. 5** Schematic illustration of the relative magnitude and the types of stress on the femoral neck under two loading modes: (a) Physiological configuration: the inferior surface experiences a large component of compressive stress, while the superior surface is under a smaller tensile stress; (b) Stress states reverse for sideways fall on the greater trochanter: the inferior surface is under a small tensile stress, while the superior surface is under a larger compressive stress. Reprinted and adapted from [66] with permission from Elsevier. 21

Fig. 1. 6 Tensile and compressive stress-strain curves for cortical bone under bending. Reprinted from [170] with permission from Elsevier..... 22

Fig. 1. 7 Epifluorescence and laser scanning confocal microscopy images showing two types of microcracks: (a) Tensile dense wavy microcracks; (b) Compressive microcracks with typical cross-hatched pattern. (a) and (b) reprinted and adapted from [171] and [145], respectively. Permissions obtained from Elsevier and John Wiley and Sons, respectively..... 23

Fig. 3. 1 X-ray image of a human proximal femur (a) and backscattered electron (BSE) image of a femoral neck sample (b). Specimens were obtained from mid-femoral neck and intertrochanter, as indicated by the arrows in (a). Femoral neck sample (b) was divided into eight sectors for analysis: superior-central to superior-anterior (SC-SA); superior-anterior to anterior (SA-A); anterior to inferior-anterior (A-IA); inferior-anterior to inferior-central (IA-IC); inferior-central to inferior-posterior (IC-IP); inferior-posterior to posterior (IP-P); posterior to superior-posterior (P-SP); superior-posterior to superior-central (SP-SC). 34

Fig. 3. 2 BSE (a-d, f) and OM (e) micrographs taken from femoral neck (a-c, e-f) and intertrochanteric (d) transverse sections (with respect to the long axis of femoral neck) showing typical peri-cortical hypermineralized tissue and underlying lamellar bone: (a) An overview showing the “grey” lamellar bone and the hypermineralized tissue (top bright zone) in the peripheral zone; (b) A close-up view of the dashed white rectangle from (a) showing the lack of lamellar structure and the multiple cracks in the hypermineralized tissue. Note the cracks (arrowheads) are frequently stopped by the lamellar bone structure. Dense mineral aggregates (arrows) disperse into the adjacent soft tissue; The hypermineralized tissue in (c) has similar fibrous structure as observed in (d), a typical region obtained from intertrochanteric area; (e) Giemsa stained section including a region (dashed white frame) with a BSE image showing in (f). A deeper coloration (deep purple) is shown in the hypermineralized fibrocartilage (H) than in bone tissue (B). The hypermineralized fibrocartilage in (f) is characterized by the rounded chondrocyte lacunae (arrows)..... 41

Fig. 3. 3 Quantification of the presence of hypermineralization in the human proximal femur: (a) Box plot of area fraction of hypermineralization in total cortical bone at each location. The mean and median values at each location are identified by a ‘×’ sign and a horizontal line, respectively. Bars give the first and third quartile of the measured values. (A: anterior; SA: superior-anterior; SC: superior-central; SP: superior-posterior; P: posterior; IP: inferior-posterior; IC: inferior-central;

IA: inferior-anterior; Tro: SA-SC sector of intertrochanter); (b) A polar plot of the thickness ratio of the hypermineralized tissue vs. total cortical bone from the six femoral necks. Each point was measured by every 2.8° in the circumferential direction of the femoral neck. The different markers with different colors represent different individuals..... 43

Fig. 3. 4 Quantitative BSE imaging showing mineral content in hypermineralized and lamellar bone tissue: (a) A pseudocolored map of the obtained Ca_{peak} (the most frequently appeared mineral content). The scale bar on the right shows the range of (0 – 40) Ca wt %; (b) Bone mineralization density distributions (BMDDs) obtained from hypermineralized tissue (Hymin), Haversian bone (Hav) and interstitial bone (Int) in (a); (c) Ca_{peak} calculated from BMDDs of the six femora and plotted against Haversian bone, Interstitial bone and hypermineralized tissue. Errors shown are standard deviations. Friedman test showed significant difference in Ca_{peak} ($p < 0.05$, marked by *); (d) Average Ca_{peak} values in hypermineralized tissue, interstitial bone, and Haversian bone at each anatomical location. (A: anterior; SA: superior-anterior; SC: superior-central; SP: superior-posterior; P: posterior; IP: inferior-posterior; IC: inferior-central; IA: inferior-anterior; Tro: SA-SC sector of intertrochanter)..... 45

Fig. 3. 5 Microindentation on hydrated femoral neck samples: (a) OM picture taken before the indentation test showing a region containing hypermineralized tissue (Hymin) and lamellar bone (Bone). The white dashed line indicates the boundary between the two types of tissue; (b) OM image taken immediately after microindentation (500 gf, 15 s dwell time) corresponding to the area of (a). Arrowheads point to the cracks induced by indentation in the hypermineralized zone; (c) OM image showing two indents (arrows) loaded under 25 gf for 15 s in the hypermineralized region (Hymin) and the lamellar bone (Bone); (d) Vickers hardness values (HV) calculated based on the size of the indents. Wilcoxon signed-rank test showed significant difference ($p < 0.05$, marked by *) between the hypermineralized tissue (Hymin) and lamellar bone (Bone). 48

Fig. 4. 1 X-ray image of a human proximal femur (b) and camera images of an intertrochanter (a) and a mid-femoral neck sample (c). All the samples were made by cutting transverse with respect to the femoral neck's long axis. Intertrochanter sample (a) was further divided into eight sectors, based on the anatomical locations (i.e. superior-central to superior-anterior (SA); superior-anterior to anterior; anterior to inferior-anterior (IA); inferior-anterior to inferior-central; inferior-central to inferior-posterior (IP); inferior-posterior to posterior; posterior to superior-posterior (SP); superior-posterior to superior-central). Mid-femoral neck sample (c) was divided into two

(superior and inferior) or four (superior to anterior, superior to posterior, inferior to anterior, and inferior to posterior) sectors depending on the size of the embedding mold. Scale bar = 1 cm. .. 57

Fig. 4. 2 Typical Raman spectra obtained from a femoral neck sample (transverse to the femoral neck's long axis) containing hypermineralized tissue (Hymin, mineralized periosteum) and lamellar bone (Bone). The Raman shift range is 400 cm^{-1} - 1750 cm^{-1} . The intensity of phosphate (ν_1 , ν_2 and ν_4PO_4) and B-type carbonate (ν_1CO_3) Raman bands are higher for hypermineralized tissue (red dashed line), whereas amide I and III, and CH_2 bands have higher intensity in lamellar bone (black line). 64

Fig. 4. 3 Representative Raman mapping images obtained under two polarization angles (i.e. 0° and 90° relative to the horizontal direction) from a femoral neck sample containing hypermineralized fibrocartilage (indicated by letter H) and lamellar bone. (a) and (b) show the ν_1 phosphate intensity calculated through a sum filter (920 cm^{-1} - 1000 cm^{-1}) under 0° (a) and 90° (b), respectively; (c) and (d) are the calculated amide I intensity (obtained in the range of 1520 cm^{-1} - 1770 cm^{-1}) under 0° (c) and 90° (d), respectively; (e) is the ratio between ν_1 phosphate and amide I Raman band intensity (mineral-to-matrix ratio) measured under 0° . The color scale and the maximum intensity values for each image are shown on the right. 66

Fig. 4. 4 Typical SAXS (a-b) and SAXS/WAXS (c) patterns obtained from laboratory and synchrotron X-ray scattering, respectively: (a) An elliptical shaped SAXS pattern indicating a strong orientation of the measured minerals; (b) A circular shaped SAXS pattern suggesting a lesser degree of preferred orientation of the minerals; (c) A WAXS pattern showing the (0 0 2) arch shaped ring (i.e. arrows), associated with crystalline hydroxyapatite. 67

Fig. 4. 5 Mineral platelet thickness T obtained from the laboratory scanning SAXS measurement: (a) An intertrochanter sample containing hypermineralized fibrocartilage and lamellar bone with T values superimposed on the BSE image. T parameter is shown color-coded; (b) Box plot of T values obtained from each sample (numbers at x axis represents sample number). The mean and median values for each type of tissue of the sample are identified by a ‘x’ sign and a horizontal line, respectively. Bars give the first and third quartile of the measured values of each type of tissue (white, cortical bone; dashed, trabecular bone; grey, hypermineralized tissue). The difference between hypermineralized tissue and lamellar bone (including cortical and trabecular) is significant ($p < 0.05$, femoral neck and intertrochanter pooled)..... 68

Fig. 4. 6 Mineral platelet thickness T , length L and spatial organization of mineral platelets obtained from SAXS/WAXS measurement using synchrotron radiation: (a-b) BSE images of a femoral neck sample containing hypermineralized fibrocartilage on the left and lamellar bone on the right, superimposed by T and L values, respectively. Both structural parameters are shown color-coded; (c-d) Description of the mineral organization derived from synchrotron SAXS measurement. Typical $G(x)$ curves in (c) were obtained from lamellar bone (Bone, red curves) and hypermineralized fibrocartilage (Hymin, blue curves); (d) Plot of $2\pi/\alpha$ versus $T2\pi/\beta$ derived from (c) shows a different pattern between lamellar bone (open red circles) and hypermineralized fibrocartilage (blue closed circles)..... 71

Fig. 5. 1 Schematic illustration of specimens prepared from human femora. Shear specimens were oriented at 0° , 30° , 60° and 90° with respect to the long axis of femoral shaft, which is indicated by the grey lines. A specimen was gripped in the custom made Wyoming Iosipescu fixture with the shear loading indicated by the arrow pointing at the top of the rod..... 80

Fig. 5. 2 Representative load-displacement curves (a) and stress-strain curves (b), for different specimens (0° , 30° , 60° and 90°) tested by Iosipescu in-plane shear. Shear stress calculation following ASTM standard (D5379/D5379M) ($\tau = PA$, where p is the loading force and A is the cross-sectional area between two notch tips), and engineering shear strain obtained from DIC ($\gamma = 2 \times \epsilon_{xy}$, where shear strain ϵ_{xy} is the average value of the displacement gradients ϵ_{xy} and ϵ_{yx} , which are the shear component on the y plane along the x direction and on the x plane along the y direction, respectively)..... 86

Fig. 5. 3 Schematic diagram of region of interest (ROI) used for digital image correlation (DIC) shear strain analysis and the representative shear strain (i.e. ϵ_{xy}) distribution beyond yielding point, for specimens in each orientation: (a) 0° ; (b) 30° ; (c) 60° and (d) 90° . Arrows indicate the shear loading direction. Size of the ROI is approximately $(2.3 \times 2.3) \text{ mm}^2$ 88

Fig. 5. 4 Typical major fracture patterns under a stereo microscope. Of interest is the relatively large crack initiation angle vs. long axis of osteons, and the multiple crack deflections observed in 0° specimen (a). 30° (b), 60° (c) and 90° (d) specimens have comparatively flat fracture routes. Arrow heads point at the fracture planes. Shear loading direction is indicated by the vertical arrow. 90

Fig. 5. 5 Scanning electron microscopy (SEM) micrographs showing major fracture interacting with osteons. (a-c) represent three scenarios observed on transverse sections (plane perpendicular

to long axis of osteons): (a) Crack was deflected by the cement line and went around the osteon (arrow); (b) Crack was deflected by bone lamellae inside the osteon, resulting in a circular crack path (arrow head); (c) Crack went through the Haversian canal with minimum deflection (chevron arrow); (d) Initiation crack was deflected along the cement line (double arrows) as observed from longitudinal section for 0° specimen. 91

Fig. 5. 6 Laser scanning confocal microscopy (LSCM) images showing microcracks distribution in the gauge sections. The obtained cross-sections were all cut perpendicular to the osteons' long axis (indicated by grey lines) for analysis as shown in the schematic illustration. (a) and (b) show the representative damage patterns for 0° and 60° specimens, respectively. 92

Fig. 5. 7 Unique microcracking pattern under shear: (a) OM image showing the lamellar structure (i.e. 0°); (b) High resolution LSCM image taken from the right side of the central osteon (dotted line) in (a). a unique peripheral arc-shaped pattern (arrows) is located at the peripheral zone of the osteon. They appear as linear microcracks on the z-plane ("cut views" at locations shown by white lines); (c) High resolution second harmonic generation (SHG) image taken from the right bottom corner in (b) showing the osteon consisting of bright and dark lamellar layers. Note that in the bright layer, the collagen fibrils are mainly lying circumferential to the osteons, while the collagens mostly align along the osteons in the dark layer; (d) Combined SHG and two photon excitation fluorescence (TPEF) image directly associating arc-shaped microcracks (arrow heads) with osteonal lamellae. 94

Fig. 5. 8 Quantitative analysis on the microcracks created under shear. More than forty osteons from each orientation at early stage of damage were analyzed. (a) Summary of occurrence frequency of six types of microcracks: osteonal arc-shaped (OA); osteonal tensile (OT); osteonal radial (OR); cement line (CE); interstitial arc-shaped (IA) and interstitial tensile (IT); (b) Frequency distribution of the location of arc-shaped microcrack initiation. The osteon was divided into five locations: at the Haversian canal (P1); inner third of the osteonal wall (P2); middle third of the osteonal wall (P3); outer third of the osteonal wall (P4) and at the cement line (P5). (c) Arc-shaped microcracks' association with lamellar structure (i.e. "bright"/ "dark" lamellae and interlamellar area). 96

Fig. 6. 1 Proximal femur and surgically removed intracapsular hip fracture samples: (a) X-ray image of a proximal femur showing the region (shaded) from which fractured femoral neck samples were retrieved during surgery. White dashed line with arrow indicated the direction of

femoral neck's long axis; (b) Retrieved femoral neck sample in a typical transverse view (plane perpendicular to femoral neck's long axis) showing the eight sectors: superior-central (SC), superior-posterior (SP), posterior (P), inferior-posterior (IP), inferior-central (IC), inferior-anterior (IA), anterior (A) and superior-anterior (SA). In each designated sector, one section was prepared parallel to the femoral neck axis (direction marked by the central circle with a dot) and normal to the periosteal surface. An example was shown by the black frame with white lines indicating the four zones in (d); (c) Retrieved femoral neck sample in a typical anterior-to-posterior view with a surgical cut and the main fracture surface. The black frame represents the same section that is shown in (b), and the four zones are marked by the white lines and the corresponding numbers. The white dashed line with arrow points to the direction of the femoral neck's long axis; (d) A longitudinal cortical bone section, corresponding to the black frame in (b) and (c), shows the stained microcracks in bright green. The region within 4 mm away from the main fracture surface was subdivided into four zones, as shown, and each zone was 1 mm in length. Scale bar in (b) and (c) is 1 cm..... 107

Fig. 6. 2 Typical laser scanning confocal microscope (LSCM) images showing four different levels of amount of microcracks: (a) is the region of interest (ROI) scored as “0” when no microcrack was found in the field of view. Only blood vessel, osteocyte lacunae and canaliculi are visible; (b) The ROI scored as “1” with very little amount of microcracks. Discrete linear interlamellar shear cracks are visible (arrows); (c) The ROI scored as “2” with some microcracks. Cross-hatched compressive microcracks appeared on the endosteal region and around Haversian system (H); (d) The ROI scored as “3” with widely spread microcracks. Some areas are saturated with bright green signals due to the intensive localized microcracking..... 110

Fig. 6. 3 Retrieved femoral neck samples showing distinctive macroscopic fracture patterns at the posterior site: (a) A retrieval sample showing a typical “U” shape fracture where the main fracture surfaces are parallel to the femoral neck's long axis at superior-posterior and inferior-posterior sites (pointed by arrows), while the posterior-central fracture is relatively straight, transverse to the femoral neck's long axis; (b) Representative “V” type fracture is characterized by a sharp turn posteriorly (pointed by arrow) and two oblique cracks at superior-posterior and inferior-posterior sites; (c) Typical “W” shape fracture has a tooth-like fracture at posterior-central, which develops in the transverse direction to the femoral neck's long axis; (d) A closer look at the superior-

posterior site in (c, indicated by arrow) revealed multiple secondary cracks running transverse to the femoral neck's long axis (arrow heads). 112

Fig. 6. 4 Chi-square test for the four levels of microcrack density (i.e. score of 0-blank bar, 1-red dashed bar, 2-grey bar, and 3-yellow bar) showed significant difference among difference zones and locations ($p < 0.01$). SA = superior-anterior, SC = superior-central, SP = superior-posterior, IA = inferior-anterior, IC = inferior-central, and IP = inferior-posterior. R1, R2, R3 and R4 represents zone 1, 2, 3, and 4, respectively..... 115

Fig. 6. 5 Microcrack density scores obtained from various locations: (a) Box-plot graph of microcrack density scores versus superior (Sup, grey) and inferior (Inf, white) sites. The shaded boxes represent 50 % of the data, limited by the upper and lower quartiles, with the median indicated by a bar within each box. The vertical bars indicate the range of the data; (b) Superior and inferior microcrack density score within each retrieved sample. 18 of 24 samples had higher score at superior rather than inferior site (indicated by red dots and lines); (c) Microcrack density scores at six sites for three typical “U” and three typical “V” type fractured samples. SA = superior-anterior, SC = superior-central, SP = superior-posterior, IA = inferior-anterior, IC = inferior-central, and IP = inferior-posterior. 116

Fig. 6. 6 Representative microcrack patterns found in retrieved femoral neck samples: (a) Tensile microcracks are dense and wavy, running in the direction normal to the “extinct” lamellae [91,106] (indicated by white dashed lines in the upper right insert picture); (b) Compressive straight and relatively long microcracks forming a cross-hatched pattern, oriented at approximately 30° to the long axis of femoral neck; (c) Long and linear shear-induced microcracks running along the direction of the long axis of femoral neck. 117

Fig. 6. 7 Schematic diagram showing compression-induced buckling and the representative buckling pattern found at the superior-anterior fracture site: (a) Low magnification confocal imaging of the porous cortical bone showing extensive microcracking at the periosteal and endosteal regions, approximately 3 mm away from fracture surface; (b-c) High magnification confocal imaging of dotted regions in (a) clearly shows dense and wavy tensile microcracks at the secondary crack; (d-e) High magnification confocal imaging at endosteal cortex (white frames in a) showing the straight and relatively long compressive microcracks forming typical cross-hatched pattern. Under macroscopic compression (schematic drawing), this corresponds to a buckling failure. 118

Fig. 6. 8 Percentage of the analyzed sections showing different dominant stress states at various locations: (a) Among all the analyzed sections from superior region (N = 72), 36 % showed longitudinal (along the long axis of femoral neck) compression and 31 % showed patterns resembling a buckling failure. Tension was observed with the lowest percentage at both superior and inferior cortex; (b) The dominant stress states at six sites showed superior-central and superior-posterior cortex were primarily failed by longitudinal compression, and buckling mostly occurred in superior-anterior cortex. For each location, a total of 24 sections were analyzed. SA = superior-anterior, SC = superior-central, SP = superior-posterior, IA = inferior-anterior, IC = inferior-central, and IP = inferior-posterior. 120

Fig. 6. 9 Hypermineralization in clinically retrieved femoral necks samples: (a) Apparent “mineral clusters” scattering into the periosteal soft tissue (white arrows); (b) Periosteal hypermineralized tissue showing signs of brittleness with cracks formed and developed within the tissue, but stopped by the lamellar bone (black arrow head). Multiple bridging (dark double arrows) could be found in lamellar bone; (c) Hypermineralization with fibrous features was found at the fracture surface; (d) Chondrocytes lacunae (marked by “*”) were also found in some regions of hypermineralization. 121

Fig. 6. 10 Percentage of specimens having hypermineralization within 4 mm zone (closed black circles) and 1 mm zone (open circles) to the main fracture surface, and the thickness ratio between hypermineralized tissue and total cortex at the main fracture surface (marked by “×”). The numbers following “×” represent the numbers of specimens having this thickness ratio. 122

Fig. 6. 11 Fracture and cracking behavior in samples containing hypermineralization: (a) BSE image showing a specimen with hypermineralization at the major fracture surface and secondary crack; (b) Higher magnification BSE image taken from the white dashed frame in (a) showing the different cracking behavior in the hypermineralized tissue and lamellar bone. The crack propagated in a relatively straight path (double arrow heads) in the hypermineralized region, in contrast to the “zig-zag” pattern in the lamellar bone (arrow head). Note that there is also crack deflection in the hypermineralized tissue (arrow), possibly due to the longitudinal oriented matrix. 124

Fig. 6. 12 Microcracks associated with major fractures in the hypermineralized tissue and lamellar bone: (a-c) are images taken at the main fracture surface, while (d-f) were taken at the secondary cracks; (a) BSE image showing the periosteal hypermineralized tissue at the main fracture surface; (b) SHG image taken from the white dashed frame in (a) demonstrating the “non-lamellar”

hypermineralized tissue and the lamellar bone; (c) TPEF overlaid SHG signal showing limited microcracking within the hypermineralized tissue; (d) BSE image showing two secondary cracks in lamellar bone; (e) is the corresponding SHG image of (d); (f) Combined SHG and TPEF signals showing extensive microcracks associated with the two major cracks. 125

Fig. S3. 1 BSE images showing various features associated with hypermineralization at femoral neck: (a) Hypermineralized tissue appears underneath periosteal lamellar bone; (b) Region of calcified fibrocartilage showing characteristic chondrocyte lacunae; (c) Typical tidemark features associated with cartilaginous tissue; (d) Multiple mineral-filled osteocytes lacunae (arrows) showing brighter and higher intensities near the peripheral region of cortical bone..... 181

Fig. S3. 2 OM and BSE images showing hypermineralization in femoral neck: (a) OM image shows no apparent hypermineralized tissue at the periosteal lamellar bone; (b) The same region under BSE signal clearly demonstrates a thin layer of hypermineralization at the peri-cortical bone. 182

Fig. S3. 3 Calibration between BSE grey-level and atomic number. 183

Fig. S3. 4 Vickers hardness as measured in the lamellar bone and the calcified fibrocartilage ($p < 0.05$, marked by “*”). 184

Fig. S4. 1 Representative Raman microspectroscopy mapping images obtained from two femoral neck samples under 0° polarization angle (relative to the horizontal direction) showing relative B-type carbonate and phosphate contents: (a) A slightly higher degree of carbonate substitution was found in hypermineralized periosteum (H); (b) Phosphate-to-carbonate ratio shows a higher phosphate content in lamellar bone (B) than in hypermineralized fibrocartilage (H). The color scale and the intensity values for each image are shown on the right color bars. 186

Fig. S4. 2 Combined SAXS and WAXS synchrotron measurement on three femoral neck samples containing hypermineralized fibrocartilage and cortical bone (numbers at the x axis represent sample number): (a) Box plot of the mineral platelet thickness T ; (b) The average length L of the mineral platelets; (c) The degree of orientation ρ of the mineral platelets. The mean and the median values for each sample are marked by a “x” sign and a horizontal line, respectively. Bars give the first and third quartile of measured values of each tissue (white, cortical bone; dashed, hypermineralized fibrocartilage). Statistically smaller T and L values were found in the hypermineralized region (Hymin) than that in the cortical bone (Cort) ($p < 0.05$, indicated by*). 188

Fig. S4. 3 Spatial organization of mineral platelets measured by laboratory SAXS on a femoral neck sample containing hypermineralized periosteum (Hymin) and lamellar bone: (a) Typical $G(x)$ curves obtained from cortical bone (Cort), trabecular bone (Trab) and hypermineralized periosteum (Hymin); (b) Plot of $2\pi/\alpha$ versus $T2\pi/\beta$ obtained from (a) showing a different pattern between lamellar bone (red and yellow dots) and mineralized periosteum (blue dots)..... 189

Fig. S5. 1 Optical microscopic images of representative pre-existing cracks in human cortical bone specimens: (a) White light microscopic image showing the crack opening; (b) Fluorescent microscopic image with red color signals from xylenol orange showing the cracks in the same area. Arrow heads point at the pre-existing cracks. 190

Fig. S5. 2 Macroscopic fracture patterns (a) and (b) and shear strain state (c-e) for 30° specimens tested under different loading conditions. When the resolved principle stress angled at 15° to the long bone axis, fracture started at the tip of notch (a) with clear shear strain concentration band (c); In contrast, when the resolved principle stress was oriented at 75° to the long bone axis, the fracture was initiated at edge (b) with no shear strain concentration (d); The in-plane strain triaxiality ratio (TR^*) vs. engineering shear strain curves showed clear different trends (e): the specimens fractured from the edge show increasing positive value, and the ones with cracks starting from the notch area show decreasing negative value. The arrows heads in (a) and (b) point at the fracture planes. The side arrows in (c) and (d) indicate shear loading direction. 192

Fig. S5. 3 Laser scanning confocal microscope (LSCM) image of microcracking patterns (other than arc-shaped) on transverse plane (with respect to the long bone axis) cut between the two notches. (a) and (c) BSE images showing the Haversian structure; (b) LSCM image taken from the top left in (a) showing cement line crack; (d) LSCM picture imaged from the top left quadrat in (c) showing radial crack resembling similarities from compression-created shear cracks..... 194

Fig. S6. 1 Retrieved femoral neck samples with final fracture patterns. All the pictures were taken in a typical posterior-anterior view with inferior site down and superior site up. The majority of the samples have a fracture pattern posteriorly resembling a letter “U”, “V” or “W”. 197

Fig. S6. 2 Microcrack density scores at the six anatomical locations (a) and the location with the highest microcrack density score within each retrieved femoral neck sample (b): (a) Box-plot graph of microcrack density score versus six sites. Higher values were found at the superior site (grey) than at the inferior site (white), but no essential difference was observed within either superior or inferior cortex. The boxes represent 50 % of the data, limited by the upper and lower quartiles,

with the median indicated by a bar within each box (median value overlaps with third quartile and first quartile for IC and IP, respectively). The vertical bars indicate the range of the data; (b) In the 24 retrieved femoral neck samples, one or multiple locations within each sample could show the highest microcrack density score. 2 or 3 samples could show the same microcrack density score at the same location (marked by ×2 and ×3, respectively). 198

Fig. S6. 3 Local oversaturated damage found at the major fracture, and the percentage of the analyzed sections at six locations showing oversaturated damage: (a) High magnification confocal image showing the typical pattern with oversaturated damage (stars) at the main fracture and associated with cross-hatched microcracks underneath (arrows); (b) The inferior site demonstrated a higher percentage of oversaturated damage compared to the superior site. SA = superior-anterior, SC = superior-central, SP = superior-posterior, IA = inferior-anterior, IC = inferior-central, and IP = inferior-posterior. 199

List of Symbols

T	Thickness of mineral platelets
ρ	Degree of orientation of mineral platelets
L	Length of mineral platelets
Φ	Mineral volume fraction
σ	Total surface area of the mineral platelets per unit volume
λ	Wavelength of X-ray beam
k	Constant related to crystallite shape
B	Full width at half maximum intensity of the (0 0 2) peak of HA
θ	Bragg angle of the (0 0 2) peak
α	Relative extent of the ordering of the mineral platelets
β	The degree of spatial correlation between successive mineral platelets
G	Shear modulus
ε_1	Maximum normal strain
ε_2	Minimum normal strain
τ	Shear stress
P	Loading force (shear)
A	Cross-sectional area between two notch tips (shear)
ε_{xy}	Average shear strain
γ	Engineering shear strain

List of Abbreviations

BMD	Bone Mineral Density
BMDD	Bone Mineralization Density Distribution
BSE	Backscattered Electron
DIC	Digital Image Correlation
DXA	Dual-energy X-ray Absorptiometry
FE(A)	Finite Element (Analysis)
HA	Hydroxyapatite
HR-pQCT	High-Resolution peripheral Quantitative Computed Tomography
LSCM	Laser Scanning Confocal Microscopy
MPM	Multi-Photon Microscopy
NCPs	Noncollagenous proteins
OM	Optical Microscopy
PBS	Phosphate-Buffered Saline Solution
PMMA	Poly(methyl methacrylate)
pQCT	peripheral Quantitative Computed Tomography
qBSE	Quantitative Backscattered Electron
SAXS	Small-Angle X-ray Scattering
SEM	Scanning Electron Microscopy
SHG	Second Harmonic Generation
TPEF	Two Photon Excitation Fluorescence
WAXS	Wide-Angle X-ray Scattering

Acknowledgements

I would like to start with my deepest gratitude to my supervisor and mentor Dr. Rizhi Wang, for his compassion for the students, for his encouragement and guidance through the years, for his attention to the details, for his motivation in studying biological materials, and for his innovative ideas that inspired numerous discussions. I am forever thankful for the study and research opportunity that he had offered, and this work could not be accomplished without him.

I owe particular thanks to my co-supervisor Dr. Peter Cripton and my PhD program committee members Dr. Tom Troczynski and Dr. Dorin Ruse for their constructive feedback and insightful comments over the course of the program, and to Dr. Warren Poole for chairing the committee meetings. I would also like to thank Dr. Heather McKay and Dr. Pierre Guy for their invaluable inputs for the bone fracture and hip fracture projects. Thanks to Dr. Peter Fratzl and Dr. Wolfgang Wagermaier for hosting my research study at Max Planck Institute.

I would like to acknowledge the research funding resources from the Canadian Institute of Health Research (CIHR). I am also grateful for the Faculty of Applied Science Graduate Award for providing the stipend. Funding for laboratory space and other equipment at the Biomaterials Laboratory, Advanced Materials and Process Engineering Laboratory (AMPEL), was provided by the Natural Sciences and Engineering Research Council (NSERC), and the Canadian Foundation for Innovation (CFI). Special thanks to the Constance Livingstone-Friedman and Sydney Friedman Foundation for supporting my research study in the Department of Biomaterials, Max Planck Institute of Colloids and Interfaces (MPICI), Potsdam, Germany.

I also wish to thank the Centre for Hip Health and Mobility (CHHM), Vancouver Coastal Health, for their strong support and for the use of their facilities. I am thankful to the UBC Life Science Institute, Dentistry department and Bioimaging Lab for the use of their microscopes. I

would like to acknowledge the experimental support from Dr. Danmei Liu of CHHM, and Caron Fournier of International Collaboration On Repair Discoveries (ICORD). Thanks to Birgit Schonert, Gabriele Wienskol, Ingrid Zenke, and Christine Pilz at MPICI and Dr. Chenghao Li and Stefan Siegel at μ Spot Beamline, BESSY II (Helmholtz-Zentrum Berlin, Germany) for their technical supports.

I would like to thank all the former and present members of the Biomaterials Lab as well as my close friends for spending time with me and sharing the laughter. I am very thankful to Vincent Ebacher and Chia-Jade Lee for helping me initiate the bone fracture project. Thanks to Millie Kwan, Menghan Ma, Mehdi Kazemzadeh, Felipe Eltit, Qiong Wang, and Christina Chen for the time that we worked together in the laboratory. I also would like to thank my friends and colleagues at MPICI for their kindness and assistance in Germany.

Finally, I am forever in debt to my parents for their unconditional love. My parents are the origin of my inspirations, without them, I could never achieve what I have accomplished today. To my husband, whom I met at UBC, wish we would have a happy and long life together.

Dedication

“Do what you love. Know your own bone; Gnaw at it, bury it, unearth it, and gnaw it still.”

— Henry David Thoreau

This work is dedicated to all the researchers who have been devoted to studying our own skeleton.

Chapter 1 Introduction

Hip fracture is one of the most common yet serious musculoskeletal injuries in the older adult population. In Canada alone, more than 24,000 hip fractures occur each year [1], and the global annual number of hip fractures was estimated to be 1.66 million [2]. Although the incidence rate of hip fracture varies considerably from population to population, it increases exponentially with age in all races and genders in most regions of the world [3]. In the United States, ~ 90 % of those diagnosed with a hip fracture are over 65 years old with the mean age of 80 years old [4]. With the current demographic and incidence trends, the worldwide annual number of hip fractures will increase to approximately 6.26 million by the year 2050 [2,5].

The outcomes of hip fractures are severe. Considering the initial and subsequent hospitalizations, rehabilitation and nursing facilities, the lifetime attributable cost of a hip fracture was estimated at \$81,300 [6]. The risk of disability and death is also considerably high following a hip fracture. Up to a third of individuals who sustain a hip fracture can become totally dependent [7]. Almost 750,000 deaths worldwide were estimated to be associated with hip fractures in people aged 50 years and older [8], and the mortality rate during the first three months following a hip fracture is about 5.75 % in older women and 7.95 % in older men (more than 50 years old) [9], which could rise to 27.3 % within one year after surgery [10]. Additionally, among the survivors of a primary/initial hip fracture, the incidence of a second hip fracture is also substantial: the one-year risk of a subsequent fracture is between 2 % to 11 % [11,12], and the lifetime risk of a second hip fracture has been estimated at about 20 % but may be as high as 55 % [13].

To reduce the number of hip fractures and the associated cost, prevention of both primary and secondary hip fractures is of great importance. However, one of the biggest challenges to hip

fracture prevention is how to better identify at-risk population. Currently, areal bone mineral density (aBMD) as measured by dual-energy X-ray absorptiometry (DXA) is the clinical standard for osteoporosis diagnosis. A low aBMD is a strong indicator of a weak hip, but cannot fully explain the incidence of hip fracture: more than 50 % of elderly hip fracture cases are not classified as being osteoporotic by DXA [14]. In part, the reason that we cannot accurately assess hip fracture risk is that some of the fundamental failure mechanisms of hip fracture are missing in the literature.

Hip fracture is the combined result of the internal bone fragility and the complicated stress state caused by external impact. Changes of the “bone quality” [15,16], factors that contribute to bone strength independent of bone mass and aBMD, will affect the biomechanical performance of the proximal femur. Yet, in contrast to the extensive studies at the geometrical and structural level [17,18], the influence of the altered femoral cortical bone tissue, e.g. hypermineralization, is not clear. Further, with external loading, femoral cortical bone deforms through microcracking and leads to ultimate fracture. A clear identification of the clinically relevant microcrack patterns is essential in understanding the deformation and fracture process. Therefore, the primary goal of this dissertation was to enhance the current understanding of the mechanisms of hip fracture at a fundamental level. In particular, the study aimed to identify the material changes at the femoral cortical bone and its potential role in hip fragility and the deformation and fracture process of clinical hip fractures.

The following sections of this chapter will provide background information on clinical hip fractures, and introduce current knowledge on bone hierarchical structure, deformation and fracture mechanisms of the human cortical bone. These contents are essential to the understanding of the material presented in the subsequent chapters of this dissertation. A summary of existing problems regarding hip fracture mechanisms was provided at the end of this chapter.

1.1 Hip anatomy and types of fracture

1.1.1 The hip joint

The hip joint is a synovial ball-socket joint between the head of the femur and acetabulum of the pelvis. Although fractures of the hip can be on either the femoral or pelvic side of the joint, the term “hip fracture” is usually reserved for clinical fracture of the proximal femur [19].

The proximal femur mainly consists of the head, neck and greater and lesser trochanters (Fig. 1.1). The head of the femur has a spherical shape with a diameter varying among individuals in a range of 40 mm to 60 mm. Projecting inferolaterally from the femoral head to the femoral shaft is the femoral neck, which connects to the diaphysis at an angle of 120°-140° (with respect to the long axis of the femoral shaft) [20]. In the lateral plane, the angular difference between the long axis of the femoral neck and the long axis of the diaphysis is normally about 15° in adulthood [21]. The intertrochanteric region of the hip is the transition zone from the femoral neck to the diaphysis where the two prominent bony features are located: the greater and lesser trochanters. Both greater and lesser trochanters are the sites of muscle insertions: iliopsoas inserts at lesser trochanter whereas gluteus medius and gluteus minimus insert at greater trochanter (Fig. 1.1). Connecting these two bony features are the anterior intertrochanteric line and the posterior intertrochanteric crest (Fig. 1.1).

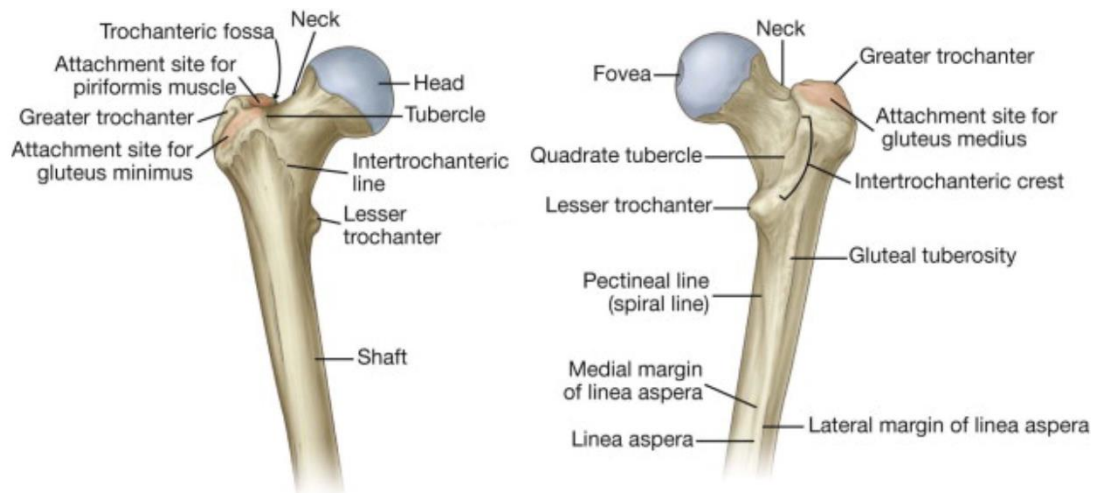


Fig. 1. 1 Illustration of human proximal femur from the posterior view (left) and anterior view (right). Main structure features include femoral head, neck, greater and lesser trochanter. Graphic reprinted and adapted from [22] (Fig. 6.8) with permission from Elsevier.

1.1.2 Intra- and extra-capsular hip fractures

Based on the anatomical sites of fractures, hip fracture is classified into two major types: intracapsular and extracapsular fractures. The former occurs in the ligamentous hip joint capsule; the latter occurs below the capsule. The incident rate for each type of fracture is comparable (45 % and 55 %, respectively) [23], although extracapsular fracture is more predominant in patients who are physiologically and chronologically older [23,24].

Intracapsular hip fractures include femoral head and femoral neck fractures. Depending on the fracture location along the long axis of the femoral neck, femoral neck fractures are subdivided into subcapital (near the head/neck junction); transcervical (across the mid-femoral neck); and basicervical (across the base of the femoral neck) fractures [25]. Femoral neck fractures have a high chance of leading to fracture healing complications [19]. The main reason is that there are retinacular arteries running along the femoral neck to provide blood supply to the femoral head; the disruption of these blood supplies can lead to avascular necrosis [19].

Extracapsular hip fractures include trochanteric fractures and sub-trochanteric fractures [25]. Although there is a considerable discrepancy among reports evaluating mortality rates for extra- and intra-capsular fractures [24,26,27], possibly due to the variation in the types of patients being included, studies have shown that there are clear differences in the functional outcomes associated with the site of the fractures [24,27].

1.2 Age-related hip fractures: an overview on etiology

1.2.1 Sideways falls in the elderly

Although the factors affecting the risk of a hip fracture are numerous: demographic variables [28], diseases [29], medications [30], gynecological history [30,31], anthropometric variables [31,32], life-style [32,33], nutrition [34,35], etc., people generally agree that age-related physical decline and an increased propensity to fall [36] and decreases in bone mass [37] are strong risk factors for hip fracture.

Previous reports have shown that over 90 % of hip fractures are a result of a fall from standing height [38–40], and that the characteristics of a fall, such as fall height and energy, fall direction, anatomical site of impact, and impact force attenuation by the body and landing surface, are important contributors to the risk of hip fracture [41]. A fall simulating study has demonstrated that a fall directly on the buttocks was associated with a larger force of impact on the greater trochanter than lateral or posterolateral falls [42]. However, because of the greater amount of posterior soft tissue, which could absorb more impact [43], the fracture rate is generally lower than falls to the side [39]. The risk for fracture is about 20 times higher in sideways falls, compared to falls in the other directions [40].

It should be noted, however, the exact type of fall or the impact to the hip is almost impossible to determine, since it mainly relies on self-reports of the patients, which may be unreliable [44], and witness accounts, which are often unavailable [45].

1.2.2 Clinical assessment

Currently, local bone mass, commonly referred to as “bone mineral density (BMD)”, is the gold standard for clinical assessment of hip fracture risk [46]. BMD is measured by dual energy X-ray absorptiometry (DXA), which measures the attenuation of X-ray beams using two different energies, in order to compensate for the surrounding soft tissue. Since the collected image is two-dimensional (2D), the output is also called areal bone mineral density (aBMD), whereby bone mineral content (BMC) is normalized by the projected area. Based on the DXA results, two parameters are frequently used for osteoporosis or osteopenia assessment: *T*-score and *Z*-score. *T*-score represents the comparison of an individual’s BMD to a sex and race matched young adult population; *Z*-score is the result of the comparison to a sex, race and age-matched population [47]. Osteoporosis is defined as the loss of bone at the proximal femur measured with clinical DXA exceeding 2.5 standard deviation with reference to the young normal values (i.e. *T*-score < -2.5) [48].

Although DXA is a widely used clinical tool due to its fast and convenient measurement, and low radiation exposure for the patients, it cannot capture some important aspects of age-related hip fragility. For instance, a recent study that followed over 7,000 volunteers over 7 years found that only 44 % of women and 21 % of men with non-vertebral osteoporotic fractures are clinically diagnosed as osteoporosis [49]. In addition, 50 % of elderly hip fracture cases are not classified as being osteoporotic by densitometry [14]; and while some nonwhite populations have been

frequently diagnosed as being osteoporotic by standards, they have relative lower hip fracture incidents [50].

1.3 The material bone: the hierarchical structure

Bone can be viewed as a nano-fibrous composite. Its basic constituents (i.e. mineral and protein) assemble together to form a complex hierarchical structure, from the individual collagen molecule and mineral platelet at the nanometer level, to the microscopic structural units of osteons and bone lamellae, and macroscopically a trabecular bone core and a cortical bone shell (Figs. 1.2- 1.4) [51–53]. Bone’s mechanical integrity derives from the interaction of its mineral content and geometry, its tissue organization and its material properties [54]. Thus, a clear understanding of this complex structure is critical to the understanding of bone’s mechanical responses.

1.3.1 Cortical and trabecular bone

At the macroscopic level, the proximal femur is comprised of a trabecular bone core and a cortical bone shell (Fig. 1.2). Cortical bone (cortex) contributes to about (40-60) % of the skeletal mass within the proximal femur, and trabecular bone contributes to the remaining weight [55]. The differences between these two tissues are visible with naked eyes (millimeter level). Cortical bone is much denser, and significantly lower in porosity (~ 5 vol %-15 vol %) than trabecular bone [56,57].

The most important measures of the microstructure of the cortical bone are its porosity and thickness, both of which might be key structural determinants of hip fragility [17]. There are significant regional differences in the porosity within the femoral neck cortex. In general, inferior cortex has lower porosity than the superior cortex. Particularly, females are reported with much higher porosity at the superior than inferior cortex [58]. More importantly, the anterior cortex is

41 % more porous in patients with femoral neck fractures than in healthy individuals [58]. The increased porosity is the result of increased Haversian remodeling activity and the formation of “super osteons” or clusters of remodeling osteons with large canal diameter and thin osteonal walls [59,60].

At the femoral neck, the cortical thickness also varies markedly from the inferior to the superior aspect of the bone: it is generally the thickest at the inferior aspect and thinnest at the superior aspect. Femoral cortical bone thinning at the superolateral cortex has been proposed to be relevant to hip fracture in the elderly [17]. In particular, studies have found that the thickness of the inferomedial cortex remains unchanged with ageing, while the superolateral cortex grows substantially thinner [61,62]. Further, femoral neck samples from fracturing patients differ from healthy controls by additional thinning, especially in the inferoanterior cortex [17,62,63]. Such change has minimum effect on bending resistance, but significantly increases the risk of buckling. Very interestingly, two recent studies using clinical computer tomography (CT) data suggest that focal thinning of the cortical bone promotes hip fragility [64,65], and that the largest patch of thinner femoral cortex corresponds to the fracture initiation site in sideways fall simulating study [66].

In contrast to cortical bone, trabecular bone has higher porosity (~ 75 vol %-95 vol % [56]). Although the loss of trabecular bone with ageing undoubtedly plays a role in hip fragility [67,68], it is the distribution of cortical bone that is believed to be critical in determining a femur's resistance to fracture [58,62]. That being said, if the failure mode of the thin superolateral cortex is buckling rather than compression, buttressing effect of the trabeculae may be critical as they can significantly reduce the possibility of buckling.

1.3.2 Unique features of human femoral neck

In addition to the variations in cortical porosity and thickness across the femoral neck, another distinct structural feature that could potentially undermine the mechanical properties of the femoral neck cortex is the lack of periosteum and the circumferential lamellar bone. Periosteal is the outer surface of the femoral neck and diaphysis (Fig. 1.2b). In the diaphysis, the periosteal is covered by a thin membrane, the periosteum, which facilitates repair and contributes to the periosteal expansion of the cortical bone [69,70]. In contrast to the high coverage of periosteum in the long bone (~ 59.2 %), the femoral neck has significantly less cellular periosteum (~ 18.4 %) [71]. Low periosteum coverage may dramatically reduce the capability of bone repair, thus may leads to a highly irregular femoral neck surface [71] and lack of robust circumferential lamellar structure (Fig. 1.2b).

More importantly, hypermineralized tissue was found at the peri-cortical bone region in the femoral neck as well as the trochanters [72,73]. By definition, hypermineralization refers to the tissue with obviously higher degree of mineralization than lamellar bone (osteonal and interstitial) [74]. In the trochanteric region, hypermineralization is known to originate from mineralized fibrocartilage, which is anatomically associated with tendinous insertion [75]. In the femoral neck, hypermineralization is reported as a result of mineralized periosteum [71] and mineralized fibrocartilage [75]. One of the early studies on hypermineralization of human femoral cortical bone at the shaft found that over 75 % of the examined samples showed highly mineralized periosteum in subjects over the age of 48 years old [76]. The large extent of hypermineralization at the mid-femoral neck was reported by Allen and Burr, in which (20-70) % of the femoral neck surface was covered by the mineralized periosteum [71]. Other studies [72,73] reported significant area fractions of hypermineralization in the trochanters and femoral neck of the elderly and

postmenopausal women, and suspected that it would undermine the fracture resistance of the local bone tissue. Thus, in cases where cortical bone thinning and possibly increase of cortical porosity resulting in trabecularization of the cortex occur, hypermineralization may be one of the key factors leading to ultimate hip fracture.

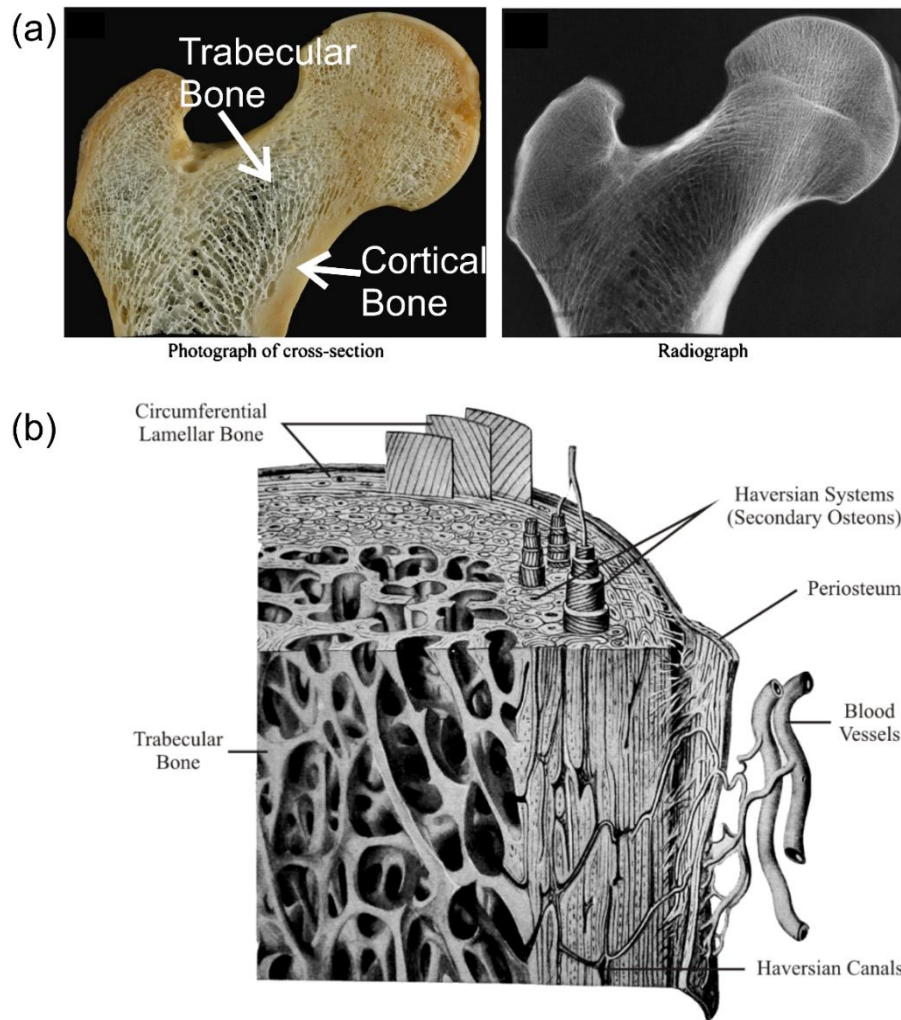


Fig. 1. 2 Camera and X-ray images and illustration of the general features found in the human proximal femur: (a) A coronal plane showing the porous trabecular bone core and the surrounding cortical bone shell. Reprinted and adapted from [77] (Fig. 7) with permission from Elsevier; (b) Characteristic structural features of the cortical bone: Haversian systems/osteons, interstitial bone, circumferential periosteal and endosteal lamellae, and periosteum. Reprinted and adapted from [56] (Fig. 2.2, p41 and Fig. 2.3 p43) with permission from Springer.

Despite its potential clinical implication to hip fracture, information on the intrinsic material properties of the hypermineralized tissue from either femoral neck or intertrochanteric

region has been very limited. Backscattered electron (BSE) imaging [72,73], standard histology [71,76], and synchrotron imaging [78] have been used to study this tissue. Specifically, a recent synchrotron radiation micro-computed tomography (SR micro-CT) has visualized this highly mineralized tissue through 3D imaging of the human femoral neck cortical bone [78]. However, these studies mainly centered on the histological and morphological features. So far, there have been no reports on quantifying its degree of mineralization and the associated mechanical properties, neither on its ultrastructural features at the level of minerals and organic matrix. A thorough understanding of its mineral properties is essential for gaining insights into its relevance to clinical hip fracture.

1.3.3 The microstructure

The Haversian system

The Haversian system or secondary osteon (Fig. 1.2b, Fig. 1.3a and b) is the best-known hierarchical structure in human cortical bone. Cooper et al. (1966) defined an osteon as a cylindrical structure that is composed of a neurovascular canal, surrounded by concentric cell-permeated bone lamellae [79]. The average diameter of an osteon is approximately 200 μm to 300 μm [56]. The central vascular channel (Haversian canal), about 50 μm to 90 μm in diameter [56], roughly aligns to the long axis of the bone. Each osteon is outlined by a layer (1 μm to 5 μm thick [56]) of highly mineralized cement line [80], and “glued” together by interstitial lamellar bone (remains of the old osteons).

The secondary osteons are the results of dynamic remodeling, which enables cortical bone to adapt to the mechanical environment [57,79]. Due to the central role of remodeling in bone adaptation and disease, the description of osteon population density, Haversian canal size, osteon size and porosity are frequently used to assess human bone quality [48,81]. These parameters have

been found to vary with sex, age, and physical activity [79]. More importantly, these structural features are closely related to bone strength and toughness [82,83]. As briefly discussed in chapter 1.4.1, the increase of cortical bone porosity could be partially attributed to the accumulation of remodeling osteons to form giant composite osteons, which ultimately lead to the trabecularization of the cortex [84]. More recent synchrotron micro-CT studies revealed the 3D structure of individual osteon in the femoral cortex [85], which could help improve our understanding of how the cortex converts into trabecular bone and results in cortical thinning. The higher rate of turnover in the older bone tissue was also associated with the decreased frequency of crack bridging, a critical bone toughening mechanism [86].

The lamellar bone and collagen fibre orientation

The lamellar structure is a widespread architectural motif of bone, and plays diverse mechanical roles. Lamellae may form as circumferential layers (Fig. 1.2b), wrapping around the outer and inner surface of the long bones, or as concentric cylindrical structures within the cortical bone, surrounding the Haversian canals (Fig. 1.2b, Fig. 1.3a and b). It is a highly organized bone structure, which consists of parallel layers of lamellae that contain bone minerals and organic matrix.

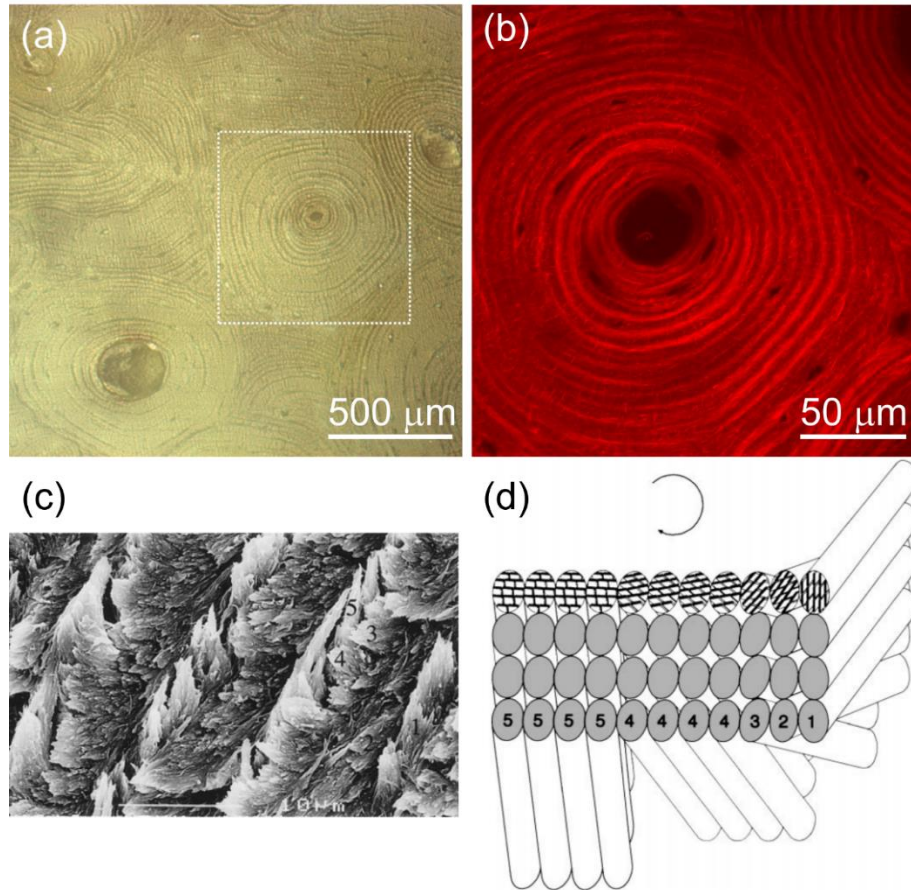


Fig. 1. 3 Lamellar bone microstructure: (a) White reflective light image of a transverse section (with respect to the long axis of the femoral shaft) showing Haversian system (e.g. white dashed frame); (b) SHG signal demonstrates a better contrast and finer details of the collagen orientation in the osteon. The bright red signal corresponds to collagen fibres oriented at large angle to the osteon’s long axis, and the darker layer corresponds to collagen fibres aligned at smaller angle to the osteon’s long axis; (c) SEM image of a fracture surface of the lamellar bone; (d) Schematic illustration of the rotated plywood structure where each pair of lamellae consists of five sublayers. (c) and (d) reprinted and adapted from [87] with permission from Elsevier.

When a transverse section of cortical bone (plane perpendicular to long bone axis) is observed with optical microscopy, there often exists the pairs of thin/thick or dark/bright alternating lamellae in each osteon (Fig. 1.3a). The alternating lamellar structure gives rise to the “birefringence” under polarized light [88]. This is mostly due to the different orientations of the collagen fibrils in each layer of lamellae, yet studies have shown that the organization of collagen fibrils is more complicated than simply alternating longitudinal and transverse arrays with respect

to the Haversian canal [89–91]. Early study by Gebhardt (1905) revealed that the collagen fibrils of one lamellae twisted around the Haversian canal with different pitches. Ascenzi and Bonucci [92] proposed lamellar structure as alternating longitudinal and transverse lamellae with respect to the osteonal long axis. Later, they refined this model as unidirectional extinct lamellae and bidirectional/multidirectional bright lamellae, based on studies of individual lamellae within osteons [93,94]. They also found that the transition between successive lamellae in certain osteons comprises a criss-crossing layer whose fibril orientations differ from those of adjacent lamellae [95]. Giraud-Guille [96] proposed a “twisted plywood” model, in which the fibril layers progressively change orientation. This model was confirmed and further developed by Weiner et al. [89] via cryo transmission electron microscopy (TEM) study. They found that fibrils are oriented in the same direction within each sub-lamellar layer, and change direction at a constant angle from one sub-layer to the next (Fig. 1.3c and d). The three-dimensional orientation of the mineralized fibrils along the radius of a single osteon was reconstructed by Wagermaier et al. [97]. More recently, Natalie Reznikov et al. [90] used dual beam microscopy and the serial surface view (SSV) method to identify three distinct sub-lamellar structural motifs at 3D space: a plywood-like fanning sub-lamella, a unidirectional sub-lamella and a disordered sub-lamella.

The orientation of the collagen fibrils is critical for bone stiffness and strength [98,99]. It has been shown in animal bones and human femoral shaft that regions of bone primarily experiencing tension tend to have the collagen fibrils oriented longitudinally (with respect to osteon long axis), while those mainly under compression tend to be oriented oblique or transverse [100–103]. The orientation of collagen fibrils in human femoral neck is not clearly understood due to the complex biomechanical conditions. Although one study compared the femoral neck’s lamellar structure between chimpanzee and modern human, and found strong birefringence both

superiorly and inferiorly in the human femoral necks. This pattern forms a clear contrast with the chimpanzee's femoral neck [104].

In the past, multiple techniques, such as SEM [90], TEM [89], AFM [105], LSCM [106], have been used to visualize and analyze the collagen fibril orientations. Compared to these conventional methods, we have seen a growing interest in another optical approach - second harmonic generation (SHG) microscopy. It has advantages over polarized light microscopy in terms of image quality and information content, and over confocal microscopy in terms of penetration depth and intrinsic optical sectioning capability (without the loss of signal from pinhole) [107]. The SHG signal intensity depends on the collagen orientation with the strongest signal from the ones lying in the plane [107]. When imaged under SHG, a high contrast image is produced, providing valuable information on the preferred orientation of collagen fibrils in bone (Fig. 1.3b). In the past decade, SHG microscopy has become a powerful technique to image collagen fibrils in biological tissues with high contrast and specificity [108]. However, there are few studies using SHG examining the collagen fibrils in bone so far [109].

1.3.4 Bone minerals and organic matrix

Bone is composed of approximately 65 wt % mineral, (20-25) wt % collagen (mainly type I collagen), 10 wt % water, and (1-2) wt % noncollagenous proteins (NCPs) [56]. Type I collagen is in the form of a triple helix that assembles in a quarter-staggered array with hole-zone between the ends of the successive molecules [110] (Fig. 1.4a). Each collagen molecule is approximately 300 nm long and 1.5 nm thick [51], and they stack together to form collagen fibrils (approximately 80 nm-100 nm in diameter) (Fig. 1.4a). The diameter of collagen fibril was reported to decrease in osteoporotic bone than in healthy bone tissue [111]. Collagen fibrils are generally cross-linked as

a result of either enzymatic [112] or nonenzymatic [113] process. Such cross-linking was found to greatly impact the mechanical behavior of the bone tissue [114–116].

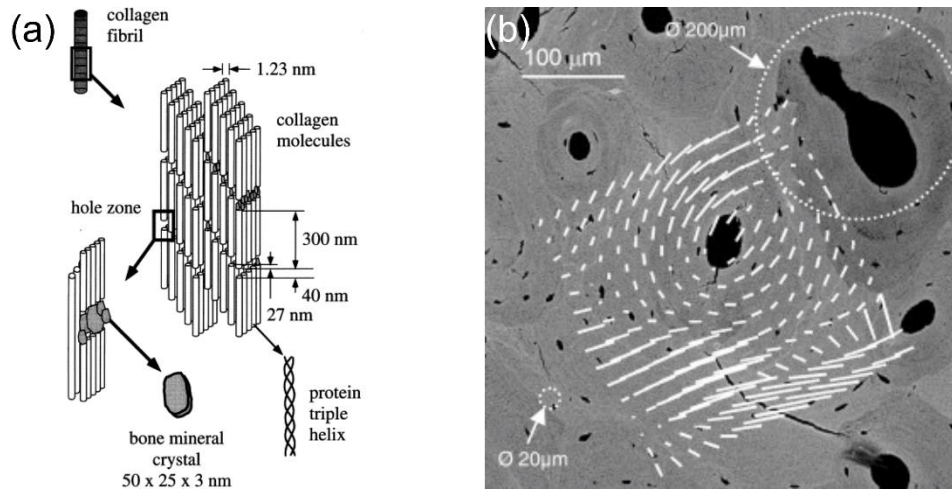


Fig. 1. 4 Bone structure at the nanometer scale: (a) Schematic illustration of periodic staggered collagen molecules and the associated gaps filled with minerals. Note that bone minerals also grow outside the gaps which are not shown here; (b) Backscattered electron (BSE) image superimposed by the white bars that represent mineral orientation. The orientation and the degree of alignment of the bone minerals are indicated by the direction and the length of the bars, respectively. (a) and (b) reprinted and adapted from [53] and [52] with permission from Elsevier.

Bone mineral mainly consists of carbonated apatite ($\text{Ca}_5(\text{PO}_4, \text{CO}_3)_3(\text{OH})$), which nucleates in the gap zones and on the surface of the collagen fibrils, and predominantly aligns with fibril's long axis [99,110,117] (Fig. 1.4a). The geometry, orientation and architecture of the bone mineral all indirectly affect the mechanical properties of bone. In particular, Currey [118] has shown that there is a positive correlation between tissue mineralization and stiffness, but also an inverse relation between mineralization and fracture toughness. With increasing mineralization, the tissue becomes more brittle, and cracks will propagate more easily than in lower mineralized bone. The size of the bone minerals also varies with tissue age, anatomical location, species, etc [119,120]. The thickness of human bone mineral is reported in the range of 1.5 nm to 9 nm for human bone minerals [121,122] (Fig. 1.4b), and the length is approximately 26 nm [123]. With bone tissue ageing, the mineral platelet grows larger and more crystalline. In diseased bone, such as

osteogenesis imperfect (OI), minerals have been shown to display decreased mineral size [123,124]. Fluoritic bone (mechanically brittle bone) has been associated with increased mineral size [125]. However, it is still not clear in osteoporotic bone, where both larger [126] and similar mineral size [119,127] have been reported in the patients compared to the healthy controls.

Analyzing bone minerals

Quantitative backscattered electron (qBSE) imaging

qBSE is based on the fact that the intensity of electrons backscattered from a thin surface layer of the bone sample is proportional to the concentration of the bone minerals (Ca wt %) [128–131]. This technique could be used to map the calcium concentrations and to determine the bone mineralization density distribution (BMDD, frequency distribution of Ca concentrations within the bone sample). The BMDD is derived from the digital images based on pixels, thus it is not a single value describing the mineral content (e.g. DXA) but rather a histogram of mineral contents in the selected regions of interest. There are several parameters that could be obtained from BMDD [132]: Ca_{peak} (most frequently occurring calcium concentration), Ca_{mean} (weighted mean Ca concentration), Ca_{width} (the full width at half maximum of the histogram). In the past, BMDD has been widely used to study diseased and drug-treated bone tissues. Deviations from normal BMDD have been reported in osteomalacia [132], osteoporosis [127], osteogenesis imperfecta [74], alendronate [132] and bisphosphonates-treated bone [133].

Raman microspectroscopy

Raman microspectroscopy is a vibrational spectroscopy technique that is used to assess the relative content and properties of the minerals and proteins of bone tissue. It has the capability of measuring under ambient/moist environment at high spatial resolution ($< 1 \mu\text{m}^3$) [133,134]. Absolute values of the Raman band intensities are rarely used in Raman analysis, and most studies

report the relative peak intensities (i.e. integrated peak area) of selective bands from the Raman spectrum. In particular, ν_1 phosphate divided by amide I band intensity corresponds to mineral-to-matrix ratio, indicating the degree of mineralization. The mineral-to-matrix ratio has been reported to be significantly altered in OI bone [135], which mainly attributes to the lack of collagen matrix. Carbonate-to-phosphate ratio is also frequently used, as the extent of carbonate substitution is associated with mineral crystallinity and size [136]. Iliac crest biopsies from the female patients who suffered from a fracture were reported to have a higher carbonate-to-phosphate ratio than healthy individuals [137].

Small- and wide-angle X-ray scattering (SAXS/WAXS)

SAXS/WAXS exploit differences in electron density distributions of the different materials within the sample [138]. SAXS can be used to measure both collagen and mineral platelets in the order of (1-100) nm, while WAXS can provide information on the spacing between crystal lattice planes [138]. Thus, by combining SAXS and WAXS in a single measurement, one can retrieve information on mineral structure, mineral platelets dimension, and collagen fibrils/minerals orientation simultaneously [138] (Fig. 1.4b). Compared to TEM, AFM and XRD, SAXS/WAXS have the advantages of allowing higher throughput of samples with shorter analysis time and non-destructive examination of local structural properties at the nanoscale. Previous studies have successfully applied SAXS/WAXS to examine the shape, size, and organization of bone mineral platelets in fracture healing [139,140], in diseased [123,141] and in drug-treated bone [125]. Additionally, SAXS/WAXS particularly allow mapping of these properties within different mineralized tissues (e.g. different mineral density, Fig. 1.4b) [142]. Due to the high brilliance of synchrotron radiation (SR), which enables higher resolution and fast acquisition of X-ray

scattering patterns, there is increasing research utilizing SR-based scanning SAXS/WAXS to investigate bone and teeth [121,143].

1.4 Bone biomechanics

The mechanical function of bone is just as complex as its hierarchical structure. At the macroscopic scale, femoral neck cortices are thought to experience different types of stress at superior and inferior aspects [66,144]. At the microscopic scale, bone deforms (inelastically) through a controlled microcracking process [54,145]. At the nanoscopic scale, the mineral platelets are able to sustain large tensile stress, and the surrounding protein matrix can effectively transfer shear stress [146–149]. Although bone has inherent defects, i.e. osteocytes lacunae, canaliculi and Haversian canals, as stress concentration and crack imitation sites [145,150], the nature designed lamellar bone structure has been shown to be a robust material that has low-notch sensitivity under complicated biomechanical environments [151].

1.4.1 Human proximal femur under a sideways fall

As mentioned in chapter 1.3.1, low-energy falls account for 90 %-95 % of hip fractures [38–40], with sideways fall having the highest fracture rate [39,40]. As such, sideways fall is the most common configuration that researchers use to simulate hip fracture process, and perform biomechanical analysis [66,144,152–155]. Many laboratory fall-simulating tests, finite element analysis (FEA) and computer tomography (CT) imaging have been widely used to analyze the stress and strain distribution at the proximal femur during a fall, and the associated failure mechanisms. Finite Element (FE) based analysis has been used to study mechanics of proximal femur failure under various loading conditions [156–161]. Early FE and biomechanical analyses from studies that simulate a fall demonstrated stress reversal compared to normal gait. That is, the

femoral neck experiences compression at the superior surface and tension at the inferior surface during a sideways fall [144,152,162] (Fig. 1.5). Recent studies used high-resolution computed tomography (CT) to develop more mechanistically accurate models at a microscopic level and found large compressive stresses developed superiorly [55,155]. High-speed video combined with digital image correlation (DIC) on *ex vivo* hip fractures demonstrated that the initiating crack frequently begins in the superolateral cortex which is under high compression [66,163–165]. Despite this progress, the deformation and fracture process in clinical cases is still not well understood. This is partially due to the fact that findings from laboratory studies invariably incorporate many simplifications (i.e. muscle forces are not included, many other physiological aspects are not simulated), which may not accurately simulate the mechanisms of clinical hip fractures *in vivo*.

Based on the observation that the superolateral cortex of the femoral neck becomes substantially thinner with ageing, Mayhew et al. [17,166] proposed that compression-induced buckling in the thin cortex is the cause of hip fragility. This hypothesis is partially supported by other geometrical and structural analyses of femoral neck biopsies: fracture cases had thinner cortices [62–64,167], and weaker trabecular bone structure along the inferoanterior-superoposterior axis, compared to controls [168]. Yet, whether cortical bone buckling can occur *in vivo* is not known [61,144].

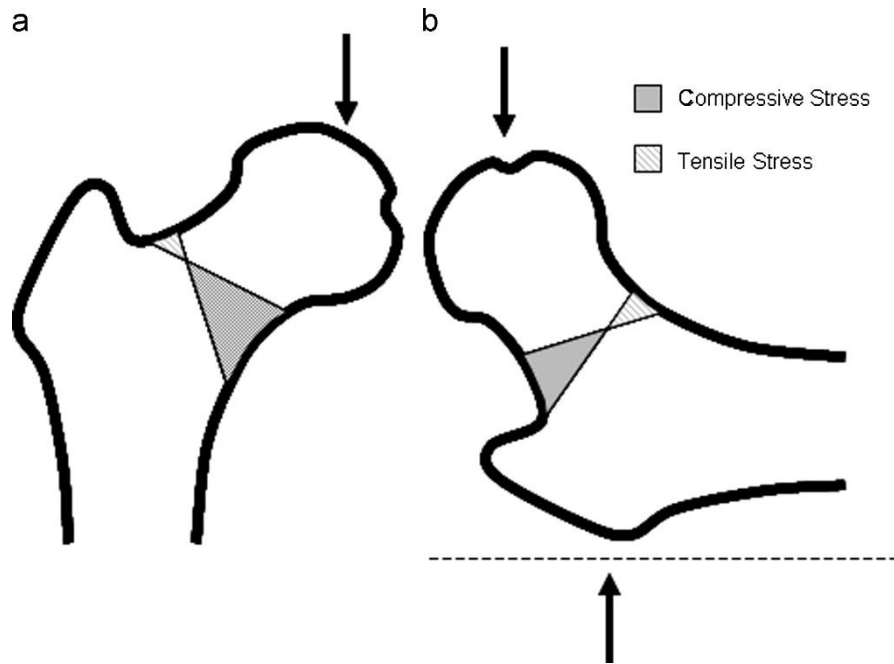


Fig. 1. 5 Schematic illustration of the relative magnitude and the types of stress on the femoral neck under two loading modes: (a) Physiological configuration: the inferior surface experiences a large component of compressive stress, while the superior surface is under a smaller tensile stress; (b) Stress states reverse for sideways fall on the greater trochanter: the inferior surface is under a small tensile stress, while the superior surface is under a larger compressive stress. Reprinted and adapted from [66] with permission from Elsevier.

1.4.2 Deformation and fracture mechanisms of bone

Stress and strain properties of bone

Bone behaves differently under tension and compression [169]: compressive strength is much higher than tensile strength, yet compressive strain is much lower than tensile strain. As such, bone exhibits a significant amount of inelastic strain under longitudinal tension. This asymmetry enables bone to achieve high strength during bending: tensile surface yields first and ultimately withstands high inelastic strain, while compressive side sustains higher stress after the shift in neutral plane towards the compressive surface [170] (Fig. 1.6). More importantly, the significant inelastic deformation in bone allows it to redistribute stress around the defects (i.e. osteocyte lacunae, canaliculi, Haversian canals), and reduce (in some cases eliminate) the stress concentration. A recent study by Ebacher et al. [145] has demonstrated that when human cortical

bone is loaded under transverse compression, the inelastic strain could reach up to 7 %, and is associated with a stable microcracking process that relieves the stress concentration at the Haversian canals.

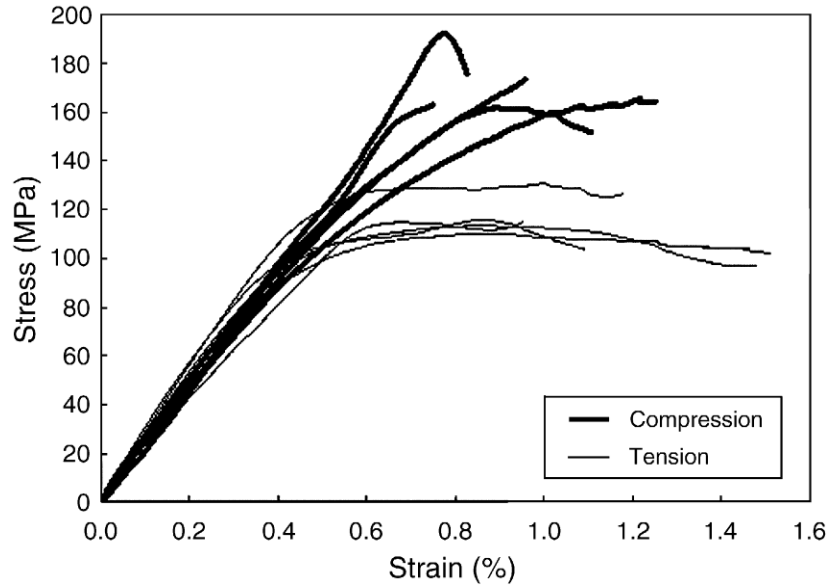


Fig. 1. 6 Tensile and compressive stress-strain curves for cortical bone under bending. Reprinted from [170] with permission from Elsevier.

Macroscopically, the inelastic deformation in bone is accompanied by the development of “whitening zones” [171] which have been associated with the deformation bands that inhomogeneously distribute across the samples. To measure these deformation bands, one could use digital image correlation (DIC), an optical full-field technique for non-contact, 2D and 3D deformation measurements. DIC is particularly suitable for biological applications due to its accuracy in determining strain in inhomogeneous, anisotropic, non-linear materials, such as bone. Nicolella et al. [172,173] have used DIC to analyse strain distribution around a microcrack in bovine cortical bone and found that the strains are the largest at the crack tip and around osteocyte lacunae. Benecke et al. [174] found that elastic deformation in bovine bone is relative homogeneous, where inelastic deformation stage shows more than one high deformation bands

across the sample. A recent study by Ebacher and Wang [145] using local DIC analysis has demonstrated that the compressive microcracks in human cortical bone are created due to the high strain concentrations at the four quadrants of osteons radiating from the Haversian canal. Despite all these progresses, how the hierarchical structure of bone affects inhomogeneous inelastic deformation and how the deformation bands are stabilized without early failure remain unclear.

Microcracking in bone

Bone has the extraordinary ability to undergo significant inelastic deformation, which directly results in its high resistance to fracture [54]. Accompanying the inelastic deformation is the formation and development of microcracks [54,175] (Fig. 1.7). As such, microcracking has been proposed to be one of the dominant toughening mechanisms in bone [54,176].

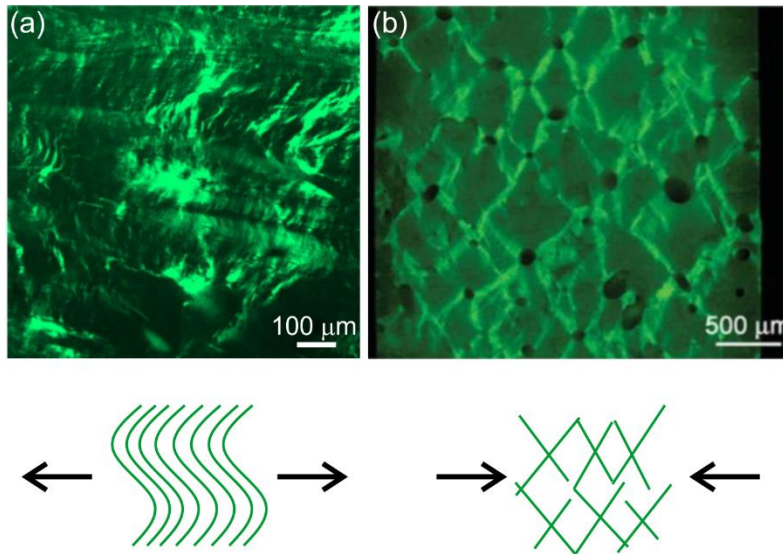


Fig. 1. 7 Epifluorescence and laser scanning confocal microscopy images showing two types of microcracks: (a) Tensile dense wavy microcracks; (b) Compressive microcracks with typical cross-hatched pattern. (a) and (b) reprinted and adapted from [171] and [145], respectively. Permissions obtained from Elsevier and John Wiley and Sons, respectively.

Early studies by Currey and Brear [177] used basic fuchsin staining clearly demonstrated the development of tensile microcracks after yielding. Later studies by Zioupos et al. [178] confirmed that microcracking coincides with the deviation from linearity in the stress-strain curves.

More importantly, studies have shown that the patterns of microcracks strongly depend on the local stress. In tension, densely distributed wavy microcracks form roughly normal to the direction of the applied stress with crack length around 2 μm to 10 μm [102,175,179] (Fig. 1.7a). Reilly and Currey [102] found that in equine radius, tensile microcracks increase in density with the increasing strain, till reaching the maximum density at strains around 0.8 %. However, the small tensile microcracks do not coalesce to form longer microcracks ($> 100 \mu\text{m}$) until very high strains, indicating a stable deformation process. In contrast, compressive microcracks are straight and relatively longer; forming a typical cross-hatched pattern, orienting at approximately 27° - 40° to the long axis of the bone [102,145,169,170] (Fig. 1.7b). Recently, confocal imaging analysis on human cortical bone under compression [180] has revealed that each set of cross-hatched cracks is consisted of groups of arc-shaped microcracks which is further resolved into finer cracks.

Tensile and compressive failures of the bone tissue at the material level have been extensively studied in the past [102,145,171,175,179], while shear deformation and fracture of human cortical bone, especially shear microcracking, has been rarely studied [181,182]. Ascenzi and Bonucci were among the earliest to investigate the shear properties of single osteons [183]. Their work on single osteons under compression [94] showed that the microcracks created by compression-induced shear form an angle of roughly 30° - 35° with the long axis of the osteon. With detailed electron microscopic study, they have found circular cracks in the osteons having alternating fibre orientations in adjacent layers [184]. Later torsional studies showed that damage appears within interstitial bone, Haversian systems, and along cement lines [185,186]. However, since torsion tests generate non-uniform shear in the specimens, they are not suitable for studying bone behavior in pure shear mode [187].

Role of hierarchical structure in microcracking

Role of osteons and lamellae

In chapter 1.4.2, I have discussed that many clinical studies evaluate bone quality based on population density of the osteons, osteonal canal size, osteonal size, etc. However, not so many studies explain the detailed mechanisms behind this correlation from the material's point of view. Osteon pullout has been identified as one of the toughening mechanisms in bone [188], whereby the cement lines between osteons and interstitial bone provide a weak interface and deflect the incoming cracks [189–191]. Others report crack deflection at lamellar boundaries [176], perhaps due to the changes in collagen fibril orientation between different lamellae leading to the alternating stiffness [192]. By testing human cortical bone under transverse compression, Ebacher et al. [145] discovered that most arc-shaped microcracks form through multiple nucleations of short micro-radial cracks and the subsequent coalescence within the thick lamellae. This study shows the crucial role of the lamellae in redistributing stress around each Haversian canal through the stable development of multiple intralamellar microcracks.

Microcracking at the sub-lamellar level

The initiation of microcracks is relatively well studied. It is known to start at the structural defects and stress concentration sites in bone. Previous studies showed that Haversian canals [102,145], osteocyte lacunae [150,180] and canaliculi [180] provide sites for microcrack initiation due to the stress concentration. However, how microcracks develop from the nucleation sites, and interact with local bone's microstructure are obscure from the literature. Recently, a LSCM study by Ebacher et al. [180] revealed a clear sub-lamellar cross-hatched pattern involving a high density of very fine cracks developing intralamellarly with a regular crack spacing size ($< 1 \mu\text{m}$), suggesting the significant role of mineralized collagen fibril bundles in governing the

microcracking process. In spite of this significant progress, direct image evidence to show the mechanical-structure link at the sub-lamellar level is still insufficient.

The invention of second harmonic generation (SHG) combined with two photon excitation fluorescence (TPEF) may be a solution for this issue. TPEF is similar to conventional LSCM, but has advantages of deeper tissue penetration (~ 1 mm), efficient light detection, and reduced phototoxicity [193]. It uses red-shifted excitation light to minimize scattering in the tissue. For each excitation, two photons of infrared light are absorbed, thus the background signal is strongly suppressed. As TPEF provides microcracking information through fluorescent staining and SHG provides micro-structural information from collagen fibril organization, the two combined within a single microscope can be very advantageous in providing complementary information about structure-function relations.

Nature of microcracking

There are multiple models [146,147,149,194] that have been developed to explain the deformation of bone at the individual mineral and collagen level. Essentially, the intrafibrillar minerals and the mineralized fibrils embedded within the interfibrillar matrix primarily sustain large tensile stress without fracture, while the collagen fibres and interfibrillar matrix (non-collagenous proteins/NCPs) transfer shear stress. In such context, the small mineral size and its subsequent large aspect ratio have been proposed to achieve the optimized fracture strength and tolerance of flaws [147].

With the nano-fibrous nature of bone, it is reasonable to expect that the formation of microcracks occur at the interfaces between the minerals and the proteins. AFM studies suggested that the NCPs on the surface of the mineralized fibrils act as adhesives that “glue” the mineralized fibrils and resist interfibrillar separation [195]. These highly coiled NCPs contain weak (sacrificial)

bonds that would break under load and result in the stretching of hidden length. This process is thought to be able to dissipate energy [196]. Based on in-situ synchrotron X-ray scattering, Gupta et al. [149,197] measured the tensile deformation at the fibrous and tissue levels, and found that the strain of collagen fibrils remains constant during inelastic deformation. Such observation suggests that during the inelastic stage, decohesion of the mineralized collagen fibrils occurs either interfibrillarly (bonds break between fibrils) or intrafibrillarly (bonds break collagen and mineral platelets). With the increasing strain, more interfibrillar decoupling could occur, and leads to the formation of larger-scale microcracks. In another model proposed by Mercer et al. [169], the inelastic deformation of bone was thought to arise from the interfacial “slip” between the minerals and the collagens through a thin adhesive layer. The “slip” concept resembles the idea of inter- and intra-fibrillar decoupling as proposed by Gupta et al. [149,197]. Further the Mercer et al. model [169] could explain stress hardening by the stretching of the collagen. In spite of these progresses, the physical nature of microcracking down to the mineralized collagen level remains to be resolved, partially due to the limited resolution of the current imaging techniques. Further, the proposed models did not consider the involvement of other hierarchical factors (i.e. different fibril orientation, lamellar structure) in the deformation and fracture process of bone.

1.5 Summary of current problems

It remains a great challenge to identify patients with high risk of hip fractures. In part, this is due to the current clinical examinations that cannot fully capture the changes at the tissue level and the indirect approaches to assess the risk of fracture. These challenges together with our lack of understanding of some fundamental aspects of bone structure and mechanics, partially explain why the mechanisms and conditions leading to bone failure at the hip remain unclear.

Cortical bone thinning of femoral neck and trochanters with ageing is well recognized as a contributor to hip fragility. Yet, the effect due to changes in cortical bone quality, such as the periosteal hypermineralization remains unclear. The high mineral content and the lack of lamellar structure in the hypermineralized tissue indicate its adverse impact to the local mechanical properties of the femoral cortical bone. It is thus important to understand the material properties and the basic constituents of this tissue: its degree of mineralization, micromechanical properties, mineral dimension, and the organization of the mineral platelets.

Bone microcracking is closely related to its deformation and fracture process, therefore offers a promising opportunity of studying clinical hip fractures. The pre-requisite would be a clear understanding of the microcracking behavior under each type of stress. Shear is of particular interest due to its involvement in femoral neck fractures. Shear microcracking is also poorly defined as compared with tensile and compressive microcracking. Therefore, a systematic study of human femoral cortical bone under shear would reveal the roles of the lamellar structure in resisting a shear fracture.

The mechanisms of clinical hip fractures are poorly understood at the fundamental level. The key questions that remain to be answered are: What are the stress and strain involved in a clinical hip fracture? What is the potential role of the hypermineralization in hip fractures? How do the microstructure of femoral neck cortical bone and the hypermineralized tissue affect the mechanical behavior of the femoral bone? To answer these questions, an effective approach needs to be developed to reconstruct the stress states at fracture sites, to associate bone's microstructure with the deformation and fracture process, and to identify key material failure mechanisms.

Chapter 2 Goal and Objectives

The ultimate goal of this dissertation was to identify the fundamental failure mechanisms of femoral cortical bone during hip fractures. Hip fracture is a product of both external impact and internal bone structural fragility. The complexity of hip structure and the diverse loading conditions make it challenging to address this issue. Hence, both fundamental and clinical research on the material changes of the femoral cortex and the deformation and fracture process of the cortical bone were conducted.

The specific objectives of this dissertation are:

Objective 1: To examine the mineral content and micromechanical properties of the hypermineralized tissue in human proximal femur

The changes of femoral bone quality with ageing contribute to hip fragility. “Dense calcified” tissue (hypermineralization) occurs at the peri-cortical bone, particularly at the superior femoral neck where cortical bone is the thinnest and sustains a larger portion of compressive stress during a hip fracture. It raises clinical concerns due to the susceptibility to crack formation and propagation. Bone mineralization is known to be closely related to its mechanical properties, i.e. strength, hardness, modulus, fracture toughness. Yet, the exact mineral content and the micromechanical properties of the periosteal hypermineralization remain unclear. For this purpose, the distribution of hypermineralization at the mid-femoral neck was thoroughly examined in this thesis to identify the critical locations with increased fragility. The mineral content of the hypermineralized tissue was quantified and compared with that of the osteonal and interstitial bone. Finally, the associated micromechanical properties (i.e. cracking and hardness) were demonstrated through microindentation technique.

Objective 2: To study the mineral size and organization of the hypermineralized tissue in human proximal femur

The mechanical integrity of mineralized tissue derives from its basic constituents: the mineral platelets and the organic matrix. Both the mineral size and the organization have profound influence on the macroscopic mechanical properties of the hypermineralized tissue. A clear understanding of the physical properties of its bone minerals is essential to address why hypermineralization could be “brittle”. Therefore, the mineral thickness and length were measured in this dissertation, and the mineral organization, including the degree of preferred orientation and spatial arrangement in the organic matrix were quantitatively studied. The investigation linked the changes at the ultrastructural level to the altered mineral content of the hypermineralized tissue.

Objective 3: To investigate deformation and fracture behavior of human femoral cortical bone under shear

Bone deforms (inelastic) and fractures through microcracking. Previous studies showed strong evidence that shear could be an important failure mechanism in femoral neck fractures. Therefore, understanding shear microcracking of femoral cortical bone through controlled tests is a pre-requisite to the study of clinical hip fractures. To this end, the study was designed to investigate the orientation dependence of the shear strength of human cortical bone, to quantitatively examine the characteristics associated with shear microcracks, and to identify the effects of hierarchical structures to shear microcracking.

Objective 4: To examine microcracking patterns and the associated failure mechanisms in clinical hip fractures

The fundamental failure mechanisms of hip fractures are poorly understood mainly due to the current approaches to assess the risk of hip fractures, which are indirect and were not verified *in vivo*. Therefore, there is a need to directly examine the stress and strain conditions, and the associated microstructural changes of the femoral neck samples from patients who sustained hip fractures. For this reason, the intracapsular hip fracture samples were retrieved at hip surgeries and examined at the tissue-level. Specifically, the microcrack density within the critical range to the main fractures was quantified at different anatomical locations. The microcrack patterns were identified and used to reconstruct the stress states based on the unique correlation with the applied types of stress. The occurrence and the fracture patterns of hypermineralization at the main fracture surfaces were examined as a means to understand its role in clinical hip fractures.

Chapter 3 Hypermineralized Tissue in Human Proximal Femur: Distribution, Mineralization and Micromechanical Properties

The important mechanical role of the femoral cortical bone in hip fracture is well known [152,155,198]. Cortical bone thinning of the femoral neck [17,63] and trochanter [199] have been shown to be highly relevant to hip fragility. Additional alterations in tissue properties of the femoral cortical bone can further affect its susceptibility to fracture. One such change could be the hypermineralization at the periosteal region of the proximal femoral cortex in people at advanced age.

In contrast to the extensive studies on the age-related changes in the geometry [18,200] and the microstructure [17,62,63], there is little information available on the periosteal hypermineralization of the femoral cortical bone. A few studies done so far on the hypermineralized tissue have either focused on its circumferential coverage at the mid-femoral neck [71], or the area fraction at femoral neck and trochanteric regions [72,73], or the morphological features by optical and electron microscopy [72,73,76]. The degree of mineralization of the hypermineralized tissue, an important indicator for the mechanical properties, has never been quantified. Based on the BSE observation that cracking is more prevalent in the hypermineralized region than in the lamellar bone, it was suspected that the hypermineralized tissue was a “brittle” material [72,73]. Yet, those studies were performed on dehydrated samples, and the mechanical properties of bone are known to change following dehydration [201]. Thus, there is a need to test the mechanical properties of the hypermineralized tissue under hydrated state (close to physiological conditions). The goal of the study in this chapter was to quantify the degree of mineralization of the hypermineralized tissue at human proximal femur, to examine the cracking

behavior, and to measure the relative hardness values of the hypermineralized tissue in comparison with the lamellar bone.

3.1 Experimental

3.1.1 Specimen preparation

Six freshly frozen human cadaver femora (four males, two females, age rang: 66-74) without reported metabolic bone tissue conditions were obtained from LifeLegacy Foundation and used for the study. Dual energy X-ray absorptiometry (DXA) scans were performed with a Hologic QDR 4500W bone densitometer (Hologic Inc., Waltham, MA) following the standard protocol for the proximal femur [47]. Donor information, total proximal femur areal bone mineral density (aBMD) and *T*-scores are presented in Table S3.1. All bone tissues were kept frozen at -20 °C until specimen preparation. The study was approved by the Clinical Research Ethics Review Board at the University of British Columbia.

Two sets of specimens were prepared from the six individuals: the first set was examined with quantitative backscattered electron (qBSE) imaging; the second set was tested with microindentation. Specifically, each femur was first manually cleaned of adherent soft tissue with a scalpel. Two transverse cuts with respect to the long axis of the femoral neck were made at mid-femoral neck and intertrochanter (Fig. 3.1a), using a water-cooled diamond saw (EXAKT Adv. Tech. GmbH, Norderstedt, Germany). At each location (i.e. mid-femoral neck and intertrochanter), one transverse cut resulted in two blocks (each was 2 mm thick): one “lateral” and one “medial”. The lateral blocks were used for qBSE imaging, while the medial blocks were used for microindentation tests.

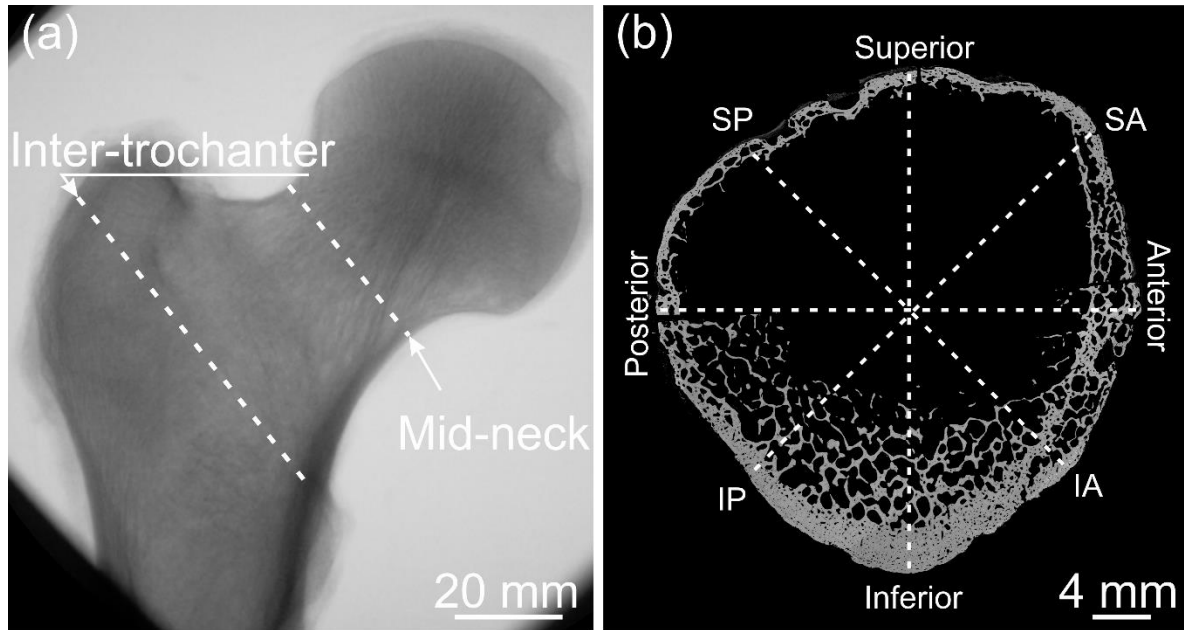


Fig. 3. 1 X-ray image of a human proximal femur (a) and backscattered electron (BSE) image of a femoral neck sample (b). Specimens were obtained from mid-femoral neck and intertrochanter, as indicated by the arrows in (a). Femoral neck sample (b) was divided into eight sectors for analysis: superior-central to superior-anterior (SC-SA); superior-anterior to anterior (SA-A); anterior to inferior-anterior (A-IA); inferior-anterior to inferior-central (IA-IC); inferior-central to inferior-posterior (IC-IP); inferior-posterior to posterior (IP-P); posterior to superior-posterior (P-SP); superior-posterior to superior-central (SP-SC).

For specimens analyzed with qBSE imaging, they were fixed in 70 % ethanol/water solution for 24 h, followed by dehydration in a graded ethanol series (80 %, 90 %, and 100 %) overnight per step and finally air-dried. All the specimens were then embedded in epoxy resin with a low curing temperature (Epothin2, Buehler) and allowed to cure overnight at room temperature. Following epoxy mounting, the samples were ground with a series of carbide sandpapers, and polished with diamond suspension starting at 6 μm , followed by 1 μm . 0.05 μm silica suspension was also used to achieve an optically flat and scratch-free surface. Selected samples were ground to $\sim 100 \mu\text{m}$ thick for histological assessment (Giemsa staining).

For those tested with microindentation, wet bone samples were embedded without prior dehydration in epoxy resin with a low curing temperature (Epothin 2, Buehler). Subsequently, the

samples were ground and polished following the same procedure as described in the previous paragraph. After being polished, they were soaked in phosphate-buffered saline solution (0.1 mol; pH 7.2-7.4) for at least 48 h, and kept at 4 °C in sealed glass jars until testing [202]. To confirm that hypermineralized tissue was indeed more mineralized than lamellar bone under hydrated condition, two femoral neck samples, wrapped with saline soaked tissue, were scanned with micro-CT (μ CT 35, Scanco, Switzerland).

3.1.2 Optical microscopy

Each polished bone specimen was first examined using reflective light under a light microscope (Nikon Eclipse E600 or Nikon Epiphot 300). For microindentation samples, they were kept wet through the whole process. An objective lens of 5 \times was used for the overview images, and an objective lens of 20 \times were used to examine the microstructural features and to identify the potential regions of hypermineralized tissue, which do not have typical lamellar structure. For samples assessed by histological staining, transmitted light (Leica DM RXA2, Leica, Germany) was used to visualize the various degrees of coloration in different tissues following Giemsa staining which predominantly stains glycosaminoglycans/GAGs content. Note that color discrimination in this study is only qualitative.

3.1.3 Quantitative backscattered electron (qBSE) imaging

The lateral set of specimens and the standard materials (i.e. graphite, magnesium fluoride, aluminum, hydroxyapatite, demineralized bone) to be analyzed with qBSE were coated with a thin layer of carbon to increase the conductivity. The imaging procedure followed a protocol published previously [74,129]. Briefly, qBSE is based on the proportional relationship between the intensity of electrons backscattered from a depth of $\sim 1.5 \mu\text{m}$ of the surface of a bone sample and the weight

concentration of bone minerals. Regions of high average atomic number/high mineral concentration are brighter than regions of low atomic number/low mineral concentration.

An automated digital scanning electron microscope (FEI Quanta 650, Oregon, USA) equipped with an annular solid-state diode backscattered electron detector was used for qBSE imaging. The accelerating voltage and the working distance were kept at 20 kV and 15 mm, and the spot size was set at 5. To confirm the linear relationship between the atomic number and grey level, reference samples of pure carbon (C, graphite), magnesium fluoride (MgF_2), pure aluminum (Al), and hydroxyapatite (HA) were imaged under a fixed setting of contrast and brightness (Fig. S3.3). For converting the grey levels into calcium content, demineralized bone was used as the 0.00 Ca wt % reference point, and hydroxyapatite (HA) was used as the 39.86 Ca wt % (fully mineralized) reference point. The backscattered electron signal was calibrated and monitored by imaging the standards of pure C and Al every 15 min during the SEM imaging.

To map the entire femoral neck and the superior-central to superior-anterior sector of intertrochanter, an external control software (ESPRIT 2, Bruker) was used to semi-automatically take images at a magnification of $50\times$ ($100\text{ mm} \times 86\text{ mm}$ field of view, $1536\text{ pixels} \times 1326\text{ pixels}$) and to montage the entire circumference of the samples. The femoral neck section was divided into eight sectors: superior-central to superior-anterior (SC-SA); superior-anterior to anterior (SA-A); anterior to inferior-anterior (A-IA); inferior-anterior to inferior-central (IA-IC); inferior-central to inferior-posterior (IC-IP); inferior-posterior to posterior (IP-P); posterior to superior-posterior (P-SP); superior-posterior to superior-central (SP-SC) (Fig. 3.1b). The composite images were used for morphological survey and quantification of the distribution of hypermineralization around the femoral neck. Specifically, the area fraction (A_r %) of the hypermineralized tissue was calculated as the ratio of the area of hypermineralization to the total cortical bone area that

consisted of two regions: the hypermineralized tissue and the lamellar bone (including the porosities, i.e. Haversian canals and lacunae). The endocortical boundary between cortical and trabecular bone was determined by following the criteria as published previously [203]. Briefly, if the diameter of the pore is smaller than the distance from the pore to the endosteal surface, the pore is included in the cortex. The thickness ratio, defined by the ratio between the thickness of the hypermineralized tissue and that of the total cortical bone, was measured every 2.8° in the circumferential direction of the femoral neck [62].

To further quantify the local calcium content, 24 images uniformly distributed in the circumferential direction of the femoral neck were taken with a magnification of $200\times$ ($636\ \mu\text{m} \times 457\ \mu\text{m}$, $1536\ \text{pixels} \times 1326\ \text{pixels}$). Since hypermineralization generally appeared on the periosteal surface, only the periosteal cortical bone was imaged. For each image, histograms of bone mineralization density distribution (BMDD) were obtained from selected regions of interest: hypermineralized tissue, Haversian bone, and interstitial bone. Finally, Ca_{peak} for the peak position of Ca wt % from each BMDD histogram was used to represent the mineral content in each type of tissue.

3.1.4 Microindentation

Microindentation could provide information on the hardness, crack formation and propagation on small samples, and be conducted under ambient environment [202,204]. Hardness reflects the resistance to deformation of the material, while cracking behavior associates to the fracture toughness of the material. Although the optimum indentation technique to accurately quantify the fracture toughness of mineralized tissue is still under debate [202], Vickers indentation fracture (VIF) test is a widely used technique in the literature to evaluate the fracture toughness [202,205–207], and to measure the hardness of bone tissue [205,208]. The goal of the

indentation study was to demonstrate any mechanical differences between the lamellar bone and the hypermineralized tissue qualitatively.

Microindentation was performed with a Buehler microhardness tester (Vickers) equipped with a light microscope. The indentation load was calibrated with pure aluminum, and two researchers (R.W. and T.T.) calibrated the testing procedure and measurement of the indentation size. Bone samples were kept wet throughout the experiment. Before microindentation tests, OM images were taken at regions of interest. In the literature, an indentation load that ranges from 10 gf to 100 gf [207,209] has been used to obtain the hardness of bone tissue. In this study, indentation loads of 500 gf and 25 gf were used to acquire cracking information and hardness values, respectively. With the 500 gf and a dwell time of 15 s, indents were produced with an approximate size of 160 μm , exceeding the thickness of the hypermineralized tissue at femoral neck. Therefore, the indentation was made part in the hypermineralized tissue and part in the lamellar bone to compare the cracking behavior between the two structures. To obtain the Vickers hardness (HV) for each type of tissue, approximately 80 indentations (25 gf, 15 s) were made in each proximal femur, and each tissue was equally tested. This resulted in a total of more than 480 indentations. Haversian canals and periosteal surface were avoided by a distance of at least 3 times the impression diagonal (some regions of hypermineralization might violate this rule due to the limited thickness). The indentation diagonals were measured immediately after each indentation (within 30 s), using the light microscope equipped with a filar type eyepiece of the hardness tester. Indentation diagonals were converted to hardness according to a standard equation (ASTM Designation E 384) [210].

3.1.5 Statistical analysis

IBM SPSS v. 24.0 (NY, IBM Corp.) was used for statistical analysis. Nonparametric Friedman test was used to assess the area fraction of hypermineralized tissue among different locations. Friedman's two-way analysis of variance by ranks was used to test any differences in C_{peak} among the different levels of types of tissue (Haversian bone vs. interstitial bone vs. hypermineralized tissue), and among the different levels of anatomical locations. For comparison among the three types of tissues, the anatomical locations were pooled, and for comparison among the different locations, various types of tissues were pooled. For post-hoc test in C_{peak} , and for differences in hardness values between the lamellar bone and the hypermineralized tissue, Wilcoxon signed-rank test was used. Two-sided $p < 0.05$ was considered statistically significant.

3.2 Results

3.2.1 Morphological features

In all the six proximal femora, there was hypermineralization at the peri-cortical bone region under BSE imaging. Fig. 3.2(a-c, f) are the representative BSE images taken from femoral neck cortical bone showing hypermineralized tissue and the underlying lamellar bone. Based on the literature, the grey levels are positively correlated to the local mineral content of the bone matrix [74,129,130,211]: brighter pixels indicating a higher mineral density. The hypermineralized tissue clearly differs from the underlying lamellar bone in two ways: there was no obvious lamellar structure; multiple cracks existed within the hypermineralized region and were generally stopped at the boundary by the lamellar bone (arrow heads in Fig. 3.2b), which has the ability of relieving stress through multiple toughening mechanisms [145,212,213]. Another striking feature of the hypermineralized tissue in Fig. 3.2(a-b) was the dense aggregates which consist of small "mineral

deposits” of different sizes and clustered together close to the bone cortex and also scattered into the adjacent soft tissue (arrows in Fig. 3.2b). Such hypermineralized tissue was typically about 50 μm -150 μm in thickness, and existed in all the six femoral neck samples. These microscopic features closely resembled the appearance of mineralized periosteum that was first observed by Zagba-Mongalima et al. [76], and later reported by Allen and Burr in the mid-femoral neck [71]. In the intertrochanteric regions, the hypermineralized tissue was of 250 μm -500 μm thick that stemmed from typical mineralized fibrocartilage (Fig. 3.2d). They mostly displayed obvious fibrous insertion into the cortical bone (as opposed to the collagen fibres of the periosteum oriented parallel to the cortical surface). Such featured mineralized tissue was also observed in femoral neck samples (Fig. 3.2c), agreeing with the previous reports [72,73,75]. In some areas of the mineralized fibrocartilage, it contained scattered chondrocyte lacunae (arrows in Fig. 3.2f, Fig. S3.1b) and/or tidemarks (Fig. S3.1c). Occasionally, in the femoral neck region, a thin layer of hypermineralized tissue could also appear underneath the circumferential lamellar bone, which could be a derivative from mineralized periosteum (Fig. S3.1a). In line with the previous studies [214,215], mineral-filled lacunae was frequently seen in the lamellar bone region adjacent to the periosteal surface (arrows in Fig. S3.1d). This is most likely due to a general tendency for increased numbers of “local plugs” in the lacuna-canalicular network with ageing [215]. It should be noted that some regions of hypermineralization cannot be clearly visualized under optical microscopy (Fig. S3.2), emphasizing the need of using SEM/BSE in imaging or confirming hypermineralization.

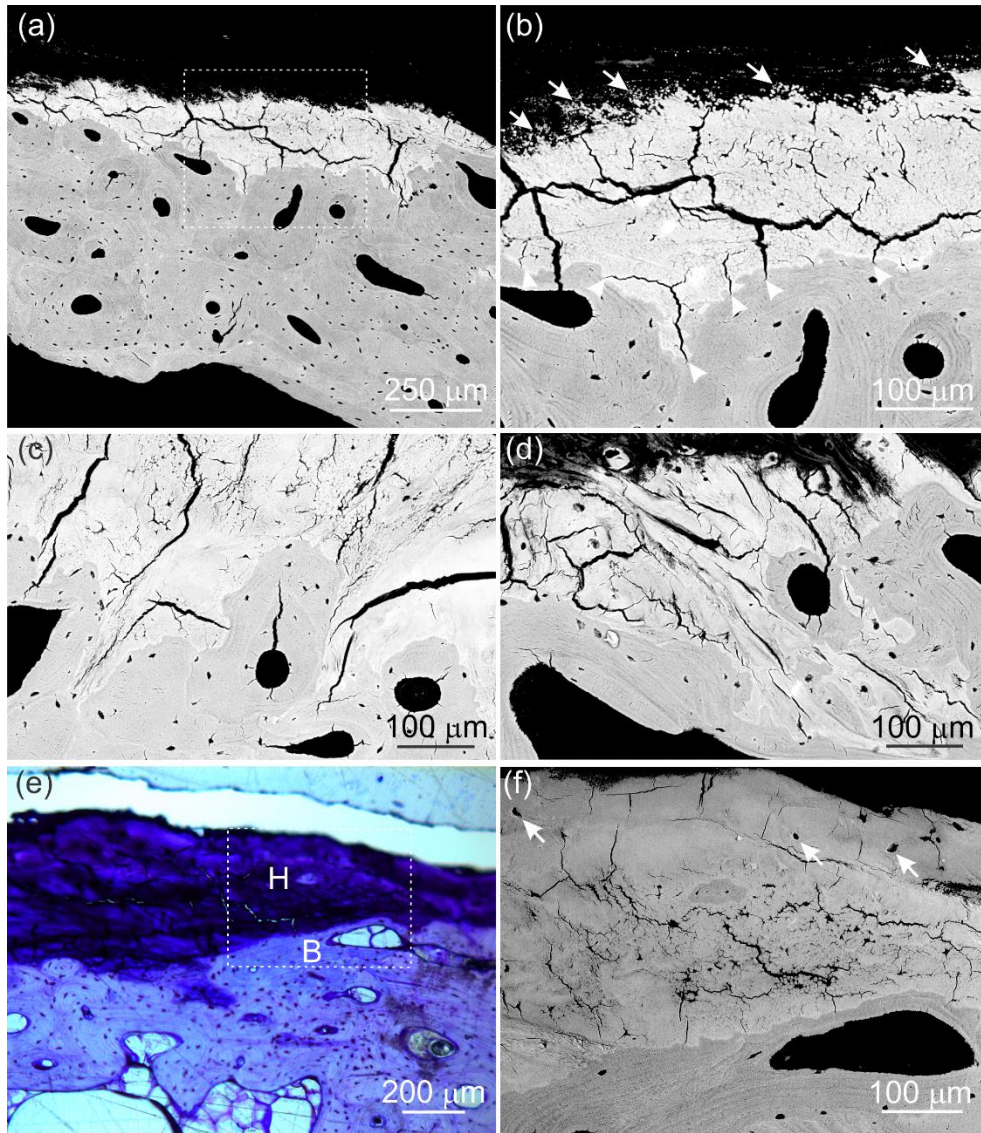


Fig. 3. 2 BSE (a-d, f) and OM (e) micrographs taken from femoral neck (a-c, e-f) and intertrochanteric (d) transverse sections (with respect to the long axis of femoral neck) showing typical peri-cortical hypermineralized tissue and underlying lamellar bone: (a) An overview showing the “grey” lamellar bone and the hypermineralized tissue (top bright zone) in the peripheral zone; (b) A close-up view of the dashed white rectangle from (a) showing the lack of lamellar structure and the multiple cracks in the hypermineralized tissue. Note the cracks (arrowheads) are frequently stopped by the lamellar bone structure. Dense mineral aggregates (arrows) disperse into the adjacent soft tissue; The hypermineralized tissue in (c) has similar fibrous structure as observed in (d), a typical region obtained from intertrochanteric area; (e) Giemsa stained section including a region (dashed white frame) with a BSE image showing in (f). A deeper coloration (deep purple) is shown in the hypermineralized fibrocartilage (H) than in bone tissue (B). The hypermineralized fibrocartilage in (f) is characterized by the rounded chondrocyte lacunae (arrows).

In the selected intertrochanter and femoral neck specimens, Giemsa staining revealed a clear contrast between the lamellar bone and the mineralized fibrocartilage. As shown in Fig. 3.2e, bone tissue (B) is slightly colored with light purple, while the mineralized fibrocartilage is deeply stained with purple. The various degrees of coloration indicated a relatively higher glycosaminoglycans/GAGs content in the mineralized fibrocartilage than that in the lamellar bone. Under the polarized optical microscopy, the lamellar bone exhibited characteristic bands of alternating brightness, whereas the hypermineralized region lacked any distinct lamellar features.

3.2.2 Area fraction and thickness ratio of hypermineralized tissue in total cortical bone

In consistent with the previous reports [72,73], hypermineralized tissue predominantly appeared on the superior aspect of the femoral neck, while the inferior region had very low amount of hypermineralization (Fig. 3.3a). Specifically, superior-central to superior-posterior (SC-SP) sector had the highest area fraction of hypermineralization (median value of 5.00 %) among all the anatomical locations at the femoral neck, while the inferior-central to inferior-posterior (IC-IP) sector had the least amount of hypermineralization (median value of 0.14 %) (Fig. 3.3a). It should be noted that there was also variation among the individuals, where one femoral neck sample showed high amount of hypermineralization at the inferior site (area fraction of 5.57 % at region of IA-IC). The area fraction of hypermineralization at the superior-central to superior-anterior (SC-SA) aspect of the intertrochanter was also measured (Fig. 3.3a, Tro). The value was significantly higher (median value of 15.63 %) than that of the femoral neck. The difference is mainly attributed to the apparent muscular insertion at the greater trochanter [73,75].

Area fraction measurement provided valuable information on how the hypermineralization was distributed around the femoral neck, while the thickness ratio between the hypermineralized region and the total cortical bone could point to the potential locations for fracture initiation. As

shown in Fig. 3.3b, the majority of the measured values were centered within the range of 0 to 0.2 (i.e. hypermineralization occupied 0 %-20 % of the total thickness). In all the six femoral neck samples, inferior-central to inferior-posterior (IC-IP) sector had the lowest thickness ratio (less than 0.1) among all the anatomical locations (Fig. 3.3b). In three femoral neck samples, superior-posterior (SP), anterior (A) and inferior-anterior (IA) sites had the highest thickness ratio of approximately 0.6 (Fig. 3.3b), suggesting more than half of the cortical beam was hypermineralized. The other three femoral necks had the highest thickness ratio between 0.3 to 0.43, which was found either at superior-central or posterior site (Fig. 3.3b).

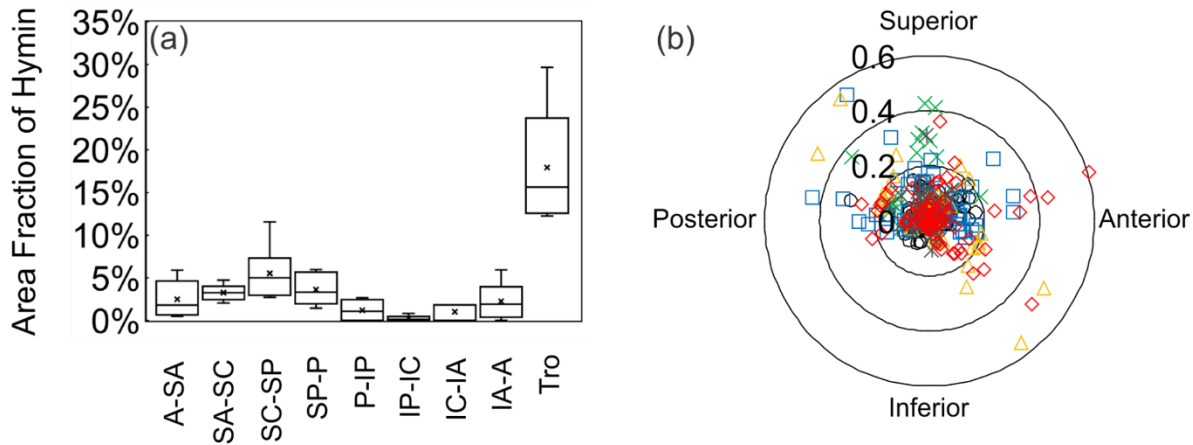


Fig. 3. 3 Quantification of the presence of hypermineralization in the human proximal femur: (a) Box plot of area fraction of hypermineralization in total cortical bone at each location. The mean and median values at each location are identified by a ‘x’ sign and a horizontal line, respectively. Bars give the first and third quartile of the measured values. (A: anterior; SA: superior-anterior; SC: superior-central; SP: superior-posterior; P: posterior; IP: inferior-posterior; IC: inferior-central; IA: inferior-anterior; Tro: SA-SC sector of intertrochanter); (b) A polar plot of the thickness ratio of the hypermineralized tissue vs. total cortical bone from the six femoral necks. Each point was measured by every 2.8° in the circumferential direction of the femoral neck. The different markers with different colors represent different individuals.

3.2.3 Bone mineralization density distributions (BMDDs)

qBSE imaging was used to characterize the mineral density of the hypermineralized tissue, based on the generally linear relationship between weighted mean atomic number and the BSE

signals. Fig. 3.4a shows a pseudocolored map of the obtained Ca_{peak} values. Higher Ca wt % is shown as white and lighter grey colors, while the neighboring lower Ca wt % in the lamellar bone is shown in darker grey colors. Representative BMDDs of the hypermineralized tissue and the lamellar bone, including Haversian and interstitial bone, are shown in Fig. 3.4b. There is a clear shift in the BMDD curve, whereby the peak position of the BMDD obtained in the hypermineralized region is at the higher end compared with that of either the osteonal or interstitial bone.

The BMDD was calculated from 174 regions of interest that could contain both the hypermineralized zone and lamellar bone from six femora. The mean value of the Ca_{peak} was significantly higher in the hypermineralized tissue (14.7 % of osteonal bone and 11.5 % of interstitial bone, $p < 0.05$, Friedman's test) (Fig. 3.4c and d, Table 3.1), independent of location. Interstitial bone had slightly but statistically higher Ca_{peak} values than that of the Haversian bone ($p < 0.05$) (Fig. 3.4c and d, Table 3.1). There was no significant difference among different anatomical locations (i.e. within femoral neck or between femoral neck and intertrochanter), neither was there any significant interaction between the tissue and the location (Table 3.1). Ca_{peak} values for osteons (25.0 wt % to 26.3 wt %) and for intestinal bone (25.8 wt % to 27.3 wt %) were consistent with the reported values in the elderly human bone [127]. Ca_{peak} as found in the hypermineralized tissue (29.6 wt % \pm 0.4 wt %) was close to those reported in calcified cartilage of human vertebra [216].

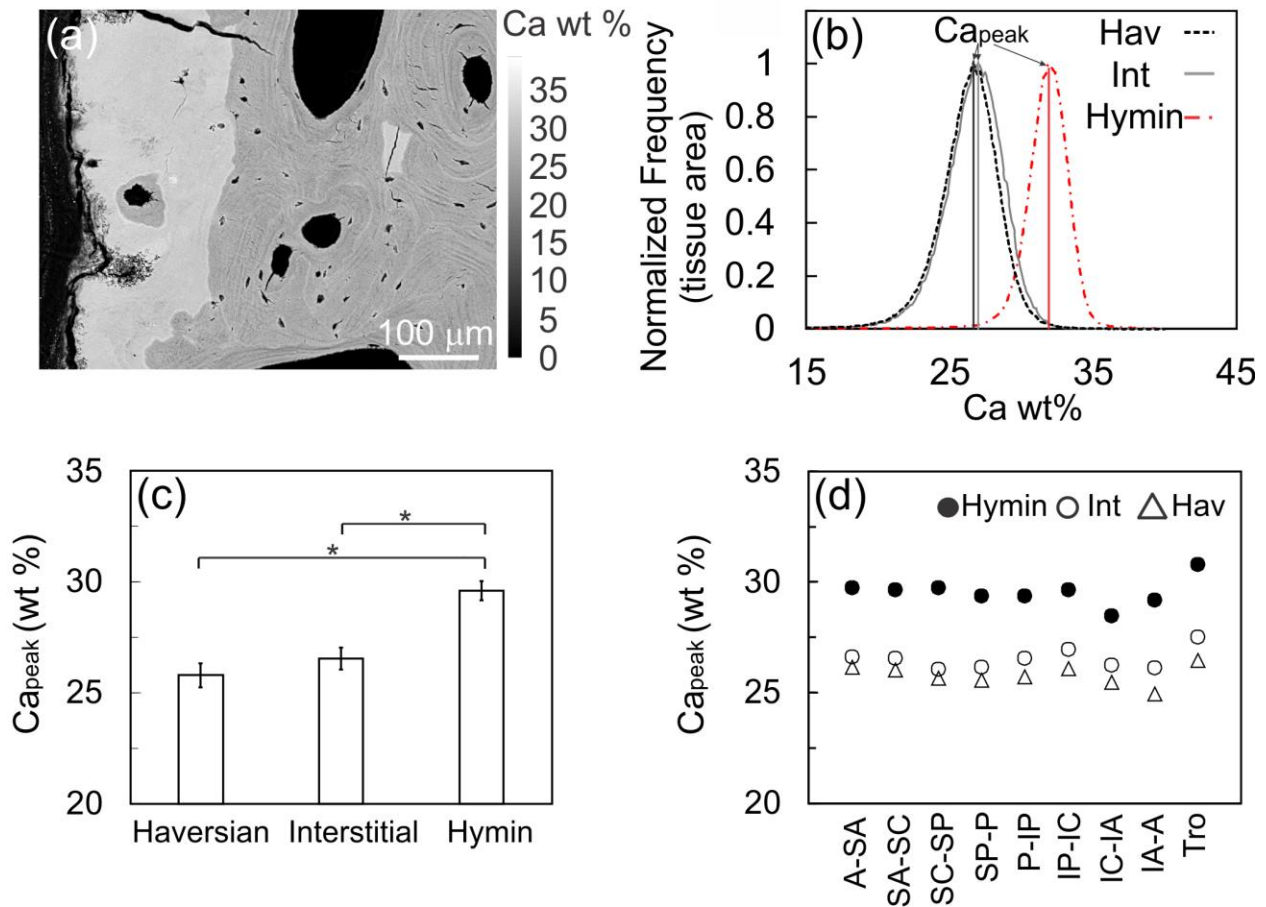


Fig. 3. 4 Quantitative BSE imaging showing mineral content in hypermineralized and lamellar bone tissue: (a) A pseudocolored map of the obtained Ca_{peak} (the most frequently appeared mineral content). The scale bar on the right shows the range of (0 – 40) Ca wt %; (b) Bone mineralization density distributions (BMDDs) obtained from hypermineralized tissue (Hymin), Haversian bone (Hav) and interstitial bone (Int) in (a); (c) Ca_{peak} calculated from BMDDs of the six femora and plotted against Haversian bone, Interstitial bone and hypermineralized tissue. Errors shown are standard deviations. Friedman test showed significant difference in Ca_{peak} ($p < 0.05$, marked by *); (d) Average Ca_{peak} values in hypermineralized tissue, interstitial bone, and Haversian bone at each anatomical location. (A: anterior; SA: superior-anterior; SC: superior-central; SP: superior-posterior; P: posterior; IP: inferior-posterior; IC: inferior-central; IA: inferior-anterior; Tro: SA-SC sector of intertrochanter).

Table 3. 1 Ca_{peak} values obtained from the BMDDs as measured by qBSE in the Haversian bone (Hav), interstitial bone (Int) and hypermineralized tissue (Hymin) of six human proximal femora from different anatomical locations.

Hav vs. Int vs. Hymin (locations pooled)				Among Different Locations (tissues pooled)										
Hav	Int	Hymin	<i>P</i>	A-SA	SA-SC	SC-SP	SP-P	P-IP	IP-IC	IC-IA	IA-A	Tro	<i>P</i>	
25.80	26.54	29.60	0.002	27.52	27.42	27.16	27.04	27.09	26.80	26.24	26.48	28.27	0.165	
(0.22)	(0.20)	(0.18)		(0.34)	(0.25)	(0.40)	(0.33)	(0.52)	(0.53)	(0.50)	(0.87)	(0.42)	NS	

Statistical analysis was done by Friedman's two-way analysis of variance by ranks. The values represent means and standard errors. A: anterior; SA: superior-anterior; SC: superior-central; SP: superior-posterior; P: posterior; IP: inferior-posterior; IC: inferior-central; IA: inferior-anterior; Tro: superior-anterior to superior-central sector of intertrochanter.

3.2.4 Micromechanical properties of hypermineralized tissue

Microindentation measurements were performed on hydrated femoral neck samples from six femora to evaluate the cracking behavior and to measure associated hardness values. Fig. 3.5a shows a typical femoral neck region that contains lamellar bone (Bone) and periosteal hypermineralization (Hymin). Because of the interference of the surface water, the characteristic morphological features of the hypermineralized tissue may not be as clear as the dehydrated samples under BSE. Nevertheless, the non-lamellar structured hypermineralized tissue was found in all the six hydrated femoral neck samples. After using an indentation load of 500 gf for 15 s, it was found that cracks indeed formed in some areas of the hypermineralized tissue, but never in the lamellar bone, thus indicating the relative “brittleness” of the hypermineralized tissue. As shown in Fig. 3.5b, the large indent induced some cracks at the sides (arrow heads) in the hypermineralized zone, and no cracks were found in the lamellar bone. The “side” cracking pattern differs from the classical radial-median cracks which usually appear at the four sharp corners of the impression [217,218], and resembles the features of secondary cracking [218].

An indentation load of 25 gf for 15 s was further used to measure the hardness in this hypermineralized tissue and compared with that of the lamellar bone. The impression size was clearly smaller in the hypermineralized region than in the adjacent lamellar bone tissue (arrows in Fig. 3.5c). Overall, the impression diameter ranged between (18-37) μm in this hypermineralized region, and between (30-54) μm in the lamellar bone region. Subsequently, the obtained microhardness values in the lamellar bone ($\sim 36 \text{ kg/mm}^2$) agree with the values reported by other researchers who have tested on human femoral cortical bone [207] and dentin [205]. In contrast, the hypermineralized tissue had significantly higher microhardness values (20 % of lamellar bone, $p < 0.05$, Wilcoxon signed-rank test) (Fig. 3.5d). The relative increase in the

microhardness values of this hypermineralized tissue could be associated with the elevated mineral content [208,219]. Interestingly, in some regions of the hypermineralized tissue, cracks did not form under the load of 500 gf and the hardness was statistically lower than that of lamellar bone (Fig. S3.4). Such areas were typically found at the intertrochanter, where large amount of calcified fibrocartilage tissue is present.

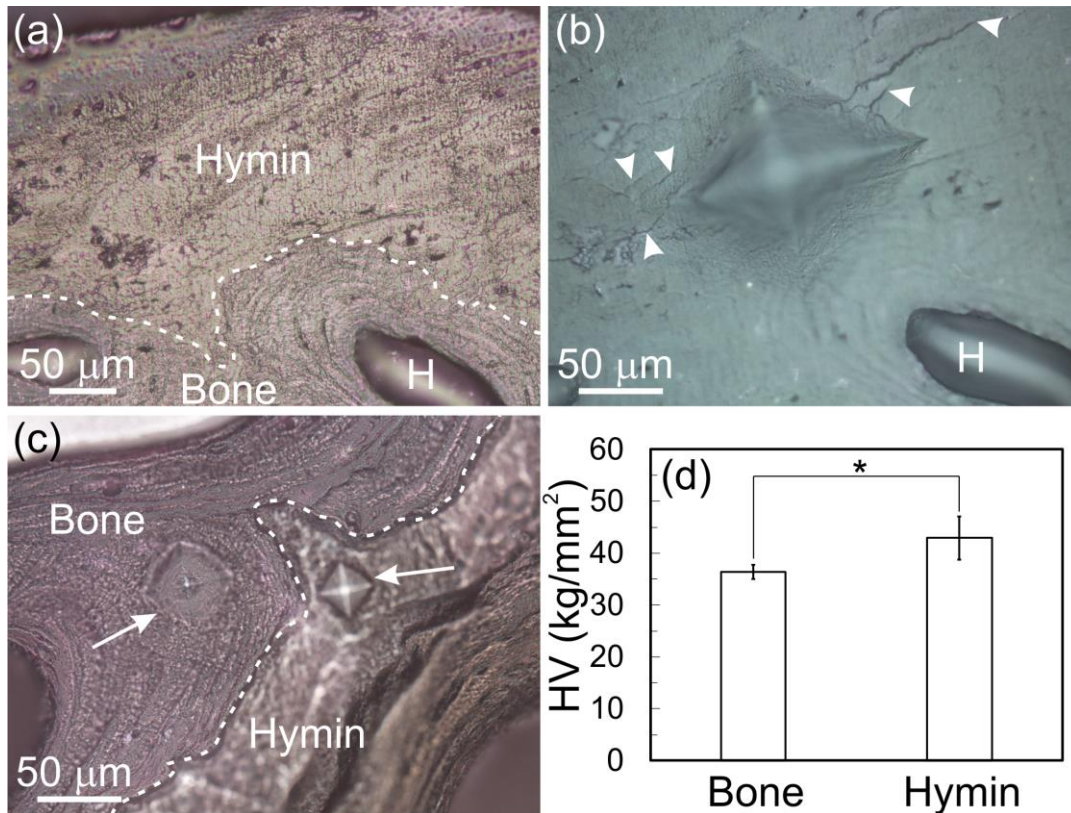


Fig. 3. 5 Microindention on hydrated femoral neck samples: (a) OM picture taken before the indentation test showing a region containing hypermineralized tissue (Hymin) and lamellar bone (Bone). The white dashed line indicates the boundary between the two types of tissue; (b) OM image taken immediately after microindention (500 gf, 15 s dwell time) corresponding to the area of (a). Arrowheads point to the cracks induced by indentation in the hypermineralized zone; (c) OM image showing two indents (arrows) loaded under 25 gf for 15 s in the hypermineralized region (Hymin) and the lamellar bone (Bone); (d) Vickers hardness values (HV) calculated based on the size of the indents. Wilcoxon signed-rank test showed significant difference ($p < 0.05$, marked by *) between the hypermineralized tissue (Hymin) and lamellar bone (Bone).

3.3 Discussion

This study quantitatively examined a clinically relevant and mechanically important tissue in the human proximal femur, and demonstrated the changes of tissue quality from the materials perspective. The results of this study indicated that the superior aspect of femoral neck had higher amount of hypermineralization (i.e. higher area fraction and thickness ratio in total cortical bone). The calcium content, represented by the $C_{a\text{peak}}$ from the BMDD curve, of the hypermineralized tissue increased by ~ 15 % compared with that of the lamellar bone. This non-lamellar microstructure has been linked to reduced resistance to fracture (i.e. cracking upon microindentation) and higher hardness value.

3.3.1 Occurrence of hypermineralization

Previous studies have found increased amount of hypermineralization at the femoral neck and intertrochanter with ageing [71–73,76]. This study confirmed the existence of peri-cortical bone hypermineralization at the human proximal femur, and found that they appeared with distinct morphological features (Fig. 3.2, Fig. S3.1). In consistent with previous observations, typical hypermineralized fibrocartilage was found at the intertrochanter [73,75], and mineralized periosteum [71] and mineralized fibrocartilage [73,75] were observed at the femoral neck.

This study quantified the occurrence of hypermineralization around the femoral neck which would be helpful to identify critical locations with increased fragility, considering the cortex is already the thinnest at the superior site [17] and needs to sustain large compressive stress during hip fracture [66,144]. So far, there are only two studies [72,73] that have quantified the distribution of hypermineralization at human femoral neck. These two studies reported that hypermineralization was more common in the superior sectors of the femoral neck [73], and that anterior to inferior-anterior sector showed increased amount of hypermineralization with ageing

[72]. The current study showed that hypermineralization predominantly appeared at superior-central (SC) to superior-posterior (SP) sector, and the inferior region had limited amount of hypermineralized tissue (Fig. 3.3a). This finding thus confirmed the previous reports [72,73]. In line with the observation on the area fraction of the hypermineralized tissue in total cortical bone, the thickness ratio between the hypermineralized region and the total cortical bone region showed the highest value at superior-anterior (SA), superior-posterior (SP) and inferior-anterior (IA) sites, and the lowest value at inferior-central to posterior sector (Fig. 3.3b). Very interestingly, Bell et al. [62] has shown that cortical bone thinning predominantly appears along the SP to IA axis in fracturing patients. Therefore, hypermineralization at SP and IA sites could be critical, as it might maintain or increase the local BMD and cross-sectional moment of inertia (CSMI) of the femoral neck, but facilitate easier crack formation.

3.3.2 Mineral content and the higher degree of mineralization in hypermineralized tissue

Bone mineralization density distribution (BMDD) is an important parameter that has been frequently used to characterize metabolic bone disease [74] and drug-treated bone [220]. More importantly, the degree of mineralization (mineral content) has been quantitatively correlated with the notch sensitivity of bone (in terms of fracture energy) [151]. By imaging the periosteal cortical bone with 200× magnification, the average values of Ca_{peak} in Haversian bone and interstitial bone were measured as approximately 25.80 wt % and 26.54 wt %, respectively (Fig. 3.4c, Table 3.1). These values were higher than the Ca_{mean} (weighted mean Ca concentration, slightly lower than Ca_{peak}) reported in young individuals [129,216,221], and close to those in older adults [216]. The Ca_{peak} value of Haversian bone was statistically lower than that of interstitial bone, which is consistent with the previous study on human tibia [222]. Interestingly, by comparing clinical fracture cases and healthy individuals, Fratzl-Zelman et al. [127] reported that the Ca_{peak} at mid-

femoral neck cortex was statistically lower in hip fracture patients than in non-fractured controls. Although these researchers also found slightly lower degree of mineralization at superior femoral cortex [127], the current study did not observe any statistical differences among the different anatomical locations at femoral neck (Fig. 3.4d, Table 3.1). This discrepancy might attribute to the different cohorts of patients and different imaging sites (periosteal vs. total cortical bone).

In all the six femoral neck samples, the degree of mineralization of the hypermineralized tissue (Hymin) was significantly higher than that in bone (osteonal or interstitial) (Fig. 3.4c and d, Table 3.1), and the obtained Ca_{peak} value of Hymin was consistent with previous measurement on calcified cartilage at human vertebra [216]. The substantial Ca wt % difference between the lamellar bone and the hypermineralized tissue could also be found at other bone-cartilage interfaces, such as human femoral head [223] and human patella [224]. The exact mechanism that contributes to the increased mineralization in the hypermineralized region is not clear. Changes in BMDD are generally determined by tissue turnover and mineralization kinetics [74]. The underlying organic-mineral packing could also contribute to the altered mineralization. As it has been shown in articular cartilage at other skeletal sites, there is only a small portion of cartilage (15 wt %-22 wt %) that is occupied by collagenous fibrils and proteoglycans; the remaining extrafibrillar space is reserved for water [223]. During mineralization, the space of exchangeable water could be gradually replaced by minerals, thus contributes to the increased mineral density under BSE [221].

3.3.3 The easier cracking behavior of hypermineralized tissue

Is hypermineralization indeed more brittle than lamellar bone and does it subsequently reduce the local fracture resistance? The BSE imaging in this study clearly demonstrated the more prominent “brittle” cracking in the hypermineralized region (Fig. 3.2b), agreeing well with the

previous observations [72,73]. To further address the concerns regarding cracking due to dehydration and imaging process under BSE, the microindentation test in the current study was performed on hydrated samples, and found cracks formed at the sides of the indents in the hypermineralized zone rather than in lamellar bone (Fig. 3.5b). Although the cracks did not initiate at the corners of the impression, a classical pattern that could be found in alumina materials [225], the “easier” cracking behavior of the hypermineralized tissue implied its relative brittleness. The possible role of hypermineralization in *in vivo* hip fractures needs to be confirmed. However, it has been shown that in cases of parasagittal condylar (third metacarpal bone) fracture in equine, fine dorso-palmar fractures originated in the calcified articular cartilage would later continue into the subchondral bone and cause ultimate fracture [226].

The mechanisms by which the hypermineralized tissue behaves differently from the lamellar bone under loading could be a combination of mineral concentration and organic matrix properties. Gupta et al. [224] has shown that at the bone-cartilage interface of human patellar, hypermineralized articular cartilage requires more mineral content to achieve the same stiffness and hardness as subchondral bone, indicating a different mineral-collagen packing and the influence from the underlying organic matrix. There is also increasing evidence that age-related changes in the collagen matrix properties could increase tissue hardness, thus affect hip fragility. By comparing iliac biopsies between osteoporotic and healthy individuals, Tjhia et al. [227] found that for a given degree of mineralization, hardness and deformation resistance increase with ageing, implying brittleness due to the altered organic matrix. This is consistent with the finding from another fracture cases vs. controls study, where organic phase was found to be stiffer and less tough in hip fracture patients [127]. Interestingly, in the current study, there were also regions of hypermineralization that did not form any cracks and had relatively low hardness values (Fig.

S3.4). This was particularly consistent at the intertrochanter, where hypermineralized fibrocartilage exists. Given the fact that the hardness was lower but mineral content was higher in these regions, it is likely that the organic matrix is organized differently from the collagen I-rich matrix of lamellar bone and the hypermineralized periosteum at femoral neck.

3.3.4 Limitations

The current study had several limitations. First it had a small sample size (few cadavers and sections for each femur), thus these findings cannot be generalized across other specimens. A larger population might be studied in the future to verify the observations. That said, according to previous study [75], the occurrence of hypermineralization should not vary significantly along the long axis of the femoral neck. Further, the statistical significance in calcium content as observed with the current sample size will still hold for a larger population due to the significant difference. Second, the current specimens are limited to aged group. This is a reflection of the nature of the hypermineralization as age has been shown to be positively correlated with the occurrence of hypermineralized tissue in the proximal femur [73]. It would be, however, valuable to study both young and older individuals in future. Third, the study had an unbalanced sex for the samples. Further studies should represent both genders more equally. However, the study did not observe any apparent differences in mineral content between the male and the female. Forth, the current study was performed on postmortem samples. Studies on diseased bones, e.g. osteoporosis and osteoarthritis, would be interesting to see how changes in bone condition affect the occurrence and material properties of hypermineralization. Fifth, this study was conducted on healthy older adults. Future studies on comparing fracturing patients and healthy controls might be helpful to determine the contribution of hypermineralization to bone fragility. Finally, the indentation tests were

performed on the transverse plane of the femoral neck (perpendicular to femoral neck's long axis), and the results might differ from the longitudinal plane due to the anisotropy of bone.

3.4 Conclusions

This study provided new information by quantifying the mineral content and identifying the micromechanical properties of the hypermineralized tissue in aged human proximal femur. qBSE imaging showed that hypermineralization was more common at the superior femoral neck cortex, and that it had higher thickness ratio in total cortical bone along the superior-posterior to inferior-anterior axis. The degree of mineralization of the hypermineralized tissue was significantly higher than that of the lamellar bone. The “easier” cracking behavior and the higher microhardness values found in the hypermineralized tissue indicated that the material properties depend on a combination of degree of mineralization and interaction between minerals and organic matrix.

Chapter 4 The Size and Organization of Mineral Platelets in the Hypermineralized Tissue*

There is increasing evidence that hip fragility also arises from changes in the intrinsic properties of bone at the mineral and collagen level [81,127,228]. Mineralized tissue, i.e. lamellar bone and hypermineralized tissue, can be viewed as nano-fibrous material that is composed of mineral platelets and organic collagen-rich matrix. These two components have different mechanical properties and both contribute to the mechanical behavior of the mineralized tissue [147]. In particular, studies have shown that the size, shape and the arrangement of the mineral platelets all play pivotal roles in affecting the strength, stiffness and toughness of bone [87].

Analyzing nano-sized bone minerals has been a challenge. One unique technique is the scanning small- and wide-angle X-ray scattering (SAXS/WAXS). They provide information on the shape, size, orientation and spatial organization of bone mineral platelets, and particularly allow mapping of these properties within the hypermineralized and lamellar bone areas [142]. On the other hand, Raman microspectroscopy is capable of mapping the distribution and organization of key matrix components at micro-level [133]. Combination of SAXS/WAXS and Raman microspectroscopy can thus provide a comprehensive characterization of the structure and composition of the mineralized tissue across several length scales. Therefore, the goal of this study was to examine the hypermineralized tissue from both femoral neck and intertrochanter with a focus on the mineral thickness, mineral length, and mineral orientation and distribution in the organic matrix.

*A version of chapter 4 has been re-submitted for publication after revision. T. Tang, W. Wagermaier, R. Schuetz, P. Fratzl, and R. Wang (2017). Hypermineralized tissue in human proximal femur has smaller and disorganized bone minerals.

4.1 Experimental

4.1.1 Specimen preparation

Six freshly frozen human cadaver femora (three males, three females, age range: 62-79) without reported metabolic bone tissue conditions were obtained from LifeLegacy Foundation and used for the study. To obtain total proximal femur areal bone mineral density (aBMD) and *T*-scores, dual energy X-ray absorptiometry (DXA) scans were performed with a Hologic QDR 4500W bone densitometer (Hologic Inc., Waltham, MA) following the standard protocol for the proximal femur [47]. Table S4.1 provided donor information, aBMD and *T*-scores. All bone tissues were kept frozen at -20 °C until specimen preparation. The study was approved by the Clinical Research Ethics Review Board at the University of British Columbia.

Each femur was manually cleaned of adherent soft tissue with a scalpel. Subsequently, two transverse cuts (with respect to the femoral neck's long axis) were made at the mid-femoral neck and intertrochanter, respectively (Fig. 4.1b), using a water-cooled diamond saw (EXAKT Adv. Tech. GmbH, Norderstedt, Germany). Twelve specimens in total were prepared (six neck samples and six intertrochanter samples). The obtained sections were then fixed in 70 % ethanol/water solution for 24 h, followed by dehydration in a graded ethanol series (80 %, 90 %, and 100 %) overnight per step and finally air-dried.

Each intertrochanter sample was cut into eight sectors, and each neck sample was cut into two or four sectors (depending on the size of the embedding mold) (Fig. 4.1a and c). All the sectors were subsequently embedded in polymethyl methacrylate (PMMA), and ground with a series of carbide grinding papers, and polished with diamond suspension starting at 4 µm and ending with 1 µm (PM5 Logitech, Glasgow, Scotland). For laboratory and synchrotron-based X-ray scattering

investigations, selected specimens were further polished to approximately 100 μm and 50 μm in thickness, respectively.

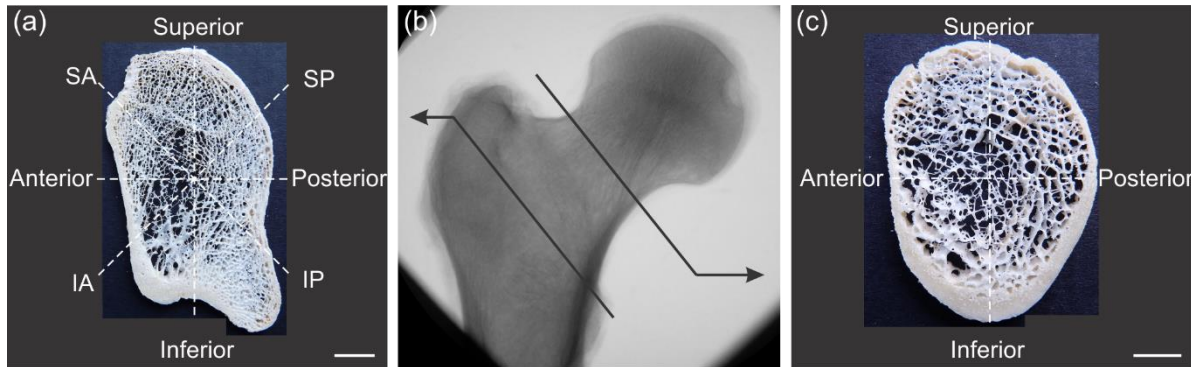


Fig. 4. 1 X-ray image of a human proximal femur (b) and camera images of an intertrochanter (a) and a mid-femoral neck sample (c). All the samples were made by cutting transverse with respect to the femoral neck's long axis. Intertrochanter sample (a) was further divided into eight sectors, based on the anatomical locations (i.e. superior-central to superior-anterior (SA); superior-anterior to anterior; anterior to inferior-anterior (IA); inferior-anterior to inferior-central; inferior-central to inferior-posterior (IP); inferior-posterior to posterior; posterior to superior-posterior (SP); superior-posterior to superior-central). Mid-femoral neck sample (c) was divided into two (superior and inferior) or four (superior to anterior, superior to posterior, inferior to anterior, and inferior to posterior) sectors depending on the size of the embedding mold. Scale bar = 1 cm.

4.1.2 Optical microscopy and backscattered electron imaging

Each polished bone specimen was first examined using reflective light under a polarized light microscope (Leica DM RXA2, Leica, Germany) equipped with a CCD camera for image acquisition. An objective lens of 2.5 \times was used for overview images and for locating regions of interest, and an objective lens of 20 \times was used to examine the structural features and to differentiate the lamellar bone and the hypermineralized tissue based on the varying morphology (i.e. hypermineralized tissue is located on the periosteal site of cortex without obvious lamellar structure).

After light microscopy examination, all bone specimens were examined with an environmental scanning electron microscope (ESEM, FEI, Oregon, USA) in low vacuum using BSE mode with an electron beam energy of 10 kV. In the resulting grey level images of the

mineralized tissue, regions of high calcium content appear bright whereas regions of low calcium content appear dark grey. BSE images were used to verify the hypermineralized tissue as seen under light microscope, and to determine the regions of interest for Raman and X-ray scattering measurements.

4.1.3 Polarized Raman microspectroscopy

All the six cadaver femora were measured by a diode-pumped 785 nm near-infrared (NIR) laser beam (Toptica Photonics AG, Graefelfing, Germany, laser power ~ 50 mW). A polarized confocal Raman microscope (CRM200, WITec, Ulm, Germany) was used to focus the beam to a micrometer sized spot on the specimen. A P-500 piezo-scanner (Physik Instrumente, Karlsruhe, Germany) and a Peltier-cooled CCD camera (PI-MAX, Princeton Instruments Inc., NJ, USA) were used in combination with a 20× (Nikon, NA = 0.4) and a 60× W (Nikon, NA = 1.0) microscope objectives. In each specimen, at least one typical region of interest, containing both hypermineralized and lamellar bone region, was located using the motorized XY stage and a video camera. The linearly polarized laser was rotated using a half wave plate.

Raman spectra were acquired from the hypermineralized tissue and the lamellar bone, behind a grating of 300 g mm⁻¹ or 1200 g mm⁻¹ with an integration time of 0.3 s-1 s. Under this condition, the polarization effect was examined under 0 and 90 degrees with respect to the specimen orientation (horizontal direction of Fig. 4.3). For mapping purpose, regions ranging from a size of (20 × 20) μm² to (30 × 30) μm², containing both hypermineralized region and lamellar bone, were scanned behind a grating of 300 g mm⁻¹ with a step of 0.5 μm and an integration time of 0.3 s-0.5 s. For selected areas of interest, the Raman spectra obtained under different laser polarization angles were obtained by rotating the polarizer in steps of 15° in the range of -90° to 90°.

The Raman spectra were baseline-corrected and fitted using WitecProjectPlus (version 2.10, WITec, Germany). Raman shifts for ν_1 phosphate (ν_1PO_4) and amide I were analyzed through the sum filter. The filter integrates the intensities within the chosen borders. For instance, ν_1 phosphate intensity was calculated between 920 cm^{-1} and 1000 cm^{-1} and amide I intensity was calculated between 1520 cm^{-1} and 1770 cm^{-1} . The mineral-to-matrix ratio was expressed as the ratio of the integration of the ν_1 phosphate to the amide I Raman bands. Since the phosphate positions in the apatite lattice are susceptible to carbonate substitution, *B*-type carbonate intensity was measured between 1049 cm^{-1} and 1095 cm^{-1} . Subsequently, carbonate-to-phosphate ratio was obtained. To avoid overlapping signals from the embedding material, phosphate-to-carbonate ratio was used when the examined region contained porosity.

4.1.4 Scanning small angle X-ray scattering (SAXS)

To provide statistical and overall information on the mineral thickness across the collected bone samples, laboratory SAXS measurement was conducted on a total of eleven specimens from six proximal femora. The experiment was performed with a “NANOSTAR” instrument (Bruker AXS, Karlsruhe, Germany), which was equipped with a rotating copper-anode generator operating at 40 kV/100 mA (Cu $K\alpha$ radiation) to produce an X-ray beam with a wavelength of 1.5418 \AA . The beam diameter at the specimen was $100\text{ }\mu\text{m}$ and the specimen to detector distance was approximately 670 mm. Bone transverse sections (perpendicular to the femoral neck’s long axis) of $\sim 100\text{ }\mu\text{m}$ in thickness were mounted on a motorized specimen holder and scanned perpendicularly to the X-ray beam. Before each measurement, an X-ray transmission image of the specimen was obtained with a diode at a step of $100\text{ }\mu\text{m}$ to determine the points of interest. Subsequently, each selected point was irradiated for 1800 s and the scattered X-rays were detected by a Bruker two-dimensional (2D) detector. The 2D patterns recorded by the detector represent

the scattering intensity distributed around the primary beam. The calibration for SAXS was done with silver behenate. The obtained SAXS patterns were analyzed with Directly Programmable Data Analysis Kit (DPDAK, Version_1.2.X_corr, Deutsches Elektronen-Synchrotron and Max Planck Institute of Colloids and Interfaces, Germany) for T parameter (i.e. mineral thickness), ρ parameter (i.e. degree of mineral orientation), $G(x)$ functions (i.e. mineral distribution and arrangement) and $G(x)$ fit (i.e. quantification of the shape of $G(x)$ curve). The background profile, caused by the scattering of the experiment setup, was subtracted from the specimen data. The dark current intensity profile was also subtracted from the background and specimen profiles.

Parameter T is determined as previously described [121] and used as an estimate of the average mineral platelet thickness. Briefly, the T parameter is defined as

$$T = 4\phi(1 - \phi)/\sigma \quad (4.1)$$

where ϕ is the mineral volume fraction and σ is the total surface area of the mineral platelets per unit volume.

The degree of alignment of the mineral platelets (ρ parameter) characterizes the ratio of the aligned minerals to the total amount of minerals in the irradiated bone specimen volume. The varying scattering patterns reflect the different orientations of the mineral platelets within the illuminated volume. If the mineral platelets are perfectly aligned, the pattern shows a narrow streak perpendicular to the long axis of the minerals, whereas the pattern is spherical when the minerals are randomly oriented. Elliptical SAXS patterns are obtained when the mineral platelets are partially aligned. The intensity was integrated azimuthally to obtain $I(\chi)$ profile (usually with two peaks), and ρ is defined as the ratio of the sum of the area under the peaks to the sum of the total area including the background [216]. As such, $\rho = 0$ indicates a total random mineral orientation and $\rho = 1$ suggests perfect alignment [121].

4.1.5 Scanning small- and wide-angle X-ray scattering (SAXS/WAXS) using synchrotron radiation

To provide in-depth information on the thickness, orientation and length of the bone mineral platelets, three femoral neck specimens from three proximal femora were selected for high resolution synchrotron X-ray measurements at μ Spot beamline of BESSY II (Helmholtz-Zentrum Berlin, Germany). Specimens were ground to a thickness of approximately 50 μm and mounted perpendicular to the X-ray beam at a distance of 315 mm to the detector. A silicon (111) monochromator was used to generate a monochrome X-ray beam with a wavelength of 0.83 \AA . The beam was focused and collimated to a size of 30 μm , and the calibration was performed with a quartz standard. The scattering patterns were obtained using an exposure time of 90 s with a position sensitive CCD-detector with a pixel size of $(73.24 \times 73.24) \mu\text{m}^2$. The acquired data was analyzed using DPDAK to obtain T and ρ parameters as described above.

The length (L parameter) of the mineral platelet was determined with WAXS signal, based on the width of the (0 0 2) peak of hydroxyapatite. L parameter is defined by Scherrer equation:

$$L = \frac{k\lambda}{B \cos \theta} \quad (4.2)$$

where k is a constant which is related to the crystallite shape and falls in the range of 0.87-1.0; λ is the wavelength of X-ray beam; B is the full width at half maximum (FWHM) intensity of the (0 0 2) peak of crystalline hydroxyapatite, and θ is the Bragg angle of the (0 0 2) peak. More specifically, Pseudo-Voigt function and least squares curve fitting with Levenberg-Marquardt algorithm were used to obtain the FWHM; 0.9 was adopted as the constant k ; and B is calculated as

$$B = \sqrt{B_s^2 - B_r^2} \quad (4.3)$$

where B_s is the line broadening at FWHM, and B_r is the instrumental broadening.

Information about the mineral distribution and organization is contained in a shape function $G(x)$, derived from the SAXS data. A detailed description of $G(x)$ can be found in the previous study [122]. $G(x)$ function has been shown to be highly sensitive to the changes in the arrangement of bone mineral platelets, as the shapes of the $G(x)$ curves vary to different degrees when measured in different bone species, ages, and mineral volume fractions [229]. Several structure models have been developed previously to quantitatively describe the $G(x)$ curves and thus the organization of the mineral platelets [125,230,231]. In this study, by utilizing the stacks of cards model [230], it produced sets of parameters to quantitatively describe the mineral organization at this structural level. Briefly, the typical spacing between the mineral platelets (in units of T) was defined by the period of the oscillation $2\pi/\beta$, and the distance $1/\alpha$, over which the periodicity in mineral platelet spacing is damped. As such, the parameter β describes the degree of spatial correlation between successive platelets, separated by an average distance of d , being defined as

$$d = T2\pi/\beta \quad (4.4)$$

and α reflects the damping of the oscillations, thus indicating the relative extent of the ordering.

4.1.6 Statistical analysis

IBM SPSS v. 24.0 (NY, IBM Corp.) was used for statistical analysis. For laboratory SAXS measurements, Friedman's two-way analysis of variance by ranks was performed for testing differences among the different levels of tissues (cortical bone vs. trabecular bone vs. hypermineralized tissue), and among different levels of anatomical locations (femoral mid-neck vs. intertrochanter). Differences between different tissues (mid-femoral neck and intertrochanter pooled, therefore, $n = 6$ for cortical bone, $n = 6$ for trabecular bone, and $n = 6$ for hypermineralized tissue) were tested for significance by Friedman test. Comparison between mid-femoral neck and intertrochanter (pooling cortical bone, trabecular bone and hypermineralized tissue; therefore, $n =$

5 for mid-femoral neck and $n = 5$ for intertrochanter) was done using Wilcoxon signed-rank test. For synchrotron-based SAXS/WAXS measurements, Wilcoxon signed-rank test was used for testing differences among the different levels of tissues (cortical bone vs. hypermineralized tissue). Two-sided $p < 0.05$ was considered statistically significant.

4.2 Results

4.2.1 Relative mineral/organic contents and polarization effects

In line with the observation in chapter 3.2.1, apparent hypermineralization was found in all the femoral neck and intertrochanter samples. Both “dense mineral aggregates” associated with hypermineralized periosteum, and obvious fibrous insertion associated with hypermineralized fibrocartilage were observed. Other features, as described in chapter 3.2.1, such as chondrocyte lacunae, tidemarks, “mineral filled” osteocyte lacunae, were also present.

Raman microspectroscopy was used to measure both femoral neck and intertrochanter specimens in the plane that was transverse to the femoral neck’s long axis. Fig. 4.2 shows typical Raman spectra (300 g mm⁻¹ gratings, 0° polarization) in the range of 400 cm⁻¹ to 1750 cm⁻¹ that were obtained from a femoral neck specimen with a region containing hypermineralized tissue (mineralized periosteum) and lamellar bone. In all the measured specimens, both hypermineralized tissue and lamellar bone tissue showed the most prominent band ν_1 phosphate at ~ 958 cm⁻¹, which is a typical marker for bone mineral. ν_2 and ν_4 phosphate bands were also observed at ~ 437 cm⁻¹ and ~ 589 cm⁻¹, respectively. The second strongest band appeared at ~ 1074 cm⁻¹, indicating *B*-type carbonate substitution in the apatite lattice. The broad bands at the high-frequency region, including amide III at ~ 1255 cm⁻¹ and amide I at ~ 1677 cm⁻¹, are mainly associated with collagens. The *CH*₂ bending mode at ~ 1457 cm⁻¹ can be attributed to both collagenous and noncollagenous

organic moieties as well as PMMA [232]. Other characteristic bands associated with organic matrix include proline ($\sim 855 \text{ cm}^{-1}$), hydroxyproline ($\sim 875 \text{ cm}^{-1}$) and phenylalanine ($\sim 1002 \text{ cm}^{-1}$). The Raman spectra showed increasing intensity in phosphate and carbonate bands (relative to the amide I, III and other organic matrix-related bands) for the hypermineralized tissue. Characteristic bands associated with transient precursors, such as amorphous calcium phosphates (broad shoulder at 945 cm^{-1}) [233] and octacalcium phosphate (955 cm^{-1} and 970 cm^{-1}) [233], were not found in the current study. The relative GAGs content was difficult to measure in this study, as the CH_3 (1365 cm^{-1} - 1390 cm^{-1}) band, representative of GAGs [234], did not show a clear peak.

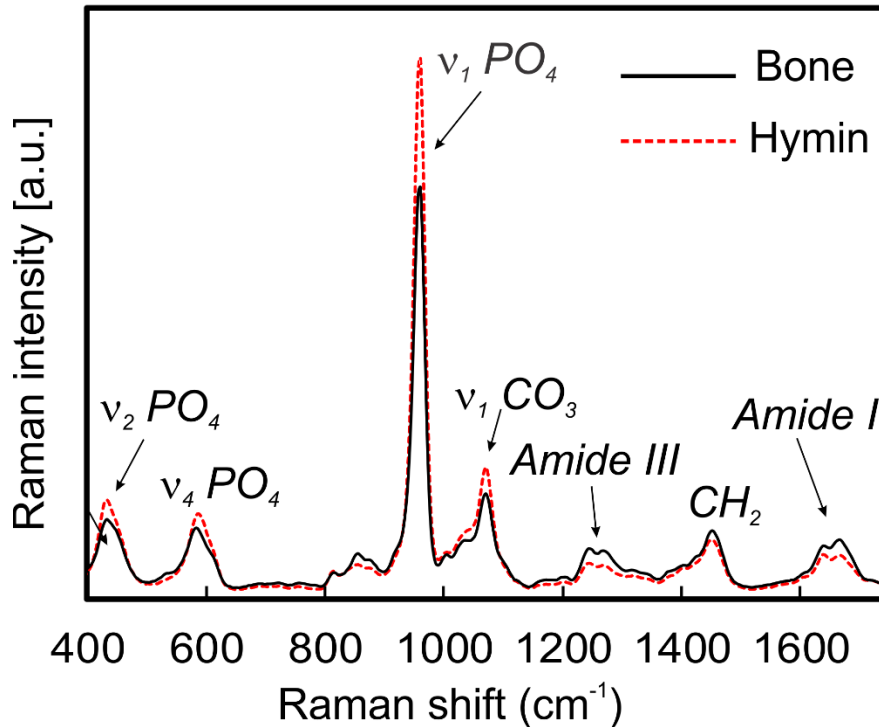


Fig. 4. 2 Typical Raman spectra obtained from a femoral neck sample (transverse to the femoral neck's long axis) containing hypermineralized tissue (Hymin, mineralized periosteum) and lamellar bone (Bone). The Raman shift range is 400 cm^{-1} - 1750 cm^{-1} . The intensity of phosphate (ν_1 , ν_2 and $\nu_4 \text{PO}_4$) and B-type carbonate ($\nu_1 \text{CO}_3$) Raman bands are higher for hypermineralized tissue (red dashed line), whereas amide I and III, and CH_2 bands have higher intensity in lamellar bone (black line).

Contrast images of amide I and ν_1 phosphate were generated through calculation of the intensity values for relative band areas for regions of hypermineralized tissue and lamellar bone. Fig. 4.3(a-d) shows the typical contrast images obtained from a femoral neck sample, containing hypermineralized fibrocartilage (indicated by letter H) and lamellar bone. In all the measured areas, ν_1 phosphate contrast images scored higher values in the hypermineralized region than in lamellar bone, whereas amide I contrast images demonstrated an opposite trend with higher intensity values in lamellar bone. Subsequently, mineral-to-matrix ratio was extracted as the ratio of the integrated areas of ν_1 phosphate to amide I Raman bands. As shown in Fig. 4.3e (0° polarization relative to the horizontal direction), the hypermineralized region displayed primarily brighter contrasts, indicating a relatively higher amount of mineral compared with that of the lamellar bone. In all the specimens that were measured under different polarization angles (-90° to 90° with a step of 15°), the amount of mineralization is consistently higher in the hypermineralized region and the relative ratio did not vary significantly (in the range of 5-7). The measured carbonate-to-phosphate ratio shows the various degrees of *B*-type carbonate substitution in the apatite lattice. The carbonate-to-phosphate ratio was slightly higher (in the range of 0.05-2) in the hypermineralized region than that in the lamellar bone (Fig. S4.1).

Another key feature is the polarization effect that provides orientation related information for the different tissues. As shown in Fig. 4.3c (0° polarization relative to the horizontal direction), in the lamellar bone, the brighter “strips” represent regions where collagen fibres are mostly out-of-plane (polarization direction parallel to amide I vibration direction), whereas, the darker layers are where the collagen fibres are primarily “in-plane” (the vibration direction of amide I is perpendicular to the polarization direction). Such contrast became invisible after the polarization light was turned to 90° (Fig. 4.3d, polarization relative to horizontal direction) as all the lamellar

layers have amide I component stretching in the direction of the incident light. The fibre orientation effect was less visible using ν_1 phosphate component (Fig. 4.3a and b), due to the significant higher phosphate content in the hypermineralized region. The polarization dependency, as found in the lamellar bone, was not shown in the hypermineralized region (H) where homogenous intensity values were observed for both phosphate (Fig. 4.3a and b) and amide components (Fig. 4.3c and d), indicating its lack of preferred orientation in the organic matrix. This orientation independence was observed in all the measured hypermineralized tissue from femoral neck and intertrochanter.

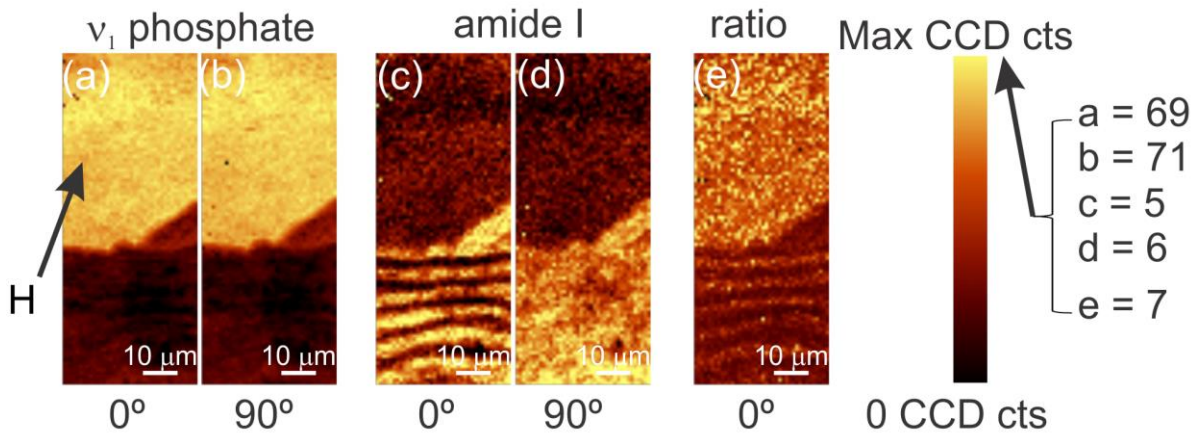


Fig. 4. 3 Representative Raman mapping images obtained under two polarization angles (i.e. 0° and 90° relative to the horizontal direction) from a femoral neck sample containing hypermineralized fibrocartilage (indicated by letter H) and lamellar bone. (a) and (b) show the ν_1 phosphate intensity calculated through a sum filter (920 cm^{-1} - 1000 cm^{-1}) under 0° (a) and 90° (b), respectively; (c) and (d) are the calculated amide I intensity (obtained in the range of 1520 cm^{-1} - 1770 cm^{-1}) under 0° (c) and 90° (d), respectively; (e) is the ratio between ν_1 phosphate and amide I Raman band intensity (mineral-to-matrix ratio) measured under 0° . The color scale and the maximum intensity values for each image are shown on the right.

4.2.2 Mineral platelet thickness and degree of orientation

Laboratory SAXS measurements were performed on six femoral neck and five intertrochanter specimens (from six proximal femora) that were transverse to the femoral neck's long axis. The obtained SAXS patterns displayed either an elliptical shape (Fig. 4.4a), indicating

a strong orientation, or a circular shape (Fig. 4.4b), suggesting a lesser degree of preferred orientation in the volume illuminated with the beam. There was no clear correlation between the scattering shape and a specific type of the tissue. By integrating the SAXS pattern radially and azimuthally, the study obtained the mean mineral platelet thickness (T parameter) and the degree of orientation (ρ parameter), respectively. For presentation purpose, the T values (color-coded) were superimposed on BSE image of an intertrochanter sample, as shown in Fig. 4.5a. There was a clear decreasing trend in the T values from the endocortical bone to the periosteal region, which corresponded to the hypermineralized fibrocartilage.

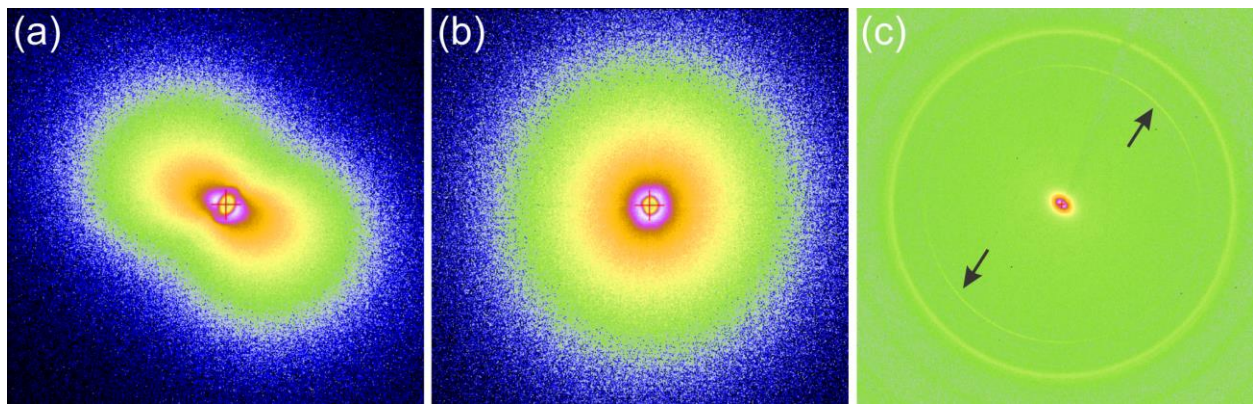


Fig. 4. 4 Typical SAXS (a-b) and SAXS/WAXS (c) patterns obtained from laboratory and synchrotron X-ray scattering, respectively: (a) An elliptical shaped SAXS pattern indicating a strong orientation of the measured minerals; (b) A circular shaped SAXS pattern suggesting a lesser degree of preferred orientation of the minerals; (c) A WAXS pattern showing the (0 0 2) arch shaped ring (i.e. arrows), associated with crystalline hydroxyapatite.

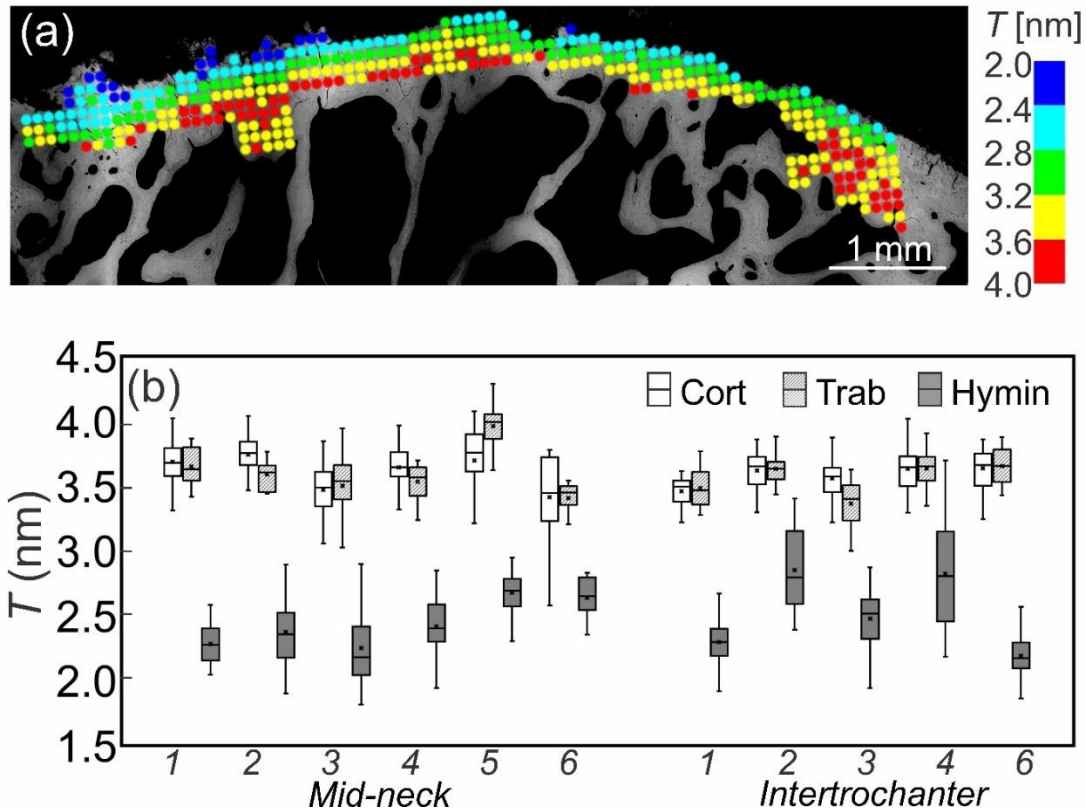


Fig. 4. 5 Mineral platelet thickness T obtained from the laboratory scanning SAXS measurement: (a) An intertrochanter sample containing hypermineralized fibrocartilage and lamellar bone with T values superimposed on the BSE image. T parameter is shown color-coded; (b) Box plot of T values obtained from each sample (numbers at x axis represents sample number). The mean and median values for each type of tissue of the sample are identified by a ‘*’ sign and a horizontal line, respectively. Bars give the first and third quartile of the measured values of each type of tissue (white, cortical bone; dashed, trabecular bone; grey, hypermineralized tissue). The difference between hypermineralized tissue and lamellar bone (including cortical and trabecular) is significant ($p < 0.05$, femoral neck and intertrochanter pooled).

T was significantly smaller in the hypermineralized tissue (-31.0 % of cortical bone and trabecular bone, $p < 0.05$, Friedman test), independent of location. No significant difference was found between femoral neck and intertrochanter, and no significant interaction between the tissue and location was found (Table 4.1). T values for cortical bone (3.53 nm-3.69 nm) and trabecular bone (3.43 nm-3.79 nm) (Fig. 4.5b) were within the range of aged human bone mineral thickness [127,216]. In contrast, T value in the hypermineralized region ($2.49 \text{ nm} \pm 0.21 \text{ nm}$) (Fig. 4.5b),

was close to what has been reported in children with osteogenesis imperfecta type I [123], and in the mineralized human cartilage of young subjects (6-month and 12-year old) [221]. The degree of orientation (ρ) was observed to be statistically higher in the trabecular bone (20.0 % of cortical bone and hypermineralized tissue, $p < 0.05$, Friedman test) (Table 4.1), and independent of location. This observation is in line with the previous study [121] where the mineral crystals were typically oriented parallel to the trabecular direction. There was no statistical difference in ρ between cortical bone and hypermineralized tissue, which was likely due to the limitation of the X-ray beam (a resolution of 100 μm) and the transverse plane as being examined in the current study where the majority of the mineralized collagen fibres are “out-of-plane”.

Table 4. 1 Mineral platelets thickness (T) and degree of orientation (ρ) as measured by laboratory SAXS. The tests were performed in cortical bone (Cort), trabecular bone (Trab) and hypermineralized tissue (Hymin), and at mid-femoral neck (Neck) and intertrochanter (Tro).

	Cort vs. Trab vs. Hymin (locations pooled)				Neck vs. Tro (tissues pooled)		
	Cort	Trab	Hymin	P	Neck	Tro	P
T (nm)	3.61 (0.03)	3.61 (0.07)	2.49 (0.09)	0.01	3.21 (0.03)	3.08 (0.13)	0.35 NS
ρ	0.30 (0.02)	0.36 (0.02)	0.30 (0.03)	0.04	0.30 (0.02)	0.32 (0.03)	0.35 NS

Statistical analysis was done by Friedman test (locations pooled) and Wilcoxon signed-rank test (tissues pooled). The values represent means and standard errors.

4.2.3 Mineral platelet thickness and length using synchrotron SAXS/WAXS

Synchrotron based measurement was done on three femoral neck samples that contained similar hypermineralized fibrocartilage as being observed at intertrochanter. Due to the constraints of the measurement time, this study chose to focus on these three typical samples as hypermineralized fibrocartilage was the typical hypermineralized tissue that occurred at both

femoral neck and intertrochanter, and this tissue has been relatively well studied at other anatomical locations [235]. Higher resolution SAXS patterns obtained by synchrotron source were similar to that of the laboratory measurements where both elliptical shape (Fig. 4.4a) and circular shape (Fig. 4.4b) were found, suggesting various degrees of preferred mineral orientation. SAXS mapping revealed an abrupt transition in mineral thickness (T) from the hypermineralized region to lamellar bone, as shown in Fig. 4.6a. The obtained T values for hypermineralized fibrocartilage ($2.31 \text{ nm} \pm 0.12 \text{ nm}$) were significantly smaller than that measured in the lamellar bone region ($T = 3.47 \text{ nm} \pm 0.15 \text{ nm}$) ($p < 0.05$, Wilcoxon signed-rank test, Fig. S4.2a). T values obtained in the cortical bone by synchrotron measurements were slightly lower than that of laboratory measurements, which could be attributed to the different sample size and the resolution. Complementing the mean thickness of the mineral platelets, WAXS data provides information on the crystallinity in the long dimension of the platelets. As all the measured areas in the current study showed the (0 0 2) peak (arrows in Fig. 4.4c), which is associated with crystalline hydroxyapatite, the L parameter was calculated based on the FWHM. Similar to the observation in the changes of T values, L values also dramatically decreased from lamellar bone to the periosteal hypermineralized region (Fig. 4.6b). Wilcoxon signed-rank test showed significantly smaller L values in the hypermineralized fibrocartilage ($15.6 \text{ nm} \pm 1.49 \text{ nm}$) than that in the lamellar bone ($29.0 \text{ nm} \pm 0.31 \text{ nm}$) ($p < 0.05$, Fig. S4.2b). ρ values were lower in the hypermineralized fibrocartilage than that in the lamellar bone for two of the three samples (Fig. S4.2c), implying a decreased degree of alignment of bone minerals in the hypermineralized fibrocartilage. This observation was different from the laboratory SAXS which was performed on mixed tissues from both mineralized periosteum and mineralized fibrocartilage. The improved resolution of the synchrotron radiation might also play a role.

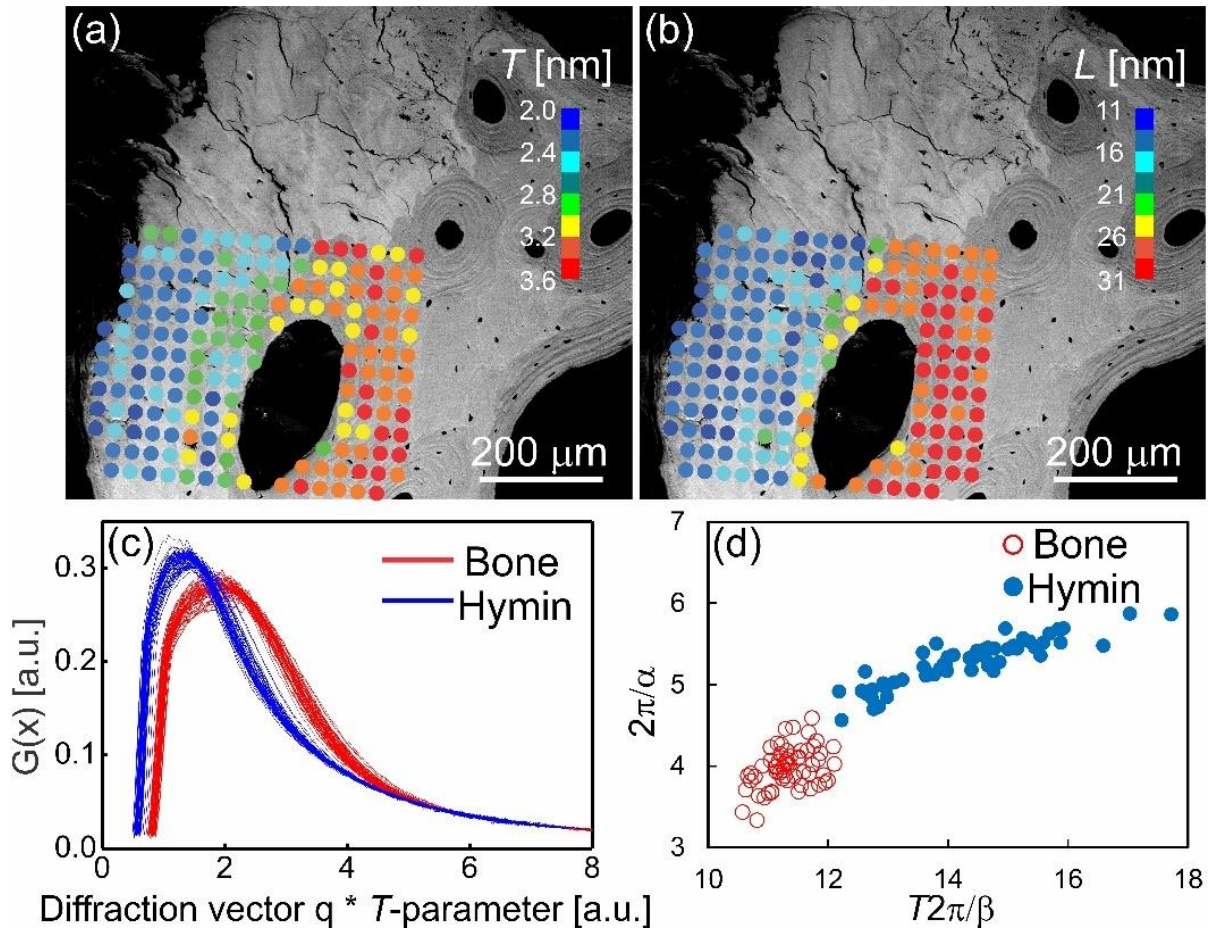


Fig. 4. 6 Mineral platelet thickness T , length L and spatial organization of mineral platelets obtained from SAXS/WAXS measurement using synchrotron radiation: (a-b) BSE images of a femoral neck sample containing hypermineralized fibrocartilage on the left and lamellar bone on the right, superimposed by T and L values, respectively. Both structural parameters are shown color-coded; (c-d) Description of the mineral organization derived from synchrotron SAXS measurement. Typical $G(x)$ curves in (c) were obtained from lamellar bone (Bone, red curves) and hypermineralized fibrocartilage (Hymin, blue curves); (d) Plot of $2\pi/\alpha$ versus $T2\pi/\beta$ derived from (c) shows a different pattern between lamellar bone (open red circles) and hypermineralized fibrocartilage (blue closed circles).

4.2.4 Spatial organization of mineral platelets using $G(x)$ curves

$G(x)$ curves were derived from the SAXS patterns measured with laboratory and synchrotron X-ray source. Fig. 4.6c shows typical $G(x)$ curves obtained from synchrotron measurement of a femoral neck sample. The study also provided typical $G(x)$ curves obtained from laboratory SAXS measurement on a femoral neck sample containing hypermineralized tissue (mineralized periosteum) and lamellar bone in Fig. S4.3. For synchrotron measurements, the $G(x)$ plots for both lamellar bone and hypermineralized tissue showed strong peaks in the lower limit of q range (i.e. 1-2). For laboratory measurements, the curves were noisier (fluctuating) due to the lower resolution, and some curves did not show an evident peak in the measured q range, yet the projection of these curves indicated the peak position at extremely small q values (Fig. S4.3a). Nevertheless, the $G(x)$ curves obtained in the hypermineralized tissue clearly differed from that of lamellar bone in terms of the peak position and the slope. In order to derive quantitative information on the mineral arrangement, the $G(x)$ curves were fitted, as described in the Materials and Methods section (i.e. last paragraph of *Scanning SAXS/WAXS using synchrotron radiation*). Subsequently, the fitted parameters α and β , which describe the periodicity of oscillation and its damping, respectively, were used to quantify the ordering. Fig. 4.6d shows the plot of $2\pi/\alpha$ versus $T2\pi/\beta$ obtained from Fig. 4.6c. Interestingly, for both laboratory and synchrotron measures, the fitted data obtained from the hypermineralized region could be clearly distinguished from those of normal cortical and trabecular bone. Specifically, in lamellar bone, the majority of $T2\pi/\beta$ and $2\pi/\alpha$ values centered within a narrower range (i.e. $11 < T2\pi/\beta < 16$; $2.5 < 2\pi/\alpha < 3.5$). In contrast, $T2\pi/\beta$ and $2\pi/\alpha$ values scattered at the higher range (i.e. $11 < T2\pi/\beta < 57$; $2.0 < 2\pi/\alpha < 5.6$) in the hypermineralized tissue. Such difference indicates a lesser degree of order in the arrangement of the minerals of the hypermineralized tissue.

4.3 Discussion

In this study, the compositional and mineral properties of the hypermineralized tissue were found to differ from lamellar bone at the ultrastructural level. Mineral-to-matrix ratio was higher in the hypermineralized region compared with that of the lamellar bone. In addition to a much more irregular mineral organization (i.e. variation in spatial distance), average mineral thickness (T) and length (L) in the hypermineralized tissue were significantly reduced from approximately 3.6 nm (T) \times 29.0 nm (L) in lamellar bone to around 2.5 nm (T) \times 15.6 nm (L). Such differences suggested that the high mineral density of the hypermineralized tissue as observed under BSE was due to changes at the individual mineral level.

4.3.1 Mineral-to-matrix ratio and matrix organization

In consistent with the study in chapter 3, typical hypermineralized tissue was found in all the individuals, including fibrocartilage at the intertrochanter [73,75], and mineralized periosteum [71] and mineralized fibrocartilage [73,75] at the femoral neck were found. Similar to what have been observed with qBSE imaging, Raman microspectroscopy provided complementary information on the degree of mineralization (i.e. mineral-to-matrix ratio). The combination of high phosphate contents and low amide contents contributed to the relatively high mineral-to-matrix ratio in the hypermineralized region. Transition from the hypermineralized region to the lamellar bone resembles the features of the calcified articular cartilage/bone interface where Fourier transform infrared spectroscopy (FTIR) revealed significantly decreased mineral content across the border in bovine tibiofemoral joints [236,237]. In all the Raman measured regions of interests, slightly higher degree of *B*-type carbonate substitution was also observed (Fig. S4.1). Various degrees of carbonate substitution are directly associated with mineral crystallinity and size [136].

Particularly, lower carbonate substitution is seen in larger, thus more stable, crystals, and vice versa [238].

The increasing degree of mineralization is a direct indication of the altered organic matrix in the hypermineralized tissue. Raman scattering is strongly dependent on both composition and organization of the organic matrix. Previous studies demonstrated that the polarization anisotropy of ν_1 phosphate band and the amide I band can be used to elucidate the orientation of bone mineral platelets and collagen fibrils [133,134]. In this study, both the mineral and the organic matrix in the hypermineralized tissue were clearly insensitive to the polarization, forming a strong contrast with the lamellar bone (Fig. 4.3). Such observation was in line with the optical and electron microscopy findings where no lamellar structure was found in the matrix of hypermineralization. The homogeneous and isotropic appearance in the hypermineralized tissue suggested a rather random distribution of the components. Similarly, FTIR studies on bovine tibiofemoral joints documented a transition from the uncalcified fibrocartilage to the mineralized fibrocartilage and bone interface where collagen fibres are randomly oriented near the interface [236,237].

4.3.2 Thinner, shorter and less organized mineral platelets in the hypermineralized tissue

The dimension of bone mineral platelets, an important indicator for bone mechanical properties, has been widely studied using transmission electron microscopy (TEM) [239], X-ray diffraction (XRD) [240], atomic force microscopy (AFM) [228], and SAXS/WAXS [121,229,241,242]. SAXS/WAXS has the advantages of allowing higher throughput of samples with shorter analysis time and non-destructive examination of local structural properties at the nanoscale. Previous studies on bone minerals using SAXS/WAXS have shown that the thickness of mineral platelets may vary from 1.5 nm to 9 nm [121,122] and the length is approximately 26 nm [123]. The T value of the mineral platelet in the cortical and trabecular bone in the present

work was approximately 3.6 nm, which is close to the reported values in human subjects with advanced ages [216,221], and the L parameter (i.e. 29.0 nm) also agrees well with the reported values [123]. Interestingly, the mineral platelets in the hypermineralized region were significantly thinner and shorter than that of lamellar bone (Table 4.1, Fig. 4.5, Fig. 4.6a and b, Fig. S4.2a and b). This is different from the previous observations at human patella or lumbar vertebral where the crystal size of the minerals did not vary between calcified articular cartilage and bone [221], and also different from the previous measurement on human femoral head with larger T values in the calcified articular cartilage than in lamellar bone [243]. Such observations imply an important role for collagenous and noncollagenous proteins in determining the mineral size. In addition, the concurrent thinner mineral platelets and higher degree of carbonation is resembling what researchers have found in mineral syntheses: higher B -type carbonate content correlates to much smaller grains [244,245]. Although the synchrotron-based measurement was primarily performed on the mineralized fibrocartilage, the laboratory SAXS measurements found similar mineral thickness and organization in the mineralized periosteum and in the calcified fibrocartilage. The mineral width (W) is not known in the current study, it is conceivable that the minerals generally had smaller sizes in the hypermineralized tissue, since W equals to or smaller than T when ϕ (mineral volume fraction) is 0.5 or higher [221]. Consequently, the higher degree of mineralization is accompanied by the decreased mineral size.

Both laboratory and synchrotron X-ray measurements found a lesser degree of organization (spatial distribution) of the mineral platelets in the hypermineralized tissue (Fig. 4.6c and d, Fig. S4.3). The previous studies on osteogenesis imperfecta (OI) type VI [124] and sodium fluoride treated bone [125] using $G(x)$ curves and the fitted parameters (i.e. α and β) have successfully demonstrated the differences in the mineral organizations at various bone locations. Similar to OI

[124] and fluorotic bone cases [125], the shifted $G(x)$ curves and the highly scattered fitted values in the hypermineralized tissue indicated a loss of positional correlations between the mineral platelets.

4.3.3 Implication to fracture risk

Could we link the altered mineral size and organization to the mechanical property of the hypermineralized tissue? Although the exact answer to the question is currently unclear, its potential link could be found in other mineralized tissues. In fluoride treated bone, researchers found increased mineral size [229], while in OI bone, a unique mineralization pattern and decreased mineral size were found [123,124]. Interestingly, the higher degree of mineralization and the smaller minerals as observed in the current study is in a manner strikingly similar to those with OI, where the significantly increased mineralization arises from reduced mineral crystal size and lack of order of mineral platelets [123,124,141]. Further, in OI patients, the composition of the mineral platelets is also altered in terms of the carbonate-to-phosphate ratio [246], and that there is less overall homogeneity of alignment of platelets within the tissue, reflecting matrix disorganization [141]. OI is commonly known as excessive fragility of bones [247], which is characterized by increased hardness [248], yet lower fracture resistance than normal bone. Such altered biomechanical behavior was also observed in the study in chapter 3: the indentation could produce cracking in the hypermineralized tissue which was associated with the increased microhardness. Therefore, the reduced mineral size and the random distribution of the minerals in the organic matrix could have indication for its mechanical properties.

4.3.4 Limitations

There are several limitations in this study. First, a small sample size was obtained from the cadaver femora. As such, it should be cautious to generalize the findings from this study across

other specimens. However, the difference in the mineral size between the hypermineralized tissue and the lamellar bone should still be true with larger population, as the current observation power is 1. Second, the specimens are from people who are older than 60 years old, which was mainly due to the clinical relevance of hypermineralization in older adults. Nevertheless, both young and old individuals should be equally studied in future. Third, the study did not examine the properties of the minerals of diseased or drug treated bone, it would be interesting to see if those changes in bone will affect the mineral dimensions and organizations. Finally, the collagen structure of the hypermineralized tissue was not studied in this thesis. It would be, however, valuable to perform an in-depth histological study to understand the biomineralization process of the hypermineralized tissue.

4.4 Conclusions

The study provided new insights into the origin of hypermineralization by illustrating how the hypermineralized tissue at human proximal femur differed from lamellar bone at the mineral level. The increased mineral-to-matrix ratio and the lack of lamellar arrangement revealed its compositional changes from the normal bone tissue. The significantly thinner, shorter and more irregularly distributed mineral platelets as found in the hypermineralized tissue, suggested that the elevated degree of mineralization was achieved by changes at the individual mineral level. Subsequently, the altered mineral configuration could be the contributor to the inferior mechanical properties of the hypermineralized tissue. The study advanced the knowledge on the nature of hypermineralization in human proximal femur and calls for future attention on its potential role in hip fragility.

Chapter 5 Shear Deformation and Fracture of Human Femoral Cortical Bone*

From a materials point of view, hip fracture is the combined result of a fragile bone structure and the complicated stress state of tension, compression, and shear caused by external impact. It is essential to understand how bone fractures under different stress states and how this relates to bone's hierarchical structures as a means to improve clinical risk assessment and to contribute to the development of solutions to prevent hip fracture.

Bone deforms (inelastic) and fractures through microcracking, and the pattern of microcracks strongly depends on the local stress [54,175]. Most previous studies of bone failure at the material level have focused on tension and compression, while far fewer studies have focused on shear-induced microcracking [182,249], despite the fact that shear is highly likely to be involved in femoral neck fractures [17]. Early shear studies by Ascenzi and Bonucci [183] was performed on single osteon. Later shear studies used torsional tests [185,186] which are not suitable for studying bone tissue behavior in pure shear mode [187]. Most importantly, how shear induces microcracks within or between lamellae at the cortical bone level is still unknown. Therefore, the purpose of this study was to investigate the shear-induced microcracking processes in human cortical bone and its relationship with bone's hierarchical structures, especially the collagen fibril orientation.

A version of chapter 5 has been published. T. Tang, V. Ebacher, P. Crompton, P. Guy, H. McKay, R. Wang. (2015) Shear deformation and fracture of human cortical bone. *Bone*. 71:25-35.

5.1 Materials and methods

5.1.1 Specimen preparation

Eight freshly frozen human cadaver femora (six males, two females, age range: 62–79) without reported metabolic bone tissue conditions from LifeLegacy Foundation were used for the study. All bone tissues were kept frozen at $-20\text{ }^{\circ}\text{C}$ until specimen preparation. The study was approved by the Clinical Research Ethics Review Board at the University of British Columbia.

Twenty-nine specimens in total were subjected to shear testing (ten 0° , nine 30° , five 60° and five 90° , respectively). The shear specimens were obtained from the cortex of the diaphysis region. This is mainly because of the limitation of the thickness in human femoral neck (approaching sub-one hundred micron), and the fact that both locations are comprised of lamellar bone structure. Further, it is a common practice in bone biomechanical study to test femoral shaft bone to assess the mechanical response at proximal femur [170]. Two cuts, each perpendicular to the femoral shaft's long axis, were made at 27 % and 48 % from the proximal end of each femur with a band saw. The medial quadrant of each bone cylinder thus obtained was then sectioned into bar specimens that were oriented at four different angles, i.e. 0° , 30° , 60° and 90° (Fig. 5.1) with respect to the long bone axis, and thus the long axes of majority osteons, by a low speed diamond saw (IsoMet 1000, Buehler Ltd, ON, Canada). The four sides of each specimen aligned either parallel or normal to the periosteal surfaces of femoral shaft. Rough machining was performed using a mini-milling machine (Sherline, model 5400, Vista, CA, USA). The specimens were subsequently manually ground, using a series of carbide grinding papers (Buehler Ltd, ON, Canada), and polished with diamond suspension starting with $6\text{ }\mu\text{m}$ and ending with $1\text{ }\mu\text{m}$ (Leco Co., MI, USA). The final specimens were 20 mm long, 5 mm wide and 3 mm thick, with the front

and back surfaces (20 mm × 5 mm) parallel to the periosteal surface of femoral shaft. By following the ASTM standard (ASTM D5379/D5379M) [250], two 90° V-shaped notches, approximately 22 % of the depth of the specimen total width, were made with a razor blade at the top and bottom surfaces (i.e. 20 mm × 3 mm). All the above steps were done under constant water irrigation. After the initial preparation, bone mineral density (mg/cm³) in all specimens was assessed using peripheral quantitative computed tomography (pQCT, model XCT 3000, Stratec, Biomedical AG, Germany) with a voxel size of (0.2 × 0.2 × 2.3) mm³. The entrance dose of the irradiation was 1 μGy which is extremely low and safe for bone specimens. Statistical comparison was further conducted for differences relatively to their orientations using Kruskal-Wallis one-way ANOVA test in SPSS with a confidence level of 95 % ($\alpha = 0.05$). In addition, specimens were inspected for pre-existing cracks after specimen preparation by xylenol orange (Sigma-Aldrich) staining at a concentration of 0.5 mM [251]. Specimens were wrapped with tissue paper, soaked with phosphate-buffered saline solution (PBS, 0.1 mol, pH 7.6), and kept at -20 °C in sealed plastic bags until the day of testing.

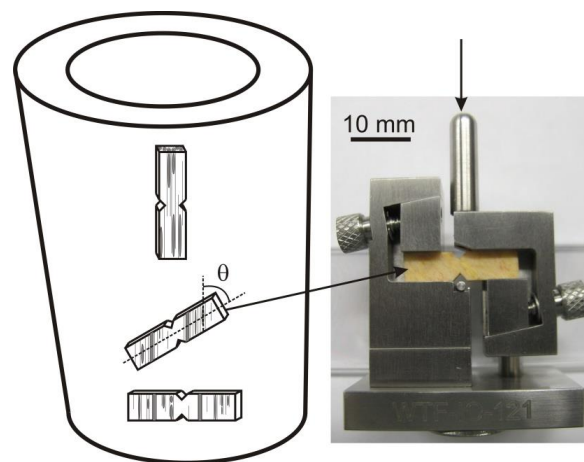


Fig. 5. 1 Schematic illustration of specimens prepared from human femora. Shear specimens were oriented at 0°, 30°, 60° and 90° with respect to the long axis of femoral shaft, which is indicated by the grey lines. A specimen was gripped in the custom made Wyoming Iosipescu fixture with the shear loading indicated by the arrow pointing at the top of the rod.

5.1.2 Shear testing

Iosipescu shear tests followed the ASTM standard (D5379/D5379M) [250]. The design of the Iosipescu method eliminates bending moment across the notched section and creates a uniform shear plane between the loading points [249]. The fixture developed by Adams and Walrath [252], known as the ‘modified Wyoming fixture’ is widely used in composite research laboratories. However, the correct measurement of shear modulus and shear strength of synthetic composite materials is τ_{xy} still debatable [253]. Shear modulus ($G = \frac{\tau_{xy}}{\gamma_{xy}}$) as measured only applies when the shear stress and strain distributions are uniform at the test section of the specimens. This is difficult to achieve practically when testing anisotropic materials such as bone [254]. To date, only a few studies have applied the Iosipescu shear test to bone [187,249]. Nevertheless, it is the most mature in-plane shear test that is used in materials testing. During the test, each specimen was gripped in a customized fixture (Wyoming Test Fixtures, Salt Lake, UT, USA) (Fig. 5.1). All the tests were performed at a cross head speed of 0.2 mm/min on an electromechanical testing machine (Minimat 2000, Maple Instruments Ltd., Toronto, ON, Canada) equipped with a 1 kN load cell. All specimens were loaded to final fracture to obtain the full load-displacement curves (i.e. at about 90 % drop from the peak load). Experiments were performed at room temperature (20 °C), and specimens were kept wet during testing. Time, load, and displacement were recorded. Shear strengths were calculated following ASTM standard (D5379/D5379M) for the four orientation groups and statistically compared using Kruskal–Wallis one-way ANOVA test with a confidence level of 95 % ($\alpha = 0.05$). The stiffness of the testing system was calibrated using a 1018 mild steel specimen (shear modulus $G = 80$ GPa).

5.1.3 Digital image correlation and strain analysis

In-plane displacement and strain fields were obtained using digital image correlation (DIC) [255]. This analysis provided information on the deformation process of human cortical bone during shear testing. The intrinsic microstructural features of the polished bone provide high contrast surface patterns, which enables one to use DIC without spraying speckle pattern on specimens' surfaces. All specimens were tested with a gage section (approximately 3.6 mm × 2.7 mm) imaged under an optical microscope (Nikon Eclipse E600) equipped with a digital CCD camera (QImaging QICAM Fast 1349, BC, Canada). A sequence of 1392 pixel × 1040 pixel with 8-bits color images was captured under the reflected light for each specimen at the frame rate of 4 frames/s. The images were later selected at regular intervals and processed using the Davis software (Davis LaVision Inc., MI, USA) to compute the in-plane displacement fields and finally the in-plane strain fields. The angles of shear strain bands on the surfaces were measured with respect to the bone's long axis with ImageJ software (U. S. NIH, Maryland, USA). During the shear tests, a high-speed video camera (Phantom V12, Vision Research, NJ, USA) equipped with a Nikon 105 mm macro f2.8 lens (Nikon Co., Tokyo, Japan) was also used to monitor the fracture progress at the frame rate of 800 frames/s.

The shear stress–strain curves presented are based on the nominal shear stress, following ASTM standard (D5379/D5379M), and engineering shear strain which was calculated based on a rectangular area covering 80 % of the surface between two notches (Fig. 5.3; illustration). The shear moduli were measured from the slope of the initial linear part of the stress-strain curves.

In traditional engineering material study, the concept of stress triaxiality is often used to assess the mechanism of fracture [256]. The value of stress triaxiality shows the loading condition

of the testing material: tension, compression or shear. Similar to stress triaxiality concept, strain triaxiality was later deducted [257], and developed to adapt to the in-plane shear test as [258]:

$$TR^* = \frac{\frac{1}{3}(\varepsilon_1 + \varepsilon_2)}{\sqrt{\frac{1}{2}[(\varepsilon_1 - \varepsilon_2)^2 + \varepsilon_1^2 + \varepsilon_2^2]}} \quad (5.1)$$

where ε_1 and ε_2 stand for maximum normal strain and minimum normal strain, respectively. When TR^* value is 0, it corresponds to pure shear. While if tension is more prominent, TR^* value should be positive, and TR^* should be negative in compression. If the absolute value is much less than 1/3, one assumes that shear strain predominates over the gauge section [258].

5.1.4 Microcracking analysis

In order to observe the microcracks' morphology, distribution and extent, all specimens were fixed, dehydrated and stained after mechanical tests, following a protocol used by Ebacher et al. [170]. Briefly, the specimens were fixed in 70 % acetone/water solution for 24 h, followed by dehydration in a graded ethanol series (80 %, 90 %, and 100 %) for 24 h per step and finally stained in a filtered saturated solution of fluorescein (Fisher Scientific) dissolved in 70 % ethanol/water overnight. The specimens were then rinsed in 100 % ethanol until the washed ethanol was clear before being air-dried.

After staining, the specimens were examined under a stereomicroscope (Nikon SMZ 1000) to characterize their macroscopic fracture patterns. The angles of the major fracture initiation with respect to the bone's long axis were measured. An optical microscope (Nikon Eclipse E600) using reflected white light and epi-fluorescence light (with excitation at approximately 490 nm and emission at approximately 525 nm) was used for initial microcrack examination. Three specimens from each group were then cut in the plane perpendicular to the bone's long axis to observe the relation between fracture and microstructure in the gauge zone. Further observation was under a

laser scanning confocal microscope (LSCM; Olympus FluoView FV1000, Olympus Canada Inc.; Leica SP5X, ON, Canada). During the high magnification LSCM imaging process, specimens were immersed in an in-house built chamber filled with pure ethanol (Commercial Alcohols Inc.) to reduce the effects of reflective index difference [180]. The 488 nm line of a multi-line Argon laser was used for fluorescein excitation, and the emission was at 519 nm. Selected sites of microcracks were further characterized in three dimensions (3D), during which the specimens were typically imaged from the surface down to depths of 15 μm -20 μm with a step size of 200 nm. Each sequence of 12-bit images thus obtained was reviewed, analyzed, and, when necessary, stacked in z-plane (Imaris 7.6.0, Bitplane AG) to obtain microcrack morphology in the third direction. Additionally, in order to verify whether the state of microcracks as seen on the longitudinal surfaces was representative of the damage in the bulk of the material, three 0° specimens were ground and polished to their centre parallel to the longitudinal surface. A variable pressure scanning electron microscope (SEM; Hitachi S-3000N, Hitachi Ltd., Tokyo, Japan) was also used to show the local bone lamellar structure and detect crack deflections at osteons.

Second harmonic generation (SHG) combined with two-photon excitation fluorescence (TPEF) imaging were used to evaluate the location of microcracks in terms of the bone's lamellar structure. This was performed on selected specimens under Olympus Multiphoton Laser Scanning Microscope FV1000 (MPM, Olympus Co., Tokyo, Japan) with the objective lens of 25 \times , NA = 1.05 and 60 \times Oil, NA = 1.4. The SHG signal originates from non-linear optical materials possessing a non-centrosymmetric molecular organization such as collagen [107]. The signal intensity depends on the collagen orientation with the strongest signal from the ones lying in the plane. It is well known that lamellar bone is made up of preferentially orientated collagen fibrils organized in lamellae [51]. When imaged under SHG, a high contrast image is produced, providing

valuable information on the preferred orientation of collagen fibrils in bone. Compared to traditional techniques for imaging bone structure at the micro-scale, SHG has advantages of better imaging resolution over polarized light microscopy, and could resolve collagen better than confocal microscopy alone [108]. In the past decade, SHG microscopy has become a powerful technique to image collagen fibrils in biological tissues with high contrast and specificity [108]. However, there are few studies using SHG examining the collagen fibrils in bone so far [109]. One unique feature of the MPM used in this study is that the fluorescence signals from TPEF were combined with SHG signals in a single microscope, which enabled me to directly link microcracking to collagen orientation.

5.2 Results

5.2.1 Effects of loading orientation on mechanical properties and strain development

Fig. 5.2 shows typical load-displacement curves and representative shear stress-strain curves of the Iosipescu V-notch specimens at four different orientations with respect to the long bone axis (obtained from eight 0°, three 30°, five 60° and four 90° specimens). As large deformation causes optical decorrelation and makes DIC analyses invalid [259], stress-strain curves were plotted only before major cracks appeared (i.e. around the load peak). All stress-strain curves generally displayed an initial linear stage followed by a nonlinear stage.

The measured shear strength depended on specimen orientation (Table 5.1). The 0° specimens showed the highest shear strength ($49.9 \text{ MPa} \pm 6.2 \text{ MPa}$), which is twice as high as that of the 60° specimens ($22.7 \text{ MPa} \pm 2.5 \text{ MPa}$) (Table 5.1) ($p < 0.05$). No statistically significant differences were observed among specimens oriented at 30°, 60° and 90° ($p < 0.05$). The shear moduli showed that 0° specimens had the highest value (i.e. 4.0 GPa), while 30° specimens had

the lowest shear modulus (Table 5.1) although no statistical difference was found among the orientations. The ratio of transverse to longitudinal shear modulus (G_{0°/G_{90°) obtained in the current study was 1.1, which is in agreement with a previous torsion study [260].

According to the pQCT measurements, there was no significant difference in bone density among the specimens ($p < 0.05$). However, one should note a larger standard deviation in 30° specimens (Table 5.1).

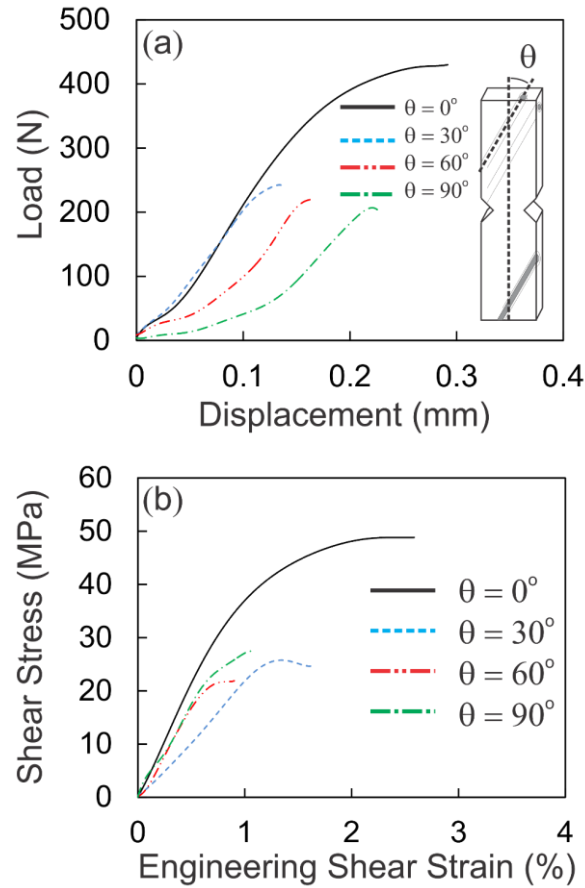


Fig. 5. 2 Representative load-displacement curves (a) and stress-strain curves (b), for different specimens (0° , 30° , 60° and 90°) tested by Iosipescu in-plane shear. Shear stress calculation following ASTM standard (D5379/D5379M) ($\tau = \frac{P}{A}$, where p is the loading force and A is the cross-sectional area between two notch tips), and engineering shear strain obtained from DIC ($\gamma = 2 \times \varepsilon_{xy}$, where shear strain ε_{xy} is the average value of the displacement gradients e_{xy} and e_{yx} , which are the shear component on the y plane along the x direction and on the x plane along the y direction, respectively).

Table 5. 1 Bone mineral density, shear mechanical properties and fracture features of human cortical bone under shear at different orientations.

Specimen Orientation	0 degree	30 degree	60 degree	90 degree
Specimen Density (mg/cm³)	1276.0 ± 38.4	1193.2 ± 438.2	1218.3 ± 118.8	1272.7 ± 58.9
Shear Modulus [GPa]	4.0 ± 0.4	2.9 ± 1.6	3.5 ± 0.8	3.5 ± 0.5
Shear Strength [MPa]	49.9 ± 6.2	31.2 ± 8.4	22.7 ± 2.5	28.9 ± 6.2
Angle of Shear Strain Band vs. Long Bone Axis* (°)	14.0 ± 6.7	14.2 ± 6.7	11.8 ± 3.4	18.5 ± 7.0
Angle of Major Crack Initiation vs. Long Axis of Osteons (°)	36.6 ± 10.5	1.8 ± 1.5	2.5 ± 0.5	4.0 ± 2.4
Major Crack Deflection by Cement Line (%)	N/A	7.0 ± 2.4	11.8 ± 8.3	4.0 ± 6.9
Major Crack Deflection by Lamellae (%)	N/A	70.5 ± 4.7	65.7 ± 10.1	55.9 ± 17.0
Major Crack Going through Haversian Canals (%)	N/A	22.4 ± 3.0	22.5 ± 14.2	40.0 ± 18.3

* The accuracy of long axis of osteons measurement under DIC is limited by resolution, thus the ideal long bone axis direction was used for comparison.

The in-plane strain triaxiality ratio (TR*) before large inelastic deformation appeared was obtained from the specimens' gauge section using DIC analysis. The absolute value remained within a range of 0 to 0.12, significantly less than 1/3. This suggests that the tested section was mainly under shear strain. The principal normal strain angle (i.e. between principal normal strain and horizontal direction which is perpendicular to specimens' long axis) for the gauge sections was $42.4^\circ \pm 2.8^\circ$. This represents fair agreement with the theoretical value for pure shear (a principal angle of 45° should be expected), and further supports that the gauge section was primarily governed by shear rather than by compression or tension.

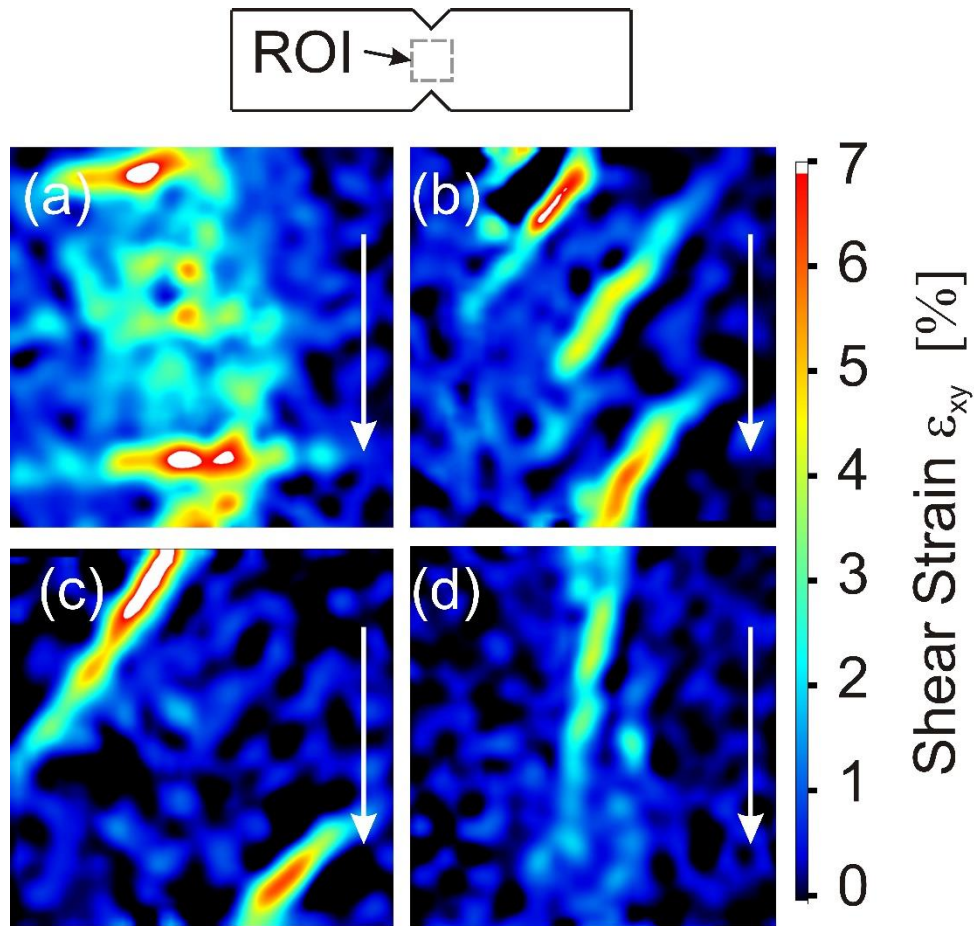


Fig. 5. 3 Schematic diagram of region of interest (ROI) used for digital image correlation (DIC) shear strain analysis and the representative shear strain (i.e. ϵ_{xy}) distribution beyond yielding point, for specimens in each orientation: (a) 0° ; (b) 30° ; (c) 60° and (d) 90° . Arrows indicate the shear loading direction. Size of the ROI is approximately (2.3×2.3) mm².

Strain mapping showed that the elastic deformation on the specimens was relatively homogeneous. In contrast, one or more high-deformation bands developed across the specimen during the inelastic stage (Fig. 5.3). The deformation bands were 100 μ m-150 μ m wide, and strain values were 5-7 times higher than the average global strain. Note the distinct directions of the developed deformation bands and their dependence on the specimens' and osteons' orientations. In the 0° specimens, the bands were generally aligned with the specimens' axes. The 90° specimens showed the bands that were more or less perpendicular to the axes. In the 30° and 60° specimens,

bands were oblique, with a lower angle in the 60° specimens. In general, shear strain concentration bands had a close association with long bone axis with an average deviation of 11.8° to 18.5° (Table 5.1). I also noted that there was a small deviation between the actual long bone axis (i.e. long axes of osteons) and the ideal orientation, which generally ranged from 8° to 10°.

5.2.2 Macro-scale fracture patterns

Representative major fracture patterns for each orientation are provided in Fig. 5.4. The cracking process strongly depended on the orientation of the specimens. Particularly, the angle between the crack initiation near the notches and the long axes of osteons was very small in 90°, 60° and 30° specimens, but dramatically increased to about 36° in the 0° specimens (Table 5.1). In the 90° specimens, where the loading direction coincided with the overall orientation of the osteons, the crack extended along the long axes of osteons in a relatively straight path (Fig. 5.4d). For the 30° and 60° specimens, the cracks mostly followed the orientation of the osteons, but were deflected more frequently than that in the 90° specimens (Fig. 5.4b and c). When the orientation of the osteons was mainly perpendicular to the loading direction (i.e. 0° specimens), specimens fractured in an off-axial two-path mode (Fig. 5.4a). From the fracture pattern that was observed for each specimen and using data recorded by high speed video, the study concluded that the crack initiated at the upper or lower notch near the notch root and propagated along a direction that largely deviated from and tended to veer towards back to the osteons' long axes.

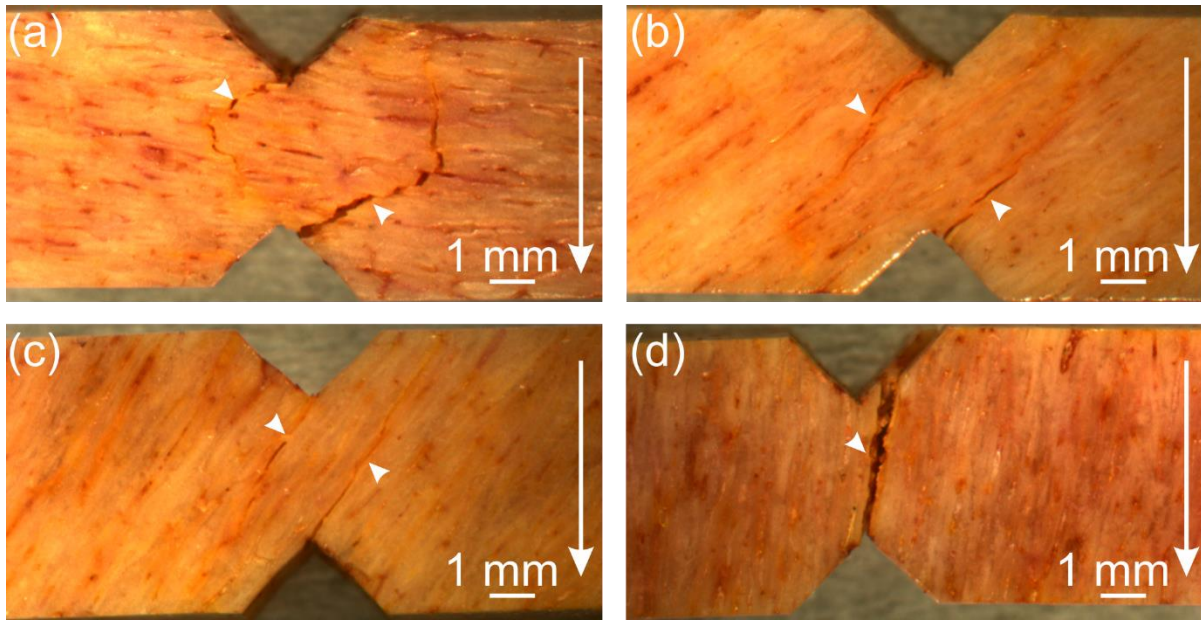


Fig. 5. 4 Typical major fracture patterns under a stereo microscope. Of interest is the relatively large crack initiation angle vs. long axis of osteons, and the multiple crack deflections observed in 0° specimen (a). 30° (b), 60° (c) and 90° (d) specimens have comparatively flat fracture routes. Arrow heads point at the fracture planes. Shear loading direction is indicated by the vertical arrow.

Assessment on the interaction between the main fracture and the osteonal structure was done using transverse sections that were perpendicular to the long axes of osteons. When the main crack reached an osteon, it would: 1) be deflected by the cement line and went around the osteon (Fig. 5.5a); 2) propagate into the osteon for a few layers of lamellae before being deflected by the lamellar structure: following a circular crack path, and exiting the osteon (Fig. 5.5b); or 3) pass through the central Haversian canal without being deflected (Fig. 5.5c). Of all the observed osteons (more than 70 osteons for each 30° , 60° and 90° orientation) at the major fracture paths, approximately 4.0 % to 11.8 % showed crack deflection at cement lines (Table 5.1). The lamellar structure, in the present study, seemed to play a major role in interfering with the cracking path. Over ~ 50 % of the observed osteons showed deflection at the lamellae (Table 5.1). However, lamellae's ability to deflect incoming cracks is a combined result of the direction of the incoming crack, the local lamellar orientation, and the loading direction. For the 0° specimens, the initiation

near the notch sites on longitudinal sections was also influenced by the lamellar structure. Out of the four observed areas (i.e. at notch tips with clear lamellar structures), three showed cracks that followed the lamellar boundaries. Crack deflection at cement line was also observed, as shown in Fig. 5.5d.

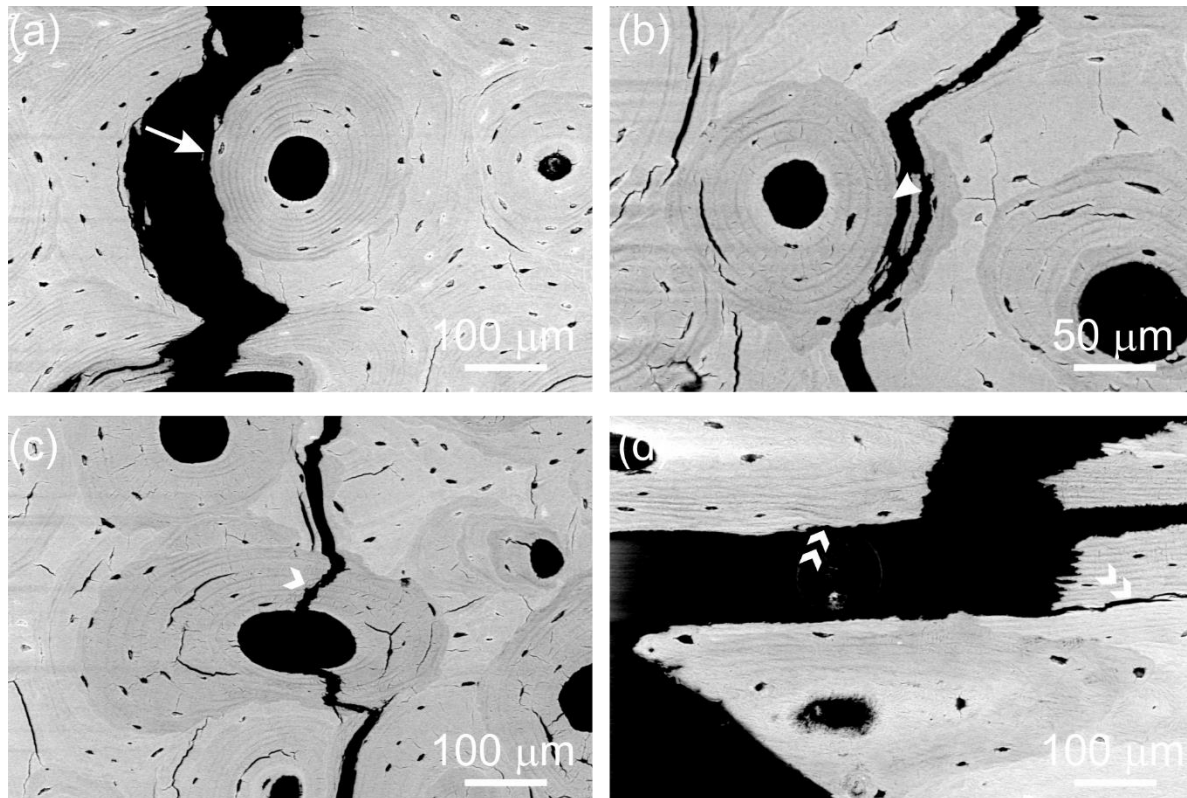


Fig. 5. 5 Scanning electron microscopy (SEM) micrographs showing major fracture interacting with osteons. (a-c) represent three scenarios observed on transverse sections (plane perpendicular to long axis of osteons): (a) Crack was deflected by the cement line and went around the osteon (arrow); (b) Crack was deflected by bone lamellae inside the osteon, resulting in a circular crack path (arrow head); (c) Crack went through the Haversian canal with minimum deflection (chevron arrow); (d) Initiation crack was deflected along the cement line (double arrows) as observed from longitudinal section for 0° specimen.

5.2.3 Microcracking and unique arc-shaped microcracks

Extensive damage was observed when the tested specimens were sectioned perpendicular to the long axes of osteons (Fig. 5.6). The intensity and distribution of microcracks stained by fluorescein depended on specimen orientation. In the 0° specimens, damage over the entire section

surface was homogeneously distributed (Fig. 5.6a). On the contrary, 30°, 60° (Fig. 5.6b) and 90° specimens displayed damage that was localized near the main fractures.

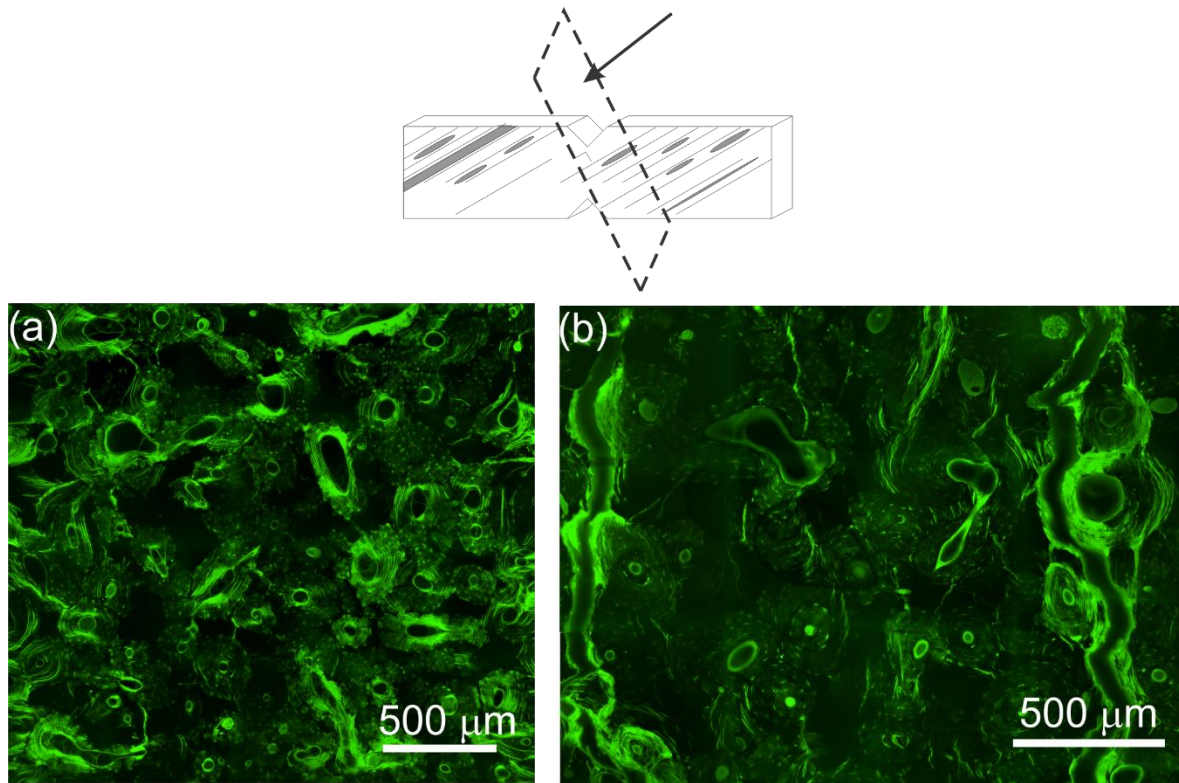


Fig. 5. 6 Laser scanning confocal microscopy (LSCM) images showing microcracks distribution in the gauge sections. The obtained cross-sections were all cut perpendicular to the osteons' long axis (indicated by grey lines) for analysis as shown in the schematic illustration. (a) and (b) show the representative damage patterns for 0° and 60° specimens, respectively.

At higher magnification, six types of microcracks were identified based on their location and shape: 1) osteonal peripheral arc-shaped cracks (Fig. 5.7b) that were usually located away from the Haversian canals and followed the general contour of the lamellar boundaries; 2) osteonal tensile cracks; 3) osteonal radial cracks (Fig. S5.3d); 4) cement line cracks (Fig. S5.3b); 5) interstitial arc-shaped cracks; 6) interstitial tensile cracks. Arc-shaped cracks clearly differed from compressive cross-hatched cracks and tensile wavy cracks in that they were linear and long microcracks often constrained within a lamella without crossing its boundaries. The 3D imaging

with LSCM (Fig. 5.7b) showed that arc-shaped cracks had a “linear” appearance through the depth (z-plane), and stayed within the same lamellae. There were subtle variations in sub-micron morphology among the arc-shaped cracks: some appeared to be smoother, while others had regular crossed-lines or feather-like fine branches. Fig. 5.8a shows the frequency of osteons showing each type of crack. Only the osteons at early stage of damage (less than ten microcracks with a length longer than 10 μm) were counted. Late stage deformation involved a more complicated stress state that might obscure the nature of the microcracking process. The final quantification depends on how many types of crack each osteon had, rather than the exact crack number. It is clear that the majority (over 80 %) of osteons at early stage of damage showed arc-shaped cracks.

When LSCM was used to examine longitudinal surfaces, there was no extensive damage at low magnification compared with the transverse sectional analysis. The longitudinal planes ground and polished to the centre of the three 0° specimens showed similar sparse-distributed damages. However, localized long and straight (linear) microcracks within bone lamellae at higher magnifications were observed, corresponding to the z-plane view when using 3D scanning on the transverse sections (Fig. 5.7b).

5.2.4 Relation between microcracks and bone lamellae

Arc-shaped microcracks were the dominant crack type. Therefore, the location of these microcracks were further analyzed in terms of lamellar structure inside the osteons. Five potential locations were defined: P1-at Haversian canal, P2-inner third of the osteonal wall, P3-middle third of the osteonal wall, P4-outer third of osteonal wall and P5-at cement line. The occurrence frequency of microcracking at these locations was shown in Fig. 5.8b. Briefly, over 70 % of arc-shaped microcracks were located in the outer third of osteonal wall (i.e. peripheral layers of the osteonal wall).

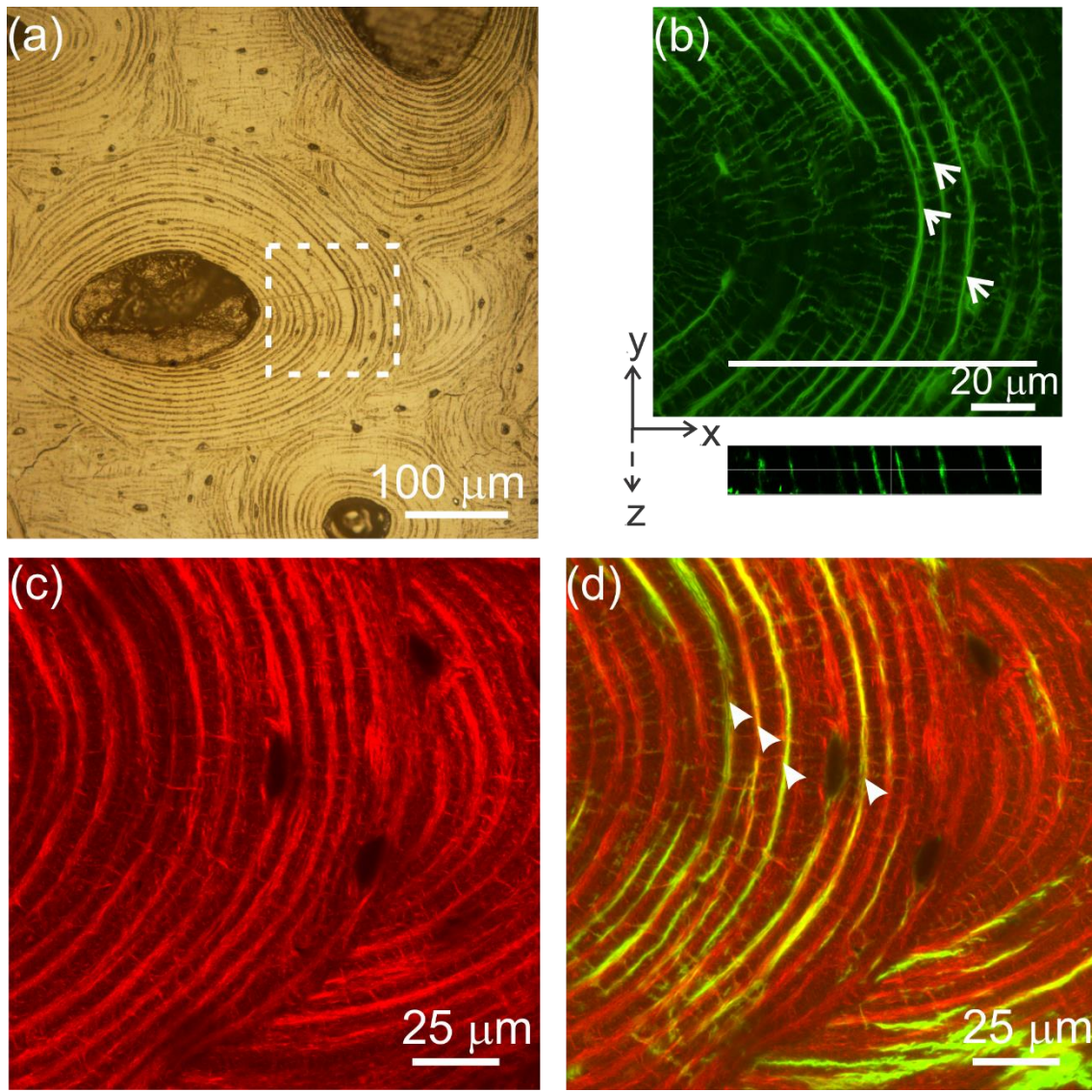


Fig. 5. 7 Unique microcracking pattern under shear: (a) OM image showing the lamellar structure (i.e. 0°); (b) High resolution LSCM image taken from the right side of the central osteon (dotted line) in (a). a unique peripheral arc-shaped pattern (arrows) is located at the peripheral zone of the osteon. They appear as linear microcracks on the z-plane (“cut views” at locations shown by white lines); (c) High resolution second harmonic generation (SHG) image taken from the right bottom corner in (b) showing the osteon consisting of bright and dark lamellar layers. Note that in the bright layer, the collagen fibrils are mainly lying circumferential to the osteons, while the collagens mostly align along the osteons in the dark layer; (d) Combined SHG and two photon excitation fluorescence (TPEF) image directly associating arc-shaped microcracks (arrow heads) with osteonal lamellae.

The preferred orientation of collagen fibrils in each bone lamella can be assessed using SHG. The SHG image of a typical osteon is of alternating thin and thick lamellae reflecting

different SHG signal intensities (Fig. 5.7c). On a transvers section, collagen fibrils in the “bright” layers are oriented circumferentially around the Haversian canal, while those in the “dark” layers are preferentially aligned with the long axis of the osteon [97,261]. TPEF image provides information about microcracking similar to what was obtained using LSCM (Fig. 5.7d, green signal). The SHG image of collagen fibrils overlaid with the TPEF image of stained microcracks enabled me to directly relate shear microcracks with the different osteonal lamellae (Fig. 5.7d). The arc-shaped cracks' association with lamellae of the early-damaged osteons showed variations among different orientations: 0°, 30° and 90° specimens showed the confinement mainly in “bright” lamellae, while 60° specimens had more cracks in the “dark” lamellae (Fig. 5.8b).

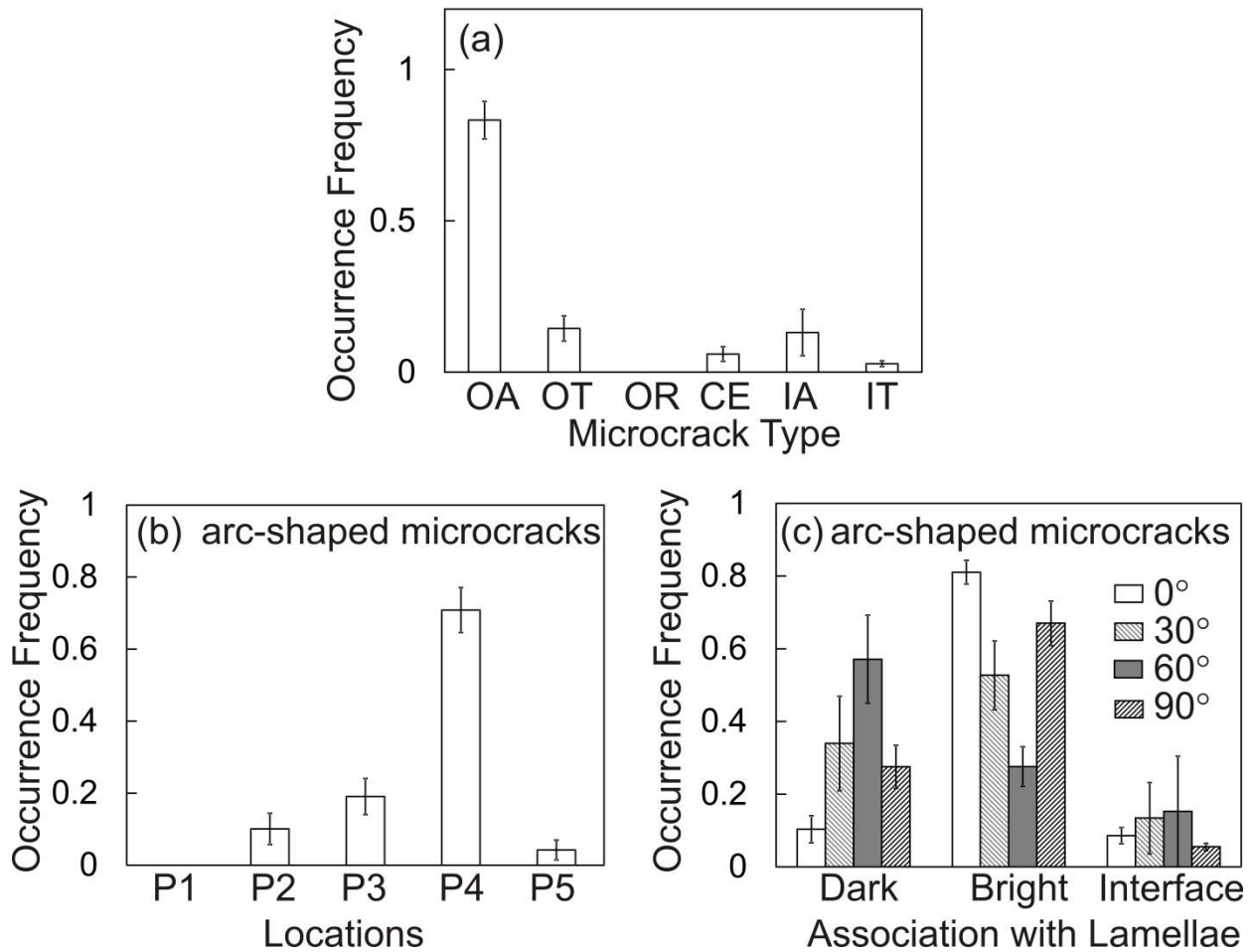


Fig. 5. 8 Quantitative analysis on the microcracks created under shear. More than forty osteons from each orientation at early stage of damage were analyzed. (a) Summary of occurrence frequency of six types of microcracks: osteonal arc-shaped (OA); osteonal tensile (OT); osteonal radial (OR); cement line (CE); interstitial arc-shaped (IA) and interstitial tensile (IT); (b) Frequency distribution of the location of arc-shaped microcrack initiation. The osteon was divided into five locations: at the Haversian canal (P1); inner third of the osteonal wall (P2); middle third of the osteonal wall (P3); outer third of the osteonal wall (P4) and at the cement line (P5). (c) Arc-shaped microcracks' association with lamellar structure (i.e. “bright”/ “dark” lamellae and interlamellar area).

5.3 Discussion

This study demonstrated that human cortical bone under shear is anisotropic in its deformation and fracture processes. Accompanying the inelastic deformation is a unique arc-shaped microcracking pattern. High resolution combined analyses using second harmonic

generation and two-photon excitation fluorescence clearly illustrated the important role for Haversian lamellae in the microcracking process.

5.3.1 The anisotropic shear behavior and the structural effects on fracture

That orientation dependence of the mechanical properties of cortical bone is well known when loading in tension [262,263] and compression [145]. Fewer studies have focused on the role of shear stress on bone's yield and ultimate failure mechanics. Turner et al. [187] reported Iosipescu shear strength against the long bone axis to be $65.3 \text{ MPa} \pm 2.5 \text{ MPa}$, and Winwood et al. [249] reported that along the long bone axis to be 15 MPa-40 MPa. Four different shear angles were evaluated and confirmed that shear properties of human cortical bone are anisotropic. Shear strength and modulus in the transverse direction (shearing perpendicular to osteons' long axes in 0° specimens) were higher than that at other orientations (Table 5.1), and the magnitudes were in reasonable concordance with those reported by Winwood [249]. The 0° specimens also demonstrated a much longer inelastic deformation stage (Fig. 5.2b). Bone can be viewed as a nano-fibre composite with mineralized collagen fibrils predominantly organized along the general direction of the long bone axis. Therefore, mechanical anisotropy may be explained using mechanisms that govern the mechanical anisotropy of engineering fibre reinforced matrix composites [54,92,264–266]. Similar to fibre composites, inter-fibril shear damage or cracks may occur in bone during the inelastic deformation stage. When bone was sheared perpendicular to its long axis (i.e. 0° specimens), mineralized collagen fibrils would bridge the inter-fibrous cracks and prevent them from developing into a major fracture, leading to higher strength and strain to failure than noted in other specimen orientations. Since bone can be viewed as composite material, but exhibits more complicated structural organizations at multiple length scales, the cracking and deformation processes would likely be more complicated than those in fibre composites. Research

on bone's microstructural elements such as bone lamellae, cement lines, and Haversian canals is needed to further clarify their roles in physiologic and failure loading regimes.

The influence of the structural organization and anisotropy of osteons on the bone specimens' deformation process is evident in the shear strain patterns that developed at the inelastic deformation stage. DIC analysis revealed localized shear deformation bands at the inelastic stage. Interestingly, the strain bands were more or less aligned with the bone's long axis for all specimen orientations (Fig. 5.3, Table 5.1). This suggests a strong structural effect on the deformation process. This localization of shear strain directly leads to similar fracture patterns for 30°, 60° and 90° specimens, which are roughly along the bone's long axis (Fig. 5.4b and d, Table 5.1). The shear bands in 0° specimens could not propagate beyond the gauge section because of a less favorable stress state (the osteons may have acted as “crack arrestors”), and the fractures eventually developed at a larger angle (Fig. 5.4a, Table 5.1), due to the principal stress in tension.

5.3.2 Shear-induced microcracks: the unique microcracking pattern

Previous studies demonstrated the importance of microcracking patterns as the basis for understanding bone's deformation and fracture processes [102,145,175,179,267]. Compared with tension and compression, studies on shear-induced microcracking have been very limited. Forwood and Parker [268] found cracks in rat tibia created under cyclic torsion running parallel to lamellae. Caler and Carter [269] and George and Vashishth [182] reported long shear microcracks (> 300 μm) under torsional loading with no or little diffuse damage. Vashishth et al. [270,271] also described torsion created shear cracks as longitudinal linear cracks. Despite these reports, the nature of shear-induced microcracking at the lamellar and sub-lamellar levels remains largely unknown. The study showed that arc-shaped microcracks located at the peripheral zone of the osteons (Fig. 5.7b) are the dominant patterns of shear-induced damage. They clearly differed from

the reported densely distributed “wavy microcracks” for tension and the “cross-hatched” compression cracks. These differences suggest the influence of the sub-lamellar structure (i.e. the collagen fibril bundles organization) on the microcracking pattern. Sectional analysis under confocal microscopy (Fig. 5.7b) found that the arc-shaped cracks propagated around the osteons and were confined to a single lamella.

The location where arc-shaped cracks initiated is worth noting. In the literature, the Haversian canal was frequently reported as a stress concentration site [102,272]. In human bone specimens subjected to transversal compression, Ebacher and Wang [145] found that Haversian canals are major strain concentration sites and are directly involved in crack initiation. However, the current study showed that the arc-shaped microcracks caused by shear happened at the peripheral zone of the osteons, closer to the cement line (Fig. 5.8b). This unique microcracking process represents a different crack initiation and propagation mechanism. It appears that Haversian canals no longer play the dominant role under the shear condition. The exact nature of preferred microcracking at the peripheral zone of the osteons is not clear. Within the outer-layered lamellae, some intrinsically weak sites such as osteocyte lacunae and canaliculi could act as crack initiation sites [102,173,180,273]. Indeed, in the LSCM examinations, both osteocyte lacunae and canaliculi sites could act as part of the arc-shaped crack initiation.

5.3.3 Role of osteonal lamellae, collagen fibrils, cement line and lamellar interface

It has been hypothesized that the lamellar structure in osteonal bone plays a critical role in preventing catastrophic failures [54,97,192]. At the micro-level, the osteons are multilayered cylindrical structural units of mineralized fibrils arranged in lamellae around a central Haversian canal. Early studies using polarized light microscopy by Ascenzi and coworkers [93,94] had suggested the existence of three types of osteons: bright (fibres in the lamellae transverse to the

osteon axis), dark (fibres parallel to the axis) and alternating (alternating fibre orientations in adjacent layers), supporting the pioneer work by Gebhardt (1906). In the current study, the majority (about 85 %-90 %) of the osteons in the bone specimens had alternating bright and dark layers under the second harmonic generation microscope. On a transverse section, the bright lamellae were usually thin with collagen fibrils mainly lying circumferential to the long axes of osteons, while the dark lamellae were often thick with collagen fibrils mostly aligning along the long axes (Fig. 5.7). The SHG contrast matches that of alternate osteons under polarized light microscopy [274]. High resolution TEM studies by Weiner and coworkers found that each pair of the alternating layers consisted of five successive layers of parallel fibrils oriented progressively every 30°, forming a rotated plywood structure [51]. Based on the results from X-ray micro diffraction and confocal microscopy, Ascenzi et al. [91] further refined their model. The collagen fibres in the dark layers predominantly form small angles with the osteonal longitudinal axis, while those in the bright layers are predominantly organized at large angles with the osteonal longitudinal axis, i.e. ± 45 with respect to the osteon long axis with smaller amount of fibres perpendicular to the osteon axis. Recent work by Reznikov et al. on the 3D structure using dual-beam microscopy [90] showed that each pair of alternating layers had arrays of collagen fibrils organized into cylindrical rods and these in turn were aligned into higher order plywood structures with angles of 45°-80° between adjacent layers. Disordered collagen fibrils were also present surrounding the ordered structural motif. Many studies investigated the contribution of fibril organization to macroscopic mechanical properties [147,191,275]. Ascenzi and coworkers studied experimentally the role that collagen fibre orientation plays in the mechanical properties of single osteons under various loading conditions including tension [93,276,277], compression [94], torsion [183] and bending [278]. While those studies clearly demonstrated the effects of collagen fibre at a single

osteonal level, directly relating collagen fibrillar organization to microcracking behavior at the tissue level remains a challenge. One innovative part of this study was that it successfully showed the relationship between lamellar structure and microcracking through the layered SHG and TPEF. Under the SHG imaging, alternating bright and dark lamellar layers could be clearly seen (Fig. 5.7c). Simultaneously acquired TPEF signals provide microcrack information of the same region (Fig. 5.7d, green signal). Subsequent quantitative analysis on the arc-shaped microcracks in 0°, 30° and 90° specimens showed that they were preferentially located in the “bright” lamellae (Fig. 5.8c), in which collagen fibrils are aligned circumferential to the long axes of osteons. In a previous study on compression-induced shear cracking of osteonal bone [180], a similar preferential microcracking in a specific layer of the bone lamellae was also observed, although with no direct information on collagen organization. The observed phenomenon can be qualitatively explained using known theory in fibre composites. For 0° and 90° specimens, the circumferential fibrils for the “bright” lamellae would always have a portion of collagen fibrils perpendicular to both components of the shear stress, while the longitudinal fibrils in the “dark” lamellae would always be parallel to one of the shear components. The relation between fibre orientation and stress is very similar to the “inter-laminar shear” described by Evans and Zok on two-dimensional ceramic matrix composites [265]. Inter-fibrillar cracks could evolve without significant interaction with the collagen fibrils in the “bright” lamellae, while in the “dark” lamellae, crack development would be impeded by surrounding collagen fibrils.

Cement lines, outlining secondary osteons, are frequently reported as points of weakness [79,189]. The current study also observed cement lines arresting and deflecting incoming cracks. However, cement line cracks only accounted for ~ 6 % of the early stage developed microcracks, significantly less frequent than intralamellar microcracking (Fig. 5.8a). Additionally, less than 10 %

of the osteons at the main fracture sites had incoming cracks deflected at the cement lines (Table 5.1). Therefore, at least for shear induced deformation and fracture, a role for the cement lines is not as central as a role for bone lamellae.

The interlamellae or lamellar interface, characterized as a transition zone between bone lamellae, is considered as a weak interface where debonding occurs under tensile force [279]. Diab and Vashishth [280] and Jepsen et al. [185] also reported that the lamellar interface damage is the primary cracking site under torsion. Although arc-shaped cracks were observed being located near the lamellar interface, the majority of microcracks were confined within the lamellar layer, i.e. intralamellar cracks (Fig. 5.8c). This was in agreement with previous studies [145,180]. Therefore, the results support the conclusion that intralamellar microcracking is an important mechanism in post-yield deformation of human cortical bone subjected to shear.

5.3.4 Limitations

Finally, the results of this study are limited to small and unbalanced bone specimen sizes. The specimens are also limited to aged group, and the medial quadrant from femoral mid-shaft. Aging has been shown to adversely affect the elastic and ultimate properties of human cortical bone [281]. Studies have also shown that collagen orientation and degree of calcification vary across the quadrants and along the shaft [103,282]. Additionally, the osteon population density and osteon size may also vary due to the different rate of cortical bone turnover and biomechanical loadings [101]. Lamellar thickness on a transverse section is not always an alternating larger and smaller value; the completeness and thickness also vary among and within osteons [106,283]. It would be interesting to see how changes in age and anatomical site affect the shear properties, the microcracking and fracture process.

5.4 Conclusions

This study extended the current literature in two important ways. First, it illustrated how arc-shaped microcracks resulted under shear loading clearly differed from tension and compression microcracks by developing peripherally, following the osteonal contour without coalescing. Second, the combined SHG with TPEF observations of human cortical bone under shear directly related microcracking to the lamellar structures of osteonal bone. This pattern was predominantly correlated with the “bright” layers, where mineralized collagen fibrils are mostly circumferential to the long axes of osteons, when shearing perpendicular to the osteons' long axes. The findings provide new evidence regarding the structural importance of microcracking at the sub-lamellar level of mineralized collagen fibrils, and represent a next step towards better understanding on how microcracks are formed at the ultrastructural level.

Chapter 6 Fracture Mechanisms of Clinical Hip Fractures and the Possible Role of Hypermineralization*

Hip fractures are generally associated with age-related increased propensity to fall, decreases in bone mass, and changes of the bone structural configuration and material properties of the femoral bone tissue [61,81,84,136]. While hip fracture prevention has focused on avoiding falls and increasing bone mineral density, the mechanisms and conditions leading to bone failure at the hip remain unclear. For better hip fracture prevention, it is essential to identify the fundamental failure mechanisms, i.e. stress conditions and associated material failures, involved in hip fractures.

Previous studies on the mechanisms of hip fracture point to two major theories: during a sideways fall on the greater trochanter, the superior femoral cortex is mainly under compression and inferior femoral cortex is predominantly under tension [55,66,144,152,155,160]; substantial cortical bone thinning at the superior side leads to buckling failure rather than longitudinal compression [17,66]. Both theories are based on indirect approaches: commonly used laboratory fall-simulating tests and finite element analysis (FEA) face the challenge of limited possibilities to accomplish *in vivo* verification of the developed models; computer tomography (CT) imaging has low resolution that cannot capture all the changes at tissue level, such as hypermineralization. One promising approach to address these challenges is to directly study clinically retrieved femoral neck components at the tissue-level. Since femoral neck cortical bone can be retrieved at operation for intracapsular hip fracture, it could be used for the study of stress conditions due to the unique correlation between microcrack patterns and different types of stress [102,145,170,171,175], and

*A version of chapter 6 has been published. T. Tang, P. Crompton, P. Guy, H. McKay, R. Wang. (2018) Clinical hip fracture is accompanied by compression induced failure in the superior cortex of the femoral neck. *Bone*. 108:121-131.

for the identification of hypermineralization. Therefore, the aim of this study was to examine the relevant structural features (i.e. hypermineralization) and microcrack patterns in the cortical bone of the femoral neck samples retrieved at surgery as a means to ascertain related fracture mechanisms.

6.1 Experimental

6.1.1 Subjects and samples collection

Patients recruited to this study suffered an intracapsular femoral neck fracture. Intracapsular hip fractures are amongst the most common types of hip fracture [284], and have higher risk of complications [285] and thus offered more possibility of clinically relevant investigation. Femoral neck bone samples from these volunteers were included if they had a complete cortical shell. The 24 fracture cases recruited (23 females, 1 male) were aged 65-96 years (mean 83.3 ± 9.2). The data on sex, age, and the side on which the fracture occurred for each retrieval sample was provided in Table S6.1. All samples were retrieved by a fellowship-trained orthopaedic trauma surgeon (P.G.) during routine hemiarthroplasty surgery. For each sample, the surgical cut was approximately 1 cm-3 cm away (in the lateral direction) from the main fracture surface (Fig. 6.1a and b). All bone tissue was frozen at $-20\text{ }^{\circ}\text{C}$ until specimen preparation. Patients provided informed consent to use their femoral neck material for research; the study was approved by the Clinical Research Ethics Review Board at the University of British Columbia (UBC).

6.1.2 Specimen preparation

To prepare for fracture and microcrack analyses, all the samples were carefully cleaned with a low-pressure water jet and a scalpel to remove bone marrow and attached soft tissue. Subsequently, samples were fixed in 70 % acetone/water solution for 24 h, followed by

dehydration in a graded ethanol series (80 %, 90 %, and 100 %) for 24 h per step, and then stained under vacuum in a filtered saturated solution of fluorescein (Fisher Scientific) dissolved in 70 % ethanol/water, following a procedure described previously [170]. Finally, they were rinsed in 100 % ethanol before being air-dried.

Following staining, samples were examined under a stereomicroscope (Nikon SMZ 1000 or Leica MZ FLIII) to characterize the macro-scale damage and to locate potential sites for microcrack analysis. They were then embedded in epoxy resin (Epothin, Buehler) without prior decalcification. Based on their anatomical orientations, each femoral neck was divided into eight sectors: superior-anterior (SA), superior-central (SC), superior-posterior (SP), posterior (P), inferior-posterior (IP), inferior-central (IC), inferior-anterior (IA), and anterior (A) (Fig. 6.1c). Since previous research suggested that the superior and inferior cortices are the regions experiencing relatively high stresses [66], one section was obtained from each of SA, SC, SP, IP, IC and IA sectors. Subsequently, for each patient, a total of six sections were obtained (one from each region). Each section was prepared parallel to femoral neck axis and normal to the periosteal surface (Fig. 6.1b and c) with a low-speed diamond saw (IsoMet™ 4000, Buehler) and manually ground, using a series of carbide grinding papers, and polished with 6 µm and 1 µm diamond suspensions.

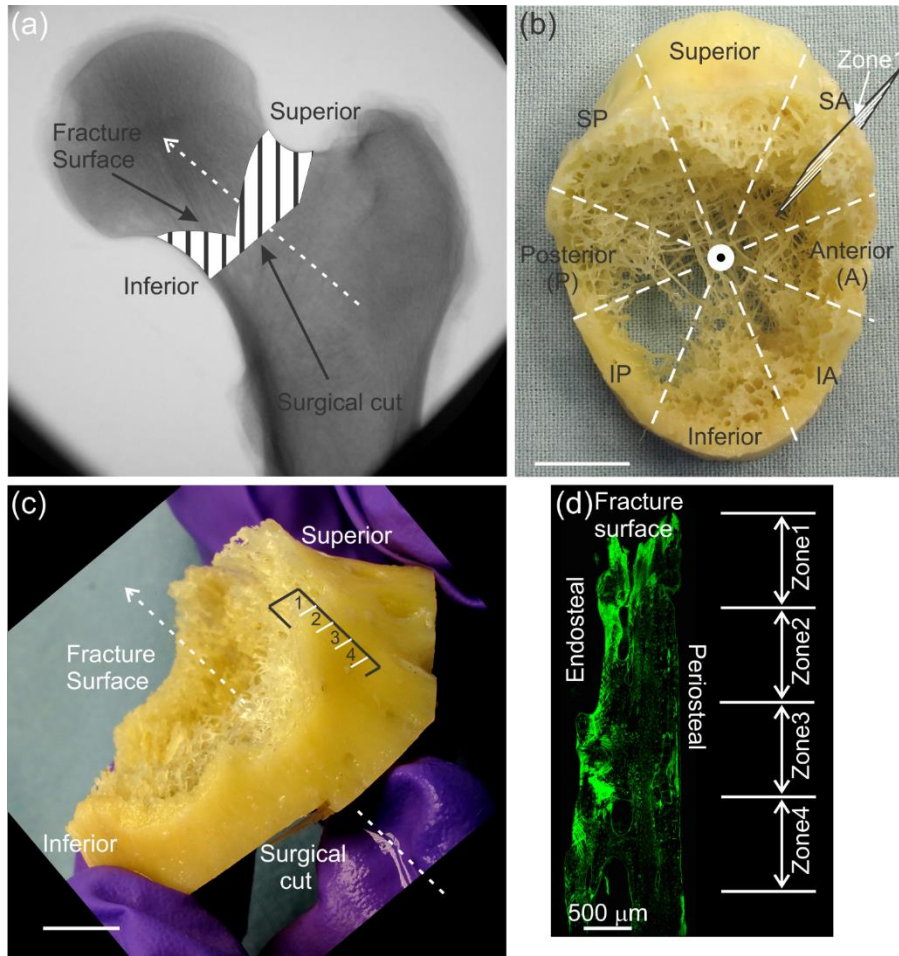


Fig. 6. 1 Proximal femur and surgically removed intracapsular hip fracture samples: (a) X-ray image of a proximal femur showing the region (shaded) from which fractured femoral neck samples were retrieved during surgery. White dashed line with arrow indicated the direction of femoral neck's long axis; (b) Retrieved femoral neck sample in a typical transverse view (plane perpendicular to femoral neck's long axis) showing the eight sectors: superior-central (SC), superior-posterior (SP), posterior (P), inferior-posterior (IP), inferior-central (IC), inferior-anterior (IA), anterior (A) and superior-anterior (SA). In each designated sector, one section was prepared parallel to the femoral neck axis (direction marked by the central circle with a dot) and normal to the periosteal surface. An example was shown by the black frame with white lines indicating the four zones in (d); (c) Retrieved femoral neck sample in a typical anterior-to-posterior view with a surgical cut and the main fracture surface. The black frame represents the same section that is shown in (b), and the four zones are marked by the white lines and the corresponding numbers. The white dashed line with arrow points to the direction of the femoral neck's long axis; (d) A longitudinal cortical bone section, corresponding to the black frame in (b) and (c), shows the stained microcracks in bright green. The region within 4 mm away from the main fracture surface was subdivided into four zones, as shown, and each zone was 1 mm in length. Scale bar in (b) and (c) is 1 cm.

6.1.3 Microcrack analysis

Throughout this manuscript, the word “microcracks” refers to those stained cracks visible under fluorescent microscope but without an apparent crack with two separated surfaces that could be visualised under stereomicroscope [171].

To locate microcracks and observe the associated bone’s microstructure, prepared sections were examined with an optical microscope using reflected white light (Nikon Eclipse E600 or Nikon Epiphot 300) and epi-fluorescence light (Nikon Eclipse E600 with excitation at approximately 490 nm and emission at approximately 525 nm). Fluorescein dye stained the microcracks, which appeared bright green under the fluorescence microscope. Other bone microstructural features, such as osteocyte lacunae, canaliculi and Haversian canals were also visible under fluorescence microscope.

Further observations were conducted under laser scanning confocal microscopes (LSCM; Olympus FluoView FV1000 or Leica TCS SP8, excitation at 488 nm and emission at 519 nm) to identify specific microcrack patterns. In order to capture all the microcracks, a sequence of low magnification images was taken with a 20× objective, starting from the main fracture surface to the region where most apparent microcracks disappeared. The whole procedure was repeated a few times to include both the endosteal and periosteal surfaces of the cortical bone. Images were then merged together using an image processing software (Photoshop Elements 4). The coverage (mm) of the microcracks in the longitudinal direction was quantified within each section (from the main fracture surface to where no apparent microcracks appeared) and most sections showed microcracks within 4 mm away from the main fracture. Subsequently, “4 mm region” was subdivided into four zones; each zone was 1 mm in length (Fig. 6.1d). The amount of microcracks in each zone was categorized as per Currey and Zioupos *et al* [171]. Briefly, a numerical value

was assigned to each zone: 0-no microcracks; 1-very little microcracks; 2-a small amount of microcracks; 3-widespread microcracks. Fig. 6.2 shows regions of interest that represent these four categories. Chi-square test was performed, using the raw data obtained from each zone (i.e. zone 1, 2, 3, and 4 in Fig. 6.1d) at each anatomical location (i.e. SA, SC, SP, IA, IC, and IP in Fig. 6.1b), as a means to strictly test the statistical difference ($p < 0.01$ is considered statistical different). However, Chi-square test was not able to demonstrate where the statistical difference was from (in terms of different anatomical locations). Therefore, based on the recommendation of the study by Currey and Zioupos *et al* [171], for each section, assigned values from the four zones were summed to provide a range of scores from 0 to 12. To examine any differences in the microcrack density between the superior and inferior cortex, the study further summed the values of SA, SC, and SP sections to represent the superior and IA, IC, and IP sections to represent the inferior. subsequently, for either superior or inferior site, the scores ranged from 0 to 36. A larger score represents a higher degree of damage. Further, to examine different types of microcrack patterns, high magnification confocal imaging with a 100× objective was used on selected regions of interest. Morphologies of the microcracks were compared with reported microcrack patterns to find the associate types of stress. For example, compressive microcracks have typical “cross-hatched” pattern, where the microcracks are straight and relatively long; orienting at approximately 27°-40° to the long axis of the bone [102,145,169,170,175,179]. Tensile microcracks are densely distributed wavy microcracks form roughly normal to the direction of the stress with crack length around 2 μm-10 μm [102,175,179]. Shear microcracks are long and linear, and are generally constraint within one layer of the lamellae [286]. The dominant stress state for each section was identified based on the most prominent microcrack pattern and subsequently classified into following categories: longitudinal (parallel to the axis of the femoral neck) compression (i.e. cross-hatched compressive

microcracks across the entire cortical beam), buckling (i.e. periosteal tensile microcracks plus endosteal compressive microcracks), and tension (i.e. mainly tensile microcracks).

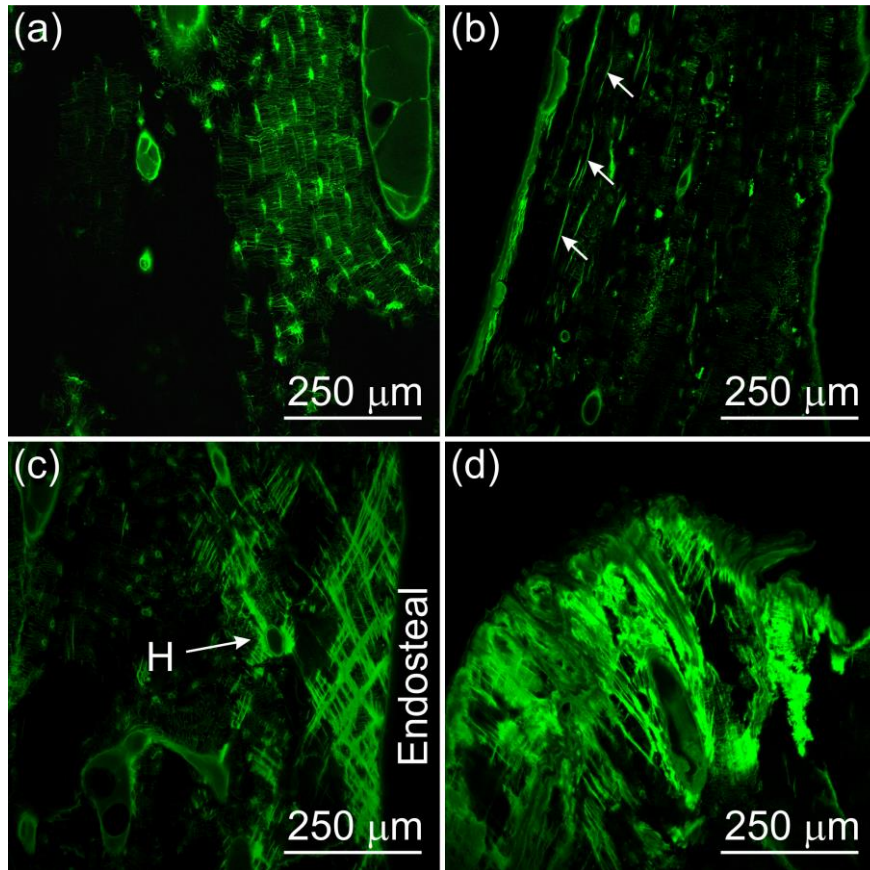


Fig. 6. 2 Typical laser scanning confocal microscope (LSCM) images showing four different levels of amount of microcracks: (a) is the region of interest (ROI) scored as “0” when no microcrack was found in the field of view. Only blood vessel, osteocyte lacunae and canaliculi are visible; (b) The ROI scored as “1” with very little amount of microcracks. Discrete linear interlamellar shear cracks are visible (arrows); (c) The ROI scored as “2” with some microcracks. Cross-hatched compressive microcracks appeared on the endosteal region and around Haversian system (H); (d) The ROI scored as “3” with widely spread microcracks. Some areas are saturated with bright green signals due to the intensive localized microcracking.

6.1.4 Microstructural analysis

All the prepared samples were first examined using reflective light under a white light optical microscope (Nikon Eclipse E600 or Nikon Epiphot 300) equipped with a CCD camera to locate regions of interest and to identify possible hypermineralization based on its morphological

features as described in chapter 3 and 4. All the prepared specimens were further imaged with a variable pressure scanning electron microscope (FEI Quanta 650, Oregon, USA) at 20 kV and 20 Pa in backscattered electron (BSE) mode to verify the existence of hypermineralization. Since the majority of microcracks appeared within 4 mm to the main fracture surface, the study only examined this 4 mm range of the total cortical bone. A few selected specimens were also examined with second harmonic generation (SHG) combined with two-photon excitation fluorescence (TPEF) in a multiphoton microscope (Olympus FV1000 MPE), following the same procedure as described in chapter 5.1.4, as means to directly link local collagen fibril organization to microcracks.

6.2 Results

6.2.1 Macroscopic fracture

Representative macroscopic fracture patterns are shown in Fig. 6.3. Major fracture patterns for all the analysed samples could be found in Fig. S6.1. The main fractures are macroscopically rough and more or less transverse to the long axis of the femoral neck, except for the fractures at the superior-posterior and inferior-posterior sites where they could propagate parallel to the neck axis (e.g. Fig. 6.3a arrows). Although the location of the main fractures along the femoral neck was difficult to define, due to the absence of other fractured components (i.e. femoral head), the fractures at the superior site appeared to be close to the femoral head-neck-junction (subcapital) with thin cortical bone exposed. Subcapital fractures were also observed at the inferior site for most of the samples, with only 9 of 24 samples having the inferior fractures pass through relatively thick mid-neck cortical bone (transcervical fracture).

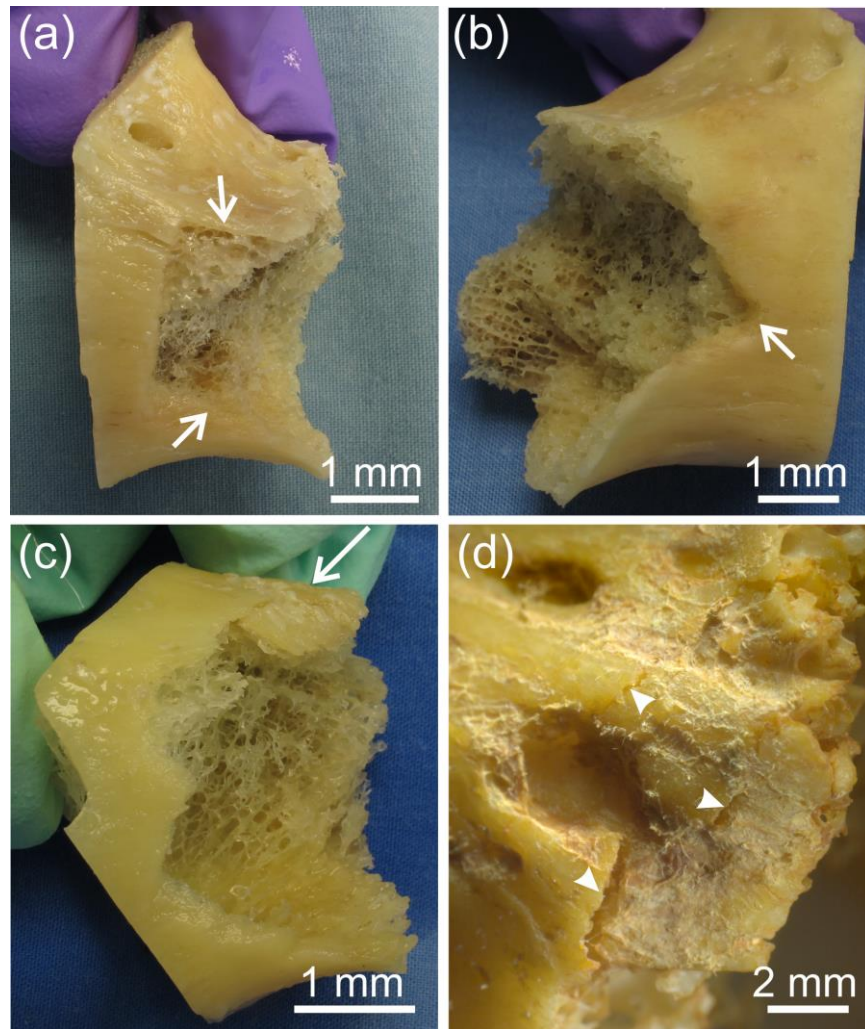


Fig. 6. 3 Retrieved femoral neck samples showing distinctive macroscopic fracture patterns at the posterior site: (a) A retrieval sample showing a typical “U” shape fracture where the main fracture surfaces are parallel to the femoral neck’s long axis at superior-posterior and inferior-posterior sites (pointed by arrows), while the posterior-central fracture is relatively straight, transverse to the femoral neck’s long axis; (b) Representative “V” type fracture is characterized by a sharp turn posteriorly (pointed by arrow) and two oblique cracks at superior-posterior and inferior-posterior sites; (c) Typical “W” shape fracture has a tooth-like fracture at posterior-central, which develops in the transverse direction to the femoral neck’s long axis; (d) A closer look at the superior-posterior site in (c, indicated by arrow) revealed multiple secondary cracks running transverse to the femoral neck’s long axis (arrow heads).

An interesting observation was that the fracture location of the posterior cortex generally appeared more laterally (away from femoral head), and together with fractures at inferior-posterior and superior-posterior sites, they resembled a shape of “U”, “V” or “W”. Particularly, for “U” shape fracture, both inferior-posterior and superior-posterior fracture ledges often run parallel to

the femoral neck axis, forming the two arms of the “U” shape (Fig. 6.3a arrows), and the posterior fracture (bottom of the “U” shape) is oriented in a transverse direction to the neck axis. For both “V” and “W” shapes, fracture was oblique to femoral neck axis at superior-posterior site. While “V” is characterized by a sharp turn formed posteriorly or inferior-posteriorly (Fig. 6.3b arrow), “W” was seen with a tooth-like fracture (bottom of the “W” shape) developed transversely at the posterior site (Fig. 6.3c). The study found that the differences between “U” and “V” type of fractures were more prominent, while some “W” fracture cases were difficult to identify definitively.

Under the stereomicroscope, multiple secondary cracks (i.e. differing from the main fracture surface) were observed in superior region. They were oriented primarily transverse to femoral neck axis (Fig. 6.3d, arrow heads). These opening cracks were usually located 1 mm-4 mm away from the main fractures and occasionally associated with structural porosities (e.g. blood vessels).

6.2.2 The amount of microcracks

In all the observed sections parallel to the long axis of femoral neck, microcracks existed at the main fracture and up to 11.5 mm away from main fracture surface. On average, microcracks were seen up to 3.4 mm away from the main fracture site. Yet, the observed damage was not uniformly distributed along the femoral neck’s long axis. In 120 of 143 analyzed sections, the first 2 mm (i.e. zone 1 and zone 2 in Fig. 6.1d) had the highest microcrack density scores among four zones. In specimens with transverse secondary cracks, highest scores were associated with the zone where a secondary crack was located.

Chi-square test demonstrated a statistical difference ($p < 0.01$) among different zones and locations (Fig. 6.4). By comparing the superior and inferior regions, Fig. 6.5a shows that the

superior cortex has larger amounts of microcracks than that of the inferior site. Specifically, the superior cortex had a median score value of 16 compared to a median score value of 11 in the inferior region. In total, 18 of 24 retrieved femoral neck samples had a higher microcrack density score in the superior region (Fig. 6.5b). The relative amount of microcracks among six regions (i.e. SA, SC, SP, IA, IC and IP) were also compared (Fig. S6.2a). SA, SC and SP regions demonstrated higher scores than did IA, IC and IP regions; however, there was no apparent difference within either superior or inferior region. Further, within each retrieved femoral neck sample, the site with the highest microcrack density score was identified (Fig. S6.2b) to represent the area of the least mechanical competence and theoretically, this was the most likely to initiate fracture. SA was the site that most likely to incur damage with 10 samples showing the highest microcrack density score at SA (comparing with other sections from the same patient), while IP was the region with the lowest chance of generating microcracks (N = 2) (Fig. S6.2b).

Next, due to the distinct macroscopic fracture patterns between “U” and “V”, the study selected six typical samples with clear “U” (N = 3) or “V” (N = 3) patterns and compared microcrack density scores at six anatomical locations (i.e. SA, SC, SP, IA, IC and IP). Microcracks in the “V” type fractured samples tended to centre along the superior-central to inferior-central axis, whereas “U” type fractured samples showed more damage at the anterior cortex (Fig. 6.5c).

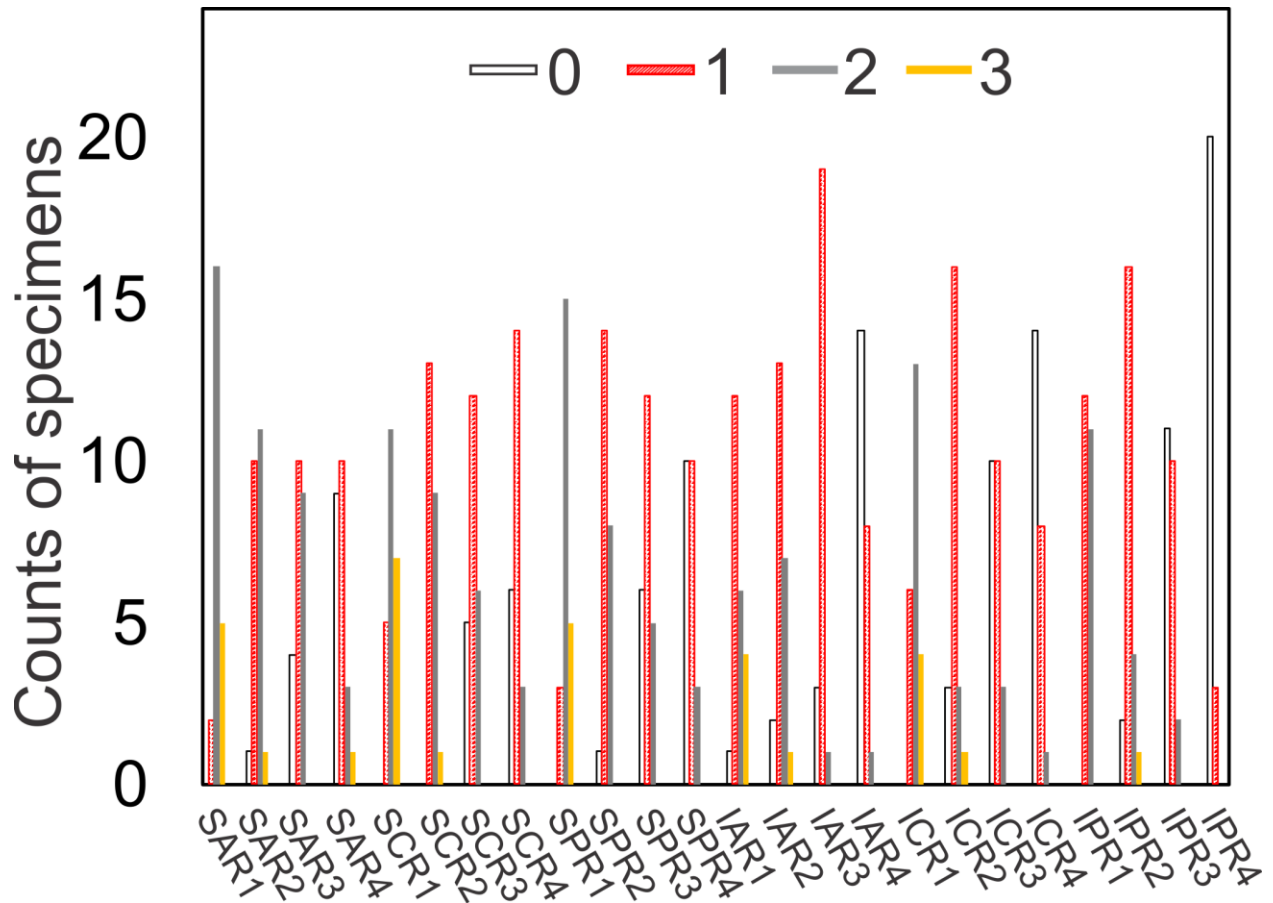


Fig. 6. 4 Chi-square test for the four levels of microcrack density (i.e. score of 0-blank bar, 1-red dashed bar, 2-grey bar, and 3-yellow bar) showed significant difference among difference zones and locations ($p < 0.01$). SA = superior-anterior, SC = superior-central, SP = superior-posterior, IA = inferior-anterior, IC = inferior-central, and IP = inferior-posterior. R1, R2, R3 and R4 represents zone 1, 2, 3, and 4, respectively.

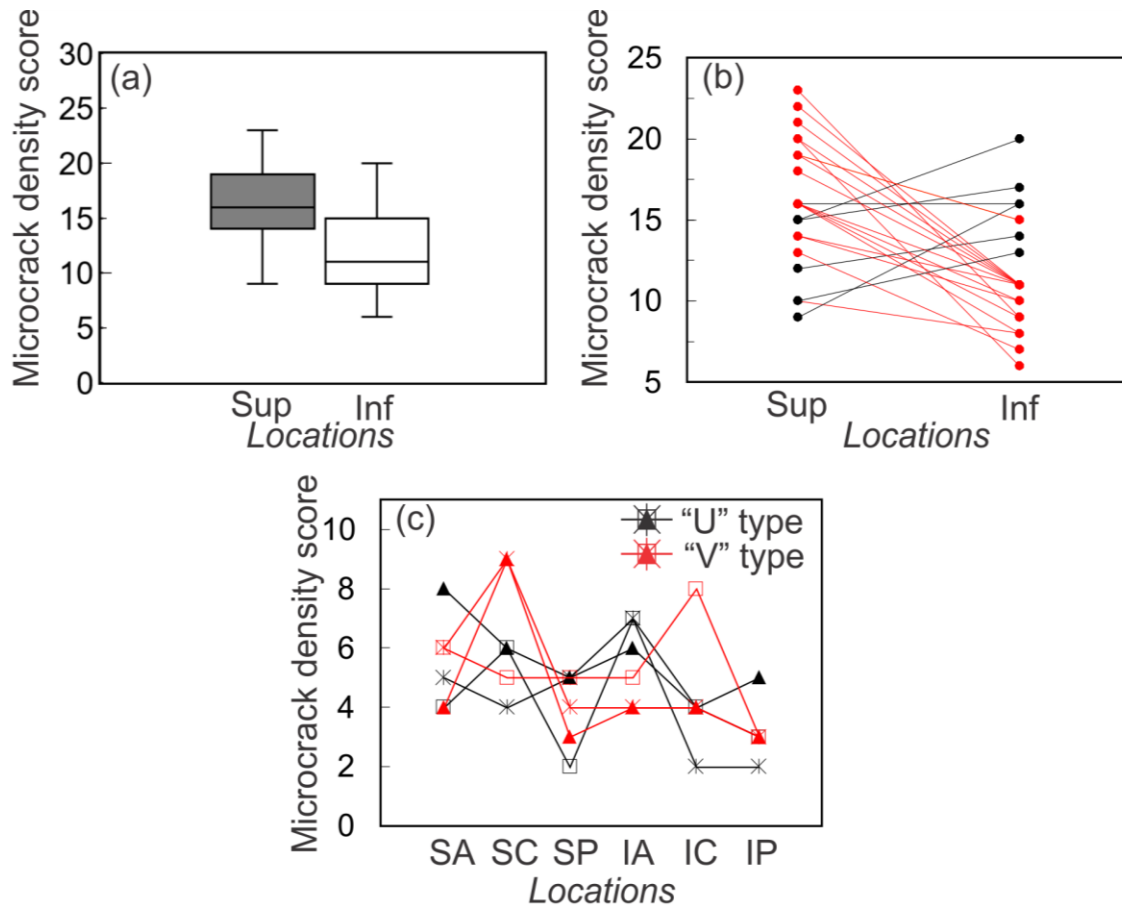


Fig. 6. 5 Microcrack density scores obtained from various locations: (a) Box-plot graph of microcrack density scores versus superior (Sup, grey) and inferior (Inf, white) sites. The shaded boxes represent 50 % of the data, limited by the upper and lower quartiles, with the median indicated by a bar within each box. The vertical bars indicate the range of the data; (b) Superior and inferior microcrack density score within each retrieved sample. 18 of 24 samples had higher score at superior rather than inferior site (indicated by red dots and lines); (c) Microcrack density scores at six sites for three typical “U” and three typical “V” type fractured samples. SA = superior-anterior, SC = superior-central, SP = superior-posterior, IA = inferior-anterior, IC = inferior-central, and IP = inferior-posterior.

6.2.3 Microcrack patterns in normal cortical bone and the dominant stress states

Three typical microcrack patterns (dense and wavy microcracks caused by tensile stress [175], cross-hatched compressive microcracks [145,170] and long, linear shear-induced microcracks [286]) were observed in the retrieval samples. Representative patterns were illustrated in Fig. 6.6. Overall, wavy tensile microcracks and cross-hatched compressive microcracks appeared most frequently. Shear microcracks were often discrete and usually

associated with compressive microcracks. Particularly, in all the analyzed sections, 58 % of them showed microcracking in compression, 34 % in tension and 15 % in shear. In 50 % of examined sections, multiple types of microcracks were observed within one section.

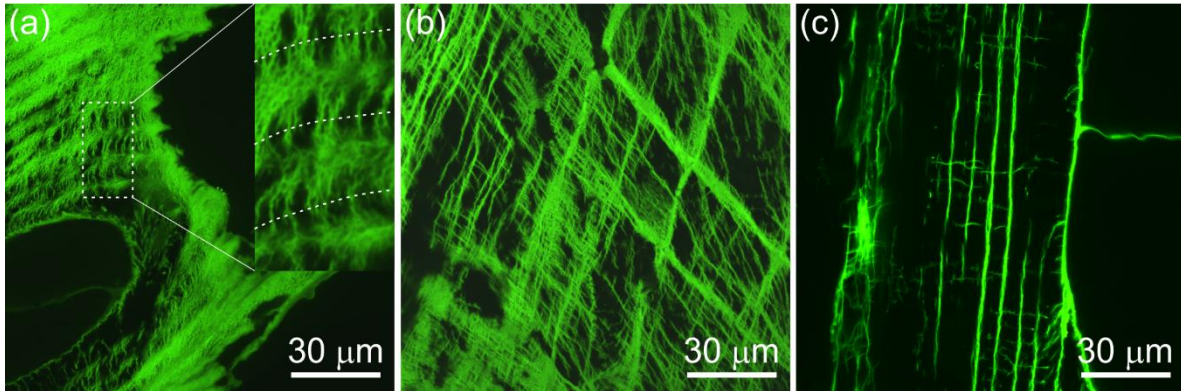


Fig. 6. 6 Representative microcrack patterns found in retrieved femoral neck samples: (a) Tensile microcracks are dense and wavy, running in the direction normal to the “extinct” lamellae [91,106] (indicated by white dashed lines in the upper right insert picture); (b) Compressive straight and relatively long microcracks forming a cross-hatched pattern, oriented at approximately 30° to the long axis of femoral neck; (c) Long and linear shear-induced microcracks running along the direction of the long axis of femoral neck.

Interestingly, 17 of 24 retrieved femoral neck samples showed a unique microcrack pattern with the periosteal under tension and the endosteal under compression at one or multiple anatomical locations (Fig. 6.7). Specifically, at macroscopic-level, the proximal part (right side of the photo in Fig. 6.7a) near the main fracture surface bent towards the endosteal side. High-resolution microcrack analysis revealed localized and intensive tensile microcracks on the periosteal side, associated with a secondary crack (Fig. 6.7b and c). On endosteal cortical bone, extensive cross-hatched compressive microcracks were found. These microcracks extended for approximately 2 mm in a longitudinal orientation with respect to the femoral neck’s long axis (Fig. 6.7d and e). The study categorized such microcrack pattern (endosteal compression and periosteal tension), as buckling.

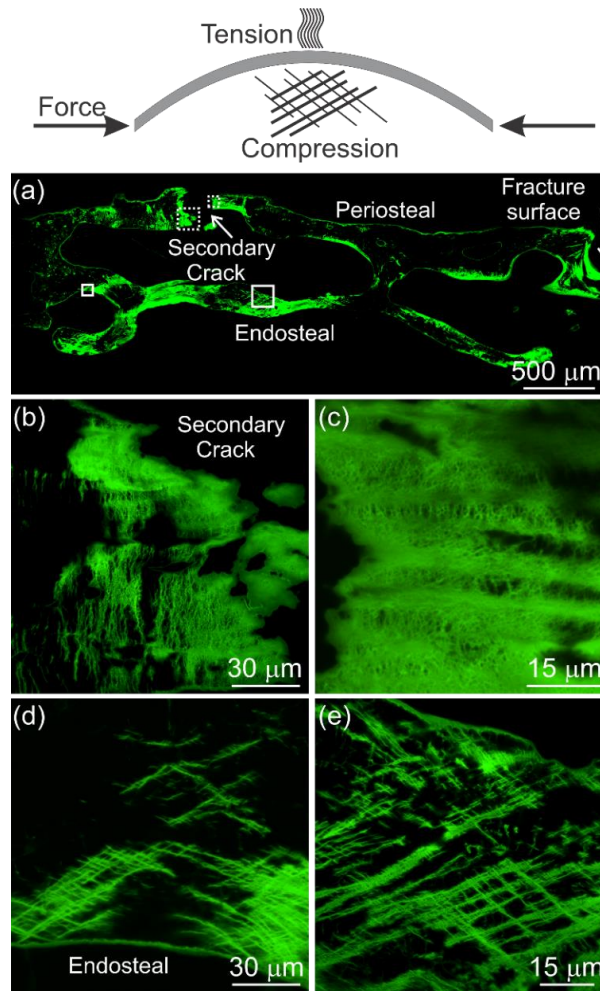


Fig. 6. 7 Schematic diagram showing compression-induced buckling and the representative buckling pattern found at the superior-anterior fracture site: (a) Low magnification confocal imaging of the porous cortical bone showing extensive microcracking at the periosteal and endosteal regions, approximately 3 mm away from fracture surface; (b-c) High magnification confocal imaging of dotted regions in (a) clearly shows dense and wavy tensile microcracks at the secondary crack; (d-e) High magnification confocal imaging at endosteal cortex (white frames in a) showing the straight and relatively long compressive microcracks forming typical cross-hatched pattern. Under macroscopic compression (schematic drawing), this corresponds to a buckling failure.

119 of 143 examined sections showed the dominant microcrack pattern that associated with one of the three types of stress: longitudinal compression, buckling and tension. The rest of the sections had too few microcracks to allow a definitive identification of the stress states. In the superior region (a total of 72 sections), 36 % of specimens were predominantly under longitudinal compression, 31 % showed evidence of buckling and only 14 % were mainly under tension. While

in the inferior region (from a total of 71 sections), the percentages for longitudinal compression, buckling and tension were 15 %, 8 %, and 10 %, respectively. Overall, 18 of 24 (i.e. three-fourths) of the retrieved femoral neck samples demonstrated either longitudinal compression or buckling as the predominant type of stress in the superior region. In particular, buckling failure pattern predominated in SA region; and longitudinal compression appeared most often in SC and SP regions (Fig. 6.8b).

The inferior side of the cortex showed less evidence of a dominant stress state as the microcracks were fewer and tended to be localized. In total, 24 % of the specimens showed oversaturated damage at the fracture surface (Fig. S6.3), which did not allow us to determine the most possible stress conditions related to the fractures. Nevertheless, 13 % of the analyzed specimens at inferior-anterior region, and 17 % of the specimens at inferior-central region appeared to have failed mainly due to tension (Fig. 6.8). Tensile stress was also seen superiorly, but only existed at the macroscopic fracture surface. Surprisingly, extensive compressive microcracks (both longitudinal compression and buckling) were present at the inferior cortex in 14 samples (Fig. 6.8). This differed from the widely-accepted model that suggests tension dominates at the inferior cortex [144].

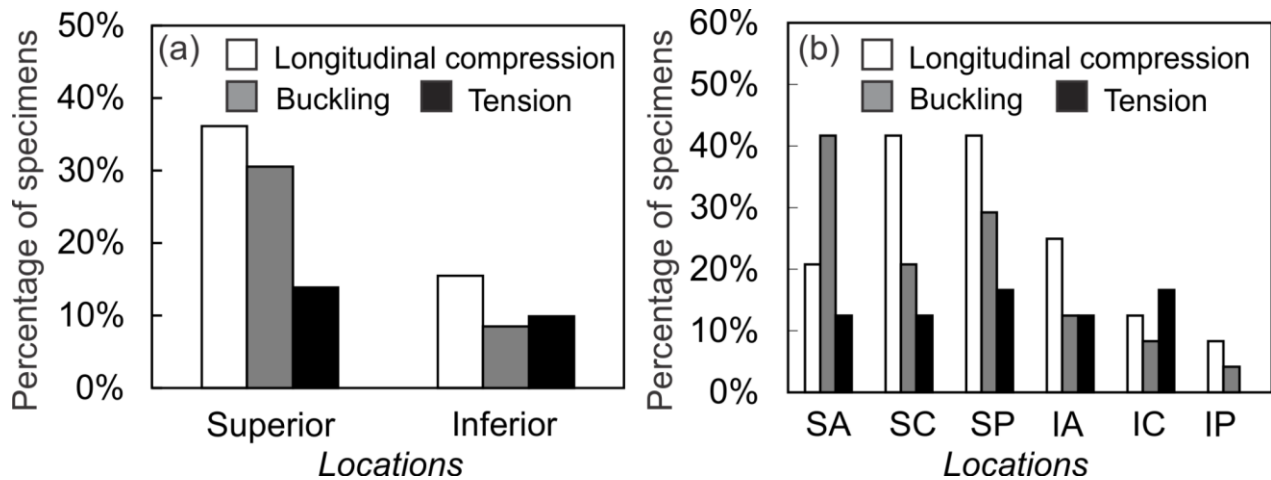


Fig. 6. 8 Percentage of the analyzed sections showing different dominant stress states at various locations: (a) Among all the analyzed sections from superior region (N = 72), 36 % showed longitudinal (along the long axis of femoral neck) compression and 31 % showed patterns resembling a buckling failure. Tension was observed with the lowest percentage at both superior and inferior cortex; (b) The dominant stress states at six sites showed superior-central and superior-posterior cortex were primarily failed by longitudinal compression, and buckling mostly occurred in superior-anterior cortex. For each location, a total of 24 sections were analyzed. SA = superior-anterior, SC = superior-central, SP = superior-posterior, IA = inferior-anterior, IC = inferior-central, and IP = inferior-posterior.

6.2.4 Occurrence of hypermineralization

Morphologically, the appearance of hypermineralization in the clinically retrieved samples resembled the features as observed in chapter 3 and 4 on intact cadaver samples. In particular, clusters of “dense mineral aggregates” associated with hypermineralized periosteum (arrows in Fig. 6.9a), obvious fibrous insertion (Fig. 6.9c), and chondrocyte lacunae (marked by “*” in Fig. 6.9d) associated with hypermineralized fibrocartilage were observed.

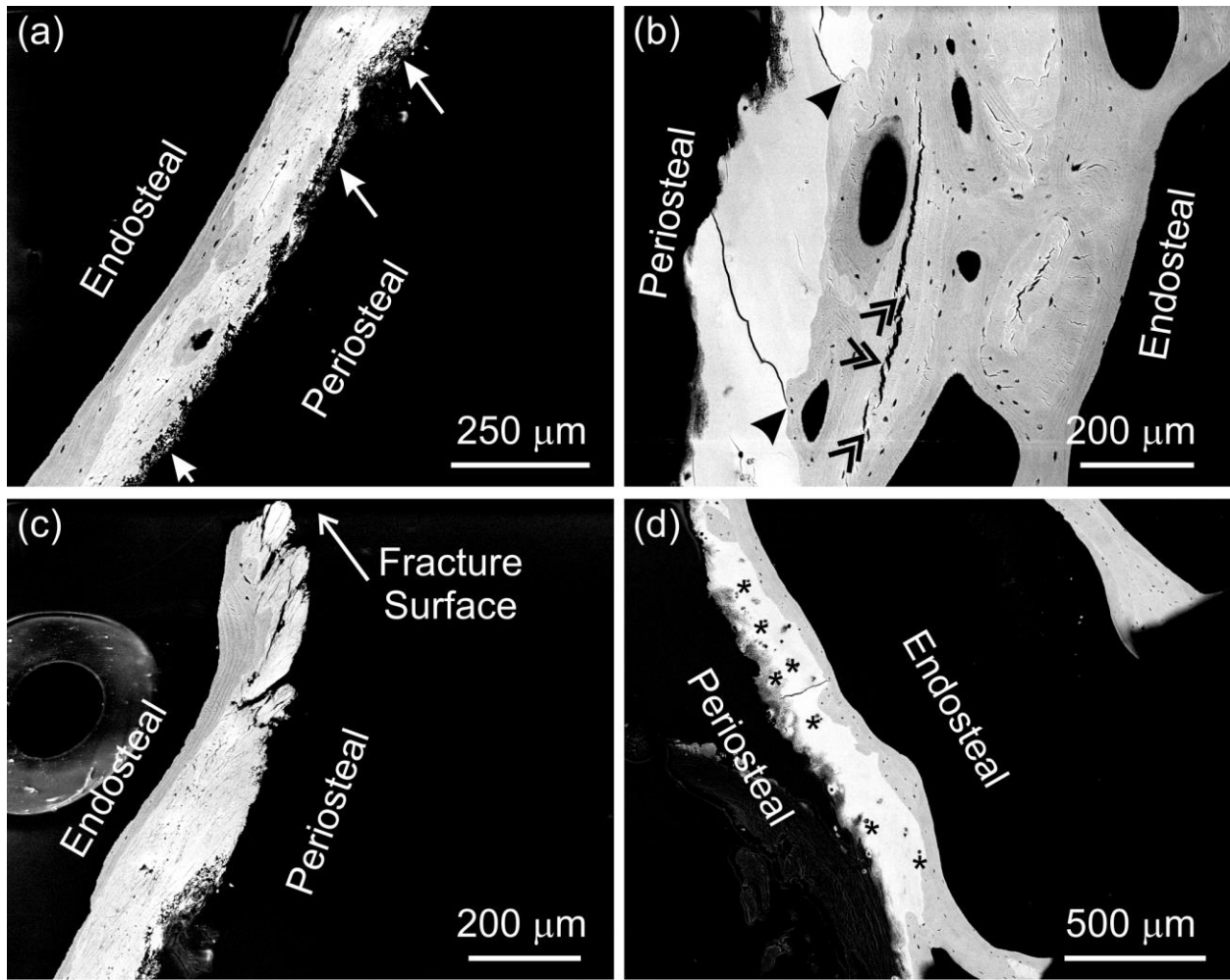


Fig. 6. 9 Hypermineralization in clinically retrieved femoral necks samples: (a) Apparent “mineral clusters” scattering into the periosteal soft tissue (white arrows); (b) Periosteal hypermineralized tissue showing signs of brittleness with cracks formed and developed within the tissue, but stopped by the lamellar bone (black arrow head). Multiple bridging (dark double arrows) could be found in lamellar bone; (c) Hypermineralization with fibrous features was found at the fracture surface; (d) Chondrocytes lacunae (marked by “*”) were also found in some regions of hypermineralization.

By examining the critical 4 mm range to the main fracture surface using SEM/BSE imaging, the study found that more than 50 % of the specimens (N = 143) showed hypermineralization within this region. In particular, as shown in Fig. 6.10 (closed black circles), 92 % of the superior-anterior (SA) specimens (N = 24) have hypermineralization. The occurrence of hypermineralization was also high at superior-central (SC), superior-posterior (SP) and inferior-anterior (IA) aspects (percentages of specimens were 71 %, 58 % and 71 %, respectively). Inferior-

central (IC) and inferior-posterior (IP) had a much lower chance of having hypermineralized tissue (i.e. 21 % and 9 %, respectively). The same trend (i.e. highest at SA, followed by SC, SP, and IA, and lowest at IC and IP) was also seen within the 1 mm zone to the fracture surface (Fig. 6.10 open circles). This finding is consistent with the observations on cadaver femora (chapter 3.2.2), where superior and anterior aspects generally contained more hypermineralized tissue (Fig. 3.3). 16 of the 24 femoral neck samples showed signs of direct involvement of hypermineralization in the fracture process. Comparing the six anatomical locations, superior-anterior and inferior-anterior had relatively higher chance of finding hypermineralized tissue at the fracture surface (Fig. 6.10, marked by “x”). By measuring the thickness ratio between the hypermineralized tissue and the total cortical bone at the fracture site (Fig. 6.10, marked by “x”), superior-anterior and superior-central sites raised particular concerns, as the cortical beam could be fully occupied by hypermineralized tissue (i.e. thickness ratio equals one).

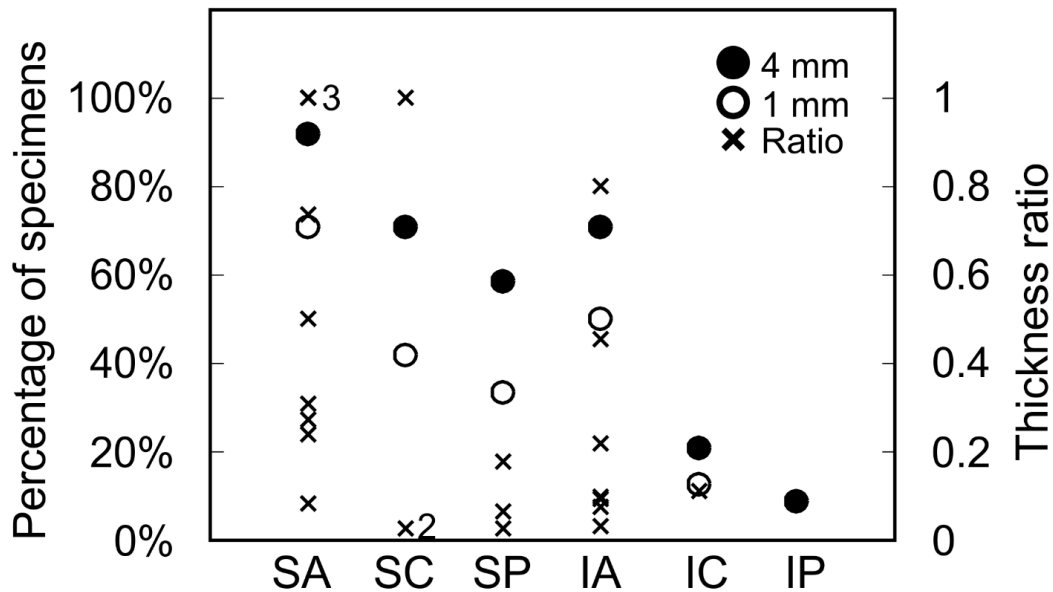


Fig. 6. 10 Percentage of specimens having hypermineralization within 4 mm zone (closed black circles) and 1 mm zone (open circles) to the main fracture surface, and the thickness ratio between hypermineralized tissue and total cortex at the main fracture surface (marked by “x”). The numbers following “x” represent the numbers of specimens having this thickness ratio.

6.2.5 Macro- and micro-cracking in hypermineralized tissue

There is also a clear contrast in the macro- and micro-cracking behavior between the hypermineralized tissue and the lamellar bone. As shown in Fig. 6.9b and Fig. 6.11, the long and more or less straight cracks formed in the hypermineralized tissue. These cracks not only stopped at the boundary of lower mineralized lamellar bone (Fig. 6.9b, arrow head), but also formed a clear contrast with the multiple “bridging” (Fig. 6.9b, double arrows) and “zig-zag” cracking pattern (deflection) in the lamellar bone (Fig. 6.11b, arrow head), where both were found as the toughening mechanisms of lamellar bone [54,190]. Such observation is in line with the findings in cadaver bone, where cracks (due to BSE imaging process) appeared to propagate easily in the hypermineralized zone and generally stopped by the lamellar bone (Fig. 3.2b, arrowheads). Further, SHG combined with TPEF revealed interesting microcracking patterns and the associated collagen organizations in the hypermineralized tissue and the lamellar bone. Fig. 6.12(a-c) clearly shows that the main fracture occurred with limited microcracking (Fig. 6.12c, bright green signals) in the hypermineralized tissue, a sign of reduced fracture resistance, and that there was no apparent collagen fibril organization (no bright red signals) in the hypermineralized zone. In contrast, when the lamellar bone structure was under stress (Fig. 6.12d), extensive microcracks formed in the process zone of the opening cracks, and these microcracks reached a saturated level at the tip of the cracks (Fig. 6.12f). The formation of these microcracks would require a substantial energy, and thus increase the fracture resistance of bone [176]. Note that the cracks in Fig. 6.12a as seen under BSE signal was not shown with fluorescein staining, possibly because they formed later during the SEM imaging process.

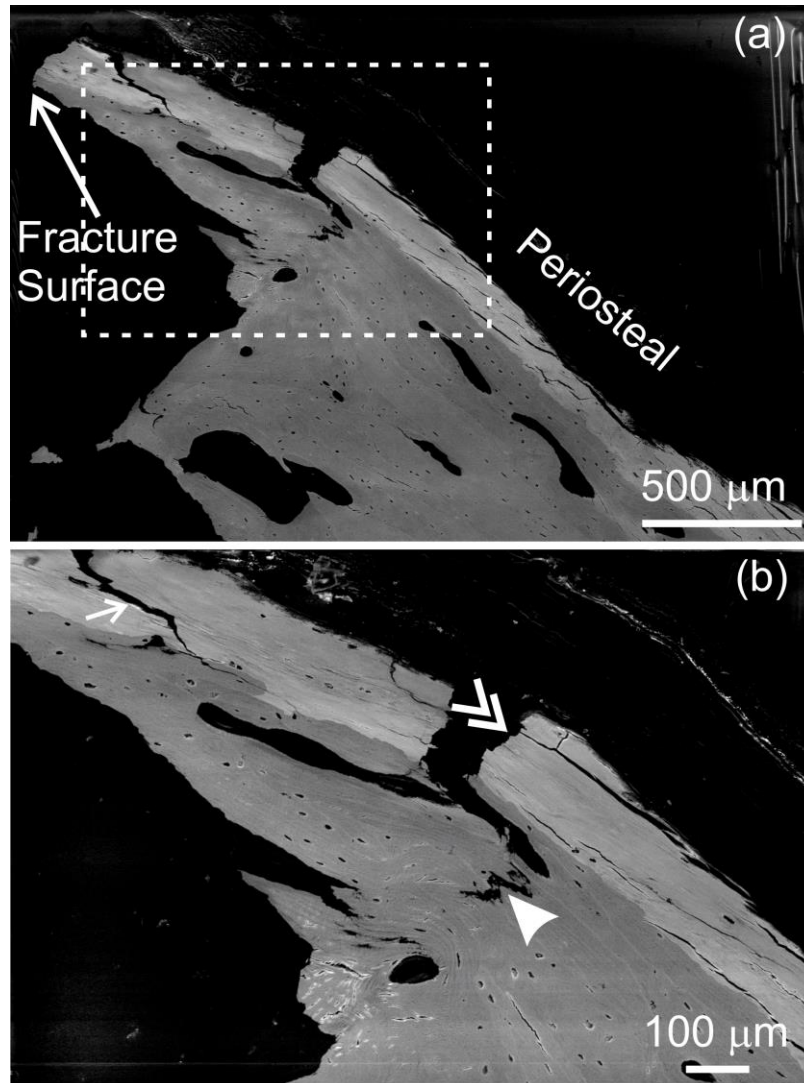


Fig. 6. 11 Fracture and cracking behavior in samples containing hypermineralization: (a) BSE image showing a specimen with hypermineralization at the major fracture surface and secondary crack; (b) Higher magnification BSE image taken from the white dashed frame in (a) showing the different cracking behavior in the hypermineralized tissue and lamellar bone. The crack propagated in a relatively straight path (double arrow heads) in the hypermineralized region, in contrast to the “zig-zag” pattern in the lamellar bone (arrow head). Note that there is also crack deflection in the hypermineralized tissue (arrow), possibly due to the longitudinal oriented matrix.

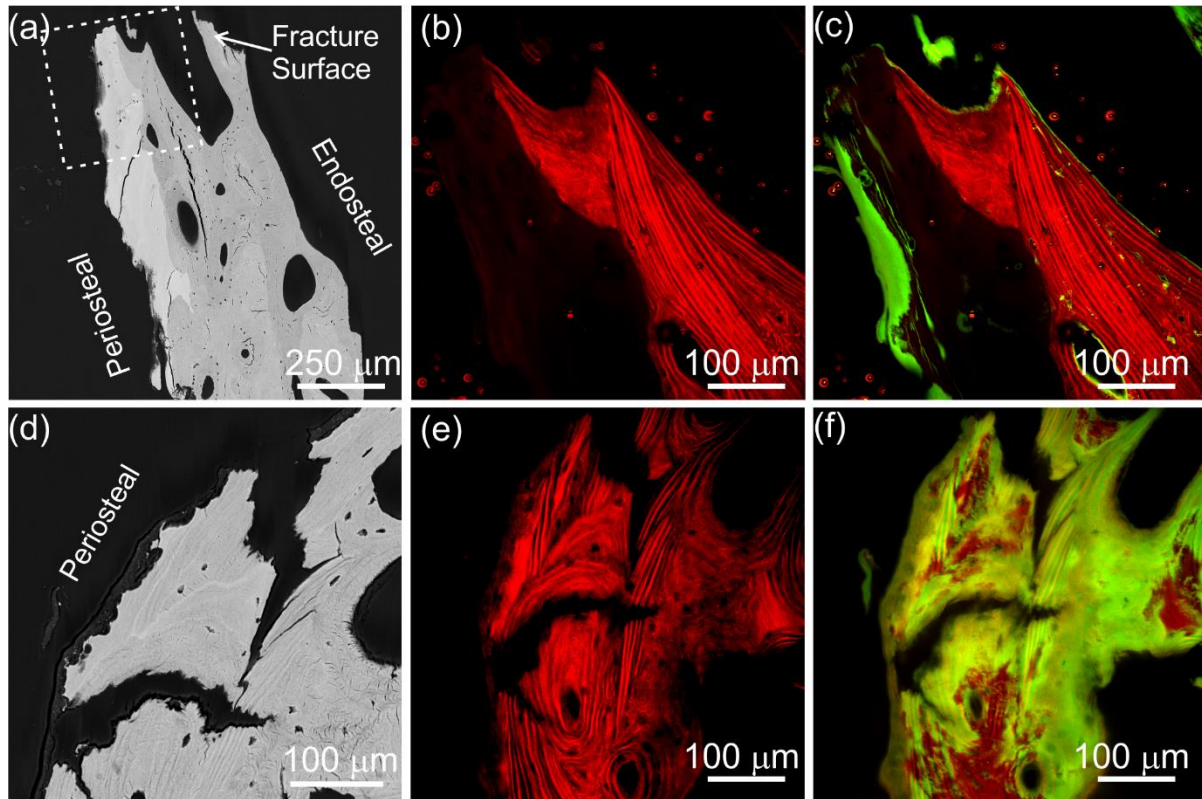


Fig. 6. 12 Microcracks associated with major fractures in the hypermineralized tissue and lamellar bone: (a-c) are images taken at the main fracture surface, while (d-f) were taken at the secondary cracks; (a) BSE image showing the periosteal hypermineralized tissue at the main fracture surface; (b) SHG image taken from the white dashed frame in (a) demonstrating the “non-lamellar” hypermineralized tissue and the lamellar bone; (c) TPEF overlaid SHG signal showing limited microcracking within the hypermineralized tissue; (d) BSE image showing two secondary cracks in lamellar bone; (e) is the corresponding SHG image of (d); (f) Combined SHG and TPEF signals showing extensive microcracks associated with the two major cracks.

6.3 Discussion

This study is the first to investigate cortical bone microcracking and microstructural changes at the fracture site of femoral neck samples retrieved from patients who suffered a hip fracture. In doing so, the study demonstrated that it is feasible to study mechanisms of fracture at femoral neck through analysis of the retrieved samples.

Overall, the superior cortex of the femoral neck experienced a higher degree of damage compared to the inferior cortex. High-resolution confocal microscopy imaging revealed failures

that were likely associated with buckling in cortical bone. By comparing the predominant microcrack patterns from different sites, it clearly illustrated that different stress states occurred at the superior compared to the inferior regions of the femoral neck. The results also highlighted the importance of hypermineralization in the process of the crack initiation and propagation in a femoral neck fracture, and represent a next step towards a better understanding of hip fragility at a fundamental level.

6.3.1 Macroscopic features of clinical hip fractures

It is generally agreed that under a sideways fall configuration, a force roughly perpendicular to the long axis of a femur is delivered to greater trochanter through soft tissue during impact. This creates a bending moment at femoral neck [144]. Clinically, long bone under bending usually creates a “butterfly” fracture pattern consisting of one or two oblique cracks on the compressive side (associated with shear fracture of the bone under compression) and connected to a transverse crack on the other (i.e. tensile) side [287]. Distinct macroscopic fracture patterns were observed in femoral neck that differed from these typical “butterfly” bending fractures. Particularly, fractures in superior-posterior and inferior-posterior regions propagated parallel or oblique to femoral neck axis and formed “U”, “V” or “W” shapes posteriorly (Fig. 6.3a-c). This indicates a more complicated fracture mechanism than pure bending. This is in line with previous investigations of fall-simulating femoral neck fractures using high-speed video [66], where there was a two-phase failure pattern—the first crack initiated superiorly and the second crack started inferiorly. Macroscopic fracture patterns also varied from sample to sample (e.g. distinctive between “U” and “V”). This implies that different mechanisms lead to major fractures, possibly a shift in the impact location or a change in principle stress directions.

When comparing damage distribution between typical “U” and “V” type fractures, the study found a clear shift in the location where microcracks occurred. In the selected “V” type fracture samples, microcracks tended to accumulate at the superior-central or inferior-central regions (Fig. 6.5c). For the three “U” type fracture samples, more damages occurred at superior-anterior or inferior-anterior site (Fig. 6.5c). Such shift implies two-distinct failure modes: a bending moment most likely occurred in frontal plane for “V” type fractures; and a bending moment tilted towards the transverse plane for “U” type fractures. Even though on limited samples, such a potential link is encouraging as it might allow us to understand the direction of impact at fall by analyzing macroscopic fracture patterns. In order to confirm this observation, laboratory controlled tests would be needed to recreate “U”, “V” and “W” shapes by varying loading conditions (e.g. increase/decrease adduction angle) and to assess the association between applied load and fracture patterns. However, “U” type fractures have never been reported in studies that used fall-simulating tests [66,165,288].

6.3.2 Different strain and stress conditions in the superior versus the inferior cortex

Strain distribution in the proximal femur has been extensively studied *ex vivo* using a single leg stance protocol [289–295]. Fewer studies focused on strain levels in the femur during a simulated sideways fall [160,162,163,165,296]. Further, it is not possible to ethically measure stress and strain on human proximal femur during a fall *in vivo*. More microcracks were observed superiorly compared to inferior region (Fig. 6.5a and b, Fig. S6.2a). Specifically, the microcrack density score was 40 % higher at superior surface of femoral neck, on average (Fig. 6.5a). Since post-yield strain is positively associated with microcracks [171], a larger amount of microcracks directly indicates a higher degree of strain or damage experienced by bone tissue during fracture. Higher degree of strain at the superior site also supports a recent DIC analysis, which measured

the surface strain, that showed significant compressive strain at the superior cortex as fracture occurred [165]. Similarly, in a recent study that used fall-simulation, the highest compressive strain at the superior surface was twice as much as the highest tensile strain at the inferior surface [163]. Most previous *ex vivo* fall-simulating studies and FE analysis predicted a broad range of locations where strain concentrates within the proximal femur [163–165,297]. However, by comparing microcrack density score at six anatomical locations within each retrieved femoral neck sample, the study identified superior-anterior site as the most likely to incur damage (Fig. S6.2b). In previous reports, cracks initiated and developed under a simulated sideways fall configuration in the SA region [66]. However, this differed from a previous FE model of a proximal femur under sideways fall where peak strain value was predicted at the SP region of femoral neck [162]. Differences might be partially attributed to limited sample size and testing conditions in the previous study [163].

Femoral neck cortical bone thinning has been shown to be highly relevant to hip fracture in the elderly [81], yet the theory that the cortical bone thinning leads to ultimate buckling failure remains to be confirmed *in vivo*. *Ex vivo* experimental hip fracture proves the probability that buckling could occur in the superolateral cortex with a sideways fall [66]. Post-fracture/*in vivo* studies mostly utilizing radiographic [298] or CT-based 3D model [299] and FEA have been difficult to determine whether buckling had contributed to a clinical fracture, as they require more refinement and verification at individual voxel level, which has not yet been incorporated successfully into FEA modeling of hip fractures. Note that the so-called “buckling ratio” derived from dual energy X-ray absorptiometry (DXA) studies [18] does not reflect the actual load required to cause buckling *in vivo*. In the current post-fracture study, 31 % of specimens (superior region, Fig. 6.8a) demonstrated features of periosteal under tension and endosteal under compression.

Although such a failure pattern could be a result of either local bending or buckling (Fig. 6.7 illustration, structure deflects outward laterally in a bending mode), it is highly likely that the structure buckled under a high compression superimposed bending [66]. The study found such buckling failure pattern was especially common at superior-anterior site (Fig. 6.8b), where cortical bone thinning occurs with ageing [166]. Although the current observation cannot be definitively affirmed as due to buckling, the material level evidence suggests the possibility. Buckling is a compressive phenomenon in essence. During failure dynamics, buckling would rapidly generate very high tensile stresses on the outer curvature of locally bended cortices, causing them to fracture. This might also explain why the periosteal tensile microcracks are often associated with secondary fractures (Fig. 6.7a and b). The observation also provides a rationale as to why the force required to fracture a femur from a sideways fall is lower (by a factor ranging from 2.16 to 4.4 [153]) compared with when the femur is loaded in physiological directions [154]. Buckling failure usually occurs at stresses that are less than the stress under which the material would fail due to yielding or crushing.

Many laboratory stress and strain measurements and FEA models showed that sideways falls involved a stress state reversal to normal gait, with significant compression superimposed on bending [55,66,152,155,160,164,165,297,300–302]. In this study, there was clear evidence of compression-induced microcracks in the superior regions (SA, SC, and SP) (Fig. 6.8b). This observation was in line with classical biomechanical and DIC analysis as well as FE models for sideways falls, where major compressive stresses occurred at superolateral cortices [55,66,155]. However, pure tensile microcracks were less obvious in the inferior region (Fig. 6.8). This could be attributed in part to a two-phase fracture process [66], whereby large deformation occurred before the first crack at superior site was initiated [163,165,296]. Perhaps, a higher strain rate

accompanied the second crack initiated at the inferior site and led to fewer, more localized microcracks at the inferior cortex [171]. It is not clear how pre-existing microcracks caused by normal physiological loading might have affected the cracking process. Interestingly, compressive microcracks including buckling were also present at the inferior cortex (Fig. 6.8). This observation might be explained by a recent FE analysis of the proximal femur under a simulated sideways fall [155], as it found that the compressive stress was dispersed across most of the cortex (including inferior regions) at the femoral head-neck-junction.

6.3.4 The possible role of hypermineralization in clinical hip fracture

So far, hypermineralization at human femoral neck has only been studied in cadaver femora [71–73]. This is the first study that reported its presence and fracture behavior in clinically retrieved samples. Both the presence and the morphological features of the hypermineralized tissue in this study resembled the observations in cadaverous bones (chapter 3 and 4), where superior and anterior aspects of the femoral neck had a higher chance of gathering hypermineralized tissue.

As it has been discussed earlier in this chapter, buckling was seen at superior aspect of the femoral neck, and particularly high at superior-anterior region. Superior-anterior also happens to be the site where more than 90 % of the specimens having hypermineralization within the 4 mm zone to the main fractures (Fig. 6.10, closed black circles). More importantly, in some superior-anterior cortex, the total cortical bone could be fully occupied by the weak hypermineralized microstructure (Fig. 6.10, marked by “×”). For a given cortex thickness and trabecular spacing, the hypermineralized microstructure observed at these sites could lead to early failure of the cortical beam.

One important observation in this study was the associated fracture and microcracking pattern in the hypermineralized zone. In general, there was little deviation in the path of the crack

that was generated from the hypermineralized site until it reached the lamellar bone (Fig. 6.9b and Fig. 6.11). Such a cracking pattern has also been confirmed in the cadaver femora in chapter 3 (Fig. 3.2b). Microcracking is also known to be a critical step in bone deformation, and has been identified as a major toughening mechanism in bone [54,176]. Mechanically, a high microcrack density is a reflection of the inelastic deformation capacity and toughness of the material. Such controlled fracturing process has been clearly shown in the study of chapter 5, where the organized collagen fibres constrained the development of shear microcracks within a specific layer of lamellae. One could also find some clues in the clinical samples consisting of regular lamellar structure: the widespread microcracks spanned the entire cortical beam (Fig. 6.12f). These microcracks are associated with an upper secondary crack that was heavily deflected by the lamellae and a lower secondary crack that had a tortuous path to the endosteal bone. This is a typical example where multiple bone toughening mechanisms (i.e. bone microcracking, crack deflection, bridging) act cooperatively to resist final fractures. In contrast, when hypermineralization was present at the fracture site, limited microcracks were generated in the deformation and fracture process (Fig. 6.12c).

6.3.5 Limitations

Turning to the limitations of this study, first, the study had a small sample size (few sections/specimens for each quadrant), thus the findings cannot be generalized across other specimens or to intact proximal femur. In future, a larger study might be conducted to verify the observations and more aptly identify prominent features related to fracture at femoral neck. That said, these findings shed light upon intracapsular fracture mechanisms *in vivo* at a microscopic level. Second, pre-existing microcracks might present in the retrieved cortical bone tissue, which might interfere with microcrack counting, but not with the recognition of microcrack patterns.

Many studies have shown that pre-existing microcracks have distinct patterns as mostly being long and isolated in interstitial bone [251,279,303–307]. This forms a clear contrast with the tensile, compressive or shear induced microcracks as reported here. And because pre-existing microcracks appear in limited numbers or density [145,279,305,308], it is believed the effect on microcrack counting will be relatively low. Third, the fracture area might undergo additional damage after fracture, which could be attributed to sample retrieval procedure during surgery and patients' post-fracture activity. However, the relatively low stress expected after fracture suggests that post-fracture activities are unlikely to lead to significant microcracks. Fourth, a sample from only one male was included in the current study reflecting the much higher fracture risk in females. There was no obvious difference in microcrack patterns between the male patient and the others. Nevertheless, it would be valuable to study men and women more equally, in future. Fifth, the exact type of impact that led to the current fractures is unknown, but it is believed the samples represent the majority of clinical fractures, which are predominantly failed by low-energy sideways falls. This might explain to certain degree the data variations observed in this study compared to the *ex vivo* fall simulating and FE analysis. Moreover, the link between patient information (i.e. BMD, other metabolic disorders, prior fracture history, etc.) and fracture patterns was not examined in this study. It would however be of great interest to examine such interactions in future. Sixth, the study did not examine how trabecular bone contributes to bone strength at the proximal femur. Further studies might find a way to evaluate the role that trabecular bone plays in fracture, despite the challenges posed by substantial damage that trabecular bone experiences as a result of a fracture. Finally, this study was not able to verify if hypermineralization is responsible for fracture initiation in *in vivo* fractures. Although it is very likely to occur based on the laboratory

characterizations and the observation in clinically retrieved samples, its definite role in hip fragility deserves further in-depth studies.

6.4 Conclusions

This study identified, for the first time, the overall damage distribution and patterns of clinical intracapsular fracture at the femoral neck of the proximal femur. The unique combination of periosteal tensile microcracks and endosteal compressive microcracks offered new insights into the buckling failure at the tissue level. Compression along the long axis of the femoral neck was the dominant stress state at the superior cortex. Yet, compressive microcracks also occurred inferiorly, suggesting the complexity and variability of loading conditions that likely lead to clinical hip fracture. The observations on hypermineralization further confirmed the important role of superior cortex in a clinical hip fracture. A combination of superior cortical thinning and the microstructural changes due to increased amount of hypermineralization could be the source of hip fragility. Therefore, hypermineralization might be a critical factor to be considered in developing prevention and treatment strategies for individuals at a high risk of hip fracture.

Chapter 7 Conclusions and Recommendations

General conclusions

The overall goal of this dissertation was to study the mechanisms of clinical hip fractures in terms of stress states and structural weakness. The findings of this research contributed to both scientific and clinical knowledge. From the scientific perspective, progresses were made in understanding the fundamental changes of periosteal hypermineralized tissue from the materials perspective and at the mineral level. The study provided evidence for reduced fracture resistance of hypermineralization and linked to clinical problems. Substantial insights were gained into shear deformation and fracture in lamellar bone and how the hierarchical structure controlled a stable microcracking process. From the clinical perspective, this research provided direct evidence on how the superior and inferior femoral neck cortex fractured and how hypermineralization was involved in clinical hip fractures.

In chapter 3, the degree of mineralization and the associated mechanical properties of the periosteal hypermineralization were investigated. This hypermineralized tissue has been proposed to reduce the local fracture resistance of femoral cortical bone. However, there is a lack of research to directly quantify its mineral properties and mechanical behavior. To address this issue, qBSE was used to quantify the mineral content of the hypermineralized tissue; microindentation was used to study the cracking behavior and the associated hardness. The results demonstrated that hypermineralization is more prevalent at the superior cortex, with localized regions showing high thickness ratio to total cortical bone. The Ca wt % peak position obtained from the mineralization density distribution curve of the hypermineralized tissue shifted towards the higher range compared with that of the osteonal and interstitial bone. Under microindentation, cracks did form in areas of hypermineralization that had higher hardness values, but not in the lamellar bone. The

inferior mechanical properties of the hypermineralized tissue could be a combined result of the higher degree of mineralization and the interaction between minerals and organic matrix.

Chapter 4 further explored the origin of the higher degree of mineralization through a combination of Raman microspectroscopy imaging, laboratory small-angle X-ray scattering (SAXS), and high resolution small- and wide-angle X-ray scattering (SAXS/WAXS) using synchrotron source. In this chapter, polarized Raman microspectroscopy was performed on cadaver human femoral neck and intertrochanter to characterize the compositions. An increased mineral-to-matrix ratio was found in the hypermineralized tissue, agreeing with the qBSE study in chapter 3. The lack of matrix orientation in the hypermineralized zone was revealed through the polarization effect. The same femoral neck samples were further tested with SAXS/WAXS to determine the mineral size, degree of orientation and spatial organization. The results showed significantly smaller mineral platelets in the hypermineralized tissue compared with normal bone minerals. Another interesting finding was the lack of organization of the minerals in the organic matrix of the hypermineralized tissue. Taken the results from chapter 3 and 4, the significantly higher mineral content in the hypermineralized tissue was due to changes at the ultrastructural level.

Chapter 3 and 4 have implications for the fragility of hypermineralization in clinical hip fractures. They provided fundamental information on how the “material quality” of human femoral cortex changed with ageing. Yet, to understand the mechanisms of hip fracture, we also need to understand the deformation and fracture process of femoral cortical bone under external loading. To do this, we need to fully understand the structure-mechanics relationship of the femoral bone tissue under various loading conditions.

Chapter 5 was aimed to investigate shear deformation and fracture of human cortical bone at the lamellar and sub-lamellar level. Based on biomechanical analysis, shear might be one of the key stress that leads to a clinical hip fracture. However, limited research has been done in this context. To address this issue, Iosipescu shear tests were combined with digital image correlation (DIC) for in-plane shear strain analysis; fluorescein staining was followed by laser scanning confocal microscopy (LSCM) for microcrack imaging. To access the interactions between bone's hierarchical structures and microcracking and deformation processes, integrated second harmonic generation (SHG) and two-photon excitation fluorescence (TPEF) imaging techniques were used to relate the microcracking pattern to bone structures at the sub-lamellar level. The results showed that human cortical bone behaved as an anisotropic material under shear, and that shear strain concentration bands generally followed the long bone axis. The major crack paths also roughly followed the direction of the long axes of osteons. Most importantly, unique peripheral arc-shaped shear microcracks were found developing intralamellar without crossing the boundaries. SHG and TPEF microscopy revealed a strong influence of the organization of collagen fibrils on shear microcracking.

Chapter 3 to 5 built the foundation for chapter 6, where the clinically retrieved femoral neck components were directly examined at the microscopic level. The questions that this study aimed to answer were how femoral cortical bone fractures during the incident and how hypermineralization is involved in the fracture process. The retrieved samples were examined using LSCM after fluorescein staining. The stained microcracks showed significantly higher density in the superior femoral cortex than that at the inferior side, indicating a greater magnitude of strain in the superior femoral neck during the failure-associated deformation and fracture process. The predominant stress state for each sample was reconstructed based on the unique

correlation between the microcrack pattern and the type of stress. The study found longitudinal compression and buckling as the primary stress states in the superior cortex. These findings pointed to the central role of the superior cortex as an important aspect of the failure initiation in clinical intracapsular hip fractures. More importantly, there was clear evidence of the involvement of hypermineralization in clinical fractures. The lack of crack deviation and the limited amount of microcracks associated with the fractures in the hypermineralized zone formed a clear contrast with the tough lamellar bone. Therefore, assessment of hypermineralization at femoral neck cortex could be an important aspect for evaluating hip fracture risk.

There are several strengths of the research in this dissertation. First, synchrotron radiation X-ray scattering measurement does not require invasive sample preparation, and provides high-resolution information at the mineral level. This system also has the advantages of linking particular measurement positions to the information derived from other techniques applied to the same sample. Second, the study combined SHG and TPEF technique to correlate bone's microcracks and collagen fibril orientation at the sub-lamellar level. Although SHG and TPEF have been used for biological and medical imaging for almost two decades, their potential has not been fully explored for imaging bone and microcracking. This combination enabled us to directly “visualize” lamellar bone's structure-mechanics relationship. Third, direct tissue analysis at the fracture sites of clinical samples provides advantages compared to the other indirect approaches, i.e. *ex vivo* fall-simulations, FE modeling and CT imaging. The importance of analyzing clinically retrieved samples have only been realized recently, and fracture analysis on these precious samples can elucidate the fracture mechanisms *in vivo*.

Recommendations for future work

Future work in the following areas is recommended to extend the current studies in this dissertation. First is the detailed investigation of the collagen structure in the hypermineralized tissue. Chapter 3 and 4 in this dissertation focused on the mineral part of the hypermineralization. Collagen, as another primary content of the hypermineralized tissue, could also affect bone strength. It has been shown that in osteoporosis, there is a decrease in the reducible collagen cross-links without an alteration in collagen concentration [309]. Further, in osteogenesis imperfecta patients, it has been demonstrated that there are defects in collagen synthesis and structural alteration [310]. Thus, a detailed histological study on collagen and noncollagenous protein could reveal how and why hypermineralization is formed.

Second interesting area is to visualize the interaction between shear microcracks and the individual mineralized collagen fibril. Currently, the origin of microcracks was mainly based on modeling [146,147] and in-situ mechanical testing with simultaneous synchrotron X-ray scattering measurement [197], both of which are indirect approaches. Super resolution microscopy (e.g. stimulated emission depletion, stochastic optical reconstruction microscopy) can achieve resolutions in the orders of magnitude that are beyond those in conventional optical microscopy (a theoretical resolution of 20 nm-50 nm) [311]. It thus might be helpful to resolve the physical nature of those microcracks at nanoscopic level. The same technique could also be applied to other types of microcracks, i.e. compression and tension, whereby different microcracking mechanisms could be revealed at the finest hierarchical level.

The third area is to investigate the effects of bone's hierarchical structures, such as lamellar morphology and collagen orientation, on the clinical fracture process. Collagen orientation is one of the key structural parameters of human bone that affects the formation and development of

microcracks [273]. Recent reports have shown that parathyroid hormone (PTH) treatment altered the lamellar width distribution in osteoporotic women [312], and that fracturing patients had smaller lamellar width than controls [313]. Collagen orientation might also add to the complexity of the buckling process. For example, results from the animal models [88,101,314–316] and human femoral shaft [93,101,316–318] have demonstrated that transverse (with respect to osteon axis) collagen fibres are most likely to occur in cortices experiencing primarily compression, and that longitudinal (with respect to osteon axis) collagen fibres are more prevalent in cortices primarily under tension. Although the exact collagen organization at superior and inferior femoral cortex is not entirely clear due to the complex loading pattern [104], the superior and inferior cortex could potentially have different collagen orientations, and affect the mechanical response. Further studies can incorporate these analyses to more accurately assess hip fragility.

References

- [1] E.A. Papadimitropoulos, P.C. Coyte, R.G. Josse, C.E. Greenwood, Current and projected rates of hip fracture in Canada, *CMAJ*. 157 (1997) 1357–1363.
- [2] C. Cooper, G. Campion, L.J. Melton, Hip fractures in the elderly: a world-wide projection., *Osteoporos. Int.* 2 (1992) 285–9.
- [3] S. Cummings, L. Melton, Epidemiology and outcomes of osteoporotic fractures, *Lancet*. 359 (2002) 1761–1767. doi:10.1016/S0140-6736(02)08657-9.
- [4] C. a. Brauer, Incidence and Mortality of Hip Fractures in the United States, *Jama*. 302 (2009) 1573. doi:10.1001/jama.2009.1462.
- [5] B. Gullberg, O. Johnell, J.A. Kanis, World-wide projections for hip fracture, *Osteoporos. Int.* 7 (1997) 407–413. doi:10.1007/PL00004148.
- [6] R.S. Braithwaite, N.F. Col, J.B. Wong, Estimating Hip Fracture Morbidity, Mortality and Costs, *J. Am. Geriatr. Soc.* 51 (2003) 364–370.
- [7] J.S. Jensen, J. Bagger, Long-term social prognosis after hip fractures, *Acta Orthop. Scand.* 53 (1982) 97–101.
- [8] O. Johnell, J.A. Kanis, An estimate of the worldwide prevalence, mortality and disability associated with hip fracture, *Osteoporos. Int.* 15 (2004) 897–902. doi:10.1007/s00198-004-1627-0.
- [9] P. Haentjens, J. Magaziner, C.-E.C. Vanderschueren D, K. Milisen, B. Velkeniers, S. Boonen, Meta-analysis: Excess Mortality After Hip Fracture Among Older Women and Men, *Ann. Intern. Med.* 152 (2010) 380–390. doi:10.1059/0003-4819-152-6-201003160-00008.Meta-analysis.
- [10] J. Panula, H. Pihlajamäki, V.M. Mattila, P. Jaatinen, T. Vahlberg, P. Aarnio, Mortality and

- cause of death in hip fracture patients aged 65 or older - a population-based study, *BMC Musculoskelet. Disord.* 12 (2011) 105. doi:10.1186/1471-2474-12-105.
- [11] S.D. Berry, E.J. Samelson, M.T. Hannan, R.R. McLean, M. Lu, L.A. Cupples, M.L. Shaffer, A.L. Beiser, M. Kelly-Hayes, D.P. Kiel, Second hip fracture in older men and women: the Framingham Study., *Arch. Intern. Med.* 167 (2007) 1971–6. doi:10.1001/archinte.167.18.1971.
- [12] H.M. Schrøder, K.K. Petersen, M. Erlandsen, Occurrence and incidence of the second hip fracture, *Clin. Orthop. Relat. Res.* (1993) 166–9.
- [13] F. Formiga, A. Rivera, J.M. Nolla, A. Coscujuela, A. Sole, R. Pujol, Failure to treat osteoporosis and the risk of subsequent fractures in elderly patients with previous hip fracture: a five-year retrospective study, *Aging Clin. Exp. Res.* 17 (2005) 96–9.
- [14] J.A. Kanis, A. Odén, E. V. McCloskey, H. Johansson, D.A. Wahl, C. Cooper, A systematic review of hip fracture incidence and probability of fracture worldwide, *Osteoporos. Int.* 23 (2012) 2239–2256. doi:10.1007/s00198-012-1964-3.
- [15] C.J. Hernandez, T.M. Keaveny, A biomechanical perspective on bone quality, *Bone.* 39 (2006) 1173–1181. doi:10.1016/j.bone.2006.06.001.
- [16] M.L. Bouxsein, Bone quality: where do we go from here?, *Osteoporos. Int.* 14 Suppl 5 (2003) S118-27. doi:10.1007/s00198-003-1489-x.
- [17] P.M. Mayhew, C.D. Thomas, J.G. Clement, N. Loveridge, T.J. Beck, W. Bonfield, C.J. Burgoyne, J. Reeve, Relation between age, femoral neck cortical stability, and hip fracture risk, *Lancet.* 366 (2005) 129–135. doi:10.1016/S0140-6736(05)66870-5.
- [18] S. Kaptoge, T.J. Beck, J. Reeve, K.L. Stone, T.A. Hillier, J.A. Cauley, S.R. Cummings, Prediction of Incident Hip Fracture Risk by Femur Geometry Variables Measured by Hip

- Structural Analysis in the Study of Osteoporotic Fractures, *J. Bone Miner. Res.* 23 (2008) 1892–1904. doi:10.1359/jbmr.080802.
- [19] J.D. Zuckerman, Hip Fracture, *N. Engl. J. Med.* 334 (1996) 1519–1525. doi:10.1056/NEJM199606063342307.
- [20] I. Gilligan, S. Chandraphak, P. Mahakkanukrauh, Femoral neck-shaft angle in humans: variation relating to climate, clothing, lifestyle, sex, age and side, *J. Anat.* 223 (2013) 133–151. doi:10.1111/joa.12073.
- [21] L.E. Thorp, Hip Anatomy, in: *Hip Arthrosc. Hip Jt. Preserv. Surg.*, Springer New York, New York, NY, 2015: pp. 3–15. doi:10.1007/978-1-4614-6965-0_113.
- [22] R.L. Drake, W. Vogl, A.W.M. Mitchell, Lower Limb, in: *Gray's Basic Anat.*, Churchill Livingstone [Imprint], 2012: pp. 265–339.
- [23] S. Haleem, L. Lutchman, R. Mayahi, J.E. Grice, M.J. Parker, Mortality following hip fracture: trends and geographical variations over the last 40 years., *Injury.* 39 (2008) 1157–63. doi:10.1016/j.injury.2008.03.022.
- [24] M.J. Parker, G.A. Pryor, J.K. Anand, R. Lodwick, J.W. Myles, A comparison of presenting characteristics of patients with intracapsular and extracapsular proximal femoral fractures, *J R Soc Med.* 85 (1992) 152–155.
- [25] M.A. Norris, A.A. De Smet, Fractures and dislocations of the hip and femur, *Semin. Roentgenol.* 29 (1994) 100–112. doi:10.1016/S0037-198X(05)80059-8.
- [26] G.S. Keene, M.J. Parker, G. a Pryor, Mortality and morbidity after hip fractures, *BMJ.* 307 (1993) 1248–1250. doi:10.1136/bmj.307.6914.1248.
- [27] R. Cornwall, M.S. Gilbert, K.J. Koval, E. Strauss, A.L. Siu, Functional Outcomes and Mortality Vary among Different Types of Hip Fractures, *Clin. Orthop. Relat. Res.* 425

- (2004) 64–71. doi:10.1097/01.blo.0000132406.37763.b3.
- [28] P. Kannus, J. Parkkari, H. Sievänen, A. Heinonen, I. Vuori, M. Järvinen, Epidemiology of hip fractures, *Bone*. 18 (1996) S57–S63. doi:10.1016/8756-3282(95)00381-9.
- [29] J. Kanis, A. Oden, O. Johnell, Acute and Long-Term Increase in Fracture Risk After Hospitalization for Stroke, *Stroke*. 32 (2001) 702–706. doi:10.1161/01.STR.32.3.702.
- [30] S. Cummings, M. Nevitt, W. Browner, K. Stone, K. Fox, K. Ensrud, J. Cauley, D. Black, T. Vogt, Risk factors for hip fracture in white women, *N. Engl. J. Med.* 332 (1995) 767–773.
- [31] G.S. Cooper, D.P. Sandler, Long-term effects of reproductive-age menstrual cycle patterns on peri- and postmenopausal fracture risk., *Am. J. Epidemiol.* 145 (1997) 804–9.
- [32] J. Kanis, O. Johnell, B. Gullberg, E. Allander, L. Elffors, J. Ranstam, J. Dequeker, G. Dilsen, C. Gennari, A. Lopes Vaz, G. Lyritis, G. Mazzuoli, L. Miravet, M. Passeri, R. Perez Cano, A. Rapado, C. Ribot, Risk factors for hip fracture in men from southern europe: The MEDOS study, *Osteoporos. Int.* 9 (1999) 45–54. doi:10.1007/s001980050115.
- [33] A.H. Holmberg, O. Johnell, P.M. Nilsson, J.Å. Nilsson, G. Berglund, K. Åkesson, Risk factors for hip fractures in a middle-aged population: A study of 33,000 men and women, *Osteoporos. Int.* 16 (2005) 2185–2194. doi:10.1007/s00198-005-2006-1.
- [34] E. Papadimitropoulos, G. Wells, B. Shea, W. Gillespie, B. Weaver, N. Zytaruk, A. Cranney, J. Adachi, P. Tugwell, R. Josse, C. Greenwood, G. Guyatt, VIII: Meta-analysis of the efficacy of vitamin D treatment in preventing osteoporosis in postmenopausal women, *Endocr. Rev.* 23 (2002) 560–569. doi:10.1210/er.2001-8002.
- [35] D.P. Trivedi, R. Doll, K.T. Khaw, Effect of four monthly oral vitamin D3 (cholecalciferol) supplementation on fractures and mortality in men and women living in the community: randomised double blind controlled trial., *BMJ.* 326 (2003) 469.

doi:10.1136/bmj.326.7387.469.

- [36] R. Cumming, R. Klineberg, Fall Frequency and Characteristics and the Risk of Hip Fractures, *J. Am. Geriatr. Soc.* 42 (1994) 774–778.
- [37] L.J. Melton, H.W. Wahner, L.S. Richelson, W.M. O’Fallon, B.L. Riggs, L.J. Melton 3rd, H.W. Wahner, L.S. Richelson, W.M. O’Fallon, B.L. Riggs, Osteoporosis and the risk of hip fracture., *Am. J. Epidemiol.* 124 (1986) 254–61.
- [38] J.A. Grisso, J.L. Kelsey, B.L. Strom, G.Y. Chiu, G. Maislin, L.A. O’Brien, S. Hoffman, F. Kaplan, Risk-factors for falls as a cause of hip fracture in women, *N. Engl. J. Med.* 324 (1991) 1326–1331.
- [39] P. Kannus, P. Leiponen, J. Parkkari, M. Palvanen, M. Järvinen, A sideways fall and hip fracture, *Bone.* 39 (2006) 383–384. doi:10.1016/j.bone.2006.01.148.
- [40] J. Parkkari, P. Kannus, M. Palvanen, A. Natri, J. Vainio, H. Aho, I. Vuori, M. Järvinen, M. Jarvinen, Majority of hip fractures occur as a result of a fall and impact on the greater trochanter of the femur: A prospective controlled hip fracture study with 206 consecutive patients, *Calcif. Tissue Int.* 65 (1999) 183–187. doi:10.1007/s002239900679.
- [41] W.C. Hayes, E.R. Myers, J.N. Morris, T.N. Gerhart, H.S. Yett, L.A. Lipsitz, Impact near the hip dominates fracture risk in elderly nursing home residents who fall, *Calcif. Tissue Int.* 52 (1993) 192–198. doi:10.1007/BF00298717.
- [42] M. Nankaku, H. Kanzaki, T. Tsuboyama, T. Nakamura, Evaluation of hip fracture risk in relation to fall direction, *Osteoporos. Int.* 16 (2005) 1315–1320. doi:10.1007/s00198-005-1843-2.
- [43] A. V. Schwartz, J.L. Kelsey, S. Sidney, J.A. Grisso, Characteristics of falls and risk of hip fracture in elderly men, *Osteoporos. Int.* 8 (1998) 240–246. doi:10.1007/s001980050060.

- [44] S.R. Cummings, M.C. Nevitt, S. Kidd, Forgetting falls. The limited accuracy of recall of falls in the elderly., *J. Am. Geriatr. Soc.* 36 (1988) 613–6.
- [45] L.M. Wagner, E. Capezuti, J.A. Taylor, R.W. Sattin, J.G. Ouslander, Impact of a falls menu-driven incident-reporting system on documentation and quality improvement in nursing homes., *Gerontologist.* 45 (2005) 835–842. doi:45/6/835 [pii].
- [46] &NA;, NIH Consensus Development Panel on Osteoporosis Prevention, Diagnosis, and Therapy, March 7-29, 2000, *South. Med. J.* 94 (2001) 569–573. doi:10.1097/00007611-200194060-00004.
- [47] National Center for Health Statistics, Dual Energy X-ray Absorptiometry (DXA) Procedures Manual, (2007) 115.
- [48] J. Reeve, Role of cortical bone in hip fracture, *Bonekey Rep.* 6 (2017) 867. doi:10.1038/bonekey.2016.82.
- [49] S.C.E. Schuit, M. Van Der Klift, A.E.A.M. Weel, C.E.D.H. De Laet, H. Burger, E. Seeman, A. Hofman, A.G. Uitterlinden, J.P.T.M. Van Leeuwen, H.A.P. Pols, Fracture incidence and association with bone mineral density in elderly men and women: The Rotterdam Study, *Bone.* 34 (2004) 195–202. doi:10.1016/j.bone.2003.10.001.
- [50] T. Aspray, A. Prentice, T. Cole, Y. Sawo, J. Reeve, R. Francis, Low Bone Mineral Content is Common but Osteoporotic Fractures Are Rare in Elderly Rural Gambian Women, *J. Bone Miner. Res.* 11 (1996) 1019–1025.
- [51] S. Weiner, H.D. Wagner, The material bone: Structure mechanical function relations, *Annu. Rev. Mater. Sci.* 28 (1998) 271–298.
- [52] P. Fratzl, R. Weinkamer, Nature’s hierarchical materials, *Prog. Mater. Sci.* 52 (2007) 1263–1334. doi:10.1016/j.pmatsci.2007.06.001.

- [53] J.Y. Rho, L. Kuhn-Spearing, P. Zioupos, Mechanical properties and the hierarchical structure of bone, *Med. Eng. Phys.* 20 (1998) 92–102. doi:S1350453398000071 [pii].
- [54] R. Wang, H.S. Gupta, Deformation and Fracture Mechanisms of Bone and Nacre, *Annu. Rev. Mater. Res.* 41 (2011) 41–73.
- [55] S. Nawathe, H. Akhlaghpour, M.L. Bouxsein, T.M. Keaveny, Microstructural Failure Mechanisms in the Human Proximal Femur for Sideways Fall Loading, *J. Bone Miner. Res.* 29 (2014) 507–515. doi:10.1002/jbmr.2033.
- [56] R.B. Martin, D.B. Burr, N.A. Sharkey, D.P. Fyhrie, *Skeletal Tissue Mechanics*, Springer New York, New York, NY, 2015. doi:10.1007/978-1-4939-3002-9.
- [57] J.D. Currey, *Bones: Structure and Mechanics*, Princeton Univ. Press, Princeton, NJ, 2002.
- [58] K.L. Bell, N. Loveridge, J. Power, N. Garrahan, B.F. Meggitt, J. Reeve, Regional differences in cortical porosity in the fractured femoral neck, *Bone*. 24 (1999) 57–64. doi:10.1016/S8756-3282(98)00143-4.
- [59] K.L. Bell, N. Loveridge, J. Power, N. Rushton, J. Reeve, Intracapsular hip fracture: Increased cortical remodeling in the thinned and porous anterior region of the femoral neck, *Osteoporos. Int.* 10 (1999) 248–257. doi:10.1007/s001980050223.
- [60] K.L. Bell, N. Loveridge, G.R. Jordan, J. Power, C.R. Constant, J. Reeve, A novel mechanism for induction of increased cortical porosity in cases of intracapsular hip fracture, *Bone*. 27 (2000) 297–304.
- [61] R.J.F. M.L.Bouxsein, E.S. R.M.D.Zebaze, M.L. Bouxsein, R.J. Fajardo, T. Sugiyama, T. Taguchi, E.S. R.M.D.Zebaze, R.J.F. M.L.Bouxsein, T. Sugiyama, T. Taguchi, J. Reeve, P.M. Mayhew, C.D. Thomas, N. Loveridge, C.J. Burgoyne, Cortical stability of the femoral neck and hip fracture risk., *Lancet*. 366 (2005) 1523–1524. doi:10.1016/S0140-

6736(05)67621-0.

- [62] K.L. Bell, N. Loveridge, J. Power, N. Garrahan, M. Stanton, M. Lunt, B.F. Meggitt, J. Reeve, Structure of the Femoral Neck in Hip Fracture: Cortical Bone Loss in the Inferoanterior to Superoposterior Axis, *J. Bone Miner. Res.* 14 (1999) 111–119. doi:10.1359/jbmr.1999.14.1.111.
- [63] N. Crabtree, N. Loveridge, M. Parker, N. Rushton, J. Power, K.L. Bell, T.J. Beck, J. Reeve, Intracapsular hip fracture and the region-specific loss of cortical bone: analysis by peripheral quantitative computed tomography., *J. Bone Miner. Res.* 16 (2001) 1318–1328. doi:10.1359/jbmr.2001.16.7.1318.
- [64] K.E.S. Poole, G.M. Treece, P.M. Mayhew, J. Vaculík, P. Dungal, M. Horák, J.J. Štěpán, A.H. Gee, Cortical thickness mapping to identify focal osteoporosis in patients with hip fracture, *PLoS One.* 7 (2012) 1–7. doi:10.1371/journal.pone.0038466.
- [65] K.E.S.S. Poole, L. Skingle, A.H. Gee, T.D. Turmezei, F. Johannesdottir, K. Blesic, C. Rose, M. Vindlacheruvu, S. Donell, J. Vaculik, P. Dungal, M. Horak, J.J. Stepan, J. Reeve, G.M. Treece, Focal osteoporosis defects play a key role in hip fracture, *Bone.* 94 (2017) 124–134. doi:http://dx.doi.org/10.1016/j.bone.2016.10.020.
- [66] P.M. de Bakker, S.L. Manske, V. Ebacher, T.R. Oxland, P. a. Crompton, P. Guy, During sideways falls proximal femur fractures initiate in the superolateral cortex: Evidence from high-speed video of simulated fractures, *J. Biomech.* 42 (2009) 1917–1925. doi:10.1016/j.jbiomech.2009.05.001.
- [67] C.D. Thomas, P.M. Mayhew, J. Power, K.E. Poole, N. Loveridge, J.G. Clement, C.J. Burgoyne, J. Reeve, Femoral Neck Trabecular Bone: Loss with Ageing and Role in Preventing Fracture, *J. Bone Miner. Res.* In press (2009) 1808–1818.

doi:10.1359/jbmr.090504.

- [68] H. Tsangari, D.M. Findlay, N.L. Fazzalari, Structural and remodeling indices in the cancellous bone of the proximal femur across adulthood, *Bone*. 40 (2007) 211–217. doi:10.1016/j.bone.2006.07.007.
- [69] M. Bradney, M.K. Karlsson, Y. Duan, S. Stuckey, S. Bass, E. Seeman, Heterogeneity in the growth of the axial and appendicular skeleton in boys: implications for the pathogenesis of bone fragility in men, *J Bone Min. Res.* 15 (2000) 1871–1878. doi:10.1359/jbmr.2000.15.10.1871.
- [70] C.B. Ruff, W.C. Hayes, Subperiosteal Expansion and Cortical Remodeling of the Human Femur and Tibia with Aging, 217 (1982) 945–948.
- [71] M.R. Allen, D.B. Burr, Human femoral neck has less cellular periosteum , and more mineralized periosteum , than femoral diaphyseal bone, *Bone*. 36 (2005) 311–316. doi:10.1016/j.bone.2004.10.013.
- [72] R.D. Boyce, T.M.; Bloebaum, Cortical Aging Differences and Fracture Implications for the Human Femoral Neck, *Bone*. 14 (1993) 769–778.
- [73] E.G. Vajda, R.D. Bloebaum, Age-related hypermineralization in the female proximal human femur., *Anat. Rec.* 255 (1999) 202–11.
- [74] P. Roschger, E.P. Paschalis, P. Fratzl, K. Klaushofer, Bone mineralization density distribution in health and disease, *Bone*. 42 (2008) 456–466. doi:10.1016/j.bone.2007.10.021.
- [75] J.E. Shea, E.G. Vajda, R.D. Bloebaum, Evidence of a hypermineralised calcified fibrocartilage on the human femoral neck and lesser trochanter, *J Annat.* 1 (2001) 153–162.
- [76] G. Zagba-Mongalima, M. Goret-Nicaise, A. Dhem, Age changes in human bone: a

- microradiographic and histological study of subperiosteal and periosteal calcifications.,
Gerontology. 34 (1988) 264–76.
- [77] I.G. Jang, I.Y. Kim, Computational simulation of trabecular adaptation progress in human proximal femur during growth, *J. Biomech.* 42 (2009) 573–580. doi:10.1016/j.jbiomech.2008.12.009.
- [78] C. Chappard, S. Bensalah, C. Olivier, P.J. Gouttenoire, a. Marchadier, C. Benhamou, F. Peyrin, 3D characterization of pores in the cortical bone of human femur in the elderly at different locations as determined by synchrotron micro-computed tomography images, *Osteoporos. Int.* 24 (2013) 1023–1033. doi:10.1007/s00198-012-2044-4.
- [79] R.B. Martin, D.B. Burr, *Structure, Function, and Adaptation of Compact Bone*, Raven Press, New York, 1989.
- [80] J.G. Skedros, J.L. Holmes, E.G. Vajda, R.D. Bloebaum, Cement lines of secondary osteons in human bone are not mineral-deficient: new data in a historical perspective, *Anat. Rec. A, Discov. Mol. Cell. Evol. Biol.* 286 (2005) 781–803. doi:10.1002/ar.a.20214.
- [81] J. Reeve, N. Loveridge, The fragile elderly hip: Mechanisms associated with age-related loss of strength and toughness, *Bone*. 61 (2014) 138–148. doi:10.1016/j.bone.2013.12.034.
- [82] Y.N. Yeni, C.U. Brown, Z. Wang, T.L. Norman, The influence of bone morphology on fracture toughness of the human femur and tibia, *Bone*. 21 (1997) 453–459. doi:S8756328297001737 [pii].
- [83] R.W. McCalden, J.A. McGeough, M.B. Barker, C.M. Court-Brown, Age-related changes in the tensile properties of cortical bone - The relative importance of changes in porosity, mineralization, and microstructure, *J. Bone Jt. surgery.American* Vol. 75 (1993) 1193–1205.
- [84] G.R. Jordan, N. Loveridge, K.L. Bell, J. Power, N. Rushton, J. Reeve, Spatial clustering of

- remodeling osteons in the femoral neck cortex: a cause of weakness in hip fracture?, *Bone*. 26 (2000) 305–313.
- [85] D.M.L. Cooper, B. Erickson, A.G. Peele, K. Hannah, C.D.L. Thomas, J.G. Clement, Visualization of 3D osteon morphology by synchrotron radiation micro-CT, *J. Anat.* 219 (2011) 481–489. doi:10.1111/j.1469-7580.2011.01398.x.
- [86] E.A. Zimmermann, E. Schaible, H. Bale, H.D. Barth, S.Y. Tang, P. Reichert, B. Busse, T. Alliston, J.W. Ager, R.O. Ritchie, Age-related changes in the plasticity and toughness of human cortical bone at multiple length scales, *Proc. Natl. Acad. Sci.* 108 (2011) 14416–14421. doi:10.1073/pnas.1107966108.
- [87] S. Weiner, W. Traub, H.D. Wagner, Lamellar bone: structure-function relations, *J. Struct. Biol.* 126 (1999) 241–255. doi:S1047847799941072 [pii].
- [88] A. Boyde, C.M. Riggs, The quantitative study of the orientation of collagen in compact bone slices, *Bone*. 11 (1990) 35–39. doi:10.1016/8756-3282(90)90069-B.
- [89] S. Weiner, T. Arad, I. Sabanay, W. Traub, Rotated plywood structure of primary lamellar bone in the rat: orientations of the collagen fibril arrays, *Bone*. 20 (1997) 509–514. doi:S8756328297000537 [pii].
- [90] N. Reznikov, R. Shahar, S. Weiner, Three-dimensional structure of human lamellar bone : The presence of two different materials and new insights into the hierarchical organization, *Bone*. 59 (2014) 93–104. doi:10.1016/j.bone.2013.10.023.
- [91] M. Ascenzi, A. Ascenzi, A. Benvenuti, M. Burghammer, S. Panzavolta, A. Bigi, Structural differences between ““ dark ”” and ““ bright ”” isolated human osteonic lamellae, *J. Struct. Biol.* 141 (2003) 22–33.
- [92] A. Ascenzi, E. Bonucci, Mechanical similarities between alternate osteons and cross-ply

- laminates, *J. Biomech.* 9 (1976) 65–71.
- [93] A. Ascenzi, E. Bonucci, The tensile properties of single osteons, *Anat. Rec.* 158 (1967) 375–386. doi:10.1002/ar.1091580403 [doi].
- [94] A. Ascenzi, E. Bonucci, The compressive properties of single osteons, *Anat. Rec.* 161 (1968) 377–391. doi:10.1002/ar.1091610309 [doi].
- [95] A. Ascenzi, A. Benvenuti, Orientation of collagen fibers at the boundary between 2 successive osteonic lamellae and its mechanical interpretation, *J. Biomech.* 19 (1986) 455–463.
- [96] M.M. Giraud-Guille, Twisted plywood architecture of collagen fibrils in human compact bone osteons, *Calcif. Tissue Int.* 42 (1988) 167–180.
- [97] W. Wagermaier, H.S. Gupta, A. Gourrier, M. Burghammer, P. Roschger, P. Fratzl, Spiral twisting of fiber orientation inside bone lamellae, *Biointerphases.* 1 (2006) 1–5. doi:10.1116/1.2178386.
- [98] F.G. Evans, R. Vincentelli, Relation of collagen fiber orientation to some mechanical properties of cortical bone, *J. Biomech.* 2 (1969) 63–71.
- [99] S. Weiner, W. Traub, Bone structure: from angstroms to microns, *FASEB J.* 6 (1992) 879–885.
- [100] C.M. Riggs, L.C. Vaughan, G.P. Evans, L.E. Lanyon, A. Boyde, Mechanical implications of collagen fibre orientation in cortical bone of the equine radius, *Anat. Embryol. (Berl).* 187 (1993) 239–248.
- [101] J.G. Skedros, K.E. Keenan, T.J. Williams, C.J. Kiser, Secondary osteon size and collagen / lamellar organization (“ osteon morphotypes ”) are not coupled , but potentially adapt independently for local strain mode or magnitude, *J. Struct. Biol.* 181 (2013) 95–107.

doi:10.1016/j.jsb.2012.10.013.

- [102] G.C. Reilly, J.D. Currey, The development of microcracking and failure in bone depends on the loading mode to which it is adapted., *J. Exp. Biol.* 202 (1999) 543–552.
- [103] M. Portigliatti-Barbos, S. Carando, A. Ascenzi, A. Boyde, On the Structural Symmetry of Human Femurs, *Bone*. 8 (1987) 165–169.
- [104] J.K. Kalmey, C.O. Lovejoy, Collagen fiber orientation in the femoral necks of apes and humans: do their histological structures reflect differences in locomotor loading?, *Bone*. 31 (2002) 327–332. doi:10.1016/S8756-3282(02)00828-1.
- [105] P.J. Thurner, E. Oroudjev, R. Jungmann, C. Kreutz, J.H. Kindt, G. Schitter, Imaging of Bone Ultrastructure using Atomic Force Microscopy, *Mod. Res. Educ. Top. Microsc.* (2007) 37–48.
- [106] M. Ascenzi, A. Lomovtsev, Collagen orientation patterns in human secondary osteons, quantified in the radial direction by confocal microscopy, *J. Struct. Biol.* 153 (2006) 14–30. doi:10.1016/j.jsb.2005.08.007.
- [107] P.J. Campagnola, L.M. Loew, Second-harmonic imaging microscopy for visualizing biomolecular arrays in cells , tissues and organisms, *Nat. Biotechnol.* 21 (2003) 1356–1360. doi:10.1038/nbt894.
- [108] R. Ambekar, M. Chittenden, I. Jasiuk, K.C.T. Jr, Quantitative second-harmonic generation microscopy for imaging porcine cortical bone : Comparison to SEM and its potential to investigate age-related changes, *Bone*. 50 (2012) 643–650. doi:10.1016/j.bone.2011.11.013.
- [109] X. Sun, E. McLamore, V. Kishore, K. Fites, M. Slipchenko, D.M. Porterfield, O. Akkus, Mechanical Stretch Induced Calcium Efflux from Bone Matrix Stimulates Osteoblasts, *Bone*. 50 (2012) 581–591. doi:10.1016/j.bone.2011.12.015.

- [110] W.J. Landis, K.J. Hodgens, J. Arena, M.J. Song, B.F. McEwen, Structural relations between collagen and mineral in bone as determined by high voltage electron microscopic tomography, *Microsc. Res. Tech.* 33 (1996) 192–202.
- [111] H. Kafantari, E. Kounadi, M. Fatouros, M. Milonakis, M. Tzaphlidou, Structural alterations in rat skin and bone collagen fibrils induced by ovariectomy, *Bone*. 26 (2000) 349–353. doi:10.1016/S8756-3282(99)00279-3.
- [112] K. Uzawa, W.J. Grzesik, T. Nishiura, S.A. Kuznetsov, P.G. Robey, D.A. Brenner, M. Yamauchi, Differential Expression of Human Lysyl Hydroxylase Genes, Lysine Hydroxylation, and Cross-Linking of Type I Collagen During Osteoblastic Differentiation In Vitro, *J. Bone Miner. Res.* 14 (1999) 1272–1280. doi:10.1359/jbmr.1999.14.8.1272.
- [113] A.J. Bailey, R.G. Paul, L. Knott, Mechanisms of maturation and ageing of collagen, *Mech. Ageing Dev.* 106 (1998) 1–56. doi:10.1016/S0047-6374(98)00119-5.
- [114] X. Wang, X. Shen, X. Li, C.M. Agrawal, Age-related changes in the collagen network and toughness of bone, *Bone*. 31 (2002) 1–7.
- [115] P. Zioupos, J.D. Currey, A.J. Hamer, The role of collagen in the declining mechanical properties of aging human cortical bone, *J. Biomed. Mater. Res.* 45 (1999) 108–116. doi:10.1002/(SICI)1097-4636(199905)45:2<108::AID-JBM5>3.0.CO;2-A [pii].
- [116] D. Vashishth, G.J. Gibson, J.I. Khoury, M.B. Schaffler, J. Kimura, D.P. Fyhrie, Influence of nonenzymatic glycation on biomechanical properties of cortical bone, *Bone*. 28 (2001) 195–201. doi:10.1016/S8756-3282(00)00434-8.
- [117] S. Weiner, W. Traub, Organization of hydroxyapatite crystals within collagen fibrils, *FEBS Lett.* 206 (1986) 262–266. doi:0014-5793(86)80993-0 [pii].
- [118] J. Currey, Incompatible mechanical properties in compact bone, *J. Theor. Biol.* 231 (2004)

- 569–580. doi:10.1016/j.jtbi.2004.07.013.
- [119] M.A. Rubin, L. Jasiuk, J. Taylor, J. Rubin, T. Ganey, R.P. Apkarian, TEM analysis of the nanostructure of normal and osteoporotic human trabecular bone, *Bone*. 33 (2003) 270–282. doi:10.1016/S8756-3282(03)00194-7.
- [120] V. Ziv, S. Weiner, Bone crystal sizes: a comparison of transmission electron microscopic and X-ray diffraction line width broadening techniques., *Connect. Tissue Res.* 30 (1994) 165–175. doi:10.3109/03008209409061969.
- [121] S. Rinnerthaler, P. Roschger, F.H. Jakob, A. Nader, K. Klaushofer, P. Fratzl, H.F. Jakob, A. Nader, K. Klaushofer, P. Fratzl, Scanning Small Angle X-ray Scattering Analysis of Human Bone Sections, *Calcif. Tissue Int.* 64 (1999) 422–429. doi:10.1007/PL00005824.
- [122] P. Fratzl, S. Schreiber, K. Klaushofer, Bone mineralization as studied by small-angle x-ray scattering., *Connect. Tissue Res.* 34 (1996) 247–254.
- [123] N. Fratzl-Zelman, I. Schmidt, P. Roschger, F.H. Glorieux, K. Klaushofer, P. Fratzl, F. Rauch, W. Wagermaier, Mineral particle size in children with osteogenesis imperfecta type I is not increased independently of specific collagen mutations, *Bone*. 60 (2014) 1220–128. doi:10.1016/j.bone.2013.11.023.
- [124] N. Fratzl-Zelman, I. Schmidt, P. Roschger, A. Roschger, F.H. Glorieux, K. Klaushofer, W. Wagermaier, F. Rauch, P. Fratzl, Unique micro- and nano-scale mineralization pattern of human osteogenesis imperfecta type VI bone, *Bone*. 73 (2015) 233–241. doi:10.1016/j.bone.2014.12.023.
- [125] A. Gourrier, C. Li, S. Siegel, O. Paris, P. Roschger, K. Klaushofer, P. Fratzl, Scanning small-angle X-ray scattering analysis of the size and organization of the mineral nanoparticles in fluorotic bone using a stack of cards model, *J. Appl. Crystallogr.* 43 (2010)

- 1385–1392. doi:10.1107/S0021889810035090.
- [126] D.D. Thompson, A.S. Posner, W.S. Laughlin, N.C. Blumenthal, Comparison of bone apatite in osteoporotic and normal Eskimos, *Calcif. Tissue Int.* 35 (1983) 392–393. doi:10.1007/BF02405064.
- [127] N. Fratzl-Zelman, P. Roschger, A. Gourrier, M. Weber, B.M. Misof, N. Loveridge, J. Reeve, K. Klaushofer, P. Fratzl, Combination of nanoindentation and quantitative backscattered electron imaging revealed altered bone material properties associated with femoral neck fragility., *Calcif. Tissue Int.* 85 (2009) 335–43. doi:10.1007/s00223-009-9289-8.
- [128] R.D. Bloebaum, J.G. Skedros, E.G. Vajda, K.N. Bachus, B.R. Constantz, Determining mineral content variations in bone using backscattered electron imaging, *Bone.* 20 (1997) 485–490. doi:10.1016/S8756-3282(97)00015-X.
- [129] P. Roschger, P. Fratzl, J. Eschberger, K. Klaushofer, Validation of quantitative backscattered electron imaging for the measurement of mineral density distribution in human bone biopsies, *Bone.* 23 (1998) 319–326. doi:10.1016/S8756-3282(98)00112-4.
- [130] J.G. Skedros, R.D. Bloebaum, K.N. Bachus, T.M. Boyce, The meaning of graylevels in backscattered electron images of bone, *J. Biomed. Mater. Res.* 27 (1993) 47–56. doi:10.1002/jbm.820270107 [doi].
- [131] A. Boyde, S.J. Jones, J. Aerssens, J. Dequeker, Mineral density quantitation of the human cortical iliac crest by backscattered electron image analysis: Variations with age, sex, and degree of osteoarthritis, *Bone.* 16 (1995) 619–627. doi:10.1016/8756-3282(95)00119-X.
- [132] P. Roschger, H.S. Gupta, A. Berzlanovich, G. Ittner, D.W. Dempster, P. Fratzl, F. Cosman, M. Parisien, R. Lindsay, J.W. Nieves, K. Klaushofer, Constant mineralization density distribution in cancellous human bone, *Bone.* 32 (2003) 316–323. doi:10.1016/S8756-

3282(02)00973-0.

- [133] S. Gamsjaeger, A. Masic, P. Roschger, M. Kazanci, J.W.C. Dunlop, K. Klaushofer, E.P. Paschalis, P. Fratzl, Cortical bone composition and orientation as a function of animal and tissue age in mice by Raman spectroscopy, *Bone*. 47 (2010) 392–399. doi:10.1016/j.bone.2010.04.608.
- [134] M. Kazanci, P. Roschger, E.P. Paschalis, K. Klaushofer, P. Fratzl, Bone osteonal tissues by Raman spectral mapping: Orientation-composition, *J. Struct. Biol.* 156 (2006) 489–496. doi:10.1016/j.jsb.2006.06.011.
- [135] E.P. Paschalis, S. Gamsjaeger, N. Fratzl-zelman, P. Roschger, A. Masic, W. Brozek, N. Hassler, F.H. Glorieux, F. Rauch, K. Klaushofer, P. Fratzl, Evidence for a Role for Nanoporosity and Pyridinoline Content in Human Mild Osteogenesis Imperfecta, *J. Bone Miner. Res.* 31 (2016) 1050–1059. doi:10.1002/jbmr.2780.
- [136] S. Gourion-Arsiquaud, L. Lukashova, J. Power, N. Loveridge, J. Reeve, A.L. Boskey, Fourier transform infrared imaging of femoral neck bone: Reduced heterogeneity of mineral-to-matrix and carbonate-to-phosphate and more variable crystallinity in treatment-naive fracture cases compared with fracture-free controls, *J. Bone Miner. Res.* 28 (2013) 150–161. doi:10.1002/jbmr.1724.
- [137] B.R. McCreadie, M.D. Morris, T. ching Chen, D. Sudhaker Rao, W.F. Finney, E. Widjaja, S.A. Goldstein, Bone tissue compositional differences in women with and without osteoporotic fracture, *Bone*. 39 (2006) 1190–1195. doi:10.1016/j.bone.2006.06.008.
- [138] S. Pabisch, W. Wagermaier, T. Zander, C. Li, P. Fratzl, Imaging the nanostructure of bone and dentin through small- and wide-angle X-ray scattering., *Methods Enzymol.* 532 (2013) 391–413. doi:10.1016/B978-0-12-416617-2.00018-7.

- [139] R.M. Hoerth, D. Baum, D. Knötel, S. Prohaska, B.M. Willie, G.N. Duda, H.-C. Hege, P. Fratzl, W. Wagermaier, Registering 2D and 3D imaging data of bone during healing, *Connect. Tissue Res.* 56 (2015) 133–143. doi:10.3109/03008207.2015.1005210.
- [140] R.M. Hoerth, B.M. Seidt, M. Shah, C. Schwarz, B.M. Willie, G.N. Duda, P. Fratzl, W. Wagermaier, Mechanical and structural properties of bone in non-critical and critical healing in rat, *Acta Biomater.* 10 (2014) 4009–4019. doi:10.1016/j.actbio.2014.06.003.
- [141] P. Fratzl, O. Paris, K. Klaushofer, W.J. Landis, Bone mineralization in an osteogenesis imperfecta mouse model studied by small-angle x-ray scattering, *J. Clin. Invest.* 97 (1996) 396–402. doi:10.1172/JCI118428.
- [142] B. Misof, P. Roschger, P. Fratzl, Imaging Mineralized Tissues in Vertebrates, in: P. Ducheyne, K. Healy, D.E. Hutmacher, D.W. Grainger, C.J. Kirkpatrick (Eds.), *Compr. Biomater.*, Elsevier, 2011: pp. 407–426. doi:10.1016/B978-0-08-055294-1.00112-4.
- [143] H. Deyhle, O. Bunk, B. Müller, Nanostructure of healthy and caries-affected human teeth, *Nanomedicine Nanotechnology, Biol. Med.* 7 (2011) 694–701. doi:10.1016/j.nano.2011.09.005.
- [144] C.H. Turner, The biomechanics of hip fracture, *Lancet.* 366 (2005) 98–99. doi:10.1016/S0140-6736(05)66842-0.
- [145] V. Ebacher, R. Wang, A Unique Microcracking Process Associated with the Inelastic Deformation of Haversian Bone, *Adv. Funct. Mater.* 19 (2009) 57–66. doi:10.1002/adfm.200801234.
- [146] I. Jager, P. Fratzl, Mineralized collagen fibrils: A mechanical model with a staggered arrangement of mineral particles, *Biophys. J.* 79 (2000) 1737–1746.
- [147] H. Gao, B. Ji, I.L. Jager, E. Arzt, P. Fratzl, Materials become insensitive to flaws at

- nanoscale: Lessons from nature, *Proc. Natl. Acad. Sci.* 100 (2003) 5597–5600.
doi:10.1073/pnas.0631609100.
- [148] H.S. Gupta, W. Wagermaier, G.A. Zickler, J. Hartmann, S.S. Funari, P. Roschger, H.D. Wagner, P. Fratzl, Fibrillar level fracture in bone beyond the yield point, *Int. J. Fract.* 139 (2006) 425–436. doi:10.1007/s10704-006-6635-y.
- [149] H.S. Gupta, W. Wagermaier, G.A. Zickler, D. Raz-Ben Aroush, S.S. Funari, P. Roschger, H.D. Wagner, P. Fratzl, Nanoscale deformation mechanisms in bone, *Nano Lett.* 5 (2005) 2108–2111. doi:10.1021/nl051584b [doi].
- [150] G.C. Reilly, Observations of microdamage around osteocyte lacunae in bone, *J. Biomech.* 33 (2000) 1131–1134. doi:S002192900000907 [pii].
- [151] J.D. Currey, K. Brear, P. Zioupos, Notch sensitivity of mammalian mineralized tissues in impact, *Proceedings Biological Sci. / R. Soc.* 271 (2004) 517–522. doi:10.1098/rspb.2003.2634.
- [152] J.C. Lotz, E.J. Cheal, W.C. Hayes, Stress distributions within the proximal femur during gait and falls: Implications for osteoporotic fracture, *Osteoporos. Int.* 5 (1995) 252–261. doi:10.1007/BF01774015.
- [153] J.H. Keyak, Relationships between femoral fracture loads for two load configurations, *J. Biomech.* 33 (2000) 499–502. doi:10.1016/S0021-9290(99)00202-X.
- [154] M. Bessho, I. Ohnishi, T. Matsumoto, S. Ohashi, J. Matsuyama, K. Tobita, M. Kaneko, K. Nakamura, Prediction of proximal femur strength using a CT-based nonlinear finite element method: Differences in predicted fracture load and site with changing load and boundary conditions, *Bone.* 45 (2009) 226–231. doi:10.1016/j.bone.2009.04.241.
- [155] S. Nawathe, B.P. Nguyen, N. Barzarian, H. Akhlaghpour, M.L. Bouxsein, T.M. Keaveny,

- Cortical and trabecular load sharing in the human femoral neck, *J. Biomech.* 48 (2015) 816–822. doi:10.1016/j.jbiomech.2014.12.022.
- [156] J.H. Keyak, S.A. Rossi, K.A. Jones, H.B. Skinner, Prediction of Femoral Fracture Load using Automated Finite Element Modelling, *J. Biomech.* 31 (1997) 125–133. doi:10.1016/S0021-9290(97)00123-1.
- [157] D.D. Cody, G.J. Gross, F. J. Hou, H.J. Spencer, S. a. Goldstein, D. P. Fyhrie, Femoral strength is better predicted by finite element models than QCT and DXA, *J. Biomech.* 32 (1999) 1013–1020. doi:10.1016/S0021-9290(99)00099-8.
- [158] J.H. Keyak, S. a. Rossi, Prediction of femoral fracture load using finite element models: An examination of stress- and strain-based failure theories, *J. Biomech.* 33 (2000) 209–214. doi:10.1016/S0021-9290(99)00152-9.
- [159] J.H. Keyak, Improved prediction of proximal femoral fracture load using nonlinear finite element models., *Med. Eng. Phys.* 23 (2001) 165–73. doi:10.1016/S1350-4533(01)00045-5.
- [160] L. Grassi, E. Schileo, F. Taddei, L. Zani, M. Juszczak, L. Cristofolini, M. Viceconti, Accuracy of finite element predictions in sideways load configurations for the proximal human femur, *J. Biomech.* 45 (2012) 394–399. doi:10.1016/j.jbiomech.2011.10.019.
- [161] J.E.M. Koivumäki, J. Thevenot, P. Pulkkinen, V. Kuhn, T.M. Link, F. Eckstein, T. Jämsä, Ct-based finite element models can be used to estimate experimentally measured failure loads in the proximal femur, *Bone.* 50 (2012) 824–829. doi:10.1016/j.bone.2012.01.012.
- [162] J.C. Lotz, E.J. Cheal, W.C. Hayes, Fracture prediction for the proximal femur using finite element models: Part II--Nonlinear analysis., *J. Biomech. Eng.* 113 (1991) 361–365. doi:10.1115/1.2895413.

- [163] L. Zani, P. Erani, L. Grassi, F. Taddei, L. Cristofolini, Strain distribution in the proximal Human femur during in vitro simulated sideways fall, *J. Biomech.* 48 (2015) 2130–2143. doi:10.1016/j.jbiomech.2015.02.022.
- [164] O. Ariza, S. Gilchrist, R.P. Widmer, P. Guy, S.J. Ferguson, P.A. Crompton, B. Helgason, Comparison of explicit finite element and mechanical simulation of the proximal femur during dynamic drop-tower testing, *J. Biomech.* 48 (2015) 224–232. doi:10.1016/j.jbiomech.2014.11.042.
- [165] B. Helgason, S. Gilchrist, O. Ariza, J.D. Chak, G. Zheng, R.P. Widmer, S.J. Ferguson, P. Guy, P.A. Crompton, Development of a balanced experimental-computational approach to understanding the mechanics of proximal femur fractures., *Med. Eng. Phys.* 36 (2014) 793–9. doi:10.1016/j.medengphy.2014.02.019.
- [166] K.E. Poole, P.M. Mayhew, C.M. Rose, J.K. Brown, P.J. Bearcroft, N. Loveridge, J. Reeve, Changing structure of the femoral neck across the adult female lifespan, *J. Bone Miner. Res.* 25 (2010) 482–491. doi:10.1359/jbmr.090734.
- [167] F. Johannesdottir, K.E.S. Poole, J. Reeve, K. Siggeirsdottir, T. Aspelund, B. Mogensen, B.Y. Jonsson, S. Sigurdsson, T.B. Harris, V.G. Gudnason, G. Sigurdsson, Distribution of cortical bone in the femoral neck and hip fracture: a prospective case-control analysis of 143 incident hip fractures; the AGES-REYKJAVIK Study., *Bone.* 48 (2011) 1268–76. doi:10.1016/j.bone.2011.03.776.
- [168] P. Milovanovic, D. Djonic, R.P. Marshall, M. Hahn, S. Nikolic, V. Zivkovic, M. Amling, M. Djuric, Micro-structural basis for particular vulnerability of the superolateral neck trabecular bone in the postmenopausal women with hip fractures, *Bone.* 50 (2012) 63–68. doi:10.1016/j.bone.2011.09.044.

- [169] C. Mercer, M.Y.Y. He, R. Wang, A.G.G. Evans, Mechanisms governing the inelastic deformation of cortical bone and application to trabecular bone, *Acta Biomater.* 2 (2006) 59–68. doi:10.1016/j.actbio.2005.08.004.
- [170] V. Ebacher, C. Tang, H. McKay, T.R. Oxland, P. Guy, R. Wang, Strain redistribution and cracking behavior of human bone during bending, *Bone.* 40 (2007) 1265–1275. doi:10.1016/j.bone.2006.12.065.
- [171] P. Zioupos, U. Hansen, J.D. Currey, Microcracking damage and the fracture process in relation to strain rate in human cortical bone tensile failure., *J. Biomech.* 41 (2008) 2932–9. doi:10.1016/j.jbiomech.2008.07.025.
- [172] D.P. Nicoletta, A.E. Nicholls, J. Lankford, D.T. Davy, Machine vision photogrammetry: a technique for measurement of microstructural strain in cortical bone, *J. Biomech.* 34 (2001) 135–139.
- [173] D.P. Nicoletta, D.E. Moravits, A.M. Gale, L.F. Bonewald, J. Lankforda, J. Lankford, Osteocyte lacunae tissue strain in cortical bone, *J. Biomech.* 39 (2006) 1735–1743. doi:10.1016/j.jbiomech.2005.04.032.
- [174] G. Benecke, M. Kerschnitzki, P. Fratzl, H.S. Gupta, Digital image correlation shows localized deformation bands in inelastic loading of fibrolamellar bone, *J. Mater. Res.* 24 (2009) 421–429.
- [175] P. Zioupos, J.D. Currey, The extent of microcracking and the morphology of microcracks in damaged bone, *J. Mater. Sci.* 29 (1994) 978–986. doi:10.1007/BF00351420.
- [176] D. Vashishth, J.C. Behiri, W. Bonfield, Crack growth resistance in cortical bone: Concept of microcrack toughening, *J. Biomech.* 30 (1997) 763–769.
- [177] J.D. Currey, K. Brear, Tensile yield in bone, *Calcif. Tissue Res.* 15 (1974) 173–179.

- [178] P. Zioupos, J.D.D. Currey, A.J.J. Sedman, An examination of the micromechanics of failure of bone and antler by acoustic emission tests and Laser Scanning Confocal Microscopy, *Med. Eng. Phys.* 16 (1994) 203–212. doi:[http://dx.doi.org/10.1016/1350-4533\(94\)90039-6](http://dx.doi.org/10.1016/1350-4533(94)90039-6).
- [179] T.M. Boyce, D.P. Fyhrie, M.C. Glotkowski, E.L. Radin, M.B. Schaffler, Damage type and strain mode associations in human compact bone bending fatigue, *J. Orthop. Res.* 16 (1998) 322–329. doi:[10.1002/jor.1100160308](https://doi.org/10.1002/jor.1100160308).
- [180] V. Ebacher, P. Guy, T.R. Oxland, R. Wang, Sub-lamellar microcracking and roles of canaliculi in human cortical bone, *Acta Biomater.* 8 (2012) 1093–1100. doi:[10.1016/j.actbio.2011.11.013](https://doi.org/10.1016/j.actbio.2011.11.013).
- [181] D. Taylor, P. O'Reilly, L. Vallet, T.C. Lee, The fatigue strength of compact bone in torsion, *J. Biomech.* 36 (2003) 1103–1109. doi:[S0021929003001040](https://doi.org/S0021929003001040) [pii].
- [182] W.T. George, D. Vashishth, Damage mechanisms and failure modes of cortical bone under components of physiological loading, *J. Orthop. Res.* 23 (2005) 1047–1053. doi:[S0736-0266\(05\)00060-4](https://doi.org/S0736-0266(05)00060-4) [pii]; [10.1016/j.orthres.2005.02.008](https://doi.org/10.1016/j.orthres.2005.02.008) [doi].
- [183] A. Ascenzi, E. Bonucci, The shearing properties of single osteons, *Anat. Rec.* 172 (1972) 499–510. doi:[10.1002/ar.1091720304](https://doi.org/10.1002/ar.1091720304) [doi].
- [184] A. Ascenzi, E. Bonucci, A. Simkin, An approach to the mechanical properties of single osteonic lamellae, *J. Biomech.* 6 (1973) 227–235.
- [185] K.J. Jepsen, D.T. Davy, D.J. Krzyzewski, The role of the lamellar interface during torsional yielding of human cortical bone, *J. Biomech.* 32 (1999) 303–310.
- [186] S. Saha, Longitudinal shear properties of human compact bone and its constituents, and associated failure mechanisms, *J. Mater. Sci.* 12 (1977) 1798–1806. doi:[10.1007/BF00566240](https://doi.org/10.1007/BF00566240).

- [187] C.H. Turner, T. Wang, D.B. Burr, Shear strength and fatigue properties of human cortical bone determined from pure shear tests, *Calcif. Tissue Int.* 69 (2001) 373–378.
- [188] L.P. Hiller, S.M. Stover, V.A. Gibson, J.C. Gibeling, C.S. Prater, S.J. Hazelwood, O.C. Yeh, R.B. Martin, Osteon pullout in the equine third metacarpal bone: effects of ex vivo fatigue, *J. Orthop. Res.* 21 (2003) 481–488. doi:10.1016/S0736-0266(02)00232-2.
- [189] F.J. O’Brien, D. Taylor, T.C. Lee, F.J.O. Brien, D. Taylor, T.C. Lee, Bone as a composite material: The role of osteons as barriers to crack growth in compact bone, *Int. J. Fatigue.* 29 (2007) 1051–1056.
- [190] R.K. Nalla, J.J. Kruzic, J.H. Kinney, R.O. Ritchie, Mechanistic aspects of fracture and R-curve behavior in human cortical bone, *Biomaterials.* 26 (2005) 217–231. doi:10.1016/j.biomaterials.2004.02.017 [doi]; S0142961204001553 [pii].
- [191] R.K. Nalla, J.H. Kinney, R.O. Ritchie, Mechanistic fracture criteria for the failure of human cortical bone, *Nat.Mater.* 2 (2003) 164–168. doi:10.1038/nmat832 [doi]; nmat832 [pii].
- [192] H.S. Gupta, U. Stachewicz, W. Wagermaier, P. Roschger, H.D. Wagner, P. Fratzl, Mechanical modulation at the lamellar level in osteonal bone, *J. Mater. Res.* 21 (2006) 1913–1921.
- [193] W.L. Rice, D.L. Kaplan, I. Georgakoudi, Two-Photon Microscopy for Non-Invasive , Quantitative Monitoring of Stem Cell Differentiation, *PLoS One.* 5 (2010) e10075. doi:10.1371/journal.pone.0010075.
- [194] A.H. Burstein, J.M. Zika, K.G. Heiple, L. Klein, Contribution of collagen and mineral to the elastic-plastic properties of bone., *J. Bone Joint Surg. Am.* 57 (1975) 956–61.
- [195] G.E. Fantner, T. Hassenkam, J.H. Kindt, J.C. Weaver, H. Birkedal, L. Pechenik, J.A. Cutroni, G.A.G. Cidade, G.D. Stucky, D.E. Morse, P.K. Hansma, Sacrificial bonds and

- hidden length dissipate energy as mineralized fibrils separate during bone fracture, *Nat. Mater.* 4 (2005) 612–616. doi:10.1038/nmat1428.
- [196] G.E. Fantner, J. Adams, P. Turner, P.J. Thurner, L.W. Fisher, P.K. Hansma, Nanoscale ion mediated networks in bone: Osteopontin can repeatedly dissipate large amounts of energy, *Nano Lett.* 7 (2007) 2491–2498. doi:10.1021/nl0712769.
- [197] H.S. Gupta, J. Seto, W. Wagermaier, P. Zaslansky, P. Boesecke, P. Fratzl, Cooperative deformation of mineral and collagen in bone at the nanoscale, *Proc. Natl. Acad. Sci. U. S. A.* 103 (2006) 17741–17746. doi:10.1073/pnas.0604237103.
- [198] G. Holzer, G. von Skrbensky, L.A. Holzer, W. Pichl, Hip Fractures and the Contribution of Cortical Versus Trabecular Bone to Femoral Neck Strength, *J. Bone Miner. Res.* 24 (2009) 468–474. doi:10.1359/jbmr.081108.
- [199] H. Zhuang, Y. Li, J. Lin, D. Cai, S. Cai, L. Yan, X. Yao, Cortical thickness in the intertrochanteric region may be relevant to hip fracture type, *BMC Musculoskelet. Disord.* 18 (2017) 305. doi:10.1186/s12891-017-1669-z.
- [200] N.J. Crabtree, H. Kroger, A. Martin, H.A.P. Pols, R. Lorenc, J. Nijs, J.J. Stepan, J.A. Falch, T. Miazgowski, S. Grazio, P. Raptou, J. Adams, A. Collings, K.T. Khaw, N. Rushton, M. Lunt, A.K. Dixon, J. Reeve, Improving risk assessment: Hip geometry, bone mineral distribution and bone strength in hip fracture cases and controls. The EPOS study, *Osteoporos. Int.* 13 (2002) 48–54. doi:10.1007/s198-002-8337-y.
- [201] J.S. Nyman, A. Roy, X. Shen, R.L. Acuna, J.H. Tyler, X. Wang, The influence of water removal on the strength and toughness of cortical bone, *J. Biomech.* 39 (2006) 931–938. doi:10.1016/j.jbiomech.2005.01.012.
- [202] J.J.J. Kruzic, D.K.K. Kim, K.J.J. Koester, R.O.O. Ritchie, Indentation techniques for

- evaluating the fracture toughness of biomaterials and hard tissues., *J. Mech. Behav. Biomed. Mater.* 2 (2009) 384–95. doi:10.1016/j.jmbbm.2008.10.008.
- [203] M.K.H. Malo, D. Rohrbach, H. Isaksson, J. Toyras, J.S. Jurvelin, I.S. Tamminen, H. Kroger, K. Raum, Longitudinal elastic properties and porosity of cortical bone tissue vary with age in human proximal femur., *Bone*. 53 (2013) 451–458. doi:10.1016/j.bone.2013.01.015.
- [204] L.P.P. Mullins, M.S.S. Bruzzi, P.E.E. McHugh, Measurement of the microstructural fracture toughness of cortical bone using indentation fracture., *J. Biomech.* 40 (2007) 3285–8. doi:10.1016/j.jbiomech.2007.04.020.
- [205] R. Wang, S. Weiner, Human root dentin: structural anisotropy and Vickers microhardness isotropy, *Connect. Tissue Res.* 39 (1998) 269–279.
- [206] E. Dall’Ara, C. Öhman, M. Baleani, M. Viceconti, The effect of tissue condition and applied load on Vickers hardness of human trabecular bone, *J. Biomech.* 40 (2007) 3267–3270. doi:10.1016/j.jbiomech.2007.04.007.
- [207] I. Zwierzak, M. Baleani, M. Viceconti, Microindentation on cortical human bone: Effects of tissue condition and indentation location on hardness values, *Proc. Inst. Mech. Eng. Part H J. Eng. Med.* 223 (2009) 913–918. doi:10.1243/09544119JEIM634.
- [208] G.P. Evans, J.C. Behiri, J.D. Currey, W. Bonfield, Microhardness and Young’s modulus in cortical bone exhibiting a wide range of mineral volume fractions, and in a bone analogue, *J. Mater. Sci. - Mater. Med.* 1 (1990) 38–43.
- [209] A.M. Coats, P. Zioupos, R.M. Aspden, Material properties of subchondral bone from patients with osteoporosis or osteoarthritis by microindentation testing and electron probe microanalysis, *Calcif. Tissue Int.* 73 (2003) 66–71. doi:10.1007/s00223-002-2080-8.
- [210] ASTM Int., ASTM E384: Standard Test Method for Knoop and Vickers Hardness of

- Materials, ASTM Stand. (2012) 1–43. doi:10.1520/E0384-11E01.2.
- [211] F.L. Bach-Gansmo, S.C. Irvine, A. Brüel, J.S. Thomsen, H. Birkedal, Calcified cartilage islands in rat cortical bone, *Calcif. Tissue Int.* 92 (2013) 330–338. doi:10.1007/s00223-012-9682-6.
- [212] E.A. Zimmermann, E. Schaible, H. Bale, H.D. Barth, S.Y. Tang, P. Reichert, B. Busse, T. Alliston, J.W. Ager, R.O. Ritchie, E. Schaible, H. Bale, H.D. Barth, S.Y. Tang, P. Reichert, Correction for Zimmermann et al., Age-related changes in the plasticity and toughness of human cortical bone at multiple length scales, *Proc. Natl. Acad. Sci.* 109 (2012) 11890–11890. doi:10.1073/pnas.1209596109.
- [213] P. Fratzl, O. Kolednik, F.D. Fischer, M.N. Dean, The mechanics of tessellations - bioinspired strategies for fracture resistance., *Chem. Soc. Rev.* 45 (2016) 252–67. doi:10.1039/c5cs00598a.
- [214] H.M. FROST, Micropetrosis., *J. Bone Joint Surg. Am.* 42–A (1960) 144–50.
- [215] P. Milovanovic, E.A. Zimmermann, A. vom Scheidt, B. Hoffmann, G. Sarau, T. Yorgan, M. Schweizer, M. Amling, S. Christiansen, B. Busse, The Formation of Calcified Nanospherites during Micropetrosis Represents a Unique Mineralization Mechanism in Aged Human Bone, *Small.* 13 (2017) 1–10. doi:10.1002/sml.201602215.
- [216] P. Roschger, B. Grabner, S. Rinnerthaler, W. Tesch, M. Kneissel, A. Berzlanovich, K. Klaushofer, P. Fratzl, Structural Development of the Mineralized Tissue in the Human L4 Vertebral Body, *J. Struct. Biol.* 136 (2001) 126–136. doi:10.1006/jsbi.2001.4427.
- [217] R.Z. Wang, Fracture toughness and interfacial design of a biological fiber-matrix ceramic composite in sea urchin teeth, *J. Am. Ceram. Soc.* 81 (1998) 1037–1040.
- [218] H.H. Xu, D.T. Smith, S. Jahanmir, E. Romberg, J.R. Kelly, V.P. Thompson, E.D. Rekow,

- Indentation damage and mechanical properties of human enamel and dentin., *J. Dent. Res.* 77 (1998) 472–80. doi:10.1177/00220345980770030601.
- [219] P. Zioupos, J.D. Currey, A. Casinos, Exploring the effects of hypermineralisation in bone tissue by using an extreme biological example, *Connect. Tissue Res.* 41 (2000) 229–248. doi:doi:10.3109/03008200009005292.
- [220] P. Roschger, A. Lombardi, B. Misof, G. Maier, N. Fratzl-Zelman, P. Fratzl, K. Klaushofer, Mineralization density distribution of postmenopausal osteoporotic bone is restored to normal after long-term alendronate treatment: qBEI and sSAXS data from the fracture intervention trial long-term extension (FLEX), *J. Bone Miner. Res.* 25 (2010) 48–55. doi:10.1359/jbmr.090702.
- [221] I. Zizak, P. Roschger, O. Paris, B.M. Misof, A. Berzlanovich, S. Bernstorff, H. Amenitsch, K. Klaushofer, P. Fratzl, Characteristics of mineral particles in the human bone/cartilage interface, *J. Struct. Biol.* 141 (2003) 208–217. doi:10.1016/S1047-8477(02)00635-4.
- [222] L.D.E. Macedo, S. Silva, *Nanoindentation Study and Quantitative Backscattered Electron Imaging of Human Cortical Bone*, (2006).
- [223] V.L. Ferguson, A.J. Bushby, A. Boyde, Nanomechanical properties and mineral concentration in articular calcified cartilage and subchondral bone, *J. Anat.* 203 (2003) 191–202. doi:10.1046/j.1469-7580.2003.00193.x.
- [224] H.S. Gupta, S. Schratte, W. Tesch, P. Roschger, A. Berzlanovich, T. Schoeberl, K. Klaushofer, P. Fratzl, Two different correlations between nanoindentation modulus and mineral content in the bone-cartilage interface, *J. Struct. Biol.* 149 (2005) 138–148. doi:10.1016/j.jsb.2004.10.010.
- [225] G.R. ANSTIS, P. CHANTIKUL, B.R. LAWN, D.B. MARSHALL, *A Critical Evaluation*

- of Indentation Techniques for Measuring Fracture Toughness: I, Direct Crack Measurements, *J. Am. Ceram. Soc.* 64 (1981) 533–538. doi:10.1111/j.1151-2916.1981.tb10320.x.
- [226] A. Boyde, The real response of bone to exercise, *J. Anat.* 203 (2003) 173–189. doi:10.1046/j.1469-7580.2003.00213.x.
- [227] C.K. Tjhia, S.M. Stover, D.S. Rao, C. V. Odvina, D.P. Fyhrie, Relating micromechanical properties and mineral densities in severely suppressed bone turnover patients, osteoporotic patients, and normal subjects, *Bone*. 51 (2012) 114–122. doi:10.1016/j.bone.2012.04.010.
- [228] P. Milovanovic, J. Potocnik, D. Djonic, S. Nikolic, V. Zivkovic, M. Djuric, Z. Rakocevic, Age-related deterioration in trabecular bone mechanical properties at material level: Nanoindentation study of the femoral neck in women by using AFM, *Exp. Gerontol.* 47 (2012) 154–159. doi:10.1016/j.exger.2011.11.011.
- [229] P. Fratzl, S. Schreiber, P. Roschger, M.H. Lafage, G. Rodan, K. Klaushofer, Effects of sodium fluoride and alendronate on the bone mineral in minipigs: a small-angle X-ray scattering and backscattered electron imaging study., *J. Bone Miner. Res.* 11 (1996) 248–253. doi:10.1002/jbmr.5650110214.
- [230] P. Fratzl, H.S. Gupta, O. Paris, A. Valenta, P. Roschger, K. Klaushofer, Diffracting “stacks of cards” - some thoughts about small-angle scattering from bone, in: *Scatt. Methods Prop. Polym. Mater.*, Springer Berlin Heidelberg, Berlin, Heidelberg, 2005: pp. 33–39. doi:10.1007/b107343.
- [231] C. Burger, H. Zhou, H. Wang, I. Sics, B.S. Hsiao, B. Chu, L. Graham, M.J. Glimcher, Lateral Packing of Mineral Crystals in Bone Collagen Fibrils, *Biophys. J.* 95 (2008) 1985–1992. doi:10.1529/biophysj.107.128355.

- [232] J.A. Timlin, A. Carden, M.D. Morris, J.F. Bonadio, C.E. Hoffler, K.M. Kozloff, S.A. Goldstein, Spatial Distribution of Phosphate Species in Mature and Newly Generated Mammalian Bone by Hyperspectral Raman Imaging, *J. Biomed. Opt.* 4 (1999) 28. doi:10.1117/1.429918.
- [233] N.J. Crane, V. Popescu, M.D. Morris, P. Steenhuis, M.A. Ignelzi, Raman spectroscopic evidence for octacalcium phosphate and other transient mineral species deposited during intramembranous mineralization, *Bone*. 39 (2006) 434–442. doi:10.1016/j.bone.2006.02.059.
- [234] S. Gamsjaeger, K. Klaushofer, E.P. Paschalis, Raman analysis of proteoglycans simultaneously in bone and cartilage, *J. Raman Spectrosc.* 45 (2014) 794–800. doi:10.1002/jrs.4552.
- [235] J. Apostolakos, T.J. Durant, C.R. Dwyer, R.P. Russell, J.H. Weinreb, F. Alaei, K. Beitzel, M.B. McCarthy, M.P. Cote, A.D. Mazzocca, The enthesis: a review of the tendon-to-bone insertion., *Muscles. Ligaments Tendons J.* 4 (2014) 333–42. doi:10.11138/mltj/2014.4.3.333.
- [236] N.T. Khanarian, M.K. Boushell, J.P. Spalazzi, N. Pleshko, A.L. Boskey, H.H. Lu, FTIR-I compositional mapping of the cartilage-to-bone interface as a function of tissue region and age, *J. Bone Miner. Res.* 29 (2014) 2643–2652. doi:10.1002/jbmr.2284.
- [237] J.P. Spalazzi, A.L. Boskey, N. Pleshko, H.H. Lu, Quantitative Mapping of Matrix Content and Distribution across the Ligament-to-Bone Insertion, *PLoS One*. 8 (2013) 1–16. doi:10.1371/journal.pone.0074349.
- [238] M.E. Ruppel, L.M. Miller, D.B. Burr, The effect of the microscopic and nanoscale structure on bone fragility, *Osteoporos. Int.* 19 (2008) 1251–1265. doi:10.1007/s00198-008-0579-1.

- [239] H.P. Schwarcz, E.A. McNally, G.A. Botton, Dark-field transmission electron microscopy of cortical bone reveals details of extrafibrillar crystals, *J. Struct. Biol.* 188 (2014) 240–248. doi:10.1016/j.jsb.2014.10.005.
- [240] R.G. Handschin, W.B. Stern, X-ray diffraction studies on the lattice perfection of human bone apatite (Crista Iliaca), *Bone*. 16 (1995) 355S–363S. doi:10.1016/S8756-3282(95)80385-8.
- [241] N. Matsushima, M. Akiyama, Y. Terayama, Quantitative analysis of the orientation of mineral in bone from small-angle x-ray scattering patterns, *Jpn. J. Appl. Phys.* 21 (1982) 186–189. doi:10.1143/JJAP.21.186.
- [242] P. Fratzl, S. Schreiber, A. Boyde, Characterization of Bone Mineral Crystals in Horse Radius by Small- Angle X-Ray Scattering, *Calcif Tissue Int.* 58 (1996) 341–346.
- [243] I. Žižak, O. Paris, P. Roschger, S. Bernstorff, H. Amenitsch, K. Klaushofer, P. Fratzl, Investigation of bone and cartilage by synchrotron scanning-SAXS and -WAXD with micrometer spatial resolution, *J. Appl. Crystallogr.* 33 (2000) 820–823. doi:10.1107/S0021889800001321.
- [244] P. Habibovic, M. V. Juhl, S. Clyens, R. Martinetti, L. Dolcini, N. Theilgaard, C.A. Van Blitterswijk, Comparison of two carbonated apatite ceramics in vivo, *Acta Biomater.* 6 (2010) 2219–2226. doi:10.1016/j.actbio.2009.11.028.
- [245] J.D.P. McElderry, P. Zhu, K.H. Mroue, J. Xu, B. Pavan, M. Fang, G. Zhao, E. McNerny, D.H. Kohn, R.T. Franceschi, M.M.B. Holl, M.M.J. Tecklenburg, A. Ramamoorthy, M.D. Morris, Crystallinity and compositional changes in carbonated apatites: Evidence from ³¹P solid-state NMR, Raman, and AFM analysis, *J. Solid State Chem.* 206 (2013) 192–198. doi:10.1016/j.jssc.2013.08.011.

- [246] Z.R. Bart, M. a Hammond, J.M. Wallace, Multi-scale analysis of bone chemistry, morphology and mechanics in the oim model of osteogenesis imperfecta., *Connect. Tissue Res.* 55 Suppl 1 (2014) 4–8. doi:10.3109/03008207.2014.923860.
- [247] D.O. Sillence, A. Senn, D.M. Danks, Genetic heterogeneity in osteogenesis imperfecta, *J. Med. Genet.* 16 (1979) 101–16. doi:10.1136/jmg.16.2.101.
- [248] B. Grabner, W.. Landis, P. Roschger, S. Rinnerthaler, H. Peterlik, K. Klaushofer, P. Fratzl, Age- and genotype-dependence of bone material properties in the osteogenesis imperfecta murine model (oim), *Bone.* 29 (2001) 453–457. doi:10.1016/S8756-3282(01)00594-4.
- [249] K. Winwood, P. Zioupos, J.D. Currey, J.R. Cotton, M. Taylor, Strain patterns during tensile , compressive , and shear fatigue of human cortical bone and implications for bone biomechanics, (2006). doi:10.1002/jbm.a.
- [250] Astm International WCPA., Standard Test Method for Shear Properties of Composite Materials by the V-Notched Beam Method, 1993. doi:10.1520/D5379.
- [251] T.C. Lee, S. Mohsin, D. Taylor, R. Parkesh, T. Gunnlaugsson, F.J. O’Brien, M. Giehl, W. Gowin, Detecting microdamage in bone, *J. Anat.* 203 (2003) 161–172.
- [252] D.F. Adams, D.E. Walrath, Further development of the Iosipescu shear testmethod, *Exp. Mech.* 27 (1987) 113–119.
- [253] J.C. Xavier, N.M. Garrido, M. Oliveira, J.L. Morais, P.P. Camanho, F. Pierron, A comparison between the Iosipescu and off-axis shear test methods for the characterization of Pinus Pinaster Ait, *Compos. Part A Appl. Sci. Manuf.* 35 (2004) 827–840. doi:10.1016/j.compositesa.2004.01.013.
- [254] F. Pierron, Saint-Venant Effects in the Iosipescu Specimen, *J. Compos. Mater.* 32 (1998) 1986–2015.

- [255] J. Quinta Da Fonseca, P.M. Mummery, P.J. Withers, Full-field strain mapping by optical correlation of micrographs acquired during deformation, *J. Microsc.* 218 (2005) 9–21. doi:10.1111/j.1365-2818.2005.01461.x.
- [256] Y. Bao, T. Wierzbicki, On fracture locus in the equivalent strain and stress triaxiality space, *Int. J. Mech. Sci.* 46 (2004) 81–98. doi:10.1016/j.ijmecsci.2004.02.006.
- [257] Y. Bai, X. Teng, T. Wierzbicki, On the Application of Stress Triaxiality Formula for Plane Strain Fracture Testing, *J. Eng. Mater. Technol.* 131 (2009) 1–10. doi:10.1115/1.3078390.
- [258] H. Daiyan, E. Andreassen, F. Grytten, H. Osnes, R.H. Gaarder, Shear Testing of Polypropylene Materials Analysed by Digital Image Correlation and Numerical Simulations, *Exp. Mech.* 52 (2012) 1355–1369. doi:10.1007/s11340-012-9591-7.
- [259] R. Shahar, P. Zaslansky, M. Barak, A.A. Friesem, J.D. Currey, S. Weiner, Anisotropic Poisson's ratio and compression modulus of cortical bone determined by speckle interferometry, *J. Biomech.* 40 (2007) 252–264. doi:S0021-9290(06)00039-X [pii]; 10.1016/j.jbiomech.2006.01.021 [doi].
- [260] X.N. Dong, X.E. Guo, The dependence of transversely isotropic elasticity of human femoral cortical bone on porosity, *J. Biomech.* 37 (2004) 1281–1287. doi:10.1016/j.jbiomech.2003.12.011.
- [261] M. Kazanci, H.D. Wagner, N.I. Manjubala, H.S. Gupta, E. Paschalis, P. Roschger, P. Fratzl, Raman imaging of two orthogonal planes within cortical bone, *Bone.* 41 (2007) 456–461. doi:10.1016/j.bone.2007.04.200.
- [262] T.L.L. Norman, D. Vashisht, D.B.B. Burr, D. Vashishth, D.B.B. Burr, Fracture toughness of human bone under tension, *J. Biomech.* 28 (1995) 309–320.
- [263] Z. Fan, J.G. Swadener, J.Y. Rho, M.E. Roy, G.M. Pharr, Anisotropic properties of human

- tibial cortical bone as measured by nanoindentation, *J. Orthop. Res.* 20 (2002) 806–810.
doi:10.1016/S0736-0266(01)00186-3 [doi].
- [264] W.R. Broughton, M. K, D. Hull, Analysis of the Iosipescu Shear Test as Applied to Unidirectional Carbon-Fibre Reinforced Composites, *Compos. Sci. Technol.* 38 (1990) 299–325.
- [265] A.G. Evans, F.W. Zok, The physics and mechanics of fiber-reinforced brittle matrix composites, *J. Mater. Sci.* 29 (1994) 3857–3896.
- [266] F.E. Heredia, A.G. Evans, In-plane Shear Properties of 2-D Ceramic Matrix Composites, *J. Am. Ceram. Soc.* 77 (1994) 2569–2574.
- [267] D. Vashishth, K.E. Tanner, W. Bonfield, Contribution, development and morphology of microcracking in cortical bone during crack propagation, *J. Biomech.* 33 (2000) 1169–1174.
doi:S0021929000000105 [pii].
- [268] M.R. Forwood, A.W. Parker, Microdamage in response to repetitive torsional loading in the rat tibia, *Calcif. Tissue Int.* 45 (1989) 47–53.
- [269] W.E. Caler, D.R. Carter, Bone creep-fatigue damage accumulation, *J. Biomech.* 22 (1989) 625–635. doi:10.1016/0021-9290(89)90013-4.
- [270] W.T. George, D. Vashishth, Influence of phase angle between axial and torsional loadings on fatigue fractures of bone, *J. Biomech.* 38 (2005) 819–825.
doi:10.1016/j.jbiomech.2004.05.008.
- [271] D. Vashishth, K.E. Tanner, W. Bonfield, Fatigue of cortical bone under combined axial-torsional loading, *J. Orthop. Res.* 19 (2001) 414–420.
- [272] D. Carter, W. Hayes, Compact bone fatigue damage: a microscopic examination, *Clin Orthop Relat Res.* 127 (1977) 265–274.

- [273] M.-G. Ascenzi, J. Gill, A. Lomovtsev, Orientation of collagen at the osteocyte lacunae in human secondary osteons, *J. Biomech.* 41 (2008) 3426–3435. doi:10.1016/j.jbiomech.2008.09.010.
- [274] M. Ascenzi, A. Roe, The osteon: the micromechanical unit of compact bone, *Front Biosci Landmark.* 17 (2012) 1551–1581.
- [275] H. Peterlik, P. Roschger, K. Klaushofer, P. Fratzl, From brittle to ductile fracture of bone, *Nat. Mater.* 5 (2006) 52–55. doi:nmat1545 [pii]; 10.1038/nmat1545 [doi].
- [276] A. Ascenzi, E. Bounucci, The ultimate tensile strength of single osteons, *Acta. Anat.* 58 (1964) 160–183.
- [277] A. Ascenzi, A. Benvenuti, E. Bonucci, The Tensile Properties of Single Osteonic Lamellae: Technical Problems and Preliminary Results, *J. Biomech.* 15 (1982) 29–37.
- [278] A. Ascenzi, P. Baschieri, A. Benvenuti, The Bending Properties of Single Osteons, *J Biomech.* 23 (1990) 763–771.
- [279] N. Wasserman, B. Brydges, S. Searles, O. Akkus, In vivo linear microcracks of human femoral cortical bone remain parallel to osteons during aging, *Bone.* 43 (2008) 856–861. doi:10.1016/j.bone.2008.07.238.
- [280] T. Diab, D. Vashishth, Morphology, localization and accumulation of in vivo microdamage in human cortical bone, *Bone.* 40 (2007) 612–618. doi:10.1016/j.bone.2006.09.027.
- [281] P. Zioupos, J.D. Currey, Changes in the stiffness, strength, and toughness of human cortical bone with age, *Bone.* 22 (1998) 57–66. doi:S8756328297002287 [pii].
- [282] F. Evans, R. Vincentelli, Relations of the compressive properties of human cortical bone to histological structure and calcification, *J Biomech.* 7 (1974) 1–10.
- [283] M. Ascenzi, M. Andreuzzi, J. Fau-Kabo, J. Kabo, Mathematical Modeling of Human

- Secondary Osteons, Scanning. 26 (2004) 25–35.
- [284] J.D. Michelson, A. Myers, R. Jinnah, Q. Cox, M. Van Natta, Epidemiology of hip fractures among the elderly. Risk factors for fracture type, *Clin Orthop Relat Res.* (1995) 129–135.
- [285] A. Winter, H. Bradman, C. Fraser, G. Holt, The management of intracapsular hip fractures, *Orthop. Trauma.* 30 (2016) 93–102. doi:10.1016/j.mporth.2016.03.003.
- [286] T. Tang, V. Ebacher, P. Cripton, P. Guy, H. McKay, R. Wang, Shear deformation and fracture of human cortical bone., *Bone.* 71 (2015) 25–35. doi:10.1016/j.bone.2014.10.001.
- [287] M.E. Muller, S. Nazarian, [Classification of fractures of the femur and its use in the A.O. index (author’s transl)]., *Rev. Chir. Orthop. Reparatrice Appar. Mot.* 67 (1981) 297–309.
- [288] M.M. Juszczuk, L. Cristofolini, M. Salvà, L. Zani, E. Schileo, M. Viceconti, M. Salva, L. Zani, E. Schileo, M. Viceconti, Accurate in vitro identification of fracture onset in bones: Failure mechanism of the proximal human femur, *J. Biomech.* 46 (2013) 158–164. doi:10.1016/j.jbiomech.2012.11.013.
- [289] H.W.. Huiskes, J.D. Janssen, T.J.J.. Sloof, A detailed comparison of experimental and theoretical stress-analysis of a human femur, *Mech. Prop. Bone.* 45 (1983) 211–234.
- [290] L. Cristofolini, G. Conti, M. Juszczuk, S. Cremonini, S. Van Sint Jan, M. Viceconti, Structural behaviour and strain distribution of the long bones of the human lower limbs, *J. Biomech.* 43 (2010) 826–835. doi:http://dx.doi.org/10.1016/j.jbiomech.2009.11.022.
- [291] L. Cristofolini, M. Juszczuk, F. Taddei, M. Viceconti, Strain distribution in the proximal human femoral metaphysis., *Proc. Inst. Mech. Eng. H.* 223 (2009) 273–288.
- [292] L. Fabeck, M. Tolley, M. Rooze, F. Burny, Theoretical study of the decrease in the femoral neck anteversion during growth., *Cells. Tissues. Organs.* 171 (2002) 269–275. doi:63127.
- [293] G.N. Duda, M. Heller, J. Albinger, O. Schulz, E. Schneider, L. Claes, Influence of muscle

- forces on femoral strain distribution, *J. Biomech.* 31 (1998) 841–846.
doi:[http://dx.doi.org/10.1016/S0021-9290\(98\)00080-3](http://dx.doi.org/10.1016/S0021-9290(98)00080-3).
- [294] A. Aamodt, J. Eine, E. Andersen, S. Husby, In Vivo Measurements Show Tensile Axial Strain in the Proximal Lateral Aspect of the Human Femur, *J. Orthop. Res.* 15 (1997) 927–931.
- [295] R.E. Field, N. Rushton, Proximal femoral surface strain gauge analysis of a new epiphyseal prosthesis, *J. Biomed. Eng.* 11 (1989) 123–129. doi:[http://dx.doi.org/10.1016/0141-5425\(89\)90121-0](http://dx.doi.org/10.1016/0141-5425(89)90121-0).
- [296] S. Gilchrist, K.K. Nishiyama, P. de Bakker, P. Guy, S.K. Boyd, T. Oxland, P.A. Crompton, Proximal femur elastic behaviour is the same in impact and constant displacement rate fall simulation, *J. Biomech.* 47 (2014) 3744–3749.
doi:<http://dx.doi.org/10.1016/j.jbiomech.2014.06.040>.
- [297] J.. H. Keyak, S.. A. Rossi, K.. Jones, C.. Les, H.. Skinner, Prediction of fracture location in the proximal femur using finite element models, *Med. Eng. Phys.* 23 (2001) 657–664.
doi:[10.1016/S1350-4533\(01\)00094-7](http://dx.doi.org/10.1016/S1350-4533(01)00094-7).
- [298] K.E. Naylor, E. V. McCloskey, R. Eastell, L. Yang, Use of DXA-based finite element analysis of the proximal femur in a longitudinal study of hip fracture, *J. Bone Miner. Res.* 28 (2013) 1014–1021. doi:[10.1002/jbmr.1856](http://dx.doi.org/10.1002/jbmr.1856).
- [299] R.D. Carpenter, G.S. Beaupré, T.F. Lang, E.S. Orwoll, D.R. Carter, G.S. Beaupre, T.F. Lang, E.S. Orwoll, D.R. Carter, New QCT analysis approach shows the importance of fall orientation on femoral neck strength, *J. Bone Miner. Res.* 20 (2005) 1533–1542.
doi:[10.1359/JBMR.050510](http://dx.doi.org/10.1359/JBMR.050510) [doi].
- [300] E. Verhulp, B. van Rietbergen, R. Huiskes, Load distribution in the healthy and osteoporotic

- human proximal femur during a fall to the side., *Bone*. 42 (2008) 30–5. doi:10.1016/j.bone.2007.08.039.
- [301] E. Dall’Ara, B. Luisier, R. Schmidt, F. Kainberger, P. Zysset, D. Pahr, A nonlinear QCT-based finite element model validation study for the human femur tested in two configurations in vitro, *Bone*. 52 (2013) 27–38. doi:10.1016/j.bone.2012.09.006.
- [302] D. Dragomir-Daescu, J. Op Den Buijs, S. McEligot, Y. Dai, R.C. Entwistle, C. Salas, L.J. Melton, K.E. Bennet, S. Khosla, S. Amin, Robust QCT/FEA models of proximal femur stiffness and fracture load during a sideways fall on the hip, *Ann. Biomed. Eng.* 39 (2011) 742–755. doi:10.1007/s10439-010-0196-y.
- [303] H.M.M. Frost, Presence of microscopic cracks in vivo in bone, *Bull. Henry Ford Hosp.* 8 (1960) 25–35.
- [304] M.B. Schaffler, K. Choi, C. Milgrom, Aging and matrix microdamage accumulation in human compact bone, *Bone*. 17 (1995) 521–525.
- [305] M.R. Forwood, D.B. Burr, Y. Takano, D.F. Eastman, P.N. Smith, J.D. Schwardt, Risedronate treatment does not increase microdamage in the canine femoral neck., *Bone*. 16 (1995) 643–50. doi:10.1016/8756-3282(95)00120-3.
- [306] P. Zioupos, On microcracks, microcracking, in-vivo, in vitro, in-situ and other issues, *J. Biomech.* 32 (1999) 209-211-259. doi:S0021929098001468 [pii].
- [307] P. Zioupos, In vivo fatigue microcracks in human bone: material properties of the surrounding bone matrix, *Eur. J. Morphol.* 42 (2005) 31–41.
- [308] P. Zioupos, Accumulation of in-vivo fatigue microdamage and its relation to biomechanical properties in ageing human cortical bone, *J. Microsc.* 201 (2001) 270–278. doi:jmi783 [pii].
- [309] H. Oxlund, L. Mosekilde, G. Ortoft, Reduced concentration of collagen reducible cross

- links in human trabecular bone with respect to age and osteoporosis., *Bone*. 19 (1996) 479–84. doi:10.1016/S8756-3282(96)00283-9.
- [310] N. Fratzl-Zelman, R. Morello, B. Lee, F. Rauch, F.H. Glorieux, B.M. Misof, K. Klaushofer, P. Roschger, CRTAP deficiency leads to abnormally high bone matrix mineralization in a murine model and in children with osteogenesis imperfecta type VII, *Bone*. 46 (2010) 820–826. doi:10.1016/j.bone.2009.10.037.
- [311] J. Tam, D. Merino, Stochastic optical reconstruction microscopy (STORM) in comparison with stimulated emission depletion (STED) and other imaging methods., *J. Neurochem.* 135 (2015) 643–58. doi:10.1111/jnc.13257.
- [312] M.-G. Ascenzi, V.P. Liao, B.M. Lee, F. Billi, H. Zhou, R. Lindsay, F. Cosman, J. Nieves, J.P. Bilezikian, D.W. Dempster, Parathyroid hormone treatment improves the cortical bone microstructure by improving the distribution of type I collagen in postmenopausal women with osteoporosis, *J. Bone Miner. Res.* 27 (2012) 702–712. doi:10.1002/jbmr.1497.
- [313] M.G. Ascenzi, J. Chin, J. Lappe, R. Recker, Non-osteoporotic women with low-trauma fracture present altered birefringence in cortical bone, *Bone*. 84 (2016) 104–112. doi:10.1016/j.bone.2015.10.010.
- [314] C.M. Riggs, L.E. Lanyon, A. Boyde, Functional associations between collagen fibre orientation and locomotor strain direction in cortical bone of the equine radius, *Anat. Embryol. (Berl)*. 187 (1993) 231–238. doi:10.1007/BF00195760.
- [315] J.G. Skedros, S.D. Mendenhall, C.J. Kiser, H. Winet, Interpreting cortical bone adaptation and load history by quantifying osteon morphotypes in circularly polarized light images, *Bone*. 44 (2009) 392–403. doi:10.1016/j.bone.2008.10.053.
- [316] K.E. Keenan, C.S. Mears, J.G. Skedros, Utility of osteon circularity for determining species

- and interpreting load history in primates and nonprimates, *Am. J. Phys. Anthropol.* 162 (2017) 657–681. doi:10.1002/ajpa.23154.
- [317] A. Boyde, P. Bianco, M. Portigliatti Barbos, A. Ascenzi, Collagen orientation in compact bone: I. A new method for the determination of the proportion of collagen parallel to the plane of compact bone sections, *Metab. Bone Dis. Relat. Res.* 5 (1984) 299–307. doi:10.1016/0221-8747(84)90017-1.
- [318] M. Portigliatti Barbos, P. Bianco, A. Ascenzi, A. Boyde, Collagen orientation in compact bone: II. Distribution of lamellae in the whole of the human femoral shaft with reference to its mechanical properties, *Metab. Bone Dis. Relat. Res.* 5 (1984) 309–315. doi:10.1016/0221-8747(84)90018-3.
- [319] K.E. Ensrud, Epidemiology of fracture risk with advancing age, *Journals Gerontol. - Ser. A Biol. Sci. Med. Sci.* 68 (2013) 1236–1242. doi:10.1093/gerona/glt092.

Appendices

Appendix A chapter 3—supplemental materials

Donor information, total proximal femur areal bone mineral density (aBMD) and *T*-scores

Table S3. 1 Donor sex, age, side from which the femur was obtained and DXA-measured BMD and *T*-scores for the femora used in this study

Donor	Sex	Age (years)	Side	aBMD (g/cm²)	<i>T</i>-score
07004	F	73	L	0.640	-2.5
08034	M	66	L	1.008	-0.2
08038	M	64	L	0.596	-2.9
08050	M	71	L	1.166	0.9
11049	M	73	L	0.877	-1.0
11051	F	74	L	0.459	-4.0

Morphological features associated with femoral neck hypermineralization

With the BSE signals, various morphological features associated with hypermineralization were observed at the femoral neck. In addition to the typical hypermineralized periosteum and calcified fibrocartilage as shown in Fig. 3.2, hypermineralization underneath circumferential lamellar bone, chondrocyte lacunae, tidemarks, and hypermineralized osteocyte lacunae were also observed.

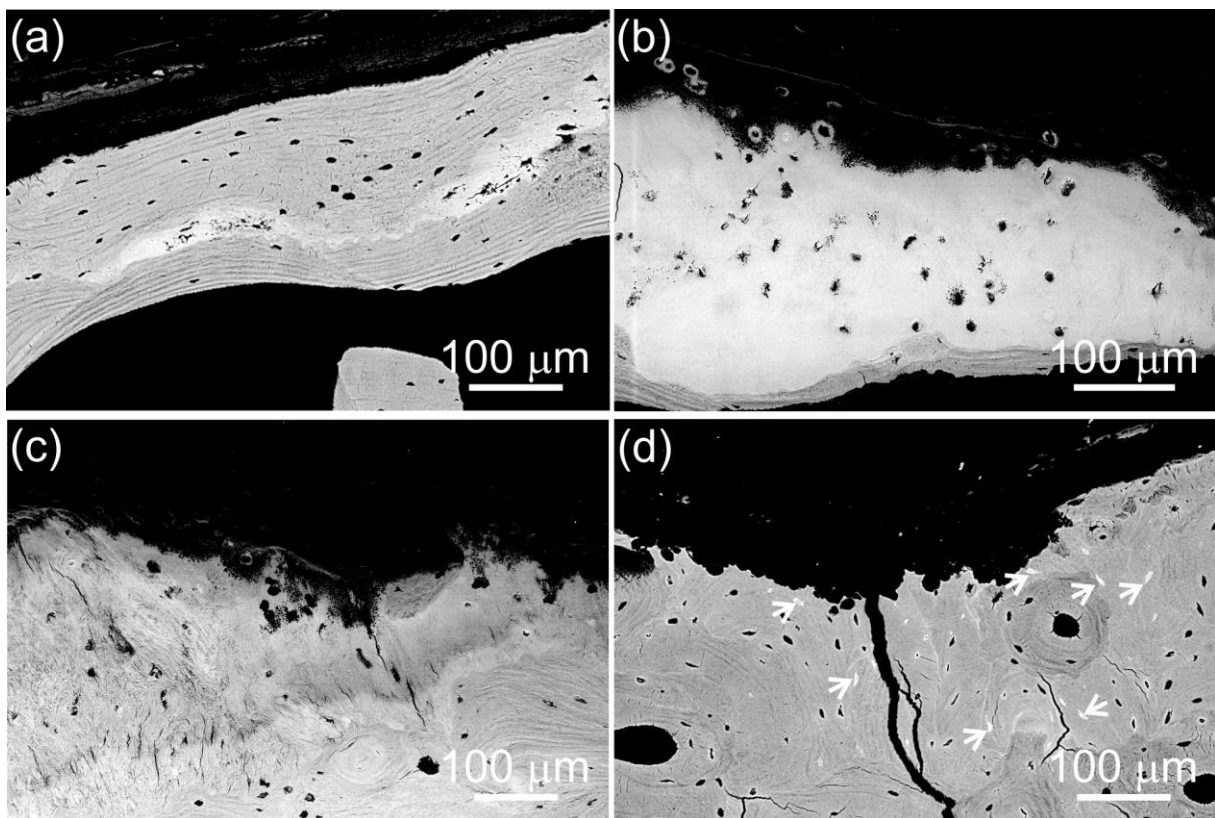


Fig. S3. 1 BSE images showing various features associated with hypermineralization at femoral neck: (a) Hypermineralized tissue appears underneath periosteal lamellar bone; (b) Region of calcified fibrocartilage showing characteristic chondrocyte lacunae; (c) Typical tidemark features associated with cartilaginous tissue; (d) Multiple mineral-filled osteocytes lacunae (arrows) showing brighter and higher intensities near the peripheral region of cortical bone.

Hypermineralization with optical microscopy and backscattered electron imaging

Based on the non-lamellar features, OM could be used for initial screening of the potential regions containing hypermineralization. When there was large area fraction of hypermineralized tissue in the cortical bone, it was relatively easy to observe. However, when the thickness of the hypermineralized tissue was limited, OM was not adequate for distinguishing hypermineralization from lamellar bone. Under BSE signal, due to the clear grey-level contrast, hypermineralized region can be easily identified.

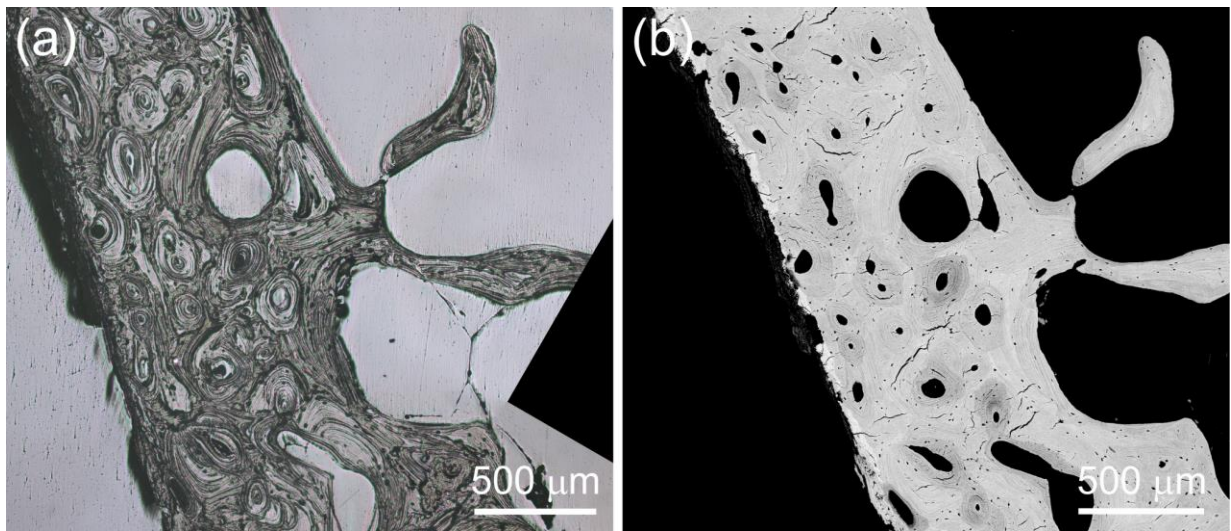


Fig. S3. 2 OM and BSE images showing hypermineralization in femoral neck: (a) OM image shows no apparent hypermineralized tissue at the periosteal lamellar bone; (b) The same region under BSE signal clearly demonstrates a thin layer of hypermineralization at the peri-cortical bone.

Validation of backscattered electron imaging linearity

The linear correlation between the BSE grey-level and the atomic number was calibrated before mineralization quantification. Four standard materials were used: carbon (C, $Z = 6$), magnesium fluoride (MgF_2 , $Z = 10.17$), aluminum (Al, $Z = 13$), and hydroxyapatite (HA, $Z = 14.06$).

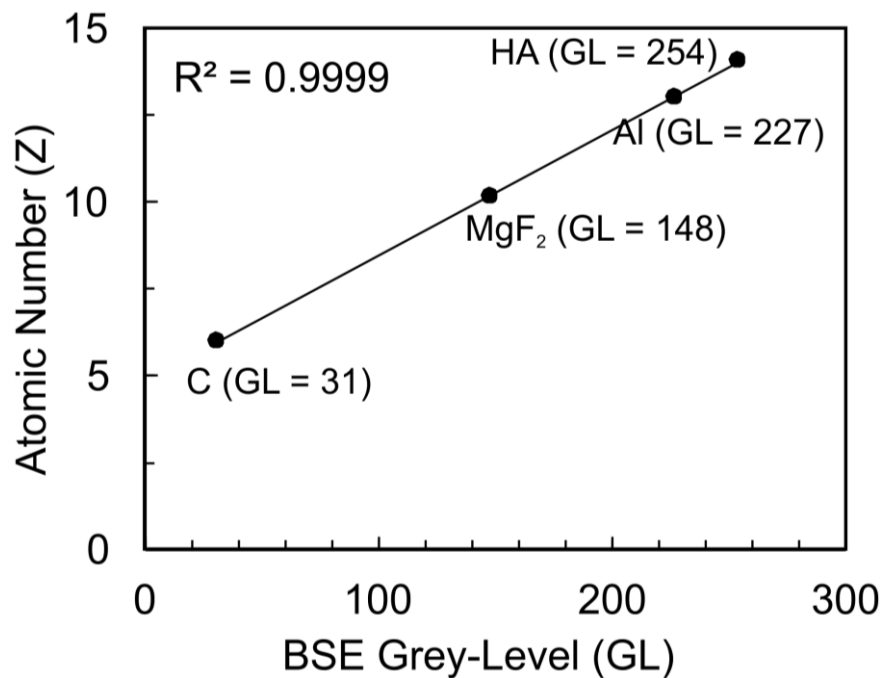


Fig. S3. 3 Calibration between BSE grey-level and atomic number.

Microhardness in calcified fibrocartilage

In some regions of the hypermineralized tissue, particularly at the intertrochanter where large amount of hypermineralized fibrocartilage is present, cracks could not be introduced by large indentation force, and the microhardness as measured in the calcified fibrocartilage was lower than that of the lamellar bone.

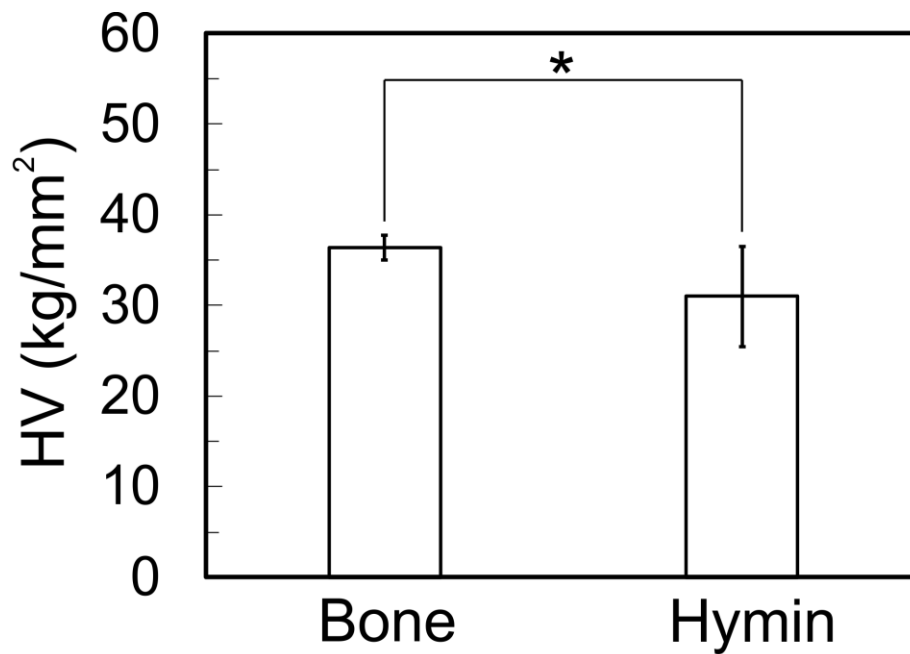


Fig. S3. 4 Vickers hardness as measured in the lamellar bone and the calcified fibrocartilage ($p < 0.05$, marked by “*”).

Appendix B chapter 4—supplemental materials

Donor information, total proximal femur areal bone mineral density (aBMD) and *T*-scores

Table S4. 1 Donor sex, age, side from which the femur was obtained and DXA-measured BMD and *T*-scores for the femora used in this study

Donor	Sex	Age (years)	Side	aBMD (g/cm²)	<i>T</i>-score
06021	M	79	L	0.708	-2.2
08016	F	74	L	0.627	-2.6
08058	M	62	L	0.861	-1.1
10031	M	76	L	0.809	-1.5
11026	F	78	L	NA	NA
11064	F	70	L	0.690	-2.1

Carbonate-to-phosphate ratio

Carbonate-to-phosphate ratio indicates the degree of carbonation in the mineralized tissue. This ratio has been shown to be correlated with the size and crystallinity of the bone minerals embedded in the organic matrix [136]. The current study found a slightly higher carbonate-to-phosphate ratio in the hypermineralized tissue than in lamellar bone, which agrees well with the SAXS/WAXS finding that bone minerals decreased in size in the hypermineralized region.

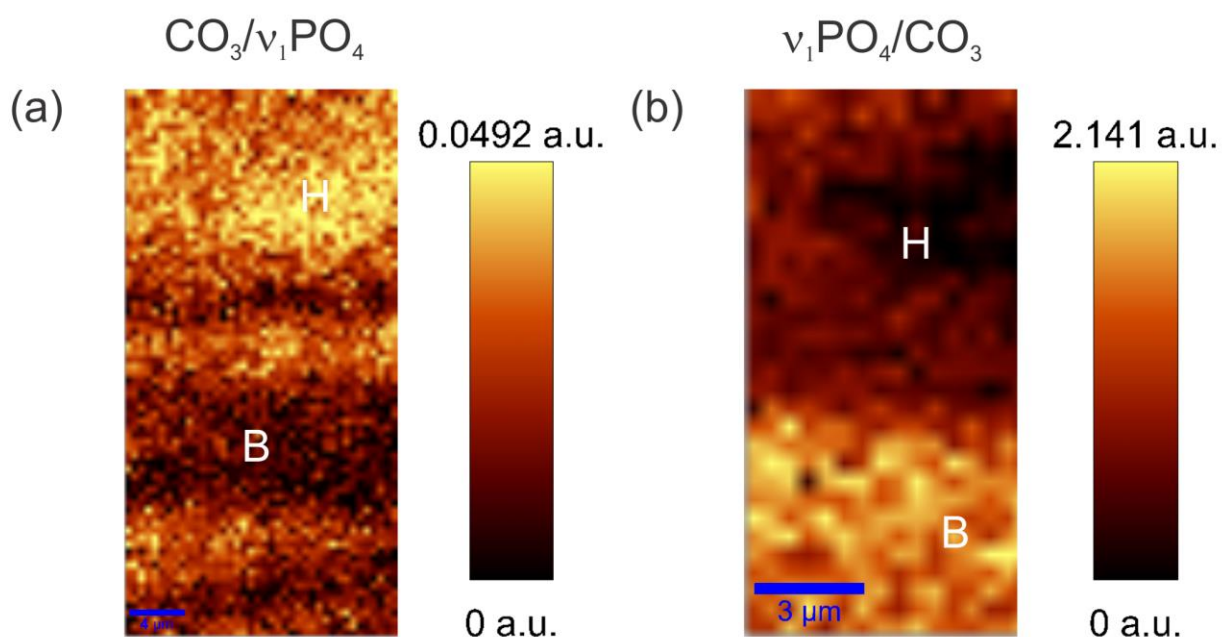


Fig. S4. 1 Representative Raman microspectroscopy mapping images obtained from two femoral neck samples under 0° polarization angle (relative to the horizontal direction) showing relative *B*-type carbonate and phosphate contents: (a) A slightly higher degree of carbonate substitution was found in hypermineralized periosteum (H); (b) Phosphate-to-carbonate ratio shows a higher phosphate content in lamellar bone (B) than in hypermineralized fibrocartilage (H). The color scale and the intensity values for each image are shown on the right color bars.

Mineral thickness, length and degree of orientation measured by synchrotron radiation

Synchrotron radiation provides higher resolution on the bone mineral thickness (T) and the degree of orientation (ρ). Additionally, it enables the simultaneous measurement of mineral length (L). Here, I provided T , L , and ρ values of the three femoral neck samples that contained hypermineralized fibrocartilage. In consistent with the laboratory SAXS results, T was significantly smaller in the hypermineralized tissue (Hymin) than in lamellar bone for all the three samples. The same decreasing trend was found for L . The observation of ρ differed from laboratory results: two samples had lower values in the hypermineralized tissue than that of the lamellar bone. This might be the result of the improved resolution of the synchrotron source, which measured fewer bone lamellae within the illuminated bone volume.

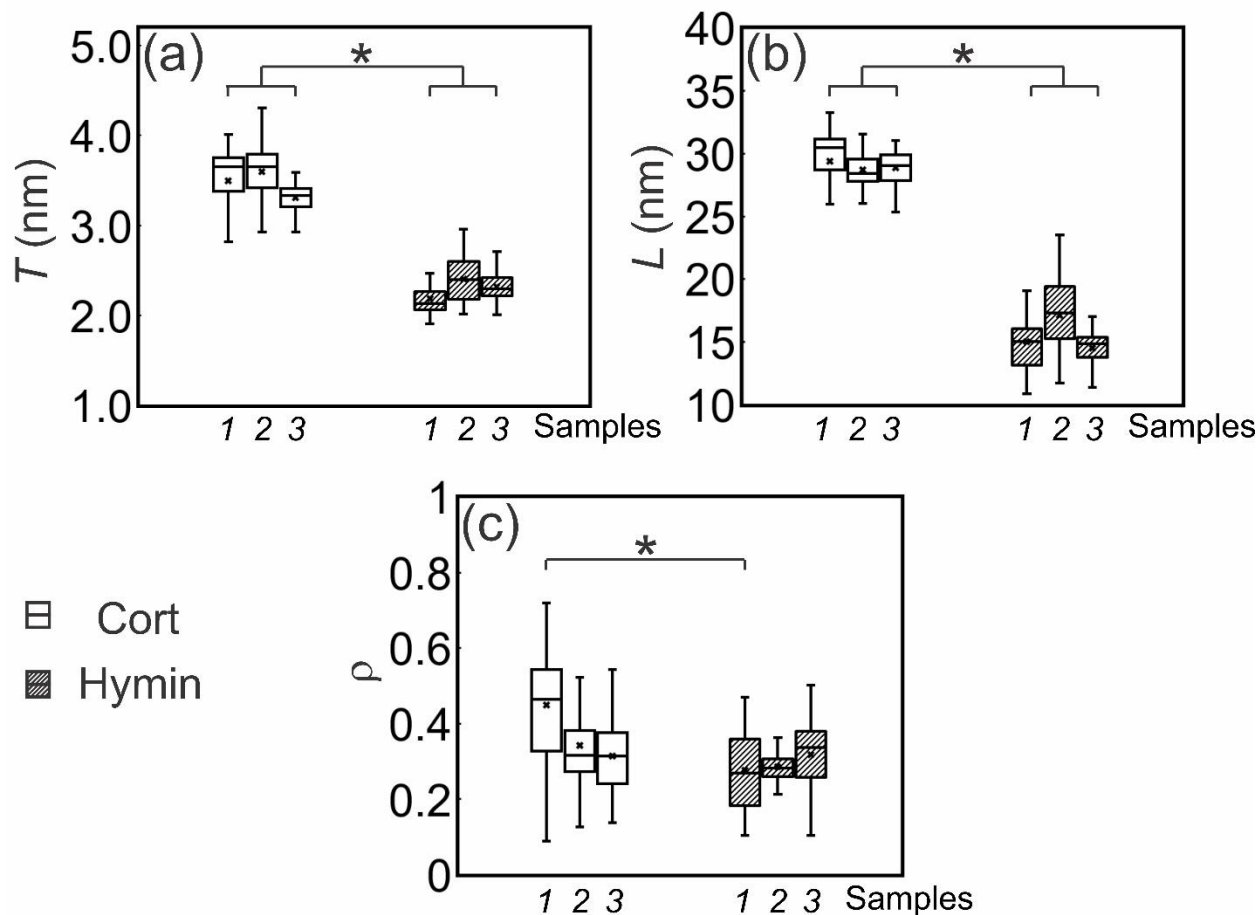


Fig. S4. 2 Combined SAXS and WAXS synchrotron measurement on three femoral neck samples containing hypermineralized fibrocartilage and cortical bone (numbers at the x axis represent sample number): (a) Box plot of the mineral platelet thickness T ; (b) The average length L of the mineral platelets; (c) The degree of orientation ρ of the mineral platelets. The mean and the median values for each sample are marked by a ‘*’ sign and a horizontal line, respectively. Bars give the first and third quartile of measured values of each tissue (white, cortical bone; dashed, hypermineralized fibrocartilage). Statistically smaller T and L values were found in the hypermineralized region (Hymin) than that in the cortical bone (Cort) ($p < 0.05$, indicated by*).

G(x) curves and the fitted parameters obtained from laboratory SAX measurements

The $G(x)$ curves as measured by the laboratory X-ray scattering resembled the features as observed with synchrotron radiation, in the way that the peak location and the slope of the curves obtained from the hypermineralized tissue differed from cortical and trabecular bone. Although there were more fluctuations as shown in Fig. S4.3a, possibly due to the limited resolution of the laboratory source, the differences among the curves obtained from different types tissue were apparent. Such difference was also seen in the pattern of the fitted parameters (Fig. S4.3b). $2\pi/\alpha$ and $T2\pi/\beta$ values for cortical and trabecular bone were in the range of 2.7-3.6 and 11-15, respectively. In contrast, the values of $2\pi/\alpha$ and $T2\pi/\beta$ for the hypermineralized tissue scattered at the higher range (i.e. 3.7-5.5 and 13-24, respectively).

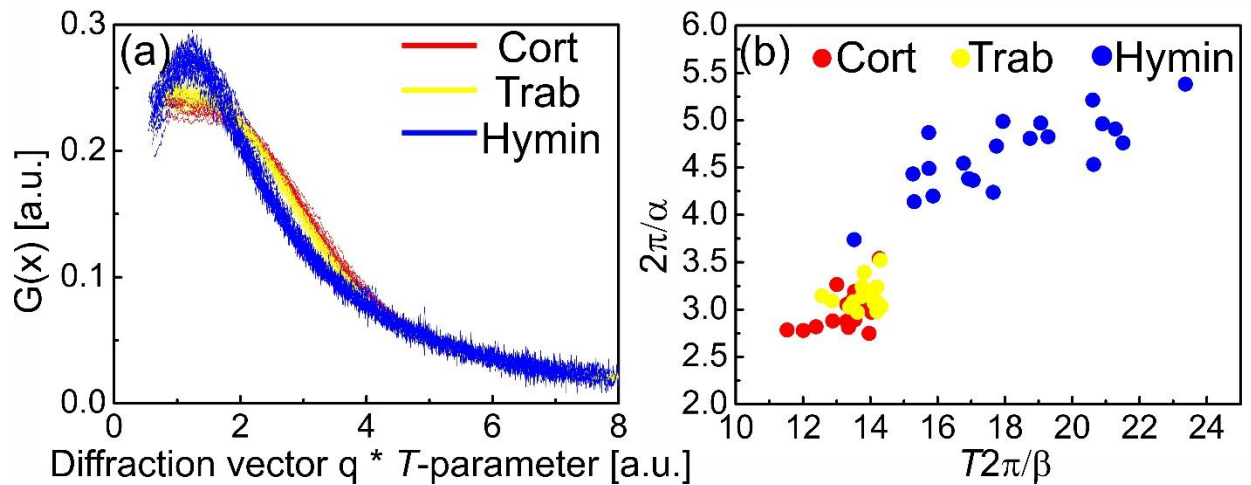


Fig. S4. 3 Spatial organization of mineral platelets measured by laboratory SAXS on a femoral neck sample containing hypermineralized periosteum (Hymin) and lamellar bone: (a) Typical $G(x)$ curves obtained from cortical bone (Cort), trabecular bone (Trab) and hypermineralized periosteum (Hymin); (b) Plot of $2\pi/\alpha$ versus $T2\pi/\beta$ obtained from (a) showing a different pattern between lamellar bone (red and yellow dots) and mineralized periosteum (blue dots).

Appendix C chapter 5—supplemental materials

Pre-existing microcracks

Before the mechanical tests, all the specimens were stained with xylene orange, and examined under an optical microscope (Nikon Eclipse E600) with a PlanFluor objective lens (10 \times /0.3 NA). Only a few (i.e. 3-5 per specimen) cracks were observed in the twenty specimens out of the total twenty-nine. The morphology of the pre-existing cracks was irregular (Fig. S5.1), which clearly differed from the mechanical testing created cracks (details described in *Microcracking* section). Also notice that the pre-existing cracks located away from the gauge section, thus had minimum effects on the shear microcracking analysis.

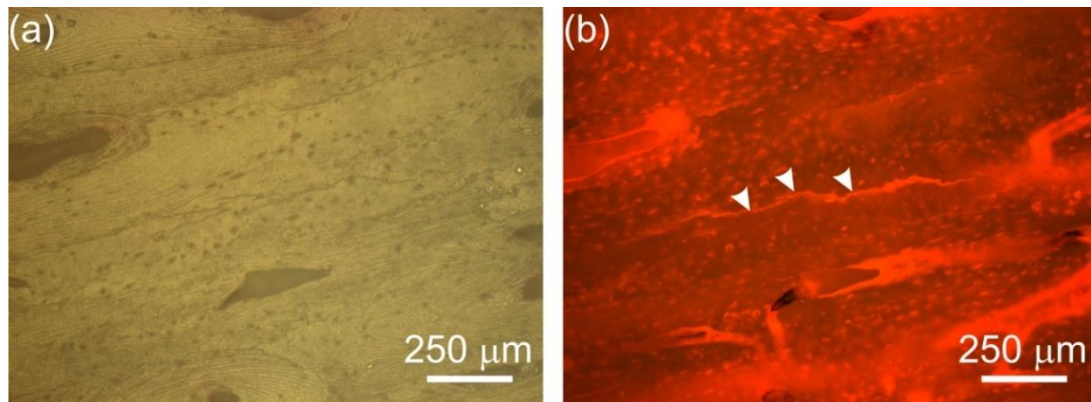


Fig. S5. 1 Optical microscopic images of representative pre-existing cracks in human cortical bone specimens: (a) White light microscopic image showing the crack opening; (b) Fluorescent microscopic image with red color signals from xylene orange showing the cracks in the same area. Arrow heads point at the pre-existing cracks.

Different failure modes of 30°-oriented specimens

Interestingly, four out of the nine 30° specimens failed with the cracks initiating outside the notch area during mechanical testing, and the only difference was that the specimens were horizontally flipped, as shown in Fig. S5.2a and b. When the shear force was loaded as the resolved principal normal stress was oriented at 75° to the long bone axis, fracture started near the notch tip. On the contrary, the specimens failed at the edge, when they were loaded with the resolved principal normal stress more or less parallel to the long bone axis. The latter situation was classified as invalid due to the unacceptable failure mode, as described in the ASTM standard (ASTM D5379/D5379M).

The average shear strain during inelastic deformation obtained from DIC for the above two loading conditions shows a big difference (Fig. S5.2c and d). For the specimens failed at the edge, no shear strain concentration occurred, indicating the fracture was caused by other stress modes rather than shear. More interestingly, compared to the notched-initiated cracking specimens, the TR* values for those failed at sides (Fig. S5.2e) showed an increasing trend in positive zone, implying an increasing tensile strain.

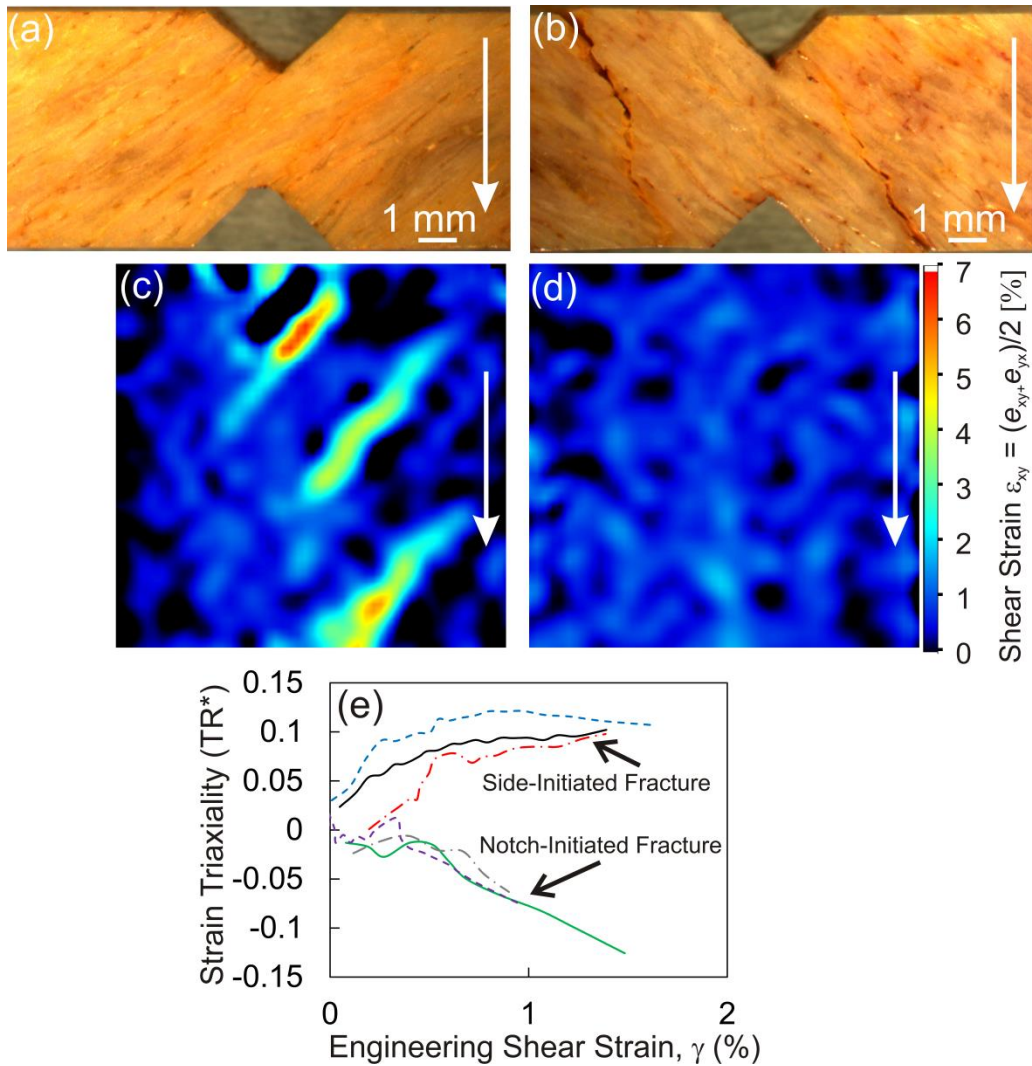


Fig. S5. 2 Macroscopic fracture patterns (a) and (b) and shear strain state (c-e) for 30° specimens tested under different loading conditions. When the resolved principle stress angled at 15° to the long bone axis, fracture started at the tip of notch (a) with clear shear strain concentration band (c); In contrast, when the resolved principle stress was oriented at 75° to the long bone axis, the fracture was initiated at edge (b) with no shear strain concentration (d); The in-plane strain triaxiality ratio (TR*) vs. engineering shear strain curves showed clear different trends (e): the specimens fractured from the edge show increasing positive value, and the ones with cracks starting from the notch area show decreasing negative value. The arrows heads in (a) and (b) point at the fracture planes. The side arrows in (c) and (d) indicate shear loading direction.

Different types of microcracks found in the human cortical bone under shear

Other than the unique arc-shaped microcracks, cement line, tensile and radial microcracks were also observed. As none of them had more than 20 % occurrence frequency (Fig. 5.8b), they were not the major cracking mechanisms when bone is loaded under shear.

The radial microcracks (Fig. S5.3d), looking very similar to the compression-induced shear cracks, were also found. According to a previous study, when osteonal bone was compressed transversely in the plane perpendicular to the osteons' long axes, shear stress concentration developed at the four quadrants of each osteon, resulting in arc-shaped microcracks within each set of the cross-hatched damage. Although the angle and the asymmetric distribution of the radial cracks in current study differed from the compression-induced shear cracks, the sub-lamellar features were similar: the cracks radiated from Haversian canal, and each crack would widen into cross-lined band. Since the radial crack was only spotted at the later-damaged state, they were likely to be created by a mix of twisting and bending when the specimens began to misalign in the fixture.

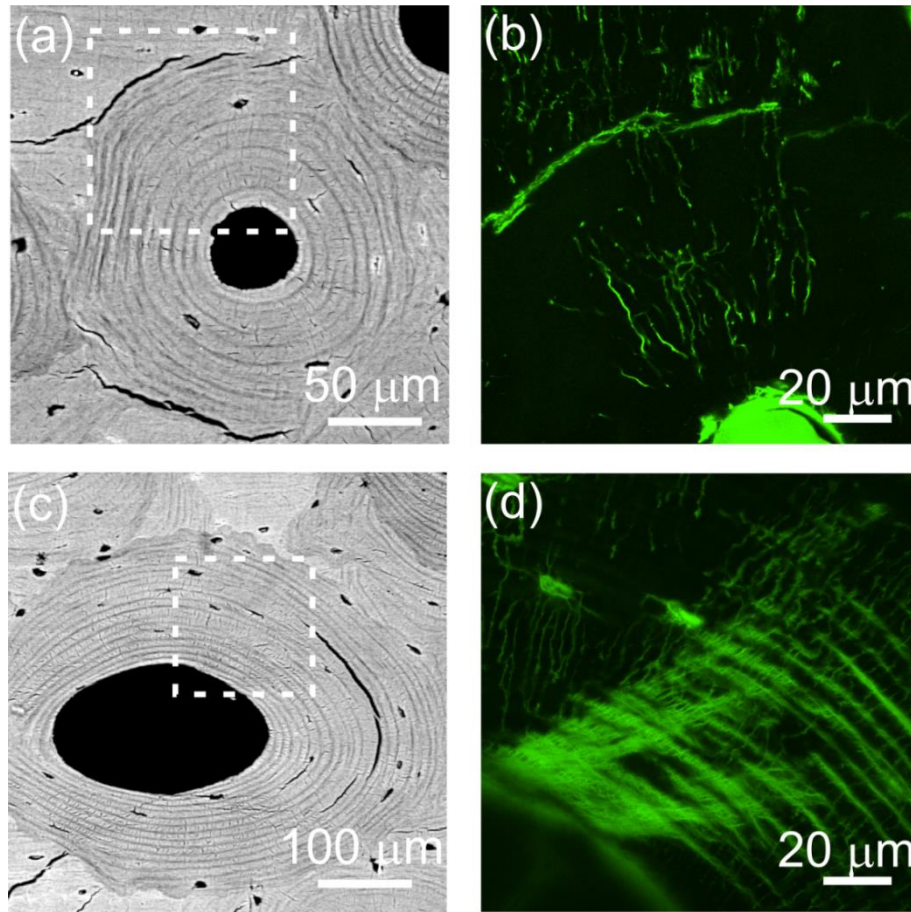


Fig. S5. 3 Laser scanning confocal microscope (LSCM) image of microcracking patterns (other than arc-shaped) on transverse plane (with respect to the long bone axis) cut between the two notches. (a) and (c) BSE images showing the Haversian structure; (b) LSCM image taken from the top left in (a) showing cement line crack; (d) LSCM picture imaged from the top left quadrant in (c) showing radial crack resembling similarities from compression-created shear cracks.

Appendix D chapter 6—supplemental materials

Information on all the retrieved femoral neck fractured samples

In the selected samples, 23 were from female patients and only one was retrieved from male patient. This is a reflection of the nature of hip fracture risk which is significantly higher in females [2]. The age of the patients, as shown in Table S6.1, are also older than 65 years old. This is in line with the previous report where the hip fracture risk increases exponentially after the age of 65 [319].

Table S6. 1 Sex, Age, and the fracture side (L= left, R= right) from which specimens were obtained

Cases	Sex	Age (years)	Side
3007	F	82	L
3010	F	65	L
3017	F	87	R
3019	F	92	L
3021	F	84	L
3028	F	71	L
3030	F	87	R
3032	F	71	L
3053	F	85	R
3056	F	90	R
3058	F	96	L
3062	F	86	R
3084	F	83	R

Cases	Sex	Age (years)	Side
3089	F	72	R
3090	F	88	L
3094	F	71	L
3095	F	93	R
3099	F	94	R
3101	F	65	R
3103	M	90	R
3109	F	86	R
3110	F	92	R
3113	F	83	L
3115	F	85	R

Macroscopic fractures for all the retrieved femoral neck samples

The samples were selected from a bigger sample pool based on the observation that is if the sample had a complete cortical shell. The posterior fractures were more discernable compared with anterior fractures. Overall, there were 7 U-type fractures, 5 W-type fractures, 10 V-type fractures, and 2 samples with inconclusive fracture patterns.

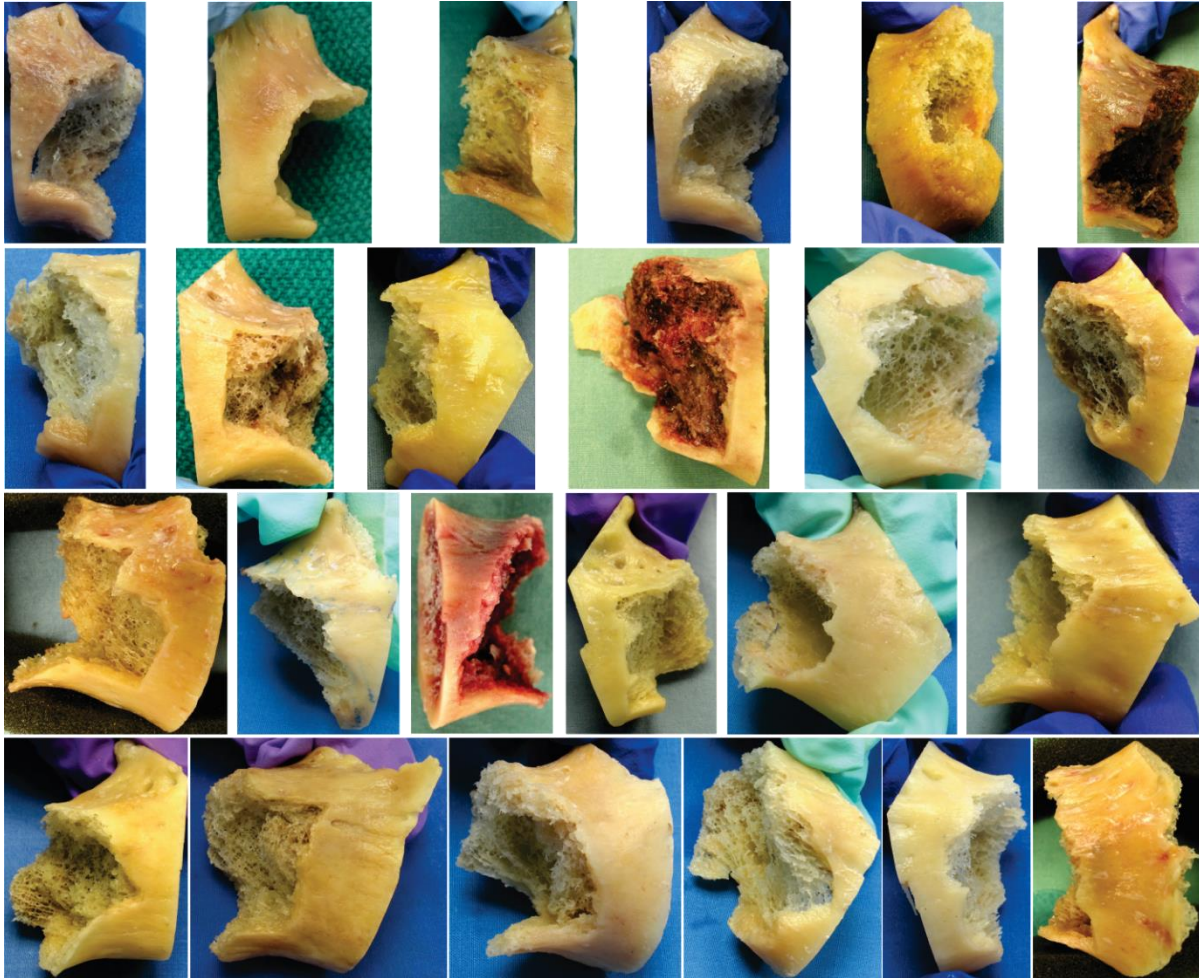


Fig. S6. 1 Retrieved femoral neck samples with final fracture patterns. All the pictures were taken in a typical posterior-anterior view with inferior site down and superior site up. The majority of the samples have a fracture pattern posteriorly resembling a letter “U”, “V” or “W”.

Microcrack density scores at various locations and the highest microcrack density score

For each sector (superior-anterior/SA, superior-central/SC, superior-posterior/SP, inferior-anterior/IA, inferior-central/IC, inferior-posterior/IP), I obtained a microcracking score in the range of 0 to 12, with 0 being no microcracking, and 12 being saturated microcracking in all the four zones (Fig. 6.1d and Fig. 6.3). The sector with the highest microcrack density score within each retrieved sample, as shown in Fig. S6.2b, indicated the region which had the least mechanical competence to resist fracture, thus, provides information on the critical location for fracture initiation.

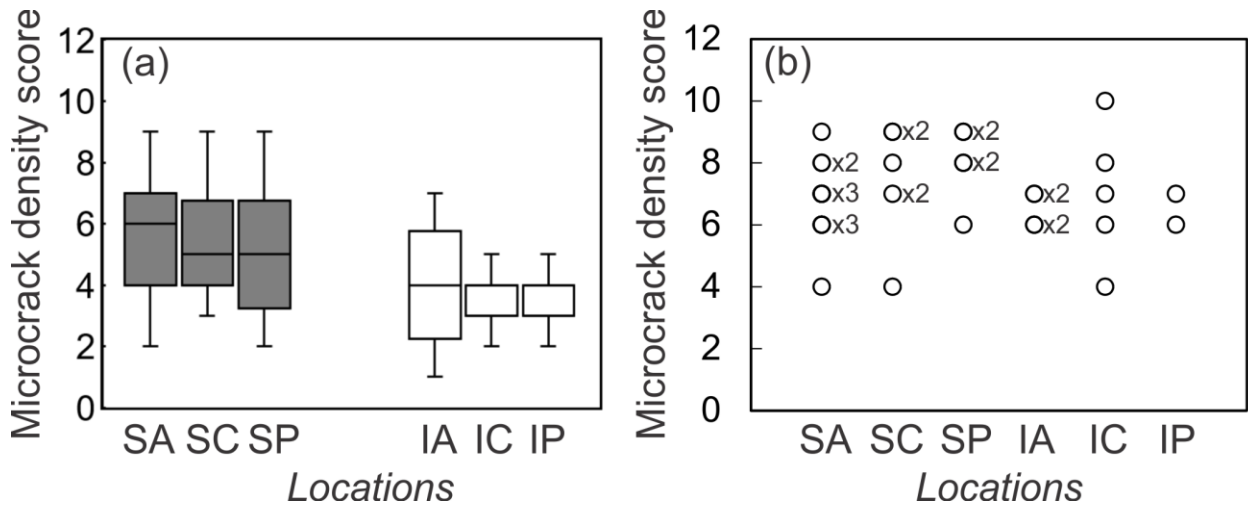


Fig. S6. 2 Microcrack density scores at the six anatomical locations (a) and the location with the highest microcrack density score within each retrieved femoral neck sample (b): (a) Box-plot graph of microcrack density score versus six sites. Higher values were found at the superior site (grey) than at the inferior site (white), but no essential difference was observed within either superior or inferior cortex. The boxes represent 50 % of the data, limited by the upper and lower quartiles, with the median indicated by a bar within each box (median value overlaps with third quartile and first quartile for IC and IP, respectively). The vertical bars indicate the range of the data; (b) In the 24 retrieved femoral neck samples, one or multiple locations within each sample could show the highest microcrack density score. 2 or 3 samples could show the same microcrack density score at the same location (marked by $\times 2$ and $\times 3$, respectively).

Microcrack pattern at the fracture surface of inferior cortical bone

Oversaturated damages at the main fracture surface were frequently seen on the inferior side of the samples. Such pattern is likely a result of the inferior fracture surface rubbing against the proximal portion of the fractured femur after the fracture event either instantaneously or later. Although the occurrence of the oversaturated microcracking pattern in the retrieved samples was over 80 %, it did not affect the conclusion on the dominant type of stress of the entire cortical beam.

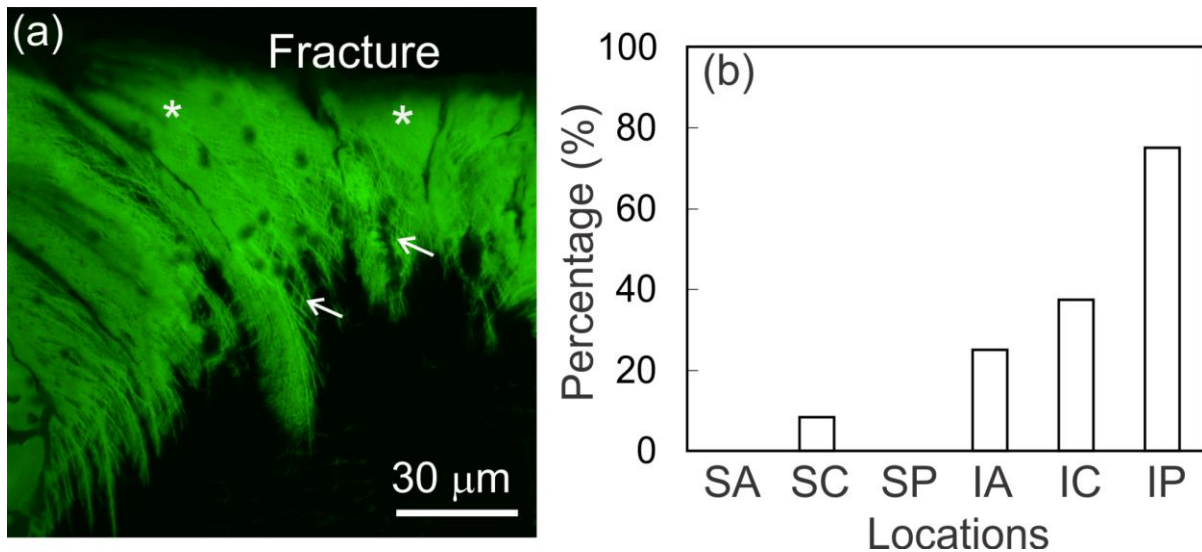


Fig. S6. 3 Local oversaturated damage found at the major fracture, and the percentage of the analyzed sections at six locations showing oversaturated damage: (a) High magnification confocal image showing the typical pattern with oversaturated damage (stars) at the main fracture and associated with cross-hatched microcracks underneath (arrows); (b) The inferior site demonstrated a higher percentage of oversaturated damage compared to the superior site. SA = superior-anterior, SC = superior-central, SP = superior-posterior, IA = inferior-anterior, IC = inferior-central, and IP = inferior-posterior.